

**Case Studies of Surface Engineering Applications  
in Thermo/Fluidic Systems**

by

Mohamad Jafari Gukeh  
M.Sc., University of Illinois at Chicago, 2020  
B.Sc., Sharif University of Technology, 2017

THESIS

Submitted in partial fulfillment of the requirements  
for the degree of Doctor of Philosophy in Mechanical Engineering  
in the Graduate College of the  
University of Illinois at Chicago, 2022

Chicago, Illinois

Defense Committee:

Dr. Constantine Megaridis, Chair and Advisor

Dr. Jie Xu

Dr. Sybil Derrible, Civil, Materials, and Environmental Engineering

Dr. George Gogos, University of Nebraska-Lincoln

Dr. Ranjan Ganguly, Jadavpur University

Copyright by  
Mohamad Jafari Gukeh  
2022

To My Parents

My dearest people in the world who dedicated their life to their children

## ACKNOWLEDGMENT

This journey could not have been completed without the support, encouragement, and help of several people in my life to whom I am so grateful and I need to express my sincere gratitude.

While I am writing this section, I am sitting in my peaceful place in Southern California. It is a lazy Saturday morning in mid July. The sun is shining and I can hear the birds enjoying the sunlight. I have my coffee in hand and thinking how to write this section so that it could be honest in capturing what I want to say. I am not a good writer, so I try to avoid complex words so when I read it again years from now, I would not regret choosing the wrong words. Of course, the first person coming to my mind is my dear supervisor, Dr. Constantine Megaridis. I have read several theses so far and when it comes to this part, I have seen a lot of cliché words used to express complex feelings or gratitude. So, here is what I want to express for my dear advisor: I would always remember the very moment he mentioned my admission to UIC as a PhD student, since it was my happiest moment in my life for a whole lot of reasons. If anyone has an Iranian friend, they would know why I say this. From our very first calls I noticed how supportive, understanding, and knowledgeable he is and it did not take long until I saw all those qualities in person. The PhD journey for every student is different and usually involves a lot of ups and downs, so I was not excluded from this. However, the comfort of having him in my life, a person whom I could honestly talk to and express my feelings without being afraid of his judgement, was a blessing in my life that I would always be grateful for. The ups and downs in my life at UIC were not limited only to my academic adventures, but in my personal life as well.



## ACKNOWLEDGMENT (Continued)

In either case, I have always brought everything to him and I felt so fortunate when I saw how supportive he is no matter how frustrated I was in several circumstances. I would always be thankful for having such a noble, unique, considerate, decent, giving, understanding, trusting, mature and last but not least, knowledgeable scholar and person in my life. Dr. Megaridis, you gave me the life that I was dreaming about and I will always remember that, thank you so much.

Dr. Theodore P. Koukoravas was one of the first persons in my new adventure in the Micro/Nanoscale Fluid Transport (MNFTL) lab and also in the US, from whom I learnt a healthy academic and personal lifestyle. He was such a decent and kind person to me and gave the most constructive advice when I needed it the most. Next is Dr. George Damoulakis also from MNTFL, who taught me several things with no words but with his actions. His dedication to his work, calmness, positivity, and being an open-minded and easy-going person had always attracted me to collaborate with him on various projects. Dear Theodore and George, thank you for being there for me; you will always have a special place in my heart.

Professors Ranjan Ganguly, Jie Xu, Parisa Mirbod, Sushant Anand, Sybil Derrible, and Jarrad Hampton-Marcell deserve special thanks for serving in my committee and/or providing me with useful advice, guidance, comments, and encouragement throughout my PhD studies. I would also like to express my gratitude toward Drs. Craig Zuhlke and George Gogos from the University of Nebraska, Lincoln for the short but so insightful collaboration throughout the ONR-supported projects.

## ACKNOWLEDGMENT (Continued)

I would like to thank my past and present colleagues in MNTFL, Dr. Uddalok Sen, Dr. Souvick Chatterjee, Dr. Reza Ghodsi, Dr. Aritra Ghosh, Dr. Ali Noaman Ibrahim, Dr. Jared M. Morrisette, Dr. Tamal Roy, Arani Mukhopadhyay, Shashwata Moitra, and Sreya Sarkar, who maintained a friendly and positive environment for sharing, learning, and supporting each other without hesitation. My dear friends, thank you all for giving me the opportunity to express and share my ideas, feelings, and concerns, and above all to learn teamwork and discipline from you.

To my parents. I have no doubts that almost every single person in this world is grateful for all the sacrifices that their parents made to get them where they are today. And I am definitely one of those people. I can remember from my early childhood till a few years ago that I could barely see my father for days. He is a such a loving, hard-working, and giving man with a big big heart. My mother on the other hand, dedicated her entire time and energy to raising me and my sister. I can clearly remember her calmness and positivity during our most difficult times, when she never missed a chance for giving love, attention, affection, and support to the family. My dear parents, I love you the most and all my thanks can not meet a fraction of what you have done for us. Thank you!

Finally, to the apple of my eye, Lena. She has been my strength and biggest fan over the past three years. An incredible life partner whose encouragement and support have kept me moving during the most challenging times. Her colorful spirit, vivid personality, and intellectual ability could not be portrayed better as her physical beauty. She is the music that brings color and love to every moment of my life, and I could not be more grateful for that.

## ACKNOWLEDGMENT (Continued)

MJG

## CONTRIBUTIONS OF AUTHORS

The work in Chapter 2 was initially conceptualized by Dr. Ali Noaman Ibrahim. Dr. Ibrahim fabricated the preliminary samples and developed the fabrication process. The author performed the UV exposure tests and measured the contact angles. The author programmed the initial machine learning codes and performed statistical analysis. The final data was collected through sample fabrication by Shashwata Moitra. The author performed the UV exposure tests, contact angle measurements, and machine learning analysis. Dr. Sybil Derrible provided guidance in the machine learning part and the author and Dr. Megaridis wrote the final journal paper. Dr. Megaridis was the primary advisor in all works in this dissertation.

The work in Chapter 3 was initially conceived by Aritra Ghosh for a gas-bubble capturing platform. The idea was later modified by Dr. Uddalok Sen for a single wedge-shaped track. The author designed the setup and performed the experiments and data analysis. Dr. Sen provided insights during the experiments. Dr. Tamal Roy contributed in the theoretical development of the scaling law. Dr. Ranjan Ganguly (Jadavpur University, India) provided technical guidance throughout the work and also helped in manuscript writing. The author wrote the manuscript, which was revised by Drs. Roy, Sen, Ganguly and Megaridis.

The work in Chapters 4, 5, and 6 and Appendices C and D was based upon research supported by the U. S. Office of Naval Research under award number N00014-20-1-2025 to the University of Nebraska-Lincoln via a subcontract to UIC.

## CONTRIBUTIONS OF AUTHORS (Continued)

The work in Chapter 4 was initialized by Dr. George Damoulakis. Later, the test condition was changed by the author. The author fabricated the test setup and performed the experiments and data analysis. Dr. Damoulakis provided technical guidance and performed error propagation. The author wrote the paper and Drs. Damoulakis and Megaridis revised the final manuscript.

The work in Chapter 5 was conceptualized by Drs. Megaridis, Mazumder, and Damoulakis. Mr. Congbo Bao fabricated the power-electronics rig and Dr. Damoulakis performed preliminary experiments. The vapor chamber was further modified by the author and became a test-ready device. The author performed the experiments and data analysis. Arani Mukhopadhyay helped in sample fabrication and setup preparation before test runs. The final manuscript was written by the author, Congbo Bao, and revised by Drs. Damoulakis and Megaridis. An earlier and more limited version of this study was submitted as a paper to the 21st Intersociety Conference on Thermal and Thermomechanical Phenomena in Electronic Systems (ITHERM 2022).

The work in Chapter 6 was conceptualized by the author and Dr. Damoulakis. The author designed and fabricated the setup rig. Also, the author performed all the experimental tests, data analysis, and wrote the paper. Dr. Damoulakis provided technical guidance and revised the manuscript. while Dr. Megaridis revised the final manuscript. An earlier and more limited version of this study appeared as a paper in the ITHERM 2021 conference.

## TABLE OF CONTENTS

<u>CHAPTER</u>	<u>PAGE</u>
<b>1 INTRODUCTION AND BASICS . . . . .</b>	<b>1</b>
1.1 Wetting Fundamentals . . . . .	1
1.1.1 Surface Tension . . . . .	1
1.1.2 Wetting and Contact Angle . . . . .	2
1.1.3 Dynamic Contact Angle . . . . .	5
1.1.4 Laplace Pressure . . . . .	6
1.2 Heat Transfer Fundamentals . . . . .	10
1.2.1 Condensation Heat Transfer . . . . .	11
1.2.1.1 Filmwise Condensation . . . . .	13
1.2.1.2 Dropwise Condensation . . . . .	15
1.2.1.3 DWC Enhancement Techniques . . . . .	17
1.2.1.4 Hybrid Condensation . . . . .	21
1.2.2 Evaporation and Boiling . . . . .	24
1.2.2.1 Thin-Film Evaporation and Capillary-fed Boiling . . . . .	25
1.2.3 Thermal Management of Local Heat Sources . . . . .	31
1.2.3.1 Vapor Chamber . . . . .	35
1.2.3.2 Heat Pipe . . . . .	50
1.3 Thesis Objectives . . . . .	57
1.3.1 Objectives for Chapter 2 . . . . .	57
1.3.2 Objectives for Chapter 3 . . . . .	57
1.3.3 Objectives for Chapter 4 . . . . .	58
1.3.4 Objectives for Chapter 5 . . . . .	58
1.3.5 Objectives for Chapter 6 . . . . .	58
1.4 Scope of Work . . . . .	59
 <b>2 WETTING PROPERTIES OF <math>\text{TiO}_2</math>-COATING, A PREDICTIVE MACHINE LEARNING APPROACH . . . . .</b>	 <b>61</b>
2.1 Background and Motivation . . . . .	61
2.2 Materials and Methods . . . . .	65
2.2.1 Data Preparation . . . . .	65
2.2.2 Machine Learning Methodology . . . . .	71
2.2.3 ML Models . . . . .	73
2.2.4 Model Specification and Evaluation . . . . .	74
2.2.4.1 Variable Scaling . . . . .	74
2.2.4.2 Model Evaluation Metrics . . . . .	75
2.3 Results and Discussion . . . . .	76
2.3.1 Regression Model Performance . . . . .	76

## TABLE OF CONTENTS (Continued)

<u>CHAPTER</u>		<u>PAGE</u>
	2.3.1.1 Parametric Models . . . . .	76
	2.3.1.2 Non-parametric Models . . . . .	76
	2.4 Conclusion . . . . .	81
<b>3</b>	<b>APPLICATION OF WETTABILITY CONFINEMENT IN AN ISOTHERMAL SYSTEM, STUDY OF SPREADING OF A GAS BUBBLE SUBMERGED IN A LIQUID . . . . .</b>	<b>83</b>
	3.1 Background and Motivation . . . . .	83
	3.2 Materials and Methods . . . . .	86
	3.3 Results and Discussion . . . . .	90
	3.3.1 Spreading Morphologies . . . . .	91
	3.3.2 Dynamics of Bubble Spreading . . . . .	95
	3.4 Conclusion . . . . .	100
<b>4</b>	<b>APPLICATION OF WETTABILITY ENGINEERING IN A NON-ISOTHERMAL SYSTEM, A REVISIT OF CONDENSATION HEAT TRANSFER ENHANCEMENT . . . . .</b>	<b>102</b>
	4.1 Background and Motivation . . . . .	102
	4.2 Materials and Methods . . . . .	106
	4.2.1 Experimental Setup . . . . .	106
	4.2.2 Data Reduction . . . . .	109
	4.3 Results and Discussion . . . . .	110
	4.3.1 Working Principle and Factors . . . . .	110
	4.3.2 Influence of Wedge-Shape Track . . . . .	111
	4.3.3 Main Results . . . . .	114
	4.4 Conclusion . . . . .	117
<b>5</b>	<b>APPLICATION OF WETTABILITY ENGINEERING IN THERMAL MANAGEMENT; A HYBRID VAPOR CHAMBER . . . . .</b>	<b>119</b>
	5.1 Background and Motivation . . . . .	119
	5.2 Materials and Methods . . . . .	124
	5.2.1 Power Electronics Design and Thermal Cooling . . . . .	127
	5.2.1.1 Circuitry Operation . . . . .	128
	5.2.1.2 Loss (Heat) Generation Mechanism . . . . .	128
	5.2.2 Wick-lined Evaporator . . . . .	130
	5.2.3 Wickless Plate . . . . .	132
	5.2.4 Gasket . . . . .	133
	5.2.5 Experimental Procedure . . . . .	134
	5.2.6 Performance Metrics and Error Analysis . . . . .	135
	5.2.6.1 Metrics . . . . .	135
	5.2.6.2 Error Propagation . . . . .	136
	5.3 Results and Discussion . . . . .	137

## TABLE OF CONTENTS (Continued)

<u>CHAPTER</u>		<u>PAGE</u>
5.3.1	Results . . . . .	140
5.4	Conclusion . . . . .	146
<b>6</b>	<b>APPLICATION OF WETTABILITY ENGINEERING IN THERMAL MANAGEMENT; A HYBRID HEAT PIPE . . . . .</b>	148
6.1	Background and Motivation . . . . .	148
6.2	Materials and Methods . . . . .	152
6.2.1	Heat Pipe Design . . . . .	152
6.2.1.1	Wick-lined Evaporator . . . . .	152
6.2.1.2	Wickless Plate . . . . .	155
6.2.1.3	Gasket . . . . .	156
6.2.2	Experimental Setup . . . . .	156
6.2.3	Experimental Procedure . . . . .	158
6.2.4	Performance Metrics and Error Analysis . . . . .	159
6.2.4.1	Metrics . . . . .	159
6.2.4.2	Error Propagation . . . . .	160
6.3	Results and Discussion . . . . .	162
6.3.1	Working Principle . . . . .	162
6.3.2	Main Results . . . . .	164
6.3.2.1	Effect of Wick Structure . . . . .	170
6.3.2.2	Effect of Fluid Charging Ratio . . . . .	174
6.3.2.3	Effect of Wickless-Plate Wettability . . . . .	180
6.4	Conclusion . . . . .	185
<b>7</b>	<b>CONCLUSION AND OUTLOOK . . . . .</b>	187
7.1	Thesis Conclusion . . . . .	187
7.2	Research Outlook . . . . .	188
7.3	Recommendation for Future Work . . . . .	189
<b>8</b>	<b>APPENDICES . . . . .</b>	194
8.1	Appendix A: Supplementary Materials for Chapter 2 . . . . .	194
8.1.1	Titanium Dioxide Formulation Composition . . . . .	194
8.1.2	Data . . . . .	196
8.1.3	Parametric Models . . . . .	197
8.1.3.1	Linear Regression Model . . . . .	197
8.1.3.2	Modified Ridge Regression: Kernel Ridge Regression . . . . .	197
8.1.4	Non-Parametric Models . . . . .	198
8.1.4.1	Gradient Boosting Regression . . . . .	198
8.1.4.2	Support Vector Machine . . . . .	199
8.1.4.3	Artificial Neural Networks Models: MLP and GRNN . . . . .	200
8.1.5	Hyperparameters . . . . .	202
8.1.6	Parametric Model Results . . . . .	203



## TABLE OF CONTENTS (Continued)

<u>CHAPTER</u>		<u>PAGE</u>
8.2	Appendix B: Supplementary Materials for Chapter 3 . . . . .	203
8.3	Appendix C: Supplementary Materials for Chapter 5 . . . . .	204
8.3.1	VC Seat . . . . .	204
8.3.2	Profilometry . . . . .	204
8.4	Appendix D: Supplementary Materials for Chapter 6 . . . . .	205
8.4.1	Maximum Deflection of Wall Plate . . . . .	205
8.4.2	Heat Pipe System Details . . . . .	207
8.4.3	Role of NCGs . . . . .	207
8.4.4	Temperature on the Wick-lined Plate . . . . .	212
8.5	Appendix E - Copyright and Permissions . . . . .	214
8.5.1	Copyright Form for Chapter 2 . . . . .	214
8.5.2	Copyright Form for Chapter 3 . . . . .	214
8.5.3	Copyright Form for Chapter 6 . . . . .	214
8.5.4	Copyright Form for Figure 3 . . . . .	215
8.5.5	Copyright Form for Figure 4 . . . . .	215
<b>CITED LITERATURE . . . . .</b>		<b>223</b>
<b>VITA . . . . .</b>		<b>276</b>

## LIST OF TABLES

<b><u>TABLE</u></b>		<b><u>PAGE</u></b>
II	Compositions and UV exposure time steps used in the experiments	68
III	Evaluation of non-parametric models. MAE and RMSE are calculated on the non-scaled data. . . . .	78
IV	Evaluation of non-parametric models on unseen data ( $\phi = 0.5$ ). MAE and RMSE are calculated on the non-scaled data. . . . .	81
V	Salient properties of the different ambient liquids (at 25°C) . . . .	91
VI	Experimental settings and equipment. . . . .	129
VII	Hyperparameters used in different ML techniques . . . . .	202

## LIST OF FIGURES

<b>FIGURE</b>		<b>PAGE</b>
1	Different modes of wettability; (a) static contact angle of a water droplet on smooth surface, (b) Adding roughness on a hydrophilic surface makes it transition to superhydrophilic state (Wenzel state), (c) Adding roughness on a hydrophobic surface makes it transition to superhydrophobic state (Wenzel state), (d) Cassie-Baxter state with air pockets trapped under the liquid, (e) Advancing contact angle ( $\theta_a$ ), (f) Receding contact angle ( $\theta_r$ ). . . . .	3
2	Two modes of condensation: (a) Filmwise, and (b) Dropwise. Blue denotes the condensed phase, while the red circles denote vapor clusters.	12
3	Schematic diagram of meniscus at the interface. Curvature, adhesion force, thermal resistance, and heat flux density variation are qualitatively depicted . . . . .	27
4	Schematic diagram of vapor formation and departure from a porous structure (A) submerged in a liquid pool (pool boiling), and (B) passively-fed via capillary action (capillary-fed boiling) . . . . .	30
5	Classification of active cooling techniques . . . . .	33
6	(a) Schematic diagram of the operation and structure of a typical vapor chamber. The hashed domains are occupied by wicks in this design, which also include wicking posts bridging the top and the bottom plate. The relative dimensions of the vertical thickness and the lateral extent of the chamber are not shown to scale. . . . .	37
7	Schematic of a heat pipe's internal structure. The hashed domains indicate the wick linings. In this design, the heat is transferred from left to right. . . . .	51
8	Schematic of the sample fabrication procedure: (a) coating a microscope slide using an airbrush; (a-i) SEM image of $\text{TiO}_2$ -coated substrate. Scale bar denotes 100 $\mu\text{m}$ ; (a-ii) sessile water droplet contact angle $\theta > 100^\circ$ for a typical coated sample before any exposure to UV light; (b-i) exposure to UV light; (b-ii) water droplet spread ( $\theta < 5^\circ$ ) on substrate exposed to prolonged UV irradiation. . . . .	66
9	Five contact-angle measurements performed at different points on the same substrate ( $\phi = 0.68$ ). The similar shapes indicate high confidence in the measured CA value, in this case, $\approx 163^\circ \pm 1.25^\circ$ . . . . .	67
10	Contact angle reduction with UV exposure time for a surface coated with the $\phi = 0.6$ formulation. Each coating was exposed to UV for the listed time before a water droplet was placed on the surface and attained the shown shape and respective contact angle. . . . .	69

## LIST OF FIGURES (Continued)

<u>FIGURE</u>		<u>PAGE</u>
11	Intrinsic (initial, before UV exposure) contact angle (left axis) and UV exposure time (right axis) for different coating compositions. The exposure time is the minimum required to impart superhydrophilicity (zero contact angle) to the coating. . . . .	70
12	Prediction of UV exposure time at the best instances (i.e. highest CV score and test/train $R^2$ values) for SVR with RBF kernel, KRR with Polynomial kernel, GBR, MLP and GRNN, respectively. The blue line (slope of 1) in each plot serves as a guide for perfect prediction. RS denotes Random State of train – test – split function. . . . .	77
13	Overall performance evaluation of SVR (RBF), KRR (Poly), GBR, MLP, and GRNN. Red circles indicate the mean value. Green lines mark the median. Whiskers bound the middle 90% of the data points. . . . .	79
14	Prediction of UV exposure time for $\phi = 0.5$ by all models. . . . .	80
15	Schematic of the sample fabrication procedure: (a) Laser etching of aluminum sample creates the elevated track; (b-i) laser engraving of microgrooves along the elevated track; (b-ii) cross-sectional depth profile of the microgrooves on the track (all dimensions are in $\mu\text{m}$ ); (c-i) passivating sample in boiling water for 1 h; (c-ii) scanning electron micrograph of sample after passivation (scale bar denotes 1 $\mu\text{m}$ ); (d-i) spin-coating Teflon on the substrate; (d-ii) scanning electron micrograph of Teflon-coated substrate (scale bar denotes 1 $\mu\text{m}$ ); (e-i) sessile water droplet contact angle $\phi = 155.6 \pm 5.6^\circ$ (scale bar denotes 3 mm); (e-ii) captive air bubble contact angle $\theta = 25.5 \pm 2.3^\circ$ for superhydrophobic substrate submerged under water (scale bar denotes 3 mm). . . . .	87
16	Schematic of the experimental setup. . . . .	88
17	(a-i) – (a-vi) Time-lapsed images of an air bubble (2.06 mm diameter) spreading on a rectangular track of $w = 1.4$ mm (scale bar denotes 5 mm); (a-vii) and (a-viii) zoomed-in view of the spreading fronts of Figure 17a-iv and Figure 17a-v, respectively, where the heights of the front, $h$ , are, respectively, 0.49 mm and 0.45 mm (axial locations where the heights are measured are shown by the red dashed lines in a-iii and a-iv); (b) definition of bulge and bubble front in a typical spreading configuration; (c) temporal evolution of the spreading air front ( $x$ ) on wettability-confined tracks of different widths ( $w$ ) submerged in water for bubble diameter, $D = 2.06$ mm; inset shows the temporal evolution of the spreading front $x$ for different bubble diameters on a track with $w = 1.4$ mm. . . . .	94

## LIST OF FIGURES (Continued)

<u>FIGURE</u>		<u>PAGE</u>
18	Variation of the height ( $h$ ) of the spreading bubble front with the lengthwise coordinate ( $x_c$ ) at two different time instants( $t$ ) for two different track widths ( $w$ ) while keeping the diameter of the bubble constant ( $D = 2.06$ mm); inset shows the variation of the spatially-averaged height ( $h_{avg}$ ) of the bubble front with the track width ( $w$ ) for different bubble diameters ( $D$ ). The dashed lines serve as guides for the eyes. . .	97
19	(a) Schematic of an air bubble spreading on a wettability-confined track showing the salient forces; (b) variation of experimentally-measured spreading velocity $v$ with $w^{-0.5}$ ( $w$ being the track width) when the substrate is submerged under water (the dashed line is a straight guide); (c) ratio of the experimentally measured ( $v_{exp}$ ) and scaling-predicted ( $v_{pr}$ ) spreading velocities for ambient liquids of different viscosities ( $\eta$ ) for track width and bubble size of $w = 1.4$ mm and $D = 2.06$ mm, respectively. . . . .	99
20	The environmental chamber (with open door) used in this study for the experimental setup. The inset shows the insulated bare cold plate with two grooves for thermocouples to measure the condensation-surface temperature during the tests. . . . .	107
21	Schematic of the wettability pattern features used in this study. Black and white denote superhydrophilic and hydrophobic domains, respectively. This quantum cell shows the design parameters. $d_1$ wide portion of the wedge track, $\beta$ opening angle, $d_2$ narrow end of the wedge track, $d_3$ central vein width, $L$ wedge track length, $d_4$ & $d_5$ distances between two adjacent superhydrophilic domains. . . . .	110
22	Five distinct wettability patterns used in this study. In each column, from top to bottom: Name of the design, wettability-pattern design, fabricated sample used in experiments, and corresponding $\phi$ ratio. Superhydrophilic areas are denoted with black, while hydrophobic domains are in white or copper color. $\phi$ denotes the superhydrophilic-to-total area ratio. The value of $\phi$ remains practically constant for all five cases. Scale bar denotes 2 cm. . . . .	112
23	Water condensate collection rate for all surfaces in an environment of 40°C and 80% RH. . . . .	115
24	Overall heat transfer coefficient for all surfaces in an environment of 40°C and 80% RH. . . . .	116
25	Major thermal resistances in a vapor chamber as the heat moves from the hot side (bottom) to the cool side (top). . . . .	122
26	Experimental setup components: (a) DC Power Supply, (b) DAQ, (c) oscilloscope, (d) logic power supply, (e) wave generator, (f) board/VC assembly. . . . .	125
27	Schematic of the experimental setup rig and thermocouple arrangement	126

## LIST OF FIGURES (Continued)

<u>FIGURE</u>		<u>PAGE</u>
28	(a) Detailed circuitry used as controllable heat source. (b) $Q_1$ and $Q_2$ are on. (c) $Q_1$ and $Q_2$ are off. (d) Simplified gate signal and loss generation mechanism. (e) Photograph of the assembled experimental prototype. . . . .	127
29	(a) Fabricated evaporator plate with elevated sintered copper powder layer on top and 3 Teflon spacers. The two red boxes indicate the MOSFET positions under the plate. (b) Fabricated uniform hydrophobic condenser plate. (c) Fabricated wettability-patterned condenser plate with wet superhydrophilic domains for contrast. Black and copper indicate superhydrophilic and hydrophobic domains, respectively. (d) Side view of the VC assembly without the sealing gasket. Bottom left: SEM images of the sintered copper powder and the superhydrophilic region of the wettability-patterned condenser. Green and blue scale bar denote 10 $\mu\text{m}$ and 1 $\mu\text{m}$ , respectively. . . . .	131
30	a) Back of the evaporator plate showing a 1 mm deep trench around the MOSFETs and 2 thermocouple grooves. The dashed lines indicate the approximate position of the MOSFETs. b) Side view of the sssembled VC. . . . .	132
31	(a) Wettability pattern used in this study (black: superhydrophilic; white: hydrophobic). (b) A single unit of the pattern with a low pressure site. (c) Growing bulge facing the wick. (d) The bulge eventually touches the wick structure and forms a capillary bridge. (e) Fluid drainage after snapping of the capillary bridge. . . . .	138
32	a) Raw thermocouple measurements vs. heating power over elapsed time for a WP-VC, (b) temperature rise of the MOSFETs as heating input increases for all VCs and the copper plate. . . . .	139
33	Temperature rise of the condenser plate vs. MOSFET temperature as heating input increases for the copper plate and two VCs with charge ratio CR2 (a), and CR3 (b). Similar markers indicate same heat input. c) Spatial condenser temperature distributions at four heating inputs. .	142
34	Comparison of copper plate thermal resistance with a) HPB-VC, and b) WP-VC at different charging ratios and several heat loads. . . . .	145
35	a) Cross section of the heat pipe showing the heater (red), the heat sinks (blue), insulation (grey), the thermocouple positions TX, and thickness of each component (disproportionate scales are used to show detail) b) Top view of the axially graded wick-lined evaporator. c) Top view of the wickless WP surface with superhydrophilic domains (black) laid on a hydrophobic background (white). . . . .	153

## LIST OF FIGURES (Continued)

<u>FIGURE</u>		<u>PAGE</u>
36	Left: Wickless wettability-patterned plate with partially wetted superhydrophilic regions. Black and copper domains denote superhydrophilic and hydrophobic areas, respectively. Right: Axially graded wick-lined evaporator plate. Middle top to bottom: SEM images of the micro/-nanostucture on the laser/chemical-etched domains on the wickless plate, coarse and finer wick structures on the wick-lined plate. . . . .	154
37	Exploded view of the experimental setup, displaying the assembly of various employed components. The Teflon Block is displayed transparent to expose the nested parts. . . . .	157
38	Raw thermocouple measurements for: (a) a flat copper plate (solid lines) and a HP charged with 25% CR (dashed lines), and (b) an empty HP (dashed lines) and the same HP charged with 25% CR (solid lines) as heat input power increased. Temperature measurement error $\pm 0.25^{\circ}\text{C}$ . . . . .	166
39	Raw thermocouple measurements vs. heating power over time (a), and (b) over placement distribution for a flat heat pipe with 25% CR. . . . .	168
40	(a) Average evaporator temperature ( $T_{1,2}$ ), and (b) average condensation temperature ( $T_{8,9}$ ) on the wickless plate of flat heat pipes for two fluid charging ratios (CR) and three distinct wick structures; AGW: axially graded, UFW: uniform fine, and UCW: uniform coarse. . . . .	171
41	(a) Thermal resistance, and (b) Effective thermal conductivity of the flat heat pipes with three distinct wick structures (AGW: axially graded, UFW: uniform fine, and UCW: uniform coarse) at two charging ratios. . . . .	172
42	(a) Average evaporator temperature ( $T_{1,2}$ ), and (b) average condenser temperature ( $T_{8,9}$ ) on the wickless plate with respect to heat input for four identical AGW-WP HPs filled with different charging ratios. . . . .	175
43	(a) Thermal resistance, and (b) Effective thermal conductivity vs. heat input for AGW-WP HPs filled with different charging ratios. . . . .	176
44	Raw thermocouple readings for locations along three flat heat pipes with the same charging ratio (37%), wick-lined evaporator, and (a) uniform wickless hydrophilic (HPL) plate, (b) uniform wickless hydrophobic (HPB) plate, and (c) wickless wettability-patterned (WP) plate. . . . .	179
45	(a) Average evaporator temperature ( $T_{1,2}$ ), and (b) Average condenser temperature ( $T_{8,9}$ ) on the wickless plate for flat heat pipes with 37% CR and three distinct wickless components (WP: wettability-patterned, HPB: uniform hydrophobic, and HPL: uniform hydrophilic). . . . .	182
46	(a) Thermal resistance, and (b) Effective thermal conductivity of three heat pipes charged with 37% CR, and each equipped with a distinct wickless surfaces (WP: wettability-patterned, HPB: uniform hydrophobic, and HPL: uniform hydrophilic). . . . .	183

## LIST OF FIGURES (Continued)

<u>FIGURE</u>		<u>PAGE</u>
47	Contact angle variation of different $\text{TiO}_2$ formulations with respect to UV exposure time. Contact angles below $10^\circ$ are considered zero due to hemi-wicking phenomena that make contact angle measurement impossible. . . . .	196
48	Overall performance evaluation of OLS (Ordinary Least Square), Kernel Ridge with a Linear function, and SVR with a linear kernel model. Red circles indicate the mean value for each model. Green lines mark the median. . . . .	203
49	Teflon plate placing on the MOSFETs to provide a flat seat for the hybrid VC . . . . .	204
50	2D profile of the superhydrophilic wedge-shape track. Blue arrow indicates the scanning direction. Red line denotes the scanned line. . .	205
51	2D profile of the superhydrophilic circular domain. Blue arrow indicates the scanning direction. Red line denotes the scanned line. . . . .	206
52	Bottom-to-top layer assembly of the HP. Thermocouple placement is also shown. (a) Thermocouples on the heater and active cold plate; (b) Wick-lined evaporator placement; (c) Gasket addition; (d) Wickless plate placement; (e) Thermocouple arrangement on the underside of the top Teflon plate and inactive cold plate; (f) Top Teflon plate has been inverted with the thermocouples now placed on its underside (not visible) and the TC wires at right hidden by the tape; (g) Thermocouple arrangement on the underside of the uniform top Teflon plate (no inactive cold plate present); (h) Top Teflon plate has been inverted with the thermocouples now placed on its underside (not visible) and the TC wires at right hidden by the tape. . . . .	208
53	Fully assembled test setup. (a) Side view of the HP with fully-insulated wickless plate. (b) Side view of the HP with partially-insulated wickless plate and the inactive cold plate. (c) Full test setup apparatus. . . . .	209
54	Raw thermocouple measurements vs. heating power over time for a HP with an insulated wickless plate. . . . .	211
55	Thermocouple T10 temperature readings of flat heat pipes for all cases considered in this study. . . . .	213
56	Copyright information for Chapter 2 . . . . .	216
57	Copyright information for Chapter 3 . . . . .	217
58	Copyright information for Chapter 6 . . . . .	218
59	Copyright information for Chapter 6 . . . . .	219
60	Copyright information for Figure 3 . . . . .	220
61	Copyright information for Figure 4 . . . . .	221
62	Copyright information for Figure 4 . . . . .	222



## SUMMARY

In recent years, progress towards fabricating multi-wettability surfaces has facilitated creation of small-scale systems on which manipulation of various liquids is achievable. In particular, distinct spreading dynamics of droplets can be achieved on spatially inhomogeneous surfaces, which effectively confine and manipulate liquid volumes in the open atmosphere with especially designed wettable and non-wettable domains separated by sharp contrast lines. Hence, achieving precise wettability properties is a vital task for effective functionality of a wettability-engineered surface. To this end, we initially have conducted a study on one of the most popular coating compounds for creation of surfaces with extreme wettabilities (superhydrophobic/hydrophilic) in the literature. The particular components used in this study (Titanium dioxide  $\text{TiO}_2$ , ethanol, and a commercial fluoroacrylic copolymer dispersion (PMC)) have proven to produce superhydrophobicity (contact angle  $> 160^\circ$ ) in particular combinations. On the other hand, by exposing such surfaces to UV irradiation, superhydrophilicity (contact angle  $< 10^\circ$ ) can be achieved. Although various applications of this and similar coatings of  $\text{TiO}_2$  have been studied in the literature, most of them involved extreme wettabilities while mid-range wettability properties were not easily achievable in a repeatable manner due to the lack of available data. Therefore, in this study, a step-by-step fabrication process was used to make several coatings that were applied on smooth glass slides and exposed to UV light for different time periods until superhydrophilicity was achieved. In this way, a comprehensive data table was made. Furthermore, this data was used as input data points for different machine learning al-

## SUMMARY (Continued)

gorithms to develop a universal model able to accurately predict a coating's required exposure time to reach a specific wettability. The study enables one to precisely control wettability of such  $\text{TiO}_2$  based coatings from too low (superhydrophobic) to too high (superhydrophilic) and any other wettability in-between. The presented generalized approach could be implemented for any multi-component coating, where precise fluid/surface interactions are demanded.

Confining liquid droplets with juxtaposed wettable and non-wettable domains is an interchangeable characteristic, where the liquid repellent region is philic to the surrounding gas, and vice versa for the liquid-wettable region. This is an interesting characteristic that enables one to not only manipulate liquids in a gas, but also do the same for a gas bubble submerged in a liquid. Spreading of droplets on wettability-confined paths has attracted considerable attention in recent years. On the other hand, the inverse scenario of a gas bubble spreading on a submerged, wettability-confined track has rarely been studied. Preferential extraction, spread, and transport of gas bubbles is a crucial task in multiple applications, such as pool boiling, hydrolysis, oil and gas industry, brewing, etc. To complete successfully each of these tasks, one requires to thoroughly understand the behaviour of gas bubbles in the vicinity of a solid, since unlike with a liquid droplet in air, a gas bubble in a liquid experiences different forces varying with its size, shape and the liquid's properties. To this end, in another study, we investigate a simple -yet important- case, where a single gas bubble spreads over a straight, supraaerophilic track under isothermal conditions. The width of the track is kept fixed along its entire length, and the spreading behavior of a gas bubble, dispensed at one end of the track, is studied. The effects of varying track width, bubble diameter, and ambient liquid are investigated. The goal

## SUMMARY (Continued)

is to better understand/predict gas bubble behaviours and facilitate design decisions in such systems.

Although surface wettability engineering in isothermal systems has been widely studied, its potential application in non-isothermal systems is yet to be thoroughly examined. Naturally, studies on isothermal systems provide some basic understanding for non-isothermal cases (i.e. spreading of a gas bubble on a track can find application in pool boiling for efficient extraction of vapor from the heated surface). Similarly, spreading of different liquids on isothermal, wettability-confined tracks have been sufficiently examined so that their application in non-isothermal systems can be further researched. Surface engineering in non-isothermal systems could be divided into two categories; condensation and evaporation/boiling. Condensation in particular is a key process in various industries, such as thermal management, water harvesting, desalination, power generation, etc. Generally, condensation of a vapor on a solid takes place in two modes; dropwise condensation (DWC) and filmwise condensation (FWC). In the former, the condensate forms individual droplets and by growing, via condensation or coalescence with nearby droplets, become large enough to depart the surface by gravity and provide new solid surface for further condensation. In FWC, the surface is covered with a liquid film after it is exposed to the hot vapor and of course, due to the low thermal conductivity of the liquid film, the condensation rate drops significantly. The condensation mode is a direct function of surface wettability and scholars have been studying this topic to take advantage of the low thermodynamic energy barrier of FWC and fast condensate departure of DWC. The combined effect could be achieved via a hybrid wettability surface and as shown, droplet confinement using

## SUMMARY (Continued)

wettability patterning is a viable tool to control the condensation mode via wedge-shape superhydrophilic tracks (promoting FWC) laid on a hydrophobic background (promoting DWC). Enhancing condensation via wettability patterning can be done in various ways since several parameters effect the condensation rate simultaneously. Hence, in our next study we investigated the role of superhydrophilic wedge-shape tracks' condensate pumping power on the overall condensation heat transfer rate. Several patterns were made on copper plates and tested in a temperature and humidity controlled chamber to further illuminate the geometrical importance of wedge-shape tracks.

As mentioned above, condensation heat transfer finds application in the thermal management field. Taking advantage of the latent heat of a liquid, mostly water, condensation has become one of the most reliable method to remove/absorb heat from a solid. One particular case is in passive heat spreaders (vapor chambers and heat pipes) where cyclic evaporation and condensation efficiently removes heat from a hot local heat source. Vapor chambers (VC) are passive heat spreaders that could dissipate high heat fluxes more efficiently by taking advantage of their working liquid's latent heat. Beside the working fluid type and amount in a VC, the thermal performance of VCs is categorized in three phenomena; evaporation, condensation, and circulation of the working fluid. Evaporation is essentially influenced by the core structure, such as the wick or the porous medium micro/nano structure's type, thickness, porosity, and permeability. Condensation, on the other hand, is influenced by physical and chemical characteristics of the condenser part of a VC. As shown, condensation heat transfer could be enhanced by a one to two orders of magnitude via precise engineering of a surface. Substantial research in

## SUMMARY (Continued)

the literature has been devoted to address the evaporation enhancement in VCs, whereas the condensation role has not been studied as extensively. Therefore, to further study and understand this role, a hybrid VC consisting of a copper wick on the evaporation side and a wick-free surface-engineered component as the condensation side was fabricated and tested. The device's cooling performance was evaluated via two silicon-based metal–oxide–semiconductor field-effect transistor (MOSFET)s to simulate a real-world application of the device. This novel approach has showed superior performance compared to a uniform hydrophobic condenser or a simple copper plate, testifying to the validity of incorporating surface-engineering in these systems.

Similar to VCs, heat pipes (HP) are another type of passive heat spreaders that are mostly made of metal wicks. Heat pipes are known as 1-dimensional heat spreaders, since they transfer heat laterally from one point to another. HPs come at different shapes and internal structures. A particular type of HP, flat-plate HPs, are usually consisted of a wick-lined plate, where on one side evaporation and on other side condensation take place, and a casing encloses the device. Almost all the literature in this type of HPs is invested in optimizing the wick structure, whereas the casing role in the condensation section has not been fully studied. This role could be critical since this type of HP is made of metals (mostly copper) which are highly conductive and in case of contact with a heat sink, play the condenser plate role and take part in heat transfer process. Therefore, in our next study, we attempted to manage the condensation phenomena on the upper casing part of a low-profile heat pipe via a similar wettability-patterning technique to control the DWC and FWC while, at the same time, enhancing the condensate return flow to the heated part. By axially grading the copper wick structure on the evaporator plate, an additional

## SUMMARY (Continued)

enhancement in condensation return flow, and as a result in heat transfer performance, was achieved.

In summary, in this dissertation, case studies of surface engineering implementation for enhanced heat and mass transport have been performed. Relations between surface morphology, surface energy, and surface-energy patterning for manipulating liquid/gas on heat-transfer surfaces have been explored and tested, along with their potential in thermal management performance enhancement.

## Nomenclature

$h$	Height	mm
$K$	Thermal Conductivity	W/m <sup>2</sup> K
$k$	Permeability Coefficient	cm/s
$M$	Mass	g
$P$	Pressure	KPa
$Q$	Heat Input	W
$R$	Interface Radius	mm
$t$	Time	s
$w$	Width	mm

## List of Greek Symbols

$\Delta P$	Laplace Pressure Difference
$\Delta T$	Temperature Difference
$\Phi$	Mass Fraction
$\gamma$	Surface Tension
$\delta$	Local width
$\epsilon$	Porosity
$\eta$	Kinematic viscosity
$\theta$	Static Contact Angle
$\kappa$	Capillary length
$\mu$	Dynamic Viscosity
$\rho$	Density
$\sigma$	Standard Deviation
$\phi$	Superhydrophilic to total area ratio
$\phi_s$	Second Roughness Parameter



## Super/subscripts

$\infty$	ambient
a	advancing
c	capillary
c	cold
cs	cross section
d	drag
eff	effective
evap	evaporator
exp	experimental
g	gas
h	hot
ins	instrument
l	liquid
pr	predicted
r	receding
s	surface

## Abbreviation

AGW	Axially Graded Wick
CAH	Contact Angle Hysteresis
CHF	Critical Heat Flux
CR	Charging Ratio
CV	Cross Validation
DWC	Dropwise Condensation
FWC	Filmwise Condensation
HP	Heat Pipe
HPB	Hydrophobic
HPL	Hydrophilic
HTC	Heat Transfer Coefficient
ML	Machine Learning
NCG	Non-Condensable Gas
UCW	Uniform Coarse Wick
UFW	Uniform Fine Wick

## SUMMARY (Continued)

VC	Vapor Chamber
WP	Wettability-Patterned



## CHAPTER 1

### INTRODUCTION AND BASICS

#### 1.1 Wetting Fundamentals

Although there have been numerous researchers and scholars in the field, when it comes to capillarity, two major sources stand out; "Capillarite: phenomenes superficiels" by Henri Bouasse (1) and "Capillarity and wetting phenomena: drops, bubbles, pearls, waves" by De Gennes and colleagues (2). It is highly recommended for a deep understanding of the wetting fundamentals and basics, one should devote some time in these two books. However, in this section, we provide a simple and short introduction of the wetting and capillarity phenomena for a better understanding of the applications in the following chapters.

##### 1.1.1 Surface Tension

There are three major states of matter; gas, liquid and solid. Every molecule in a single state is attracted by its surrounding molecules. This attraction causes the cohesion force applied by the same molecules of matter. The cohesion forces create a stable and balanced state for the molecules in the bulk of a material. However, when different states meet each other, this balance undergoes change, since the molecules at the interface of two phases or two different materials, experience an imbalance of the forces exerted on them. This imbalance for solids is not critical, since the cohesion among the molecules of a typical solid is big enough to avert deformation. However, in the case of a liquid contacting a solid, or two immiscible liquids, this imbalance

creates a deformation at the liquid's interface to maximize the number of molecules in-touch with their own type, or in other words, minimize the interface area between the two phases. This force that applies along the interface can be measured and is called Surface Tension. So, a liquid surface resembles a stretchable membrane where the opposition to distortion is applied by the surface tension, which is quantified by the force per unit length of the interface between the liquid and the surrounding fluid.

For characterizing the effective length scale below which surface energy/tension plays the dominant role, the capillary length ( $\kappa$ ) is defined as

$$\kappa = \sqrt{\frac{\gamma}{\rho g}} \quad (1.1)$$

where  $\gamma$  is the liquid-gas surface tension,  $\rho$  the liquid density, and  $g$  the gravitational acceleration.  $\kappa$  determines the maximum length scale (normally in mm, for instance 2.7 mm for water at 20°C) below which the role of gravitational forces is negligible and intermolecular and surface forces govern the motion mechanics.

### **1.1.2 Wetting and Contact Angle**

In a two-phase system where one phase/type of material is in contact with another phase/type, e.g., liquid and gas or two immiscible liquids, the surface tension at the interface minimizes the contact area of the minor phase/material. This leads to uniform surface deformation and the minimum surface area is achieved via a spherical shape. This could be commonly seen in nature where gas bubbles in liquids or oil droplet in water attain a perfect spherical shape. However,

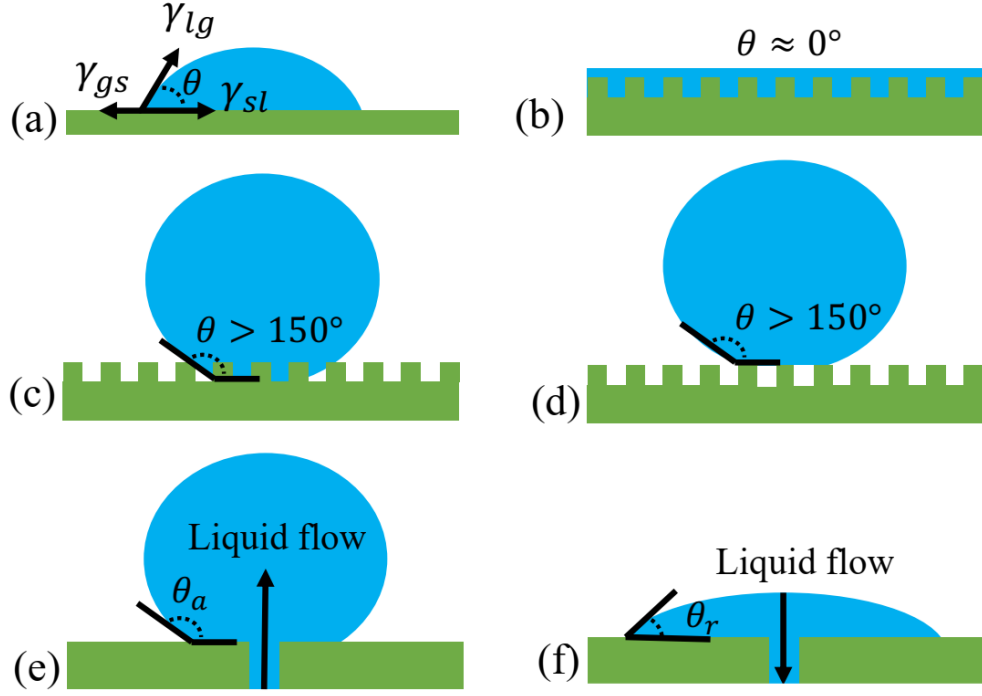


Figure 1: Different modes of wettability; (a) static contact angle of a water droplet on smooth surface, (b) Adding roughness on a hydrophilic surface makes it transition to superhydrophilic state (Wenzel state), (c) Adding roughness on a hydrophobic surface makes it transition to superhydrophobic state (Wenzel state), (d) Cassie-Baxter state with air pockets trapped under the liquid, (e) Advancing contact angle ( $\theta_a$ ), (f) Receding contact angle ( $\theta_r$ ).

when three phases/states of materials come together, this shape could be non-spherical and varies as a function of the balance among the involved states. For example, Figure 1a showcases a water droplet on a solid surface in air. In this case, three phases, namely gas, liquid and solid interact with each other and deform the liquid/gas interface, since the solid/liquid interface is not prone to deformation. Here, three surface energies/tensions,  $\gamma_{lg}$ ,  $\gamma_{sl}$ ,  $\gamma_{gs}$  represent the liquid/gas, solid/liquid, and gas/solid values. The three phases meet at the three-phase contact

line and create an angle  $\theta$ , which for an atomically smooth surface, is called the static contact angle and could be found (2) by

$$\gamma_{gs} = \gamma_{sl} + \gamma_{lg} \cos \theta \quad (1.2)$$

As seen, the key factor in designating  $\theta$  is the surface energy. Usually, surface energy of gas states are very close, since the molecules are far from each other, however, the solid and liquid surface energies could vary, and as seen, the lower the solid surface energy the higher the  $\theta$  and vice versa. Wetting of a solid surface is categorized using Equation 1.2, where for  $\theta < 90^\circ$  and  $\theta > 90^\circ$  the surface is referred as liquid-philic or liquid-phobic and in the case of water, hydrophilic and hydrophobic, respectively.

This equation holds for a chemically homogeneous and, as said above, atomically smooth solid surface. But, in real life achieving super smooth surfaces is costly and usually there is roughness on each solid surface. In practice, the contact angle is different than what Equation 1.2 predicts, and is known as apparent contact angle. By introducing roughness in this equation, Wenzel (3) incorporated the influence of added surface due to the roughness and derived the following equation

$$\gamma_{gs} = \gamma_{sl} + \gamma_{lg} \frac{\cos \theta^*}{r} \quad (1.3)$$

where  $\theta^*$  is the apparent contact angle and  $\cos \theta^* = r \cos \theta$ . This shows that by adding roughness (quantified by  $r$ , which is the ratio of actual/projected area of a surface), if a surface is liquid-philic, it will become more philic, while if it is liquid-phobic, it will become more phobic or repellent to that liquid. Equation 1.3 has opened the door for exploring the extreme scenarios



where super-attractant (Figure 1b) and super-repellent (Figure 1c) states could be achieved via increasing the roughness factor on the surface. Wetting phenomena have been further investigated by Cassie and Baxter (4; 5) who found that solid/liquid contact is not always energetically favorable. This is a case when a liquid contacts a repellent surface with high roughness and the liquid prefers to minimize its deformation, resulting in leaving dry solid beneath with air pockets trapped in the protrusions (Figure 1d). To explain this, Cassie and Baxter introduced another roughness factor in

$$\cos \theta^* = -1 + (1 - \phi_s) \cos \theta \quad (1.4)$$

where  $\phi_s$  is the dry-to-total area ratio. Following these equations shows that the wetting property of a solid surface could be significantly changed to the extremes by either physically or chemically engineering the surface. In the literature, numerous methods have been proposed and tested for fabrication of superhydrophilic (6; 7) and superhydrophobic (8; 9) surfaces. In Chapter 2, one of these methods will be introduced and discussed in detail.

### 1.1.3 Dynamic Contact Angle

Static contact angle alone can not capture the entire wetting behavior of a surface. Dynamic contact angle is another property that is determined by a moving three-phase contact line. Consider a surface with a fine pore ( $\sim 200\mu\text{m}$  in diameter) so that liquid could be pumped in and out of the surface in a very slow rate. By pumping a sufficient amount of liquid to the pore, a droplet forms. Further pumping causes the droplet to grow. In some cases, while the droplet

volume increases the three-phase contact line remains pinned. In other cases, as the droplet volume increases, the contact line moves with constant velocity (Figure 1e). The dynamic contact angle of the droplet in the growing stage designates the "advancing contact angle",  $\theta_a$ . In the opposite case, if the droplet loses volume by pumping out liquid, the three-phase contact line retracts with constant velocity and the contact angle defines the "receding contact angle" (Figure 1f),  $\theta_r$ . These two contact angles are crucial factors in many applications; their difference is called "Contact angle hysteresis" (CAH), and is defined by

$$\text{CAH} = \theta_a - \theta_r \quad (1.5)$$

The CAH defines the stickiness/slipperiness of the surface and has been the subject of research in many applications, such as condensation, boiling, etc, where the dynamic behavior of droplets/bubbles are key in particular applications.

#### **1.1.4 Laplace Pressure**

As discussed above, surface tension causes deformation of the liquid's interface in the presence of a solid and a gas phase. This deformation creates a by-product which has become the point of attraction for various applications. Consider a case where a liquid is confined by a solid (e.g., liquid in a capillary tube or straw). If the solid is attractant to the liquid (liquid-philic), the liquid tends to spread as much as possible on the solid wall. In a confined space, the contact line moves beyond the liquid column level and creates a concave interface, which causes a lower pressure in the liquid compared to the ambient pressure. On the other hand, if

the solid is repellent to the liquid (liquid-phobic), the surface tension shrinks the interface to minimize contact, and as a result, the pressure in the liquid below the interface is higher than the ambient. This reduction or enhancement in the pressure at the interface is quantified as

$$P_c = \gamma_{lg} C_i \quad (1.6)$$

where  $C_i$  is the curvature of the interface. Equation 1.6 is known as the Young-Laplace Pressure, which in its more general form is

$$P_c = \gamma_{lg} \left( \frac{1}{R_1} + \frac{1}{R_2} \right) \quad (1.7)$$

where  $R_1$  and  $R_2$  are the interface radii of curvature in two orthogonal planes. This quantity has been the source of many natural phenomena, such as reaching water to the leaves of the trees and has inspired researchers to design and fabricate systems working with this simple concept (10; 11; 12; 13). One main advantage of this curvature-driven pressure difference is its passive nature. This could induce pumpless transport of a liquid in a porous medium, such as a paper towel, or on an open surface. The former is known as "wicking" and is a slow process with low-volume transport capacity. Moreover, once the porous medium is saturated the wicking stops. On the other hand, taking advantage of curvature differences, scholars have been able to manipulate and transport liquids from one point to another on an open surface. The typical capillary rise was also observed in a wedge corner created by two vertical plates with a small diverging angle ( $\sim 2^\circ$ ). The rising liquid interface was found to be a hyperbola, and the rise occurred only if  $\alpha/2 + \theta < \pi/2$ , where  $\alpha$  and  $\theta$  are the diverging angle and static contact angle

of the droplet on the plates (14). In cases where the plates are not parallel and rather have different wedge angle on the bottom and top side, a larger rise is observed since the meniscus undergoes larger curvature differences (15). Laplace pressure differences can also be achieved on a 2D plane. The wedge-shape created by two vertical plates could be transformed on a surface where a diverging track of hydrophilic nature is laid on a hydrophobic background. In this case, due to geometrical gradients, there will be a curvature difference at the two ends of the liquid droplet and moreover, due to wettability contrast, the liquid is bounded onto the track with the wettability contrast line also applying inward force, which propels the liquid droplet forward, from the narrow to the wider end of the track (16). There have been numerous studies in this area where various fabrication techniques have been used to passively and continuously transport liquid droplets from one point to another (17; 18; 19; 20; 21; 22). One great advantage of this method is the minimized resistance in fluid flow (pressure loss/drop), which in turn can generate transport velocities up to  $O(10 \text{ cm/s})$  (23). Besides, other type of passive transport could be achieved on a 2D plane by using different circular wettable wells at two different locations and connect them via a wettable path. In this case, when a liquid film covers the wells and connecting path, the liquid naturally moves from one well to the other, again due to a capillary pressure difference (24). Similar directional spontaneous transport could also be achieved via a 3D conical shape needle (25; 26). Laplace pressure differences have also been created by wettability gradients. Khoo and Tseng created Laplace pressure gradients via a radial pattern that passively drove and moved droplets (27). Bliznyuk et al (28) designed a radially patterned surface with varying wettability from a hydrophobic center to a hydrophilic

exterior via a set of hydrophilic stripes of different widths. The spontaneous droplet movement from center to the perimeter of the pattern was achieved due to increased surface area of the hydrophilic regions and Laplace pressure generation due to different curvature at the two ends of the liquid. Li et al (29) also used radially varying wettability stripes to precisely control and transport a liquid droplet from the center of the pattern to the periphery. The pumpless directional transport could be applied for any liquid in liquid mixture only if proper wettability and shape gradient was applied. For example, a similar shape-gradient concept has been applied for passive transport of gas bubbles submerged in liquid (30). In this case, the track was superhydrophobic (i.e. superaerophilic) and was laid on a superhydrophilic (i.e. superaerophobic) background. Gas bubbles tended to stick onto the track, being confined by the wettability contrast line. Similarly, the gas bubble was propelled from the narrow to the wider side of the track (31; 32). In a similar manner, superaerophilic cones have also been used to collect and transport gas bubbles under water (33). In chapter 3, an application of Laplace pressure difference for gas bubble manipulation under water is presented and discussed. Moreover, all application studies in this thesis are designed using the above concept.

Passive transport of liquids and gases on open surfaces via wettability engineering has been widely studied in the literature. This has raised opportunities to control and transport thermal energy through precise manipulation of liquid/gas interactions on a surface. For instance, heat removal via pool boiling could be enhanced from a non-engineered to a wettability-engineered surface by controlling vapor bubble motion on the surface (34). This notion has inspired researchers to employ the knowledge of manipulating liquids/gases in isothermal systems into

non-isothermal systems in order to enhance their efficiency and solve new problems. To this end, we will provide an introduction of heat transfer principles and application of wettability engineering in its different aspects.

## 1.2 Heat Transfer Fundamentals

Heat is a form of energy transferred due to temperature differences between two points in space (35). There are three forms of heat transfer; conduction, convection, and radiation. Conduction occurs due to vibration of the individual molecules, so it is maximum in the solid state of a material and minimum in the gas phase. Convection is transport by moving molecules from one point to another, while radiation takes place between two facing surfaces (36). Conduction heat transfer is mainly governed by the molecular motion and density of a medium. The governing law of conduction heat transfer is known as Fourier's law (37)

$$\vec{q} = -K\nabla T \quad (1.8)$$

where  $\vec{q}$  is the heat flux,  $K$  the thermal conductivity of the medium, and  $\nabla T$  the temperature gradient in space. The minus in Equation 1.8 signifies that the heat is transferred from the hot to the cold side. Convection heat transfer is the diffusion of energy by random molecular motion in addition to energy transfer via bulk motion. Convective heat transfer is governed by Newton's law of cooling and is as follows (38)

$$q' = h(T_s - T_\infty) \quad (1.9)$$

where  $h$  is the heat transfer coefficient, and  $T_s$  and  $T_\infty$  the surface and ambient temperatures, respectively.  $h$  is a function of fluid thermal properties, fluid motion dynamics and surface geometry. Convection heat transfer has two major sensible modes: natural and forced. In the former mode, the temperature difference inside the fluid creates a density gradient, which produces buoyancy forces and as a result, the hotter lighter fluid moves to the colder denser domains and vice versa. In the latter, the fluid is forced to move (i.e., via pumps, fans, etc.) and by forced motion the heat is transferred more efficiently. These two modes are characterized by temperature variation of the fluid. However, there are two other isothermal modes in which heat is spent to change the phase of a medium either from liquid to gas (evaporation/boiling) or from gas to liquid (condensation). The energy transferred during these isothermal processes is called latent heat of the medium (39).

### **1.2.1 Condensation Heat Transfer**

Condensation phenomena occur when vapor is cooled below the saturation temperature at the same pressure. During this process, the latent heat of the vapor is released and vapor gets converted to liquid. Condensation could take place in two major modes, filmwise (FWC) (Figure 2a) and dropwise (DWC) (Figure 2b). FWC occurs when condensate droplets on the surface spread and grow either by coalescence or growing individually. This spreading leads to a liquid film formation on the surface and reduces the condensation heat transfer due to the low thermal conductivity of the liquid. On the other hand, DWC is a mode in which condensate droplets tend to "bead up" and grow individually. It has been shown that DWC could reach one to two orders of magnitude higher heat transfer coefficient (HTC), however

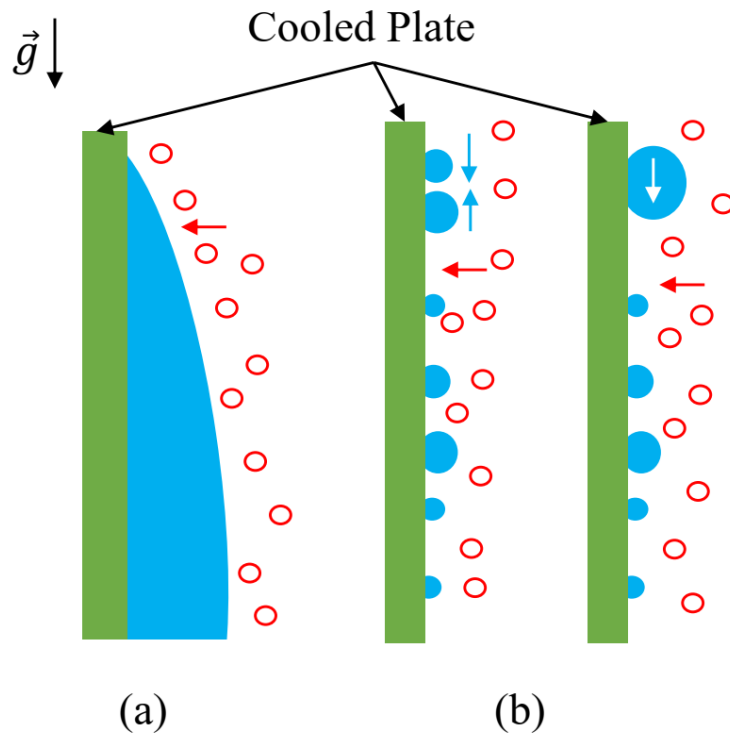


Figure 2: Two modes of condensation: (a) Filmwise, and (b) Dropwise. Blue denotes the condensed phase, while the red circles denote vapor clusters.

it is harder to attain at industrial scale (37; 40). Another factor affecting condensation heat transfer efficiency is the presence of non-condensable gases (NCG)s, such as air, nitrogen, argon, etc. Donald Othme (41) was the first who examined condensation of steam in the presence of NCGs. In his experiment, he used a chilled copper tube as the condenser and installed it in a boiler. He found that by increasing the air volume fraction only to 0.5%, the HTC drops by almost 50%. Following that, there have been several studies investigating this effect for other gases, such as hydrogen, neon, etc. (42; 43; 44; 45). The results revealed the presence of NCGs



significantly reduces both condensation rate and heat transfer coefficient. The main reason for this reduction is that the NCG molecules act as a diffusion barrier between the condenser surface and the vapor molecules (46). This effect also poses resistance to vapor mass transfer towards the cooled surface, which results in lower heat transfer rate (47).

#### 1.2.1.1 Filmwise Condensation

The classic nucleation theory introduced by Volmer (48) points out to a direct correlation between the free energy barrier and the surface wettability to form a liquid nucleus on a solid surface. The free energy barrier,  $\Delta G$ , is given by

$$\Delta G = \pi\gamma_{LG}(r^*)^2(2 - 3\cos\theta + \cos^3\theta)/3 \quad (1.10)$$

where  $\theta$  is the static contact angle and  $r^*$  is the critical radius derived from Kelvin's classical equation given by

$$\ln \frac{p}{p_\infty} = 2\gamma_{LG}/n_L^*K_B T r^* \quad (1.11)$$

where  $K_B$  is Boltzmann's constant,  $n_L^*$  the number of molecules per unit volume of liquid,  $T$  the temperature,  $p$  the vapor pressure at the curved interface, and  $p_\infty$  the vapor pressure over a flat interface. Equation 1.10 shows that lower contact angle is preferred for condensation, since it reduces the free energy barrier. However, surfaces with low contact angles (hydrophilic state), will be quickly covered with a liquid film. The liquid film thickness increases over time and adds another thermal resistance for the upcoming fresh vapor, eventually reducing the heat

transfer rate, and making it a less preferred condensation mode. Equation 1.9 could be used to determine the condensation heat transfer via

$$q_{\text{cond}} = h_{\text{cond}}(T_{\text{sat}} - T_w) \quad (1.12)$$

where  $T_{\text{sat}}$  and  $T_w$  are the saturation temperature of vapor and the wall temperature, respectively. Their difference is known as the degree of subcooling. Nusselt (49) introduced the first heat transfer coefficient of condensation for laminar FWC for a vertical isothermal flat plate and a horizontal cylinder surface. Nusselt's estimation of  $h_{\text{cond}}$  is idealistic and usually overestimates this value by disregarding in-practice barriers, such as NCGs and surface morphology (50). In the past few decades, more comprehensive models have been proposed using heat transfer in counter-current and co-current scenarios (51), filmwise condensation in high aspect ratio geometries (52), similarity-based solutions (53), and filmwise condensation over a curved surface (54). An effective method to rectify a part of the reduced heat transfer rate due to liquid film thickness is by controlling and reducing it. One way to achieve this goal is by adding extra surface area to the condenser surface via fins (55; 56; 57). In this scenario, liquid film curvature differences at the bottom and tip of the fins induce a thinning effect and promote increased liquid drainage, and in turn, increased heat transfer coefficient. Ho et al. (58; 59) carried out a through investigation on the role of the fin's geometry and showed that a conical shape outperforms both sinusoidal and cylindrical fins by reducing condensate flooding. As shown in (60), geometrical features of the fins are critical factors in determining the

heat transfer enhancement. Even though numerous studies have been performed to enhance condensation heat transfer in FWC (61; 62; 63), it has been shown that DWC could produce one order of magnitude enhancement in HTC and is more promising for effective heat transfer (64).

#### **1.2.1.2 Dropwise Condensation**

In DWC occurring on a vertical surface, initially small droplets form on the solid. These droplets grow by direct condensation on top of them and also by coalescing with nearby droplets. As time goes by and condensation persists, the droplets reach a critical volume/mass, where due to gravity and shear tension, they depart from the surface leaving new domains for nucleation of new condensate. The origin of DWC has been a source of controversy in the literature and two major theories have been studied and discussed in the past decades. One theory was suggested by Eucken (65) who considered certain nucleation sites for individual droplet nucleation and growth. Also, he assumed that the space between these sites remain dry until the droplets merge. McCormick and Baer (66) supported this theory and furthermore, Umur and Umur (67) showed the applicability of this theory under low subcooling. Another theory was introduced by Jakob (68) who suggested that during condensation a very thin layer of liquid film forms on the surface first. By continuing condensation, this film reaches a critical thickness and ruptures, resulting in formation of droplets. In his theory, Jakob supposed that droplet nucleation could take place in between the older droplets and, due to surface tension effects, the new droplets would move towards the bigger droplets. Besides, the droplets also grow by direct condensation on their surface. Welch and Westwater (69) later showed this theory to be

valid and they supported this idea. Rose et. al. (70) developed the first DWC heat transfer model based on various resistances. Based on their findings, the condensation heat transfer coefficient for a pure DWC mode could be given as

$$h_{DWC} = T_v^{0.8}(5 + 0.3\Delta T) \quad (1.13)$$

where  $h$  is in  $KW/m^2K$ ,  $T_v$  is the vapor temperature, and  $\Delta T$  is the subcooling. In the last few years, various models have been proposed for DWC in vertical plates (71; 72; 73; 74; 75; 76) and horizontal tubes (77; 78). The most important factor in DWC is the droplet size distribution and as shown, high number of small droplets favors high numbers of larger droplets (79). However, formulating a mathematical model to describe the above mechanism is a challenging task due to the complex nature of droplet interaction on the surface. But numerical analyses have revealed localized heat transfer at the three-phase contact line to reach 4 orders of magnitude higher HTC compared to the exposed area of the droplets (80; 81).

Water DWC can take place even at very low subcooling. Depending on the surface properties, it could initiate at  $1^\circ C - 3^\circ C$  (82). Based on Equation 1.13, an increase in subcooling would lead to higher HTC. However, some studies showed that at a certain point this became constant (83; 84). At very high subcooling, however, the DWC gradually shifts to FWC, resulting in a great reduction in HTC. Under higher subcooling, the nucleation site density and nucleation rate of droplets increase significantly (85; 86). This results in forming "pinned-Wenzel" droplets on the surface and if the droplet formation and growth rates exceed the droplet departure rate,

a film forms on the surface. Therefore, a critical factor for maintaining DWC on a surface is its capability to shed droplets. It can be understood that efficient condensate removal requires high droplet repellency or hydrophobicity, in which high static contact angle and low hysteresis could induce faster and more efficient droplet departure.

#### **1.2.1.3 DWC Enhancement Techniques**

In order to promote (super-)hydrophobicity two major factors must be met by a surface: low surface energy and physical roughness. There have been numerous techniques in the literature to promote DWC on a surface and below the most frequent ones are mentioned.

1. Polymer Coatings: This is one of the most traditional and practical methods, since it can be applied on a existing condenser and also does not rely on the substrate surface morphology or chemistry. Of course, two critical factors must be considered for proper coating: 1- sufficient adhesion to the surface, and 2- low film thickness. Usually the coating should not add more than 1% of the total thermal resistance of condensation; this can be achieved via thickness of  $< 1\mu\text{m}$  (87). Applying polymer coatings such as oleic acid (88) in a marine condenser has shown stable DWC for almost 2 years. PTFE and fluoropolymers, due to their high melt viscosity, insolubility in most organic solvents, and high chemical inertnes (89) are also very popular in enhancing DWC. Numerous studies have shown HTC enhancement (up to 5 times) by applying PTFE on metal surfaces (90; 91; 92; 93). Ma et. al (94) by adapting a new method of deposition were able to deposit PTFE on Stainless Steel, Brass, Copper, and Carbon Steel. On Brass tubes about 1.6 – 2.8 times enhancement in HTC and 0.3–4.6 times in heat flux compared to FWC

was observed. Despite this great enhancement, the method was not scalable for larger surfaces and also could not withstand more than 40h of operation. Beside using pure polymers, other attempts have been made to enhance DWC via enhancing the polymer conductivity (95), enhancing polymer endurance and anti-fouling (96; 97).

2. Metal Coatings: One of the main challenges with polymers is their inherent low thermal conductivity. On the other hand, metals possess high thermal conductivity and also high surface energy. However, noble metals, such as rhenium, ruthenium, rhodium, palladium, silver, osmium, iridium, platinum, and gold are known to have low surface energy and could be electrodeposited on other metals. Despite having low surface energy, these metals have also been reported as hydrophilic and source of this problem was attributed either to oxides (98; 99) or organics (100; 101). Studies with electroplated gold (102; 103) have shown pure DWC could be achieved with even ~200nm thickness. Other studies with silver electroplating have shown (104) up to 58% enhancement in HTC. Nickel has also been deposited on copper surfaces for DWC enhancement (105; 106) and it was shown that the corrosion rate compared to pure copper over 15 days was only 0.16%, while the heat flux was enhanced up to 5 times. Despite all the benefits of noble metals, their high manufacturing cost limits their application at larger scale.
3. Self-assembled monolayer (SAM) coatings: Bigelow et al. (107) were among the first to find that polished metal or non-metallic substrates show hydrophobic and oleophobic property after submerging in a non-polar solvent via a polar organic solution. The organic layer on the substrate has a polar group (e.g. thiol, silane) which bonds them to the surface

and an alkyl group, which renders them hydrophobic. The great advantage of SAMs is their molecular level thickness (several Angstroms (108)). Das et al. (109; 110) used SAM on copper, gold, copper-nickel tubes, and gold-coated aluminum tubes, and they achieved 5-14 times higher HTC. In other studies, Bonne (111; 112) used a thiol-based SAM on copper and gold-coated copper and observed HTC enhancement up to 8 times over FWC. They also recorded a lifetime of 9 months for the sample used in their experiments without degradation. There have been several studies using a variety of SAM methods (113; 114) where similar enhancements have been reported. Monolayer thickness, very low required amount for coating large area, and simple and facile coating methods, such as immersion, have made SAMs a popular approach for promoting DWC in literature. However, the single molecular thickness is highly susceptible to degradation and fouling and even a small damage could expose the underlying substrate. So, longevity of SAMs is a critical factor, which needs to be taken into account for promoting DWC in long periods of time.

4. Superhydrophobicity via micro/nano structured surfaces: Even though enhancing DWC through chemical modification can be readily achieved, the nucleation sites and rates, which are key elements in condensation heat transfer, are random on a physically homogeneous surface. However, by creating physically heterogeneous surfaces, these two factors could be controlled and engineered. As mentioned earlier, superhydrophobic surfaces possess high static contact angle and low contact angle hysteresis, which in turn could significantly promote DWC by increasing condensate departure at the smaller size range. It is important to note that droplets in the Cassie mode are in a meta-stable state,

as opposed to the Wenzel state (the most energetically stable state on a rough solid surface). So, droplets on superhydrophobic surfaces tend to transition to the Wenzel state as they grow larger (115; 116). DWC on superhydrophobic surfaces has been examined on surfaces with only micro or nano roughness, and on surfaces with micro and nano structure. Condensation on micro-structured surfaces takes place on top and in between the structures. This creates a quick transition to the sticky Wenzel state and reduces the heat transfer rate (117; 118). On a uniform nano-structured surface, this problem is slightly different. A surface with nanohairs or nanograss and roughness  $r$  has almost  $r$  times higher nucleation sites than a smooth surface (119). However, this significantly increases the number of nucleation sites and thus causes higher heat transfer rates, but slow departure of condensate could easily create surface flooding and reduce the heat transfer (120). Chen et al. (121) pioneered condensation testing on micro and nano structured superhydrophobic surfaces. They were able to maintain Cassie state during condensation and achieved 100% higher HTC compared to a uniform hydrophobic surface. Sharma et al (122) reported 700% higher HTC compared to a uniform hydrophilic case via a laser and micro-machined structure. Parin et al. (123) created a superhydrophobic surface via chemical etching and achieved 8 times higher HTC against FWC. Zhu et al. (124) used Electro-chemical deposition to create micro/nano features and, by depositing Fluorosilane, fabricated a superhydrophobic surface, which could reach 125% higher HTC compared to FWC on copper. There have been countless studies in this area (125; 120; 126; 127) following similar concepts and using a variety of methods however, a turning point in



this domain was Boreyko and colleague's finding (128) of self-propelled jumping droplets. The self-removal phenomenon without requiring external forces was explained by surface energy conversion to kinetic energy, resulting in droplets jumping off the surface after coalescence. This phenomenon inspired many scholars to further analyze and investigate the physics and efficiency of the mechanism for condensation purposes (129; 130; 131). In a recent study, Wand et al. (132) created an oblique nanowire structure which could prevent vapor from penetrating into the cavities even at high subcooling (30K). The structure was also able to induce self-propelled jumping on the condensate droplets. Even though all these efforts showed great potential for enhancement of DWC over metal surfaces, technical challenges, such as surface flooding at high subcooling, random nucleation sites and high sensitivity toward fouling and removal of either the surface coating or the micro-nano structure in addition to high cost and complex fabrication processes have prevented this technology to be implemented at larger and industrial scales.

5. Other methods, such as ion-implanted surfaces (133; 134; 135), graphene and CNT based coatings (136; 137; 138), micro-grooved surfaces (139; 140; 141), Lubricant infused surfaces (142; 143), etc, have also been implemented to enhance DWC and more details could be found in recent reviews (117; 144; 64; 82).

#### **1.2.1.4 Hybrid Condensation**

One way to benefit from the low energy condensation barrier of FWC and the more efficient condensate departure of DWC could be by combining FWC and DWC. This way, nucleation and departure rate could be selectively controlled and adjusted to reach an overall enhance-

ment. In an operational mode, high wettability domains shortly after exposure to vapor form a liquid film on the surface (FWC), whereas in the low wettability regions the droplets nucleate and grow individually (DWC) adjacent to FWC domains. So, when the droplets in the DWC regions grow large enough to come in contact with FWC domains, they get sucked in the liquid-covered FWC domains, thus creating new nucleation sites for new upcoming vapor. As a result, a combination of two distinct wettabilities potentially could enhance HTC. This hypothesis has been extensively investigated by scholars in the literature. Garimella et al. (145) have made a biphilic surface with straight strips and observed a chain coalescence and departure of droplets from DWC to FWC domains. The inertia of coalescing droplets led to other droplets coalescing and merging into the FWC domains. They found that there is an optimal DWC/FWC ratio in which the surface would not undergo uniform flooding (FWC). This finding was aligned with literature where an optimum DWC strip width was reported to show enhancement compared to uniform uncoated (FWC) and Coated (DWC) substrate (146; 147; 148; 149). Another interesting approach was taken by Varanasi and colleagues (150; 151) who created a micro-post structured surface with hydrophilic top-post and hydrophobic background. They showed preferential condensation on top of the posts. By growing larger, droplets experienced the Cassie state, due to air gaps underneath, and showed a great potential for condensation applications. Numerous studies have shown hybrid surfaces could enhance HTC compared to uniform wettability surfaces. Alwazzan et al. (152) showed a Hydrophobic/superhydrophobic hybrid surface could enhance HTC up to 180% compared to a hydrophobic surface. Egab et al. (153) showed a similar combination could achieve up to 80% enhancement in heat flux compared to a uniform

DWC. Yang et al (154) showed a surface combination of hydrophilic-hydrophobic wettability with inclined strips could reach 16% and 6% higher HTC compared to uniform hydrophilic and hydrophobic surface, respectively. Even though researches show that hybrid surfaces are likely to outperform uniform wettabilities, design of wettability patterns is a critical obstacle. As shown in (155; 156), using a hybrid surface may not be necessarily beneficial if a proper drainage path by lower-wettability regions are not provided. This results in lower drainage compared to uniform DWC, and as result, lower HTC. Similarly, wider DWC bands can enhance HTC, however, at some point, the high ratio of DWC to FWC areas prevents proper drainage and reduces HTC (157; 158). In case of more wettable islands on less wettable background, the problem of bridging between wettable regions is a critical challenge for HTC enhancement. This problem recently has been addressed by Lo et al. (159), who used 3D hydrophilic channels to drain the condensate and promote bridge break up. They achieved high heat flux up to 650 KW/m<sup>2</sup> at relatively high subcooling (18°C). Beside using strips or patches, there have been other studies with novel approaches to create hybrid surfaces for condensation. Schmiesing et al. (160) fabricated a hybrid aluminum tube via methylated silica nanospring (SN)-coating approach and reached 84% enhancement in droplet departure rate in addition to reducing droplet departure size. In a similar study, a porous anodic aluminum oxide (AAO) membrane with wettability difference on the sides was able to reach 200% enhancement in heat flux and keep the hydrophobic side dry even at 12°C subcooling. In a comparative study Mondal et al. (161) passed hydrophilic steel nano needles through a hydrophobic membrane made of polyethylene polymer and silica nano-particles. This approach led to drop formation on steel nano needles

while staying in Cassie state due to the background hydrophobicity. This technique reached to 4 and 2 times higher HTC compared to uniform FWC and DWC, respectively. There have been other novel approaches and techniques to create hybrid surfaces (162; 163; 164) with similar enhancement results.

It has been shown that hybrid surfaces, if designed properly, could enhance HTC by several fold depending on the test condition. However the method seems promising, but reaching an optimum design is a challenging task and requires parametric studies and numerical analysis. Moreover, another challenge in this method is the complex and expensive fabrication process, which also needs to be simplified for large-scale use.

### **1.2.2 Evaporation and Boiling**

Another heat transfer mechanism is evaporation. Evaporation of a liquid occurs when liquid molecules on a surface absorb enough energy to overcome the ambient vapor pressure and enter the gas phase. When evaporation takes place, the liquid molecules take the energy from and off the liquid phase, which results in evaporative cooling (165). The great advantage of evaporation, similar to condensation but opposite, is that this process is an isothermal process and the latent heat of the liquid is absorbed by the liquid to evaporate. This phenomenon has found application in various industries, including cooling towers, air conditioning (HVAC), micro-climates, thermal management, etc.

To date, three major approaches for evaporation modeling exist: continuum mechanics, classical kinetic theory, and statistical rate theory (SRT) (166). The continuum mechanics approach works best for diffusion-limited cases. In this case, it is assumed that evaporation

is taking place at equilibrium and vapor mass diffusion governs heat and mass transfer. This approach is designed for humid air as opposed to pure vapor environments. So, the vapor molecule diffusion is the major transfer mechanism rather than density-induced convection of vapor between dry and humid air. On the other hand, in the absence of NCGs (e.g., in wick structures, micro- or nanoporous surfaces) diffusion of vapor molecules is not dominant and gas kinetics of vapor molecules governs the evaporation. Hence, Classical Kinetic theory is applied in these systems. The final theory, statistical rate theory (SRT), which is newer compared to other two, is used for non-equilibrium evaporation cases (167; 168). The focus of this thesis is on the theory and application of the second approach, Classical Kinetics, which finds application in various thermal management solutions (see next section).

#### **1.2.2.1 Thin-Film Evaporation and Capillary-fed Boiling**

In 1964, Derjagin et al. (169) conducted an experiment and found that isothermal liquid flow in a rising thin film of liquid on the inner walls of a capillary tube increases the evaporation rate from the walls. The gradient in the long-range intermolecular force field was deemed to be the reason for the enhanced liquid flow in the thin film. After that, modeling of a moving meniscus in conical capillaries was performed by Kiseleva et al. (170). A major framework for modeling interface transport was given by Shrager (171) who inspired many researchers to further decipher the thin-film evaporation phenomena in absorbed films driven by surface diffusion. Since the intermolecular forces are the major factor in these processes, the transport in thin films has been widely explored by scholars using surface treatments and modifications, and has become a critical field of research in heat and mass transfer.

To this end, surface modifications created either by chemical treatment or by additive structural features could influence phase change by altering three interrelated phenomena (172). First, the morphology of the surface features determines which solid/liquid/vapor interactions are strengthened or weakened. Macroscopic scale features have shown to change the solid/liquid interface, increase the contact area, and enhance the heat transfer between the fluid and the underlying solid (173). However, micro-scale surface features create an increased solid/liquid interface in addition to acting as capillary wicking platform (174; 175), which also enhances the phase change by increasing the number of nucleation sites (176; 177). Also, as discussed above, changing the surface chemistry alters the surface energy, and, as a result, changes the solid/liquid interaction. The surface energy can also be locally changed via micro/nano size features (178; 179; 180). Finally, adding micro/nano structures, could increase hydrodynamic slip at the solid/liquid interface in addition to increasing the adsorbed film thickness (181; 182; 183).

Thin-film evaporation can be studied using a meniscus. For clarity, the evaporating meniscus is divided in three regions (Figure 3) (185). Region 1 is the adsorbed/nonevaporating film. This film has a uniform thickness and because of the joined effects of solid/liquid attractive forces, substrate temperature, and vapor pressure, it can not evaporate and has zero heat flux removal. In Region 2, the solid/liquid attractive forces are reduced and the liquid/vapor form a measurable curvature, with the liquid being more probable to leave the surface. The evaporation causes a thickness and curvature gradient at this region, which naturally drives the liquid towards this domain by intermolecular forces and capillary action. Region 3 is the

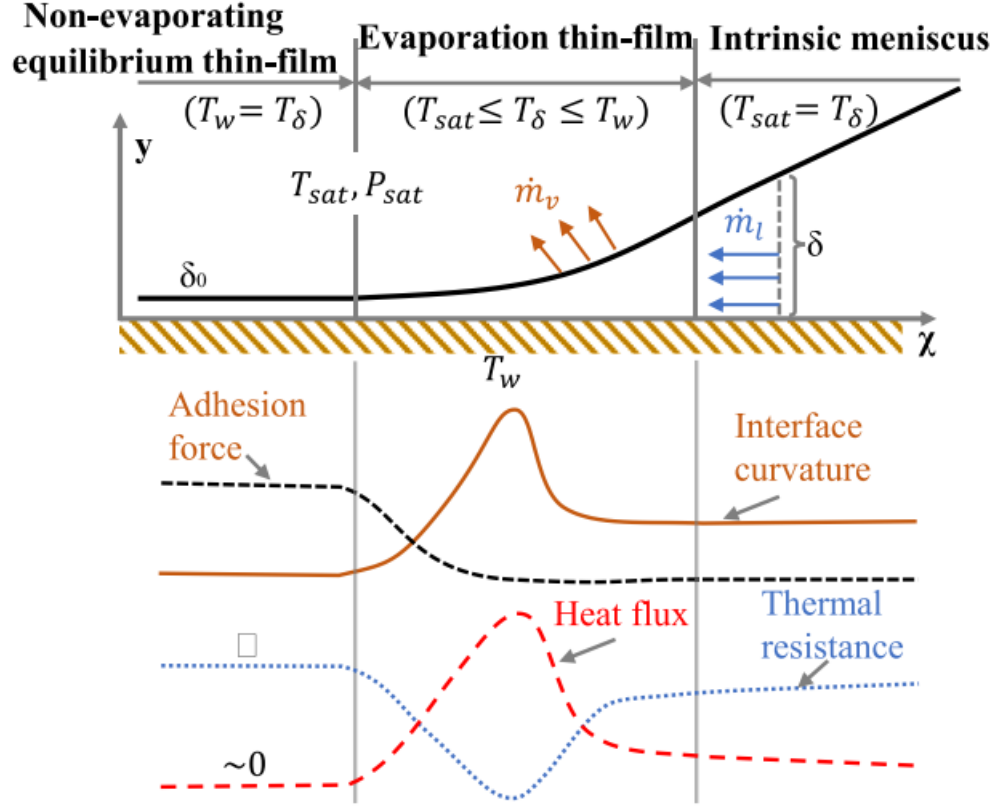


Figure 3: Schematic diagram of a meniscus at the interface. Curvature, adhesion force, thermal resistance, and heat flux density variation are qualitatively depicted. Reprinted from (184) Copyright 2021, with permission from Elsevier. Also Lancet special credit -Reprinted from (185) Copyright 2014, with permission from Taylor & Francis (see Appendix E).

intrinsic meniscus, where an almost constant curvature is dominant. This region is technically the reservoir that supplies liquid to Region 2. The liquid/vapor interface slope at the start of this region is defined by the contact angle. The overall heat transfer is constituted by the above regions and their corresponding thermal resistances. Using a static meniscus as the baseline, three major resistances are involved in the evaporation process: (1) conduction

through the solid, which, due to the high conductivity of the solid (usually metal), is small, (2) conduction through the liquid bulk, which is a function of the liquid film thickness and which is relatively high due to the low thermal conductivity of the liquid, and (3) heat transfer of vaporization or liquid/vapor interfacial heat transfer resistance, which is a function of liquid intermolecular forces (these depend on liquid/vapor interface curvature, the presence of NCGs, and the ambient vapor pressure). The latter thermal resistance is the dominant thermal resistance in Region 2, where the maximum evaporation takes place and hence, the liquid's latent heat plays a great role in this region. Figure 3 shows a qualitative illustration of the thermal resistance trend along the evaporating meniscus. Thermal resistance in Region 1 is practically infinite since no evaporation takes place there. Also, due to the thick liquid film, thermal resistance is relatively high in the intrinsic meniscus region too. Thermal resistance is minimum in Region 2, where a comparatively thin liquid film creates lower conduction thermal resistance. However, the thickness is marginally large enough such that minimal increases in film thickness increase the interfacial resistance swiftly. The aforementioned features have been confirmed experimentally (186; 187; 188) and characterized numerically (189; 190; 191) in the literature. Besides the heat transfer resistance, the hydrodynamic resistance is part of the play, too. The hydrodynamic limits of forcing a vapor molecule into a vapor space (192), the thinning capability of a meniscus before destabilizing or rupturing (193; 194), and the liquid delivery capability of a thin film to the evaporation area via a flow in the thin-film (friction limit and wetting), or via the intrinsic meniscus (capillary limit), or via the solid micro/nano structure, such as wicks (capillary and viscous limit) (195; 174; 196; 197; 198; 199; 200) are other key



factors that determine the evaporation rate and heat flux. Overall, one can conclude that to maximize the heat transfer or phase change, Region 2 must be maximized, where the thermal resistance is minimized and moreover, the hydrodynamic resistances for the liquid flow toward the evaporation zone must be minimized. Thin-film evaporation usually takes place at lower heat fluxes ( $< \sim 50 \text{ W/cm}^2$ ) while by increasing the heat flux, the evaporation is no longer the active mechanism with boiling having initiated. The boiling initiation depends on many factors, such as surface chemistry, morphology, ambient pressure, liquid saturation temperature, and heat flux. In heat transfer studies, two main types of boiling have been explored: pool boiling and capillary-fed boiling. The physics and mechanics of boiling from a porous surface submerged in liquid is different from boiling a liquid passively fed by capillary action.

Figure 4 illustrates the fundamental differences in heat transfer regimes between pool (A) and capillary-fed (B) boiling. In pool boiling, initially, heat is transferred via natural convection at low heat fluxes. By increasing the heat flux, nucleate boiling starts on the substrate and continues till the maximum or critical heat flux is reached. On the other hand, in capillary-fed boiling, heat transfer starts via thin-film evaporation at low heat fluxes. At increased heat flux, boiling initiates at the bottom (base of the porous structure). Moreover, in capillary-fed boiling, the vapor bubble departure characteristics change significantly due to the free-surface boundary between liquid/vapor at the interface. Although in pool boiling generally two major components (surface geometries, working fluids) are investigated, in capillary-fed boiling, vapor formation characteristics, heat transfer regimes (e.g., natural convection vs. evaporation at low

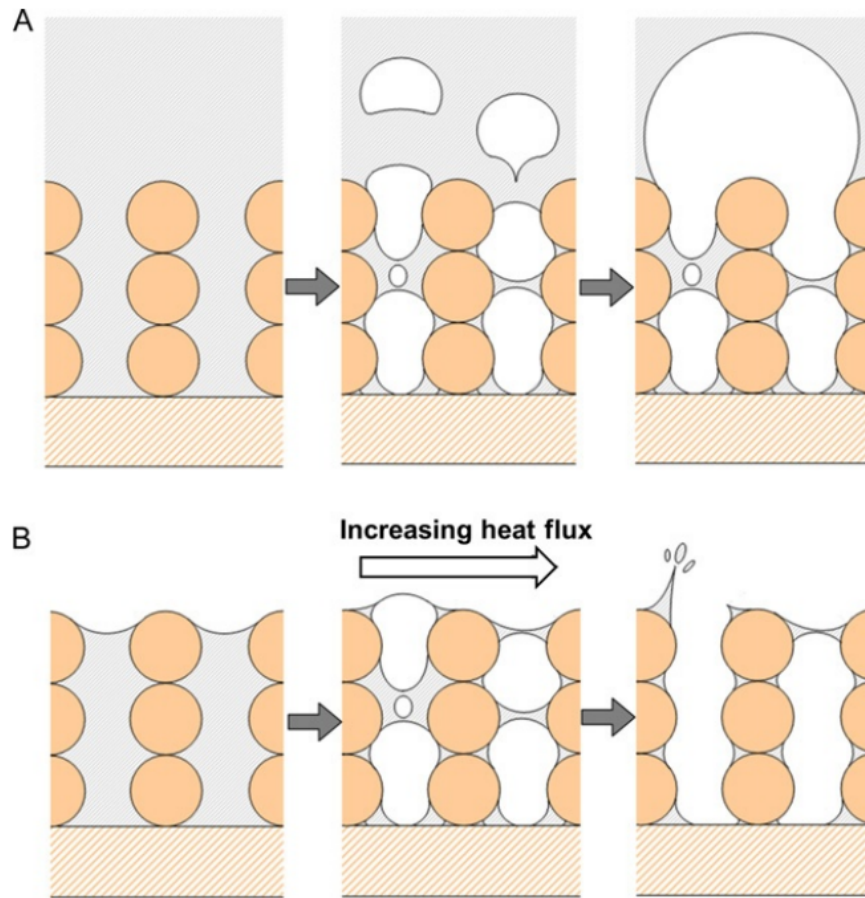


Figure 4: Schematic diagram of vapor formation and departure from a porous structure (A) submerged in a liquid pool (pool boiling), and (B) passively-fed via capillary action (capillary-fed boiling). Reprinted from (201) Copyright 2013, with permission from Elsevier (see Appendix E).

heat fluxes) and transition criteria for incipience/dryout are variables that vary in different circumstances and demand individualized studies.

Thin-film evaporation and capillary-fed boiling are the main driving mechanisms for removing high heat fluxes from local heat sources (e.g., electronic devices, LEDs, solar cells, batteries,

etc.) and are widely used in passive heat spreaders, such as vapor chambers and heat pipes, which are discussed in the next section.

### **1.2.3 Thermal Management of Local Heat Sources**

Thermal management of high-power devices is required for the efficient removal of the excess heat generated by an operating device to maintain the operational condition in addition to avoiding failures due to high thermal stresses (burn-outs). In the past few decades, advances in fabrication of miniaturized, high-power, and high-density integrated devices (e.g. electronic packages, Lithium-ion batteries in electric vehicles, etc.) have posed critical challenges in thermal management and cooling technologies (202; 203; 204). After the introduction of "Moore's law" in 1960 (205), which predicted that the number of transistors on a microchip doubles every two years, the integrated circuits have become increasingly smaller and denser. The major challenge facing the heat transfer community is removing higher heat amounts from smaller dissipation areas. This results in high heat fluxes, causing a sharp temperature increase at a local spot. When the rated operational temperature is exceeded, the reliability, performance, and lifetime of the device is significantly diminished (206). For example, the efficiency of LEDs radiation linearly decreases when the junction temperature increases, thus diminishing its performance (207; 208). CPU reliability also drops by 10% for each 2°C rise above the permissible operating temperature (209). Service life of a lithium-ion battery is reduced by 60% if the working temperature exceeds 50°C for a long period of time (210; 211). Considering the current pace of progress in high-power device technologies, traditional cooling techniques are not able to meet the required heat removal capacity at high heat fluxes (212). Several

advanced cooling methods have been proposed and implemented by researchers to meet these requirements. Usually, these thermal management techniques are categorized as active or passive cooling methods (213). The main difference between active and passive techniques is the presence or absence of an external force for inducing cooling. The passive method relies on natural convection, whereas active cooling is supplied by an external device, such as a fans or chiller, to enhance the heat removal efficiency and capacity. Of course, active cooling can handle higher heat fluxes, hence, most of the cooling techniques for thermal management of high-power electronic devices nowadays are being developed based on this approach. Therefore, in this thesis a general introduction to various active cooling techniques is presented and two particular systems, vapor chamber and heat pipe, are discussed in detail in Chapters 5 and 6. Another characteristic of cooling technologies is the direct or indirect contact of the cooling medium to the heat source.

Figure 5 summarizes the active cooling techniques. In direct-contact approaches, liquids have gained more popularity due to their superior heat dissipation capacity and efficiency. One popular method is Spray Cooling, which has been studied widely in the literature (214; 214). Spray cooling is a droplet atomization method through nozzles and high-pressure pumps. The generated spray uniformly covers the heating area and has a high cooling capacity for high heat flux applications with the advantage of great temperature uniformity and scalable cooling area. A similar approach to spray cooling is Jet Impingement, with the difference that no atomization is required and the liquid jet directly impinges on the heating surface. Studies in this area focus on optimizing the liquid properties, jet hydrodynamics and thermodynamics

behavior, as well as heating surface chemistry and morphology (215). For cooling large scale and multi-component electronics, Immersion Cooling has been developed and is mostly being used in data centers and servers (216; 217). Another approach in direct cooling is droplet electrowetting to manage heated areas of electronic devices. In this method, the droplet motion is manipulated on the surface by engineering the surface wettability and structure to achieve efficient heat removal (218; 219).

During indirect cooling the heat is dissipated by the cooling medium through a heat sink. These devices have been studied widely by engineers. As opposed to direct cooling, since in indirect cooling the space between the heating surface and the cooling medium is filled by a third medium, the contact thermal resistance plays a great role in efficiency of this method.

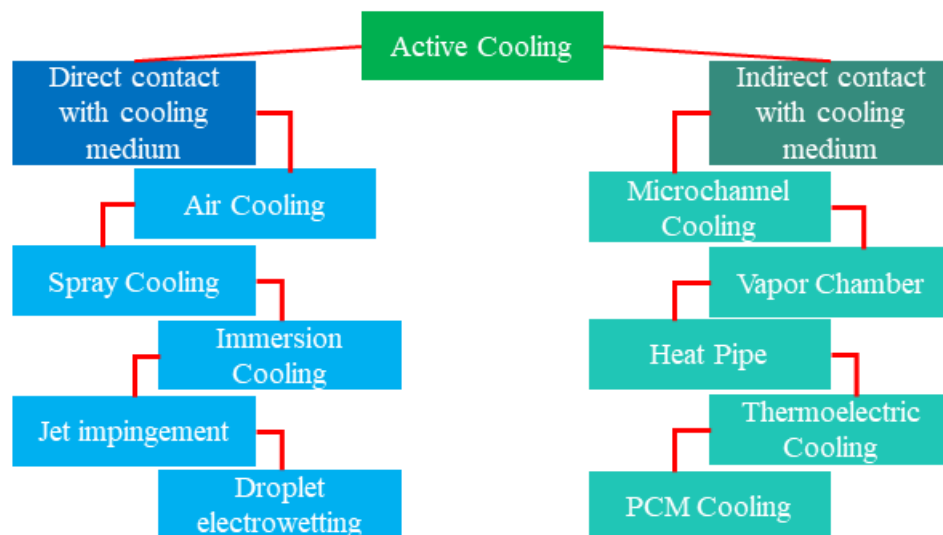


Figure 5: Classification of active cooling techniques

Hence, thermal interface materials (TIMs) are employed and nowadays play a critical role in the cooling of electronic devices (220). Thanks to their high heat transfer capacity and miniature size, microchannel heat sinks have gained much attention in the past decade (221; 222; 223). The major objective when optimizing microchannel heat sinks is the balance of heat transfer enhancement and flow resistance reduction. Toward this goal, much work has been done exploring the liquid characteristics (224; 225), the microchannel structure (226), and the phase change flow and heat transfer performance processes (227; 228). Another cooling method is offered by heat pipes and vapor chambers. These two devices are passive heat spreaders and alike in their internal structure and thermodynamic cycle with some differences. Mostly, they are sealed devices made of a wicking structure, and transfer heat via phase change. Their working principles include evaporation on the heated area, condensation on the cold area and circulation of a working liquid in their inner space. Heat pipes are known as one-dimensional heat spreaders as compared to vapor chambers, which are known as two-dimensional heat spreaders (229). Following the miniaturization of electronics in everyday devices, e.g., laptops, cellphones, tablet, etc, heat pipes and vapor chambers have been the subject of numerous studies to achieve smaller and more efficient heat removal. These two devices will be discussed in detail in the following sections. Additionally, another practical and efficient technique for thermal management of electronics is the Thermoelectric (TE) cooler. TEs have the advantages of long operating life, no pollution, and are noise free. Various studies have been carried out to optimise the TE material to enhance the cooler operational performance (230). Furthermore, the phase change material (PCM) cooling method is another feasible solution for thermal management

under high heat fluxes. The working principle of PCMs is based on latent heat storage, in which a high energy storage density is achieved via maintaining a constant temperature (231). PCMs are mostly useful for electronics with pulsed heat flux density, in which they can absorb the energy during the pulse generation and return it to the device in between successive pulses; in this way, the device working temperature is stabilized. To date, many studies have focused on optimization of PCM characteristics (232), structures of PCM-based heat sinks (233), and integration with other thermal management systems (234).

#### **1.2.3.1 Vapor Chamber**

The booming electronic industry has imposed serious challenges to the thermal management community by leading towards higher heat generation in smaller dissipation areas, where the heat fluxes reach 100-1000 W/cm<sup>2</sup> (235; 201); as for example in radio frequency (RF) systems (236), high-power light emitting diodes (LED) (237), solid-state laser light sources (238), and high performance graphics processing units (201). Integrated and compact semiconductor devices (e.g., microprocessors) could produce local hot spots via a large heat flux up to 5-10 times higher than the average heat flux (239), introducing hotspot cooling challenges. The sharp and rapid increase in temperature inside a microprocessor reduces its performance and could possibly lead to burnout (240; 241). Thus, it is crucial to efficiently manage these high heat fluxes under low superheat. In the literature, phase change of liquid/vapor has shown great promise for control and removing these high heat fluxes (242; 243). Among all aforementioned thermal management solutions, vapor chambers and heat pipes have been extensively and successfully used in a variety of systems. Vapor chambers are compact passive heat spread-

ers which can efficiently spread heat from a local hotspot to two dimensions, facilitating the heat removal by an adjoining heat sink. It has been proven that under certain operational conditions, effective thermal conductivity of a vapor chamber could reach three times higher than that of the copper plate with similar dimensions (244; 245). Furthermore, it was shown by Huang et al. (246) that thermal diffusivity of a vapor chamber could reach to up to  $44 \text{ cm}^2/\text{s}$  as opposed to  $\sim 1 \text{ cm}^2/\text{s}$  for a copper plate of similar size. Moreover, Mizuta et al (247) showed that the in-plane effective thermal conductivity of a vapor chamber could reach up to  $\sim 25$  times larger than a single-phase copper plate. Overall, vapor chambers have great anti-gravity (248; 249) and structural flexibility (250; 251) which makes them attractive to implement in many conditions and circumstances, such as in microgravity or in space.

### **Vapor Chamber Structure and Operation**

Figure 6 showcases a general schematic diagram of the internal structure of a vapor chamber. A vapor chamber is an enclosed system composed of an evaporator section, which is usually made of a wick structure, and a condenser side, which could be wick-lined or wick-free. In most cases, capillary posts or solid spacers exist between two sides, for liquid circulation and mechanical stability. The entire structure is usually enclosed via a thin metal casing. Prior to enclosing, the device is vacuumed of NCGs to enhance evaporation and condensation heat transfer, and charged with a certain amount of a working liquid, mostly water due to its high latent heat and surface tension. In a normal condition, the wick structure is saturated with the working fluid and a free space is maintained for phase-change of liquid to vapor. The operational principle of a vapor chamber is as follows:



1. Heat is conducted from the heat source through the solid casing to the wick structure.
2. Heat is conducted through the wick structure and the infused liquid.
3. At the liquid/vapor interface, the heat is absorbed by the liquid and via thin-film evaporation is removed by the vapor molecules.

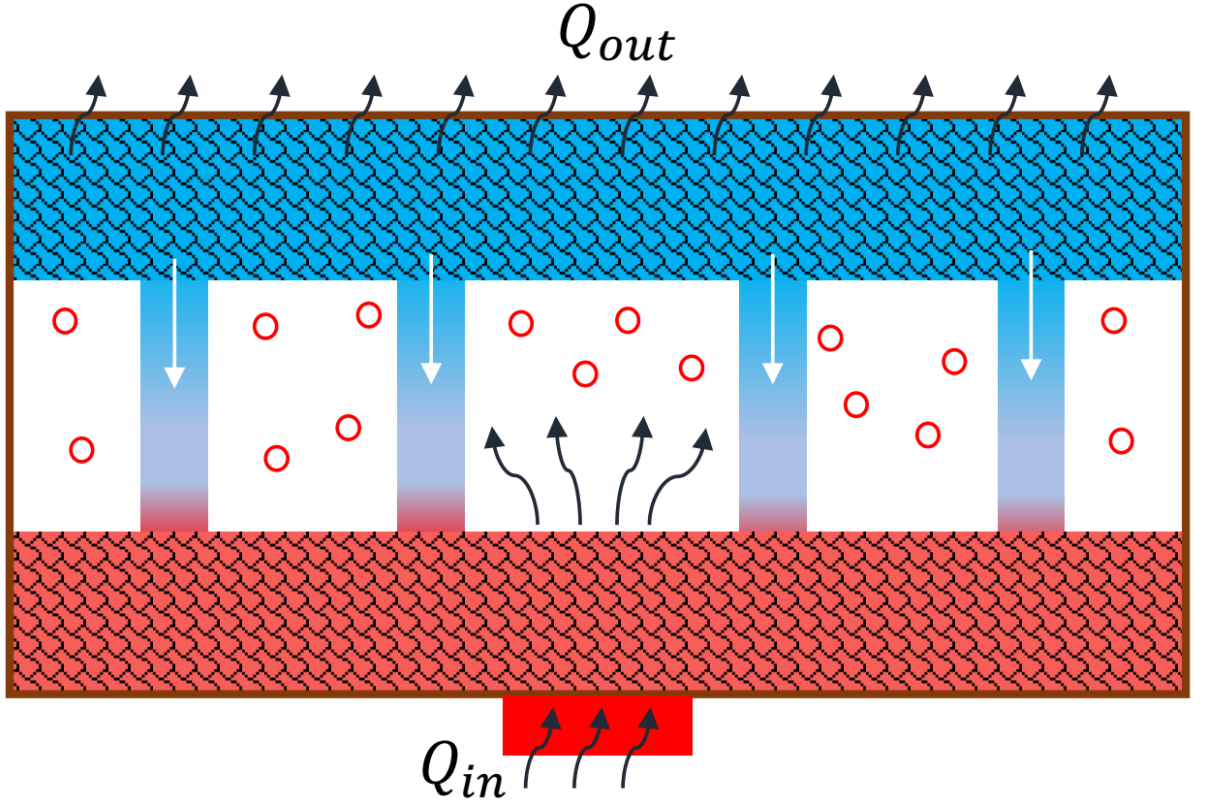


Figure 6: (a) Schematic diagram of the operation and structure of a typical vapor chamber. The hashed domains are occupied by wicks in this design, which also include wicking posts bridging the top and the bottom plate. The relative dimensions of the vertical thickness and the lateral extent of the chamber are not shown to scale.

4. The vapor diffuses through the interior chamber space and gets condensed on the condenser side, where it releases heat on a heat sink, in turn removing heat from the device.
5. The condensed vapor now is drawn back to the evaporator plate via capillary action (e.g., wicking posts or capillary bridges from the condenser to the evaporator) and the cycle is completed.

The evaporator wick is a multi-task component in a vapor chamber and governs heat transfer, capillary flow, and liquid/vapor phase change in the porous structure. Hence, enhancing the vapor chamber performance requires optimization of the wicking structure, which requires a complete understanding of evaporative heat and mass transfer rate of the meniscus, effective thermal diffusion through the porous framework, and capillary wicking capacity. To this end, countless studies have been conducted in the literature to enhance vapor chamber (and similarly heat pipe) performance, and the main aspects of these studies could be categorized in six groups:

- Materials: including silicon (252), aluminium (253), copper (254), stainless steel (255), etc.
- Fabrication methods: laser etching (256), electrochemical deposition (199), sintering (257), chemical etching (258), orthogonal ploughing/extrusion (259), deep reactive ion etching (DRIE) (260), additive manufacturing (261), etc.
- Capillary structure design: Including homogeneous wick structures (such as, sintered particles/ powder (262), micropillar arrays (263), micro-grooves (264; 259), graphite foams (265), woven meshes (266; 267), multi-artery wicks (268), and metal foams (269),

heterogeneous and hierarchical wick structures (such as, micro-mesh and micropillars (270), sintered particles and grooves (271), copper foams and micropillar (272)), nanostructured wicks (such as, nano-textured surface structures (195), carbon nanotubes (273), and copper nanowire arrays (274)).

- Capillary evaporation/boiling mechanism: Including nucleate boiling in porous wicks (201), thin-film evaporation (275), capillary transport and critical heat flux (276).
- Condenser design: Including wettability modification (277; 278; 279), wick modification (280; 281; 282), and extended condenser (283; 284; 285).
- Working fluid: Beside water, nano-fluids (286; 287) and organic compounds (288; 289).

### **Evaporator Wick Characteristics**

Thermal performance of evaporator's wick is generally characterized with two main components as follows.

- Capillary transport performance: Working liquid circulation in a wick is a process governed by the micro/nano structure of the porous medium and is generally dominated by the wick permeability and capillarity (261). Permeability is a parameter that describes the degree of fluid flow resistance. Spontaneous transport of liquid in a porous structure by capillary action is a slow process, and usually the inertia is negligible, so pressure drop governs the transport. Based on Darcy's law (290), Equation 1.14 below, the pressure

drop of fluid flow in a porous structure is proportional to fluid viscosity  $\mu$  and velocity ( $V$ ), and inversely proportional to the permeability coefficient ( $K$ )

$$\frac{\Delta P}{L} = \frac{\mu}{K} V \quad (1.14)$$

For flow velocities exceeding 0.1 m/s, the dynamics changes and the pressure drop increases. Equation 1.14 takes the form of modified Darcy's law (291)

$$\frac{\Delta P}{L} = \frac{\mu}{K} V + \rho C V^2 \quad (1.15)$$

where  $\rho$  and  $C$  are, respectively, the liquid density and the resistance compensation coefficient, which is a function of the structure of porous medium.

On the other hand, capillarity is a factor that characterizes the porous structure capability to drive the liquid flow, and can be determined by the Laplace pressure

$$\Delta P = 2\gamma/r_{\text{eff}} \quad (1.16)$$

where  $\gamma$  is the surface tension and  $r_{\text{eff}} = r_p / \cos \theta$  the effective radius of curvature, which depends on the average pore size ( $r_p$ ) and the static contact angle  $\theta$ . A common test to characterize porous structures features capillary-rise experiments by placing the wick structure in a liquid and visually recording the liquid rise as a function of time (292). The

final equation describing the height rise of a liquid based on the porous properties could be summed in the well known Washburn equation(293)

$$h^2 = \frac{4\gamma K t}{\mu \epsilon r_{eff}} \quad (1.17)$$

where  $\epsilon$  is the porosity of the wick structure. Equation 1.17 could be rewritten as

$$\Delta PK = \mu \epsilon h^2 / 2t \quad (1.18)$$

where permeability and capillarity are absorbed into one factor described by the total height-rise ( $h$ ) and the time to reach to that height ( $t$ ). Equation 1.18 is frequently used to describe the porous medium characteristics (294; 295).

- Critical heat flux (CHF) and evaporator thermal resistance: Another factor for characterizing a vapor chamber (or a heat pipe) is defined by its critical heat flux (CHF). CHF is the maximum heat flux that the device could tolerate before it dries out. The dry-out occurs when replenishment of fluid at the heating area gets slower than liquid/vapor phase change, so the liquid meniscus at the liquid/vapor interface recedes to the bottom of the wick structure and breaks, creating a local dry spot. In addition to the CHF, the evaporator's wick thermal resistance ( $R_{evap}$ ) is another factor that determines the performance of a vapor chamber.  $R_{evap}$  is dependent on the evaporator superheat ( $\Delta T_{evap}$ ), which is

the temperature difference between the wick over the heat source and the released vapor from the meniscus

$$R_{\text{evap}} = \Delta T_{\text{evap}}/Q \quad (1.19)$$

where  $Q$  is the total heat input. As seen, higher superheat is required to remove the same amount of heat for a wick with higher thermal resistance. This is a disadvantage for practical applications, such as electronics cooling. So, many scholars have targetted this parameter by optimizing the wick structure. But the story does not end here. Flow and heat transfer in a wick structure is very complex and difficult to model. To increase liquid pumping capacity, the pore size must be reduced, and by doing so, the flow resistance is increased. Moreover, from thin-film evaporation theory, larger pore sizes create less thin-film evaporation area, so larger superheat will be generated if higher fluid flow is required. All this contradictions in wick optimization have inspired many researchers to come up with various structures to address these issues; a brief summary of these efforts is presented in the next section.

### **Vapor Chamber Performance Characteristics**

Three main performance metrics are defined to characterize a vapor chamber's thermal performance as follows

- Total thermal resistance: Calculating  $R_{\text{evap}}$  is a challenging task and requires placing thermocouples inside a vapor chamber to measure the vapor's temperature or a specific facility to evaluate the wick's thermal performance. Hence, facilitate thermal performance

evaluation and have a better comparison among different vapor chambers a total thermal resistance metric is defined as

$$R_{\text{total}} = (T_h - T_c)/Q \quad (1.20)$$

where  $T_h$  is the heat source temperature and  $T_c$  the average temperature of the entire condenser side of the vapor chamber. Generally, lower thermal resistance is preferable ( $<0.1$  K/W), since it makes it easier for heat to be dissipated from a small area to a larger one. Furthermore, thermal resistance is not the sole factor that determines a vapor chamber's performance, since it is highly dependent on the testing platform (e.g., heater size, cooling method, such as natural or forced convection or liquid cooling, etc.). Technically, vapor chambers are designed to spread heat from a localized spot to a larger area for efficient removal subsequently by heat sink. In test platforms where the heat source area is comparable to the vapor chamber dissipation area, the heat spreading is more efficient since less spreading is required. Therefore, larger heater area-to-vapor chamber area ratio naturally produces lower total thermal resistance. On the other hand, heat removal approach, such as natural or forced convection and cold plate, is a key factor in determining the thermal resistance. Natural or forced convection heat sinks tend to create uniform temperatures on the cooled side of the VC while keeping the device at high working temperatures as opposed to cold plates in which the device works at lower

temperatures with larger temperature gradient on the condenser side. Therefore, it is crucial to mention these factors together when describing a vapor chamber's performance.

- Effective thermal conductivity: Another factor used to characterize a vapor chamber is its cross-plane effective thermal conductivity, which is defined as

$$K_{\text{eff}} = \frac{Qdx}{A\Delta T} \quad (1.21)$$

where  $dx$  is the vapor chamber thickness,  $A$  the heat source area, and  $\Delta T$  is the same  $T_h - T_c$  used in thermal resistance. Similar argument regarding the heater versus vapor chamber's heat dissipation area and heat sink type holds for this parameter as well. Therefore, a precise description of the test platform is necessary for better interpretation of the effective thermal conductivity.

- Charging ratio: The amount of working liquid in a vapor chamber (or heat pipe) can determine the optimum performance range. Since, different devices have different capacity of the charging fluid, a universal definition is introduced to better describe the system. the charging or filling ratio is defined as follows

$$CR = \frac{\text{amount of liquid volume}}{\text{total internal empty space of device}} \quad (1.22)$$

This ratio describes how much of available space in a vapor chamber is occupied by the working fluid and, in general, there is no preference for a specific value, rather its value is critical for an individual apparatus to achieve its designed thermal performance.



## Advancements in Conventional Vapor Chambers

In attempts to improve a vapor chamber's (likewise, heat pipe's) thermal performance via optimizing the wick structure, researchers have taken various approaches, such as:

- Homogeneous structures: Ryu et al. (296) suggested a new dual-height micro-pillar array with superhydrophilic property. A parametric study was performed via simulation and it was shown that dual-height micro-pillar structures do not influence the capillary transport capacity but notably enhance the thin-film area. This led to an HTC enhancement of three times over single-height micro-pillar structures. Li et al. (281) fabricated a biomimetic grooved wick structure based on topology optimization. By minimizing the entrance dissipation rate, a leaf vein pattern structure with optimal conductivity was obtained. The simulation revealed that the pattern creates great temperature uniformity and capillary transport capacity. Wei et al. (297; 298) conducted geometry optimization on uniform micro-pillar array structures and via a semi-empirical approach, could predict the CHF. The simulation predicted CHF of the optimal micro-pillar structure would reach  $93 \text{ W/cm}^2$  with  $15^\circ\text{C}$  superheat. The simulation result was further validated by experimental data with  $< 7\%$  error reported. The micro-pillar arrangement and optimization was also pursued by Cho et al. (299). The capillary rise and forced-flow tests were performed and in the meantime, the meniscus geometry and capillarity calculations were done by Surface Evolver, which was interfaced with a finite-volume algorithm for heat transfer performance simulation. The simulation and experimental result aligned and both showed rectangular arrangement of micro-pillars to be favorable compared to

square or hexagonal arrays. In a comparative study, Peng et al. (300; 301) proposed a leaf-vein structure network for the evaporator wick. The results showed the capillary network to reduce thermal resistance and create a greater temperature uniformity along the condenser. Their finding was later confirmed by other scholars, showing that similar vein-like structures could produce similar thermal performance enhancement (281; 302).

- Heterogeneous structures: A novel two-layer wick structure was proposed by Sudhakar et al. (303; 304). A thin homogeneous wick structure was designed to promote evaporation and boiling at the bottom of the wick and designate vents to allow vapor to escape the structure rapidly. The top layer was designed for collecting and directing the liquid to the heating area via wicking posts. The simulation predicted maximum CHF of  $1 \text{ KW/cm}^2$ . Experimental results showed optimum copper particle size range is  $180\text{-}220\mu\text{m}$  in which a CHF of  $485 \text{ W/cm}^2$  was achieved via minimum thermal resistance of  $0.052 \text{ K/W}$ . By improving their design, they pushed the CHF to  $512 \text{ W/cm}^2$  with thermal resistance  $0.08 \text{ K/W}$  (305). Patel et al. (306) fabricated a vapor chamber with multi-layer graphite foams in the vapor core. The light-weight graphite layers act as a conductive material in addition to providing channels for liquid transport. The hybrid wick structure was shown to reduce the junction temperature by 30%. Chen et al. (307) fabricated an ultra-thin vapor chamber by combining copper mesh and micropillar arrays. The results showed 30 times higher thermal conductivity compared to a copper plate with this device, and the performance under anti-gravity scenario, where gravity opposes the capillary flow, only reduced by 11%. Li et al. (308) conducted experiments on the influence of copper pow-

der and foam structure wicks and found that the copper powder effectively reduced the thermal resistance while the copper foam enhanced the temperature uniformity. Another type of hybrid wick was proposed by Velardo et al. (309) who combined screen mesh and sintered powder and showed significant enhancement compared to uniform structures. Wang et al. (310) showed that by adjusting the evaporator and condenser wick structure, maximum pressure drop could be less or equal to the maximum capillary pressure, resulting in enhanced thermal performance. They revealed that using coarser wick on the evaporator side, as compared to the finer wick on the condenser, they could improve the fluid circulation and enhance CHF.

- Nanostructures: Weibel et al. (311) proposed the implementation of carbon nanotubes (CNT)s in a vapor chamber. In their numerical investigation, they used CNTs in combination with conventional sintered powder wicks to balance the permeability and capillarity, while reducing the overall thermal resistance. Their study showed that for the optimal cases, the thermal resistance was reduced 13 times compared to uniform sintered powder wick. In their follow-up study, Weibel and Garimella (312) conducted an experimental study of thermal performance of a vapor chamber made with sintered copper powder and CNTs. They compared several cases with uniform and hybrid structures and found that pure sintered powder wicks outperformed the CNT-coated wick in terms of CHF ( $> 514 \text{ W/cm}^2$  against  $437 \text{ W/cm}^2$ ) while having very close thermal resistance ( $0.0875$  and  $0.0925 \text{ K/(W/cm}^2)$ ). However, they observed that the CNT-coated evaporator eliminated the evaporation/boiling transition regime, which was present with the non-coated

sintered wick. Le et al, (313), by controlling the chemical oxidation time, created various nanoflower/grass type CuO nano structures on a flat copper plate. They ran capillary-rise and thin-film evaporation tests and characterized the thermal characteristics of different structures. Jung et al. (314; 315) introduced a new type of high-functionality material made of copper and a hybrid of nanowires and copper sponges. This high-porosity wick structure was fabricated with a metal nanowire synthesis method. The wick structures had high surface area, capillarity and flexibility in addition to low density, showing great potential for application in vapor chambers and heat pipe. Wen et al. (266) fabricated a copper wick structure with sintered multilayer copper micro-meshes where they could create micro-cavities and nano-needles on the wick structure via chemical oxidation technique. The micro-nano structures have shown higher CHF where 3 and 5-layer structured wicks reached maximum heat fluxes of  $145.7 \text{ W/cm}^2$  and  $198.6 \text{ W/cm}^2$ , respectively.

### **Vapor Chambers with Wickless Components**

As discussed earlier, a large portion of the literature has been devoted to optimizing the wick structures of vapor chambers. Beside all the advantages of wicks, there are a few drawbacks which depending on the application could pose minor or major problems. Most drawbacks of wicks are related to their physical characteristics, such as their capillary limit, pore-clogging, added-thickness and weight to the device, and fabrication cost along with design complexity. Replacing the wick structures with wickless components while keeping the wicks' advantages is a challenging task but it is a necessary adventure for achieving more-reliable, robust, and high-performance devices. Going wickless is an ongoing effort and so far, there have been various

attempts in the literature to create a competitive, fully or partially wickless vapor chamber. Boreyko et al. (316) fabricated a vapor chamber combining a wick-lined evaporator and a wickless condenser. The wickless superhydrophobic condenser took advantage of jumping droplet condensation with HTC of  $\sim 10 \text{ KW/m}^2\text{K}$ . In an attempt for a fully-wickless vapor chamber, Hsieh et al. (317), fabricated a vapor chamber with no wick structure and gravity-reliance; this device was able to handle  $220 \text{ W/cm}^2$  heat flux at minimum thermal resistance of  $0.2 \text{ K/W}$ , however, the device's high thickness, 103 mm, made it difficult to implement in practice. In another attempt, Zhao et al. (318) fabricated a bio-inspired vapor chamber with beetle-inspired condenser, in which hydrophilic bumps were placed on a superhydrophobic background. The hydrophilic bumps were the condensate accumulation points, where the drops returned to the evaporator via electrostatic forces. In another study (319), an almost wick-free and adaptive vapor chamber was proposed and fabricated. The vapor chamber evaporator was coated via thermo-responsive polymer brushes that changed wettability, becoming more wettable when heated. However, the brief thermal characterization did not allow a comprehensive understanding of the thermal performance of this system. The concept of using superhydrophobic surfaces as the condenser was further implemented by Boreyko et al. (316; 279). In this study, the droplet jumping out of a superhydrophobic surface was the main returning mechanism to the superhydrophilic wick-lined evaporator. In continuation of their work, Wiedenheft et al. (320) used the same wickless condenser opposed to a 1-mm tall microstructure evaporator to make a vapor chamber for a hot-spot cooling application. Furthermore, the role of nanofluids in heat transfer performance of a wickless vapor chamber was studied by Shukla et al. (321).

Recently, this idea was further evolved by Edalatpour et al. (322) who used a wick-free hydrophobic condenser in a Vapor Chamber–Thermal Diode device with bridging-droplet return mechanism from the condenser to the superhydrophilic wick-lined evaporator. A similar approach was also presented by our group (278; 323) where a wick-lined evaporator opposed to a wickless wettability-engineered condenser was used both as a vapor chamber and a thermal diode. In an attempt to remove wick structure from the evaporator, Shaeri et al. (324) fabricated a vapor chamber with a wickless and biphilic evaporator with hydrophobic domains on the heating zone surrounded by superhydrophilic background. However, the results were not conclusive in whether the hybrid wettability was beneficial or not, since the biphilic vapor chamber had lower critical heat flux and higher thermal resistance compared with a wick-lined device. There have been several other studies that used wettability patterning on the wick of the vapor chamber (325; 326; 327; 328) but Damoulakis and Megaridis (329) presented the first scheme of fully wickless and wettability-patterned (evaporator and condenser) vapor chamber. In their study, multiple combinations of various wettability patterns were studied and for the best combination, a maximum heat load of 200 W with minimum thermal resistance of 0.18 K/W was reported.

### **1.2.3.2 Heat Pipe**

Similar to vapor chambers, heat pipes are another type of passive heat spreaders that transfer heat from the heat source to a certain location (1 dimensional). Heat pipes have gained tremendous popularity in the heat transfer community since their introduction in 1944 by Gaugler (330). Since then, heat pipes have been extensively used in thermal management

of electronics due to their high reliability, simple implementation, flexible geometry, and high efficiency heat removal performance (331). The heat pipe family consists of various designs, such as heat pipe-thermosyphon (332), pulsating/oscillating heat pipe (333), loop heat pipe (334), and conventional heat pipes (335). In this thesis, we explore conventional heat pipes, structures and their performance metrics, and apply recent advances to enhance performance.

### Heat Pipe Structure and Operation

Figure 7 shows a schematic diagram of heat and fluid circulation in a conventional low-profile, long heat pipe. As seen, the internal structure is very similar to a vapor chamber's; the heat pipe is usually fully wick-lined with the difference that the heater and chiller/heat sink are located on the two opposite sides of the device. Following the exact working operation of the vapor

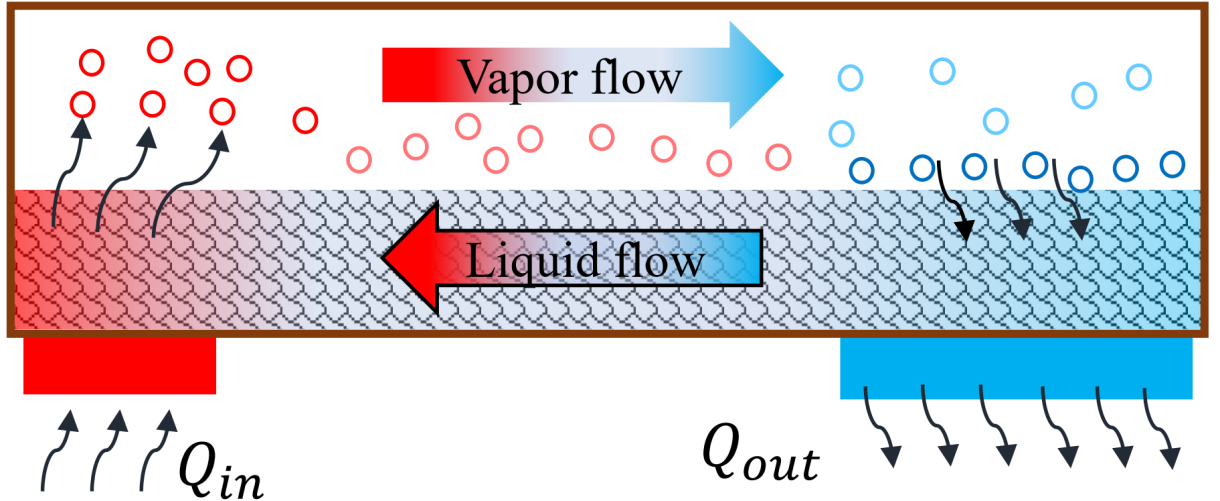


Figure 7: Schematic of a heat pipe's internal structure. The hashed domains indicate the wick linings. In this design, the heat is transferred from left to right.

chamber, a heat pipe transfers heat from the heat source to the heat sink via phase change and after condensation, the working fluid returns to the heat source through the capillary wick from only one direction. That is the major difference between vapor chambers and heat pipes, where this long travel of the working liquid imposes the major inhibition, due to large pressure drops, towards reaching high CHF's. Due to large similarities between heat pipes and vapor chambers, the research approaches are also alike as mentioned in the previous section. However, there is a minor difference in the performance metrics due to their physical differences:

- Thermal Resistance: Based on Figure 7, the total thermal resistance in a heat pipe is defined as

$$R_{\text{total}} = (T_h - T_c)/Q \quad (1.23)$$

where  $T_h$  is the temperature of the heat source and  $T_c$  the average temperature of the cooled side of the device; depending on the chiller position,  $T_c$  could be on the same, opposite, or both sides of the wick-lined plate.

- Effective thermal conductivity: Similarly, the effective thermal conductivity of the heat pipe is defined as

$$K_{\text{eff}} = \frac{QL}{A\Delta T} \quad (1.24)$$

where in this case,  $L$  is the operational length of the heat pipe, and  $A$  the cross section of the from the heater to the chiller.

In heat pipes, particularly conventional heat pipes, wick structures also play the most crucial role in thermal performance of the device so, studies mostly have focused on the capillary



transport and the CHF enhancement via optimizing the wick structure. A number of methods has been developed and employed for improving the heat transfer performance of heat pipes. A wide range of techniques has been employed to enhance flat-plate heat pipes' thermal performance. Shioga et al. (336) fabricated an ultra-thin flat heat pipe using chemical etching and diffusion-bonding method. Their method was able to fill the gap between the heat pipe casing and the wick structure. A minimum thermal resistance of 0.03 K/W was achieved at 20 W. Zhou et al. (337; 338) used spiral woven meshes as the wick structure, which served two purposes without one affecting another: 1- reduced the heat pipe weight compared to other type of meshes, and 2- enhanced the heat transfer capability. They also fabricated a heterogeneous wick structure, combining copper mesh and copper foam, which enhanced heat transfer capacity in addition to the mechanical strength (339). Chen et al. (340) also fabricated an ultra-thin heat pipe via a stamping method. Their surface functional wicks were created via a micro-milling method, in which an orthogonal groove network was covered via grain-like microstructures. Their device tolerated a maximum heat load of 150 W with 0.15 K/W thermal resistance. Wang et al. (341) fabricated a bio-inspired hierarchical wick structure from *Salix Flamingo* plant. They performed mathematical modeling and experimental tests and showed a good agreement between them, indicating the great potential of the wick structure for heat pipe application. Li et al. (342) fabricated a superhydrophilic wick structure from copper mesh via annealing at high temperatures for their flat heat pipes. This approach has shown effective thermal conductivity of 30 to 80 times higher than a pure copper plate. Tharayil et al. (343) used thermal evaporation method to coat sintered copper mesh with various copper nanopar-

ticle thicknesses. They found 22% enhancement in thermal resistance with 400 nm thickness and 15°C reduction in evaporator temperature at maximum heat load of 380 W.

Another critical factor in heat pipe performance is their inclination angle, which has been widely studied in the literature. Zhang et al. (344) fabricated an aluminum heat pipe with and without wick structure and showed the wick to help the heat pipe performance under 30° and 60° inclination angle. However, on the vertical condition, the non-wicked heat pipe showed lower thermal resistance. The reason was pointed out as the liquid back flow from the condenser and its blocking the vapor pathway in inclined modes. Yao et al. (345) also shown that the effective thermal conductivity of a micro heat pipe is significantly reduced from 5820 to 295 W/m.K when the inclination angle is changed from 90° to -75°. Further, Li et al. (346) tried various porous wick structures on a rotary wheel and found that sintered wick structures provide sufficient capillary pressure to overcome centrifugal acceleration and maintain the heat pipe's thermal performance.

Finally, the thermal performance of a heat pipe is highly influenced by its working fluid type. Sardarabadi et al. (347) found that combinations of a nanofluid with sodium functional group could enhance the heat pipe's thermal performance. Xu et al. (348) revealed that a mixture of HFE-7100 and water could raise the heat transfer capacity of the heat pipe by delaying its dry-out onset. The dry-out was delayed due to the working liquid having low boiling point and high saturation vapor pressure. Ramkumar et al. (349) revealed that acetone, instead of methanol as the working fluid, could enhance the heat transfer coefficient by 80%. Lastly, the filling ratio of the heat pipe has also been the subject of research and many studies have shown

there is an optimum charging ratio where for a certain heat pipe, the thermal performance is maximized (350; 351; 352).

### **Flat Plate Heat Pipe with Wettability-Engineered Component**

Even though various efforts have been made to replace or remove the wicked parts of vapor chambers, due to operational differences, this aim for heat pipes remains more challenging. The main reason behind this is the long-range transport of the working liquid and moreover, in heat pipes, vapor and liquid have opposite direction. Thus, miscalculated addition, removal or modification of a surface component may lead to worse performance. Having said that, there have been a handful of studies that investigated the role of wettability modification and patterning in flat plate heat pipes. Wong et al. (353) conducted a visualization study on mesh-wick flat-plate heat pipes with the modified wettability on the evaporator and condenser sections. They examined 4 different wettabilities for each section separately  $\theta = 0^\circ$ ,  $13^\circ$ ,  $80^\circ$ , and  $120^\circ$  and reported that the evaporation resistance for  $\theta = 0^\circ$  and  $13^\circ$  was alike. However, the condensation resistance for  $\theta = 0^\circ$  was maximum, since the condenser section was flooded. They observed that increasing contact angle in the condensation section enhances dropwise condensation on the mesh islands, however, for  $\theta = 120^\circ$  they reported that the water level at the condenser was minimum but due to larger droplets, the thermal resistance was increased. It was shown that  $\theta = 13^\circ$  for both evaporator and condenser performed best in terms of CHF and thermal resistance. In a numerical study, Singh et al. (354) investigated a wickless micro heat pipe with triangular cross-section and wettability gradient. They developed a mathematical model and described the role of wettability in the evaporator and condenser. Based on their calculations,

higher wetting evaporator and lower wetting condenser are preferred at the same time. They also showed that the best wettability gradient featured linear variation from  $\theta = 50^\circ$  at the condenser to  $\theta = 10^\circ$  at the evaporator. In their follow-up study (355) they repeated their analysis for a trapezoidal cross-section micro heat pipe and similarly found that the optimized wettability gradient can outperform uniform high wettability ( $\theta = 10^\circ$ ) by 65%. Liu et al. (356) fabricated a flexible flat heat pipe for deployable structures via laser etching the casing material (aluminum compound packing film). They used multilayer stainless steel mesh as the capillary core and applied wettability gradient via attaching catalytically grown nanowire structure onto the core mesh. They showed that the wettability gradient enhanced the device heat transfer performance even for a bending angle of  $180^\circ$ . Their heat pipe reached a minimum thermal resistance of 0.52 K/W at 12 W. In another study, Xie et al. (357) fabricated a micro flat plate heat pipe via pulsed laser fiber etching to create micro-grooved structure as the wicking medium. Using various laser settings in addition to applying wettability gradient on the grooved surface by immersion into hydrogen peroxide, they prepared various combinations of capillary and wettability surfaces as the heat pipe core. They found the maximum heat load was achieved via a microgrooved surface possessing a wettability gradient from  $45^\circ$  on the condenser to  $0^\circ$  on the evaporator. The heat pipe reached a thermal resistance of 0.002 K/W at 50 W, which was 10 fold smaller than without wettability gradient. And finally, Lou et al. (358) fabricated a fully wickless micro flat heat pipe and replaced the wick a wettability-patterned surface. They used laser etching method and fabricated several patterned surfaces with superhydrophobic/superhydrophilic stripes of different width as the heat pipe and compared their

steady state temperature, start-up time, and axial maximum temperature difference, and also the thermal resistances. They found that the superhydrophobic-superhydrophilic strip width had a significant influence on drop dynamics, capillary forces, and hysteresis. And as a result, the heat transfer performance was found to be a direct function of the wettability pattern. Their results showed laser-textured wettability-patterned surfaces could be viable substitutes for wicks in micro heat pipes and could be implemented for cooling of microelectronics.

### **1.3 Thesis Objectives**

The overall objective of this work is to investigate and implement wettability-engineered surfaces in thermo/fluidic systems.

#### **1.3.1 Objectives for Chapter 2**

- Create a comprehensive data set of various  $\text{TiO}_2$  coatings.
- Study wettability properties of different  $\text{TiO}_2$  coatings as a function of UV exposure time.
- Analyze and model the  $\text{TiO}_2$  coating wettability via different statistical approaches to find a universal model describing different  $\text{TiO}_2$  coating wettability as a function of UV exposure time and its constituents.

#### **1.3.2 Objectives for Chapter 3**

- Study the spreading dynamics of a gas bubble submerged in a liquid and under wettability confinement
- Explore various influential factors in spreading dynamics, such as geometrical and hydrodynamic variables.

- Develop a scaling law describing the spreading dynamics of a micro-volume gas bubble confined on a track.

### **1.3.3    Objectives for Chapter 4**

- Revisit the influential factors on condensation enhancement via using a wettability-engineered metal surface.
- Isolate the key parameters and explore their role in condensation heat transfer improvement.
- Fabricate and test different patterns and examining the key factor experimentally.

### **1.3.4    Objectives for Chapter 5**

- Fabricate and test a custom-made high-power electronic module with two metal–oxide–semiconductor field-effect transistors (MOSFET)s as the heat sources for cooling application.
- Explore the feasibility of a hybrid vapor chamber for a real-life application of cooling two electronics components with the aforementioned setup.
- Examine the hybrid vapor chamber thermal performance and compare it with a single-phase copper heat sink under low heat-removal condition (forced convection).

### **1.3.5    Objectives for Chapter 6**

- Investigate the feasibility of wettability engineering on a wickless component in a flat-plate heat pipe.
- Fabricate and test a hybrid heat pipe for cooling  $> 100\text{W}$  heat loads.

- Explore the role of wettability of the wickless component, wick structure, and charging ratio in the heat pipe's thermal performance.

#### 1.4 Scope of Work

This dissertation aims to study different aspects of wettability engineering technology and its implementation in both isothermal and non-isothermal thermal-fluidic systems. Initially, in Chapter 2, we investigate the wettability properties of a specific  $\text{TiO}_2$  coating against water to further understand and predict its behavior for practical applications, where a specific surface wettability is required. This study enables us to precisely and selectively control wettability of a surface, which has so many applications and in particular liquid transport on open surfaces (16). Interaction of liquid droplets in such wettability-confined spreading and transport have been widely studied (359). However, for the case of a gas bubble in a liquid, studies have mostly focused on applications, with a fundamental understanding of this case still lacking. Hence, in Chapter 3, we have used the wettability difference/contrast concept to confine a gas bubble in a liquid and study its underlying spreading dynamics as a function of the solid geometry, gas bubble size, and liquid properties. Confining liquid/gas bubbles via wettability patterning is a facile and robust task, with tremendous geometrical flexibility, fabrication technique variety, and substrate diversity. These qualities of wettability engineering enable researchers to incorporate such surfaces in a variety of systems, both isothermal (fog-harvesting, gas harvesting, oil and gas, biomedical, inkjet printing, open-surface microfluidics, etc.) and non-isothermal (condensation, evaporation, boiling, thermal management, etc.). In Chapter 4, inspired by the ever-rising demands in the electronics industry and great potential of wettability engineer-

ing in this domain, we redirected attention to implementation of wettability engineering in a non-isothermal system. In this chapter, in attempt to further illuminate the role of wettability patterning on condensation heat transfer enhancement, we conducted a parametric study on the geometrical layout of the superhydrophilic tracks. Next, in Chapter 5, to further take advantage of this technology in thermal management applications, a wettability-engineered condenser was implemented in a hybrid vapor chamber with a wick-lined evaporator. This is a follow-up study to the original work by Koukoravas et al. (278), with the present work designed for cooling two high-power MOSFETs via forced convection. Next, in Chapter 7, the feasibility and efficiency of wettability engineering implementation in a heat pipe was studied. In this work, similar to the hybrid vapor chamber, a hybrid heat pipe was built and its thermal performance was tested. This way, a range of thermal management systems, starting from sole condensation, 2D and 1D heat spreading via evaporation and condensation, with wettability engineering was studied and evaluated.



## CHAPTER 2

### WETTING PROPERTIES OF $\text{TiO}_2$ -COATING, A PREDICTIVE MACHINE LEARNING APPROACH

*"This chapter is reprinted with permission from M. Jafari Gukeh, S. Moitra, A. N. Ibrahim, S. Derrible, and C. M. Megaridis. Machine learning prediction of  $\text{TiO}_2$ -coating wettability tuned via UV exposure. ACS Applied Materials & Interfaces 13, no. 38 (2021): 46171-46179. Copyright 2021, American Chemical Society". (see Appendix E)*

#### 2.1 Background and Motivation

Water repellency (hydrophobicity) and water attraction (hydrophilicity) have been studied extensively in the scientific community. When a solid surface comes into contact with a water droplet two scenarios can occur: (1) the water spreads on the surface, which is then termed hydrophilic, and has contact angle below 90 degrees, or (2) the water beads up and does not spread, implying hydrophobicity with a contact angle greater than 90 degrees (2). In the extreme case where the surface roughness and surface energy increase, the surface is said to be superhydrophilic, and the contact angle is less than 10 degrees. On the opposite end, a surface with low energy and high roughness, is superhydrophobic and displays a contact angle greater than 150 degrees (2). Over time, developments in surface engineering techniques have facilitated the manipulation of different liquids on wettable and non-wettable surfaces. In

particular, different spreading behavior of liquids on wettable and non-wettable surfaces has demonstrated a variety of applications by confining and transporting liquid volumes passively via spatially juxtaposed wettable and non-wettable regions, partitioned by a sharp wettability contrast line (23; 16; 24). In the past two decades, applications of such surfaces have become increasingly popular in different areas, such as electronic cooling (278; 360; 361; 323), condensation heat transfer (362; 363), open-surface microfluidics (364), and air bubble manipulation underwater (365).

There are two well-established requirements for a surface to be superhydrophilic or superhydrophobic. The common factor is the roughness (366) (e.g., micro/nano spatial features); the differentiating factor is the surface energy of the solid. Numerous techniques have been developed over time to create superhydrophobic surfaces, including by roughening a low-surface-energy material (367), plasma etching (368), laser etching (369), chemical etching (23; 370), lithography (371), sol-gel processing (372), electrochemical reaction and deposition (373), and electrospinning (374). Inspired by nature, scientists have fabricated superhydrophobic surfaces using different one-dimensional nanomaterials with inherent morphology reflecting the lotus leaf papillae, including  $\text{TiO}_2$  (375; 376), SiC nanowires (377; 378), ZnO (379; 380), and carbon nanotubes (CNTs) (381; 382). One of the limits of using these 1-D nanomaterials is that they need to be grown directly on the substrates to ensure a homogeneous micro/nano structure, implying a strong dependency on the substrate itself. Furthermore, fabrication methods usually include complex processes, notably involving strong chemicals and/or high temperatures.

In contrast, coating the substrate with functionalized nanoparticle composites is one of the easiest and most scalable techniques to make superhydrophilic/hydrophobic surfaces. For these coatings, nanoparticles impart the micro/nano features on the substrate and having them functionalized with a low-surface-energy material produces a superhydrophobic surface. Recently, different types of nanoparticles have been developed for such purposes, such as  $\text{SiO}_2$  (383),  $\text{ZnO}$  (381), and  $\text{TiO}_2$  (16). One class of coatings consisted of  $\text{TiO}_2$  nanoparticles bonded with a fluoroacrylic copolymer (PMC), which reduces surface energy to the point that the water contact angle on the coated surface can reach 170 degrees. Of course, one may consider different solution compositions to generate coatings with different water contact angles. On the other hand,  $\text{TiO}_2$  is a photocatalytic material (384) which by exposure to UV irradiation degrades and retains higher surface energy. This property implies that a superhydrophobic coated surface can be converted to superhydrophilic after sufficient exposure to UV light. This feature enables one to control the wettability of the surface, which is crucial in many areas, such as printing (385). This property is especially beneficial for thin porous substrates since the UV light can penetrate through the pores and interact with the coating on each side of the porous substrate, which has inspired researchers to develop different fluid manipulation applications (386; 387).

While a large number of studies has been published on  $\text{TiO}_2$ -coated surfaces, fundamental knowledge is still lacking on their wettability properties and their modulation with composition and UV exposure time. No mathematical relation exists to correlate the wettability of a  $\text{TiO}_2$ -coated substrate with its composition or after timed UV exposure. Determining the required UV exposure time to attain a specific contact angle with a given coating composition is a

challenging and time-consuming task, if left only to experimentation. In the material science literature, a wide variety of statistical techniques have been used to address similar issues.

In their review, Schmidt et al. (388) showed how machine learning (ML)-based algorithms can help material scientists. Elton et al. (389) used ML techniques to predict the properties of CNOH energetic molecules from their molecular structures. They successfully modeled their data with Kernel Ridge Regression with an accuracy of 83%. B  lisle et al. (390) employed several learning-based techniques to predict properties of materials. Using Gaussian process regression to achieve a Root-Mean-Square Error (RMSE) of 0.0585, Shandiz and Gauvin (391) predicted three crystal systems (monoclinic, orthorhombic and triclinic) of silicate-based cathodes with Li-Si-(Mn, Fe, Co)-O compositions using common classification ML algorithms. Evans and Coudert (392) predicted elastic response and shear moduli for all-silica zeolites using Gradient Boosting Regression with a RMSE of 0.102; they could successfully link characteristic features of a zeolite with its elastic behavior with this method. Gurgenc et al. (393) used experimentally-obtained wear loss data for a magnesium alloy coated via two different spray coating methods. They achieved 99% accuracy with an Extreme Learning Machine (ELM) method. Arisoy and   zel (394) used the Random Forest approach to predict machining-induced microhardness and grain size on a titanium alloy; they used the predicted microhardness profiles and grain sizes for optimization. Altay et al. (395) used experimental data to predict wear losses of a coated steel surface with different ML algorithms. They achieved 96% accuracy with a Support Vector Machine (SVM) method.

As these examples show, ML offers a promising approach to mitigate the lack of a physics-based model for predicting the wettability of  $\text{TiO}_2$  coating formulations after timed exposure to UV (used here as a wettability tuning parameter). In this study, a parametric study was conducted with different ML algorithms to predict the required UV exposure time for imparting specific contact angles to  $\text{TiO}_2$ /PMC coatings of different compositions. Since for most applications the surface wettability is predetermined, here the goal is to determine the required UV exposure time to attain a desired wettability (i.e. contact angle) for a  $\text{TiO}_2$ /PMC coating of certain composition. Toward this goal, 8 different compositions of the  $\text{TiO}_2$ /PMC formulation were made and sprayed on glass slides, before being dried and exposed to UV light for pre-specified intervals. The water contact angle was measured after each exposure period. This data was used to train, test, and compare the 8 models. The models were tuned and tested over different training sets and were examined over an unseen data set to determine the most reliable and accurate model. The outcome of this study can be useful for design purposes in different applications of  $\text{TiO}_2$ -based coatings. More importantly, the methodology can be followed for other coatings consisting of different ingredients whose wettability properties are affected by UV or other factors (e.g. exposure to plasma, heat, etc.).

## **2.2 Materials and Methods**

### **2.2.1 Data Preparation**

The chemicals used in this work comprise a fluoroacrylic copolymer dispersion (PMC) manufactured by DuPont (20 wt.% in water; Capstone® ST-100), titanium (IV) dioxide  $\text{TiO}_2$  nanoparticles (Anatase, 21 nm, 99.7% trace, Sigma Aldrich) and ethanol (200 Proof, Decon

Labs). These three materials can be combined together in formulations with infinite possible combinations. Each coating formulation imparts unique wettability properties to the coated surface and is described by the  $\text{TiO}_2$  mass fraction ( $\phi$ ) defined as the mass ratio of  $\text{TiO}_2$  particles in the dry coating, i.e.,

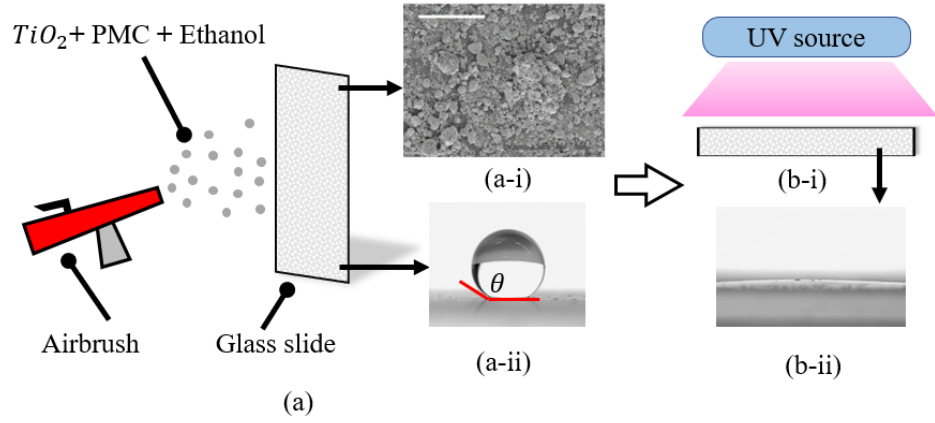


Figure 8: Schematic of the sample fabrication procedure: (a) coating a microscope slide using an airbrush; (a-i) SEM image of  $\text{TiO}_2$ -coated substrate, reproduced with permission from Ghosh et al. (16) Scale bar denotes 100  $\mu\text{m}$ ; (a-ii) sessile water droplet contact angle  $\theta > 100^\circ$  for a typical coated sample before any exposure to UV light; (b-i) exposure to UV light; (b-ii) water droplet spread ( $\theta < 5^\circ$ ) on substrate exposed to prolonged UV irradiation.

$$\phi = \frac{M_{\text{TiO}_2}}{M_{\text{TiO}_2} + M_{\text{PMC}}} \quad (2.1)$$

where  $M_{\text{TiO}_2}$  represents the mass of  $\text{TiO}_2$  nanoparticles (powder) and  $M_{\text{PMC}}$  the PMC mass in the aqueous copolymer. The latter serves as the primary low-energy component of the superhydrophobic surface; a smooth PMC film has a water contact angle  $\sim 117^\circ$  (396). In

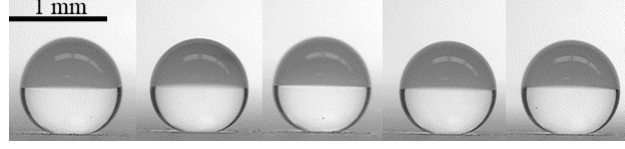


Figure 9: Five contact-angle measurements performed at different points on the same substrate ( $\phi = 0.68$ ). The similar shapes indicate high confidence in the measured CA value, in this case,  $\approx 163^\circ \pm 1.25^\circ$ .

contrast, the  $\text{TiO}_2$  nanoparticles impart the required micro- and nano-scale roughness and promote hydrophilicity through well-known mechanisms and photocatalytic degradation of the hydrophobic chemistries (396) upon exposure to UV irradiation. An experimental dataset is built with 8 different  $\text{TiO}_2$  formulations exposed to UV with the intent to bring the wettability from its initial value to the extreme wettability limit (superhydrophilic) attained after adequate UV exposure.

To derive the value of  $\phi$  for any formulation, all three component masses are needed:  $M_{\text{TiO}_2}$ ,  $M_{\text{PMC}}$  and  $M_{\text{ethanol}}$  (mass of solvent), which are denoted hereafter as  $f$  ( $\text{TiO}_2$  filler),  $p$  (PMC polymer dispersion in water) and  $s$  (solvent), respectively. All three are inter-related via Equation 2.2 below (see appendix A for details)

$$\begin{bmatrix} d-1 & d-c & d \\ 1 & 1 & 1 \\ \phi-1 & c\phi & 0 \end{bmatrix} \begin{bmatrix} f \\ p \\ s \end{bmatrix} = \begin{bmatrix} 0 \\ M \\ 0 \end{bmatrix} \quad (2.2)$$

TABLE II: Compositions and UV exposure time steps used in the experiments

$\phi$	0.2	0.35	0.42	0.5	0.6	0.68	0.75	0.8
TiO <sub>2</sub> (g)	0.24	0.42	0.504	0.6	0.72	0.82	0.9	0.96
PMC solution (g)	4.8	3.9	3.48	3	2.4	1.92	1.5	1.2
Ethanol (g)	9.96	10.68	11.016	11.4	11.88	12.2	12.6	12.84
Time step (min)	3	2	1	1	1	1	0.5	0.5

where  $M = f + p + s$  is the total mass of all three components (solids and liquids), and  $d$  is the mass ratio of the solid components ( $f + cp$ ) in the total mass of the dispersion used to apply the coating. The value of  $d$  was kept constant (0.08) in all cases here and was on the high end of the range that can be used in coating dispersions.  $c$  is the weight percent of the PMC in water (as-received product) which in our case is 0.2 (20 wt.% in water). For the following values of  $\phi$  (0.2, 0.35, 0.42, 0.5, 0.6, 0.68, 0.75, 0.8) solving the system of Equation 2.2 for  $f, p$  and  $s$ , provides the respective values listed in Table II.

The different TiO<sub>2</sub> formulations in Table II were prepared by adding the TiO<sub>2</sub> nanoparticles in ethanol and mixing in a probe sonicator (VCX 750, 20 KHz, 750 W; SONICS MATERIALS. INC.) at an energy setting of 1000 Joules for 45 seconds. After adding PMC to the mixture, the complete formulation was bath-sonicated for 30 min (8891 Ultrasonic Cleaner, 2.5 gallon; Cole-Parmer) to achieve a homogeneous dispersion.

To generate enough data, the range of mass fractions covers a wide spectrum of ingredient concentrations,  $\phi$ , with the contact angle measured for each formulation and UV exposure ranging from zero to the minimum time for the contact angle to reach zero (superhydrophilicity). Figure 8 shows the fabrication process. In a typical test, two 75mm  $\times$  25 mm microscope slide



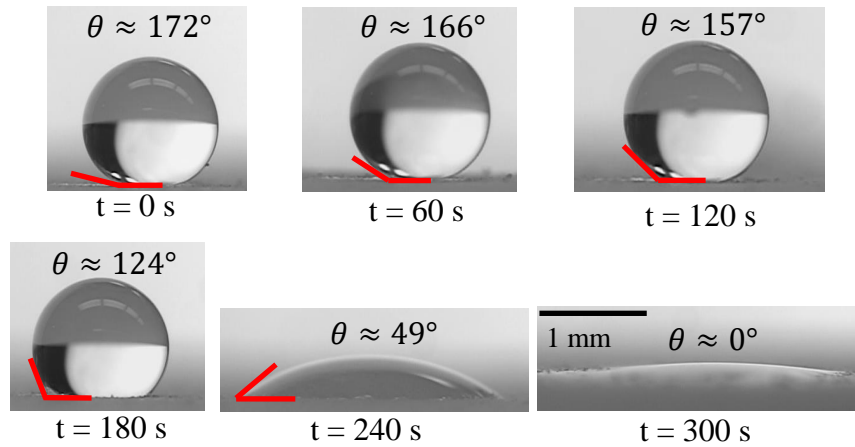


Figure 10: Contact angle reduction with UV exposure time for a surface coated with the  $\phi = 0.6$  formulation. Each coating was exposed to UV for the listed time before a water droplet was placed on the surface and attained the shown shape and respective contact angle.

(Thermo Scientific) was coated by a specific  $\text{TiO}_2$  formulation using a manual airbrush sprayer (TS3L, siphon fed; Paasche) at a pressure of 40 psi and using nitrogen as the spraying medium from a distance of  $\sim 10\text{cm}$ . After drying the coating in a laboratory oven (Model 10 Lab oven, Quincy Lab, Inc.) for 10 minutes at  $120^\circ\text{C}$ , the contact angle was measured by depositing a  $4.7\ \mu\text{l}$  water droplet and inspected with a camera (1080 HD MINTRON). For each sample, three different random spots were chosen to measure the contact angle and the average defined the respective contact angle value.

Figure 9 shows different droplets placed on five different spots of a coated substrate with  $\phi=0.68$ . The similarity of all five shapes demonstrates the uniformity of the coating on this substrate. Next, each sample was exposed to UV light for increasing time periods, with the contact angle measurement being performed intermittently throughout this process until each

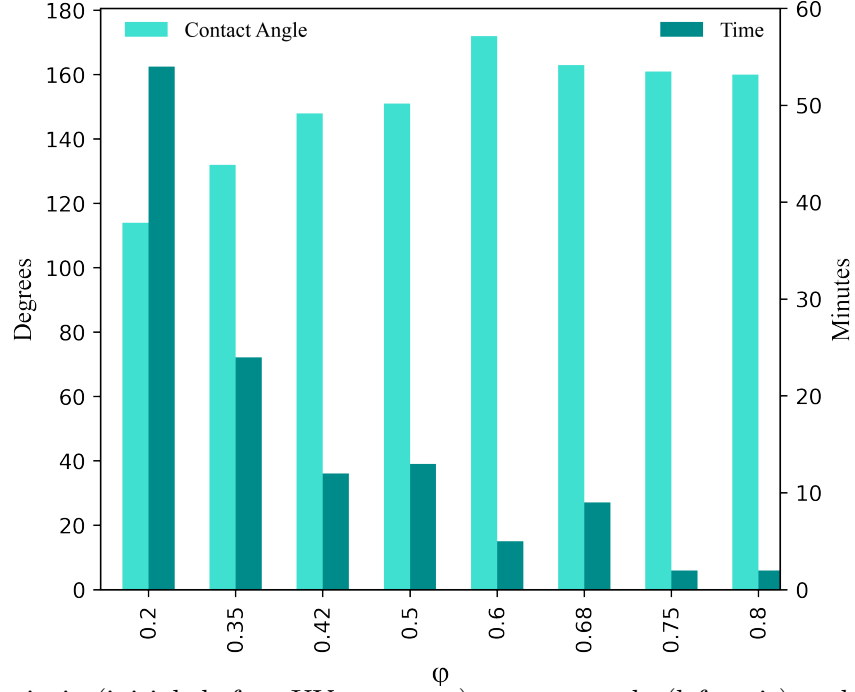


Figure 11: Intrinsic (initial, before UV exposure) contact angle (left axis) and UV exposure time (right axis) for different coating compositions. The exposure time is the minimum required to impart superhydrophilicity (zero contact angle) to the coating.

sample achieved superhydrophilicity. As expected, the wettability reduction rate with sustained UV exposure was different for each coating formulation due to the different composition  $\phi$ . Different exposure time steps, chosen by trial and error to collect data more efficiently, were used and are listed in Table II. Overall 85 data points were collected and are shown in Appendix A (Figure 47). Figure 10 shows the contact angle gradual reduction with rising UV exposure time for  $\phi = 0.6$ . In that particular case, the UV exposure time required for attaining zero contact angle is 300s. Figure 11, which displays the intrinsic (initial) contact angle for each

coating formulation and the minimum UV exposure time needed to attain hydrophilicity for each  $\phi$ , reveals no specific trend. For instance, as  $\phi$  rises, there is no clear variance of the minimum UV exposure time to impart zero contact angle to the coating.

### **2.2.2 Machine Learning Methodology**

This study tests the performance of six regression techniques to measure the correlation between  $\text{TiO}_2$  composition, UV exposure time, and the wettability of the resulting coating.

The non-parametric techniques belong to the general family of ML whose main advantage is the use of algorithms to train often structurally complex models. ML approaches often achieve high accuracy thanks to their ability to capture and model non-linear behaviors, which have made them very popular in the scientific community, and have been used to model countless systems (397; 398; 399; 400). Nevertheless, because ML models tend to be structurally complex, it is often more difficult to validate trained ML models. A commonly used synonym for ML is "data driven," as in the models developed only from observed data as opposed to those from theoretically established physical reasoning.

In a real world problem, wettability (as designated by the corresponding contact angle) of a desired system is known and predetermined, but reaching that certain contact angle requires experimental processing steps. Here, in order to facilitate design and fabrication procedures, the data is divided in two categories; intrinsic contact angle and  $\phi$  as input (x), and UV irradiation time to reach a specified contact angle, as output (y). In this way, based on predicted UV exposure times to attain a desired wettability, the optimal  $\text{TiO}_2$ /PMC composition can be selected for the coating.

In terms of validation, ML algorithms are trained over a subset of data (called *training set*) and tested over the remaining data (called *testing set*), the two datasets being mutually exclusive (401). The score for each resultant model offers quantitative guidance for the reliability of future unseen data set prediction by this model. The validation procedure adopted in this article is detailed below.

In order to detect and limit over-fitting issues and provide a better assessment of the models, the acquired data was split into three sets: train, test, and unseen set. For application purposes and to further evaluate the models, the data for  $\phi = 0.5$  was kept out of the training sets to confirm the universality and avoid possible over-fitting. The algorithms were therefore trained on 80% of the acquired data and then tested on the remaining 20%, excluding the data created for  $\phi = 0.5$ . In addition, a 5-fold cross validation (CV) process was performed. The training set (i.e., 80% of the data) is divided into five partitions, where four of the five partitions are used for model training and the rest for model evaluation. This process gives five trained models such that the average and standard deviation of the performance of each model can be computed. Next, each model is trained over the whole training set and evaluated with a test set. In this way, cross-validation helps to test stability in model performance and can be used for hyperparameter tuning prior to the final evaluation of the model on the test set. To tune the hyperparameters of each model, a `GridSearchCV` function was used to find the best regression parameters for each model. This function examines each possible combination of given hyperparameters and identifies the model with the highest CV score, which eventually will be evaluated with the corresponding test set. Table VII in appendix A shows different

hyperparameters that have been examined for each technique. The final models are available in a github repository <sup>1</sup>.

We have considered two critical factors for selecting the best-performing ML technique. First, we evaluate the performance of a model with the highest accuracy (i.e., lowest error), then we investigate the overall performance of the same model over a range of different train and test data sets to reveal the stability of the model. A stable model is more or less independent of the training set or the test set that has been evaluated with. The second criterion is displayed by a box plot showing the mean and variance of  $R^2$ s over 50 different splits of the entire data set to test and train sets. This number of splits was chosen based on the minimum number of data points in the train set, which is 80% of all (71) available data (disregarding the  $\phi = 0.5$  unseen data points). In this way, the many combinations of picking 56 data points out of 71 were chosen by varying the random states in the `train – test – split` function of Python. This number (50) of different train and test sets is assumed to be sufficient enough to evaluate the models thoroughly. Therefore, each model is trained and tested on the same 50 pairs of mutually exclusive train/test set. All of the computing work was performed using the `Scikit – learn` package (402).

### 2.2.3 ML Models

As a benchmark for more complex methods, three linear parametric models, including the common Ordinary Least Square (OLS) regression, Kernel Ridge regression (KRR) (403), and

---

<sup>1</sup><https://github.com/Mjafarig94/TiO2-Project>

Support Vector regression (SVR) (404) with linear kernels have been used. Next, four non-parametric ML methods including KRR and SVR with non-linear kernels, General Regression Neural Network (GRNN) (405), Multi Layer Perceptron (MLP) (406), and Gradient Boosting Regression (407) were employed to discover non-linear patterns in the data (see section 3 of appendix A for more technical details).

## **2.2.4 Model Specification and Evaluation**

### **2.2.4.1 Variable Scaling**

In the present study, the input and output variables are recorded based on the experimental data, and each feature has a varying value range. The different value ranges may result in biased assessment, particularly for the non-parametric algorithms that are affected by scale changes, such as MLP, GRNN and SVR. Accordingly, calculating and using scaled values ( $z_i$ ) for both the independent and dependent variables makes it easier to assess and compare models. For consistency, we have opted to use the scaled values to train and test all models. The traditional min-max scaling method has been applied to input ( $\mathbf{x}$ ) and output ( $\mathbf{y}$ ) variables as follows:

$$z_j = \frac{x_j - \min(\mathbf{x})}{\max(\mathbf{x}) - \min(\mathbf{x})} \quad (2.3)$$

where  $z_j$  is the scaled value of the  $j$ th data point,  $x_j$  the original value of the  $j$ th data point, and  $\min(\mathbf{x})$  and  $\max(\mathbf{x})$  are the minimum and maximum values in each feature. To prevent data snooping/leakage issues (408), the dataset was first split into train and test set and next

the train set was scaled. The same parameters were used to scale the test data so that the test set information is not revealed to the train set prior to the training.

#### 2.2.4.2 Model Evaluation Metrics

Three common metrics were used to evaluate each model: mean absolute error (MAE), root mean squared error (RMSE), and r-squared ( $R^2$ ). MAE and RMSE are mainly used to measure the deviation between the actual and predicted target values  $y$  for  $n$  data points:

$$MAE = \frac{1}{n} \sum_{i=1}^n |y_i - \hat{y}_i| \quad (2.4)$$

$$RMSE = \sqrt{\frac{1}{n} \sum_{i=1}^n (y_i - \hat{y}_i)^2} \quad (2.5)$$

where  $\hat{y}_i$  is the predicted value for the  $i$ th entry in the input data set.  $R^2$  quantifies how close the predicted values are to the actual values, and is defined as

$$R^2 = 1 - \frac{(y_i - \hat{y}_i)^2}{y_i^2} \quad (2.6)$$

Since the whole data set is scaled from 0 to 1, these three metrics, MAE, RMSE, and  $R^2$  can provide valuable insight on the performance of each model compared to the rest.

## 2.3 Results and Discussion

### 2.3.1 Regression Model Performance

#### 2.3.1.1 Parametric Models

Preliminary examination of the data revealed that the performance of linear models is poor, suggesting that the impact of the two input features ( $\phi$  and Contact angle) on the dependent variable (UV exposure time) is non-linear. All parametric methods have shown poor performance on both train and test sets, as shown in appendix A ( Figure 48), and highlighted the non-linear nature of current problem. Therefore, those results will not be discussed further.

#### 2.3.1.2 Non-parametric Models

Figure 12 shows the best performance of all non-parametric techniques for predicting the scaled UV exposure time of the test set. This plot represents the random split instance of the data for each method which achieves the highest train  $R^2$ , test  $R^2$ , and CV score simultaneously, while there might be instances that one or two of these measures are higher. And Table III shows the  $R^2$  scores, MAE, RMSE, and hyperparameters of the corresponding models of Figure 12. All three measures are significantly higher than the parametric methods. This figure clearly shows that the predicted values coincide with the measured values within the margin of error. Close test and train accuracies of greater than 0.96 suggest that these non-parametric methods can reliably capture the non-linearity in this problem. Figure 12 also emphasizes the importance of feeding different train and test sets to different models, since they have the highest accuracy on different splits of the data to train and test sets. Table III shows small errors and high



accuracy scores for all the models, which suggests that other criteria must be considered to further compare model performance.

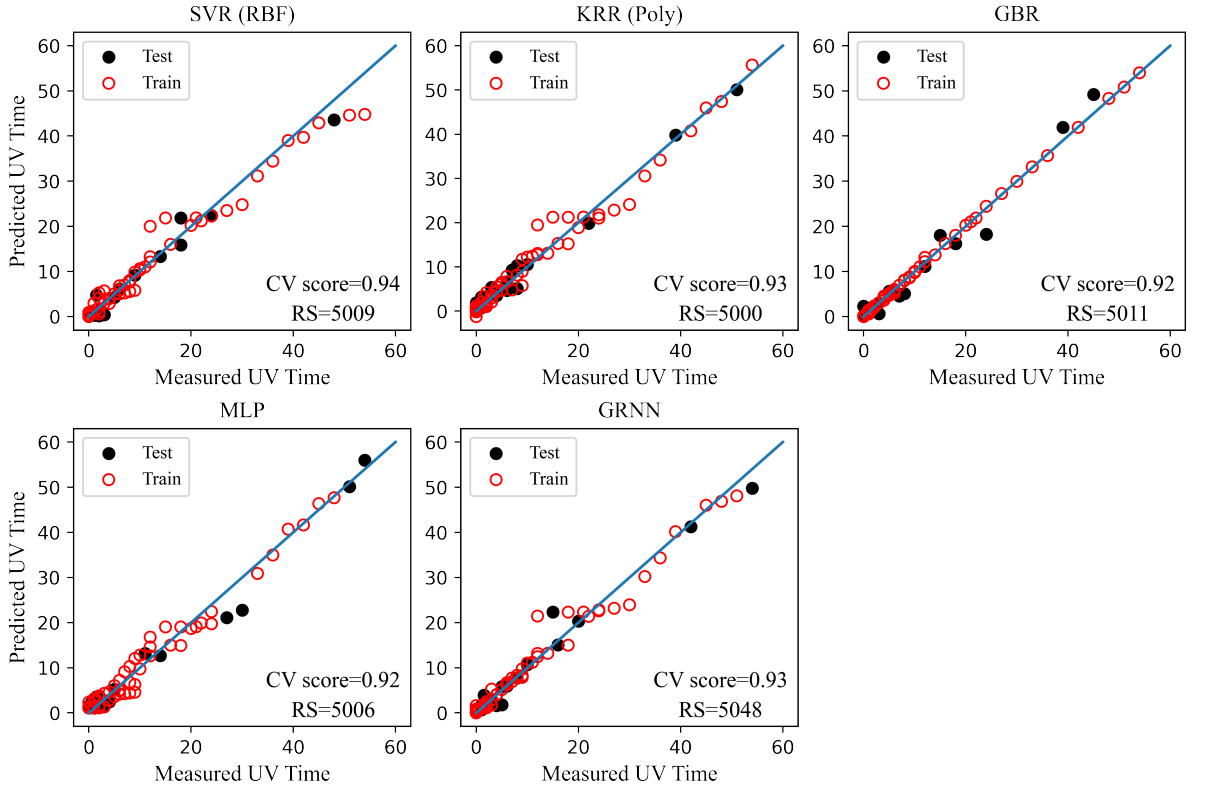


Figure 12: Prediction of UV exposure time at the best instances (i.e. highest CV score and test/train  $R^2$  values) for SVR with RBF kernel, KRR with Polynomial kernel, GBR, MLP and GRNN, respectively. The blue line (slope of 1) in each plot serves as a guide for perfect prediction. RS denotes Random State of train – test – split function.

To identify the impact of the train and test set variation on each model performance, the  $R^2$ s of 50 different splits of data to train and test sets is shown in Figure 13. It is worth mentioning

TABLE III: Evaluation of non-parametric models. MAE and RMSE are calculated on the non-scaled data.

Data			Test Data			Train Data		
Method	hyperparameter	Function/Value	$R^2$	MAE	RMSE	$R^2$	MAE	RMSE
SVR	Kernel	rbf	0.97	1.59	2.07	0.96	1.43	2.51
	epsilon	0						
	C	0.91						
KRR	Kernel degree	Poly 5	0.99	1.40	1.66	0.98	1.48	2.13
MLP	hidden layer sizes*	(2, 2, 1)	0.98	2.01	2.76	0.97	1.69	2.00
	activation function	tanh						
	solver	lbfgs						
	learning rate	constant						
GBR	loss function	huber	0.96	2.06	2.59	1.00	0.20	0.30
	n_estimators	5						
	criterion	mse						
	max depth	4						
GRNN	sigma	0.05	0.97	1.63	2.53	0.98	1.12	1.97

\*The length of the tuple is the number of layers; each indicates the number of neurons in each layer.

that each data point in the figure is the score of a model on one distinct split of the data to train/test set; i.e., the test sets are not seen by the model in any capacity. The first and last 5% of the data points are shown as outliers. The overall higher mean values for each metric reveal that non-parametric ML algorithms are more suitable for the data. Nevertheless, a variation in each metric among the techniques is noticeable. As seen, the average and deviation of the cross-validation scores are similar with an average of  $\sim 0.90$  and a deviation of  $\sim 0.1$ . In contrast, the accuracy in the test sets have a larger deviation among the different methods. Although the average test sets  $R^2$  for different methods are close and above 0.90, neglecting the outliers, the largest deviations belong to GBR, MLP, and KRR (Poly) with deviation of 0.26, 0.24, and

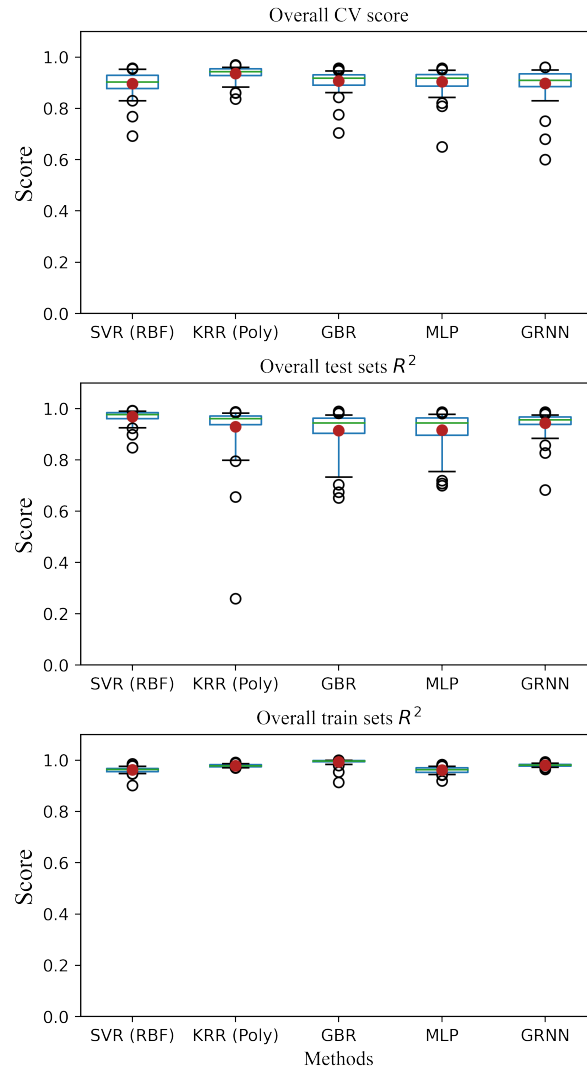


Figure 13: Overall performance evaluation of SVR (RBF), KRR (Poly), GBR, MLP, and GRNN. Red circles indicate the mean value. Green lines mark the median. Whiskers bound the middle 90% of the data points.

0.18, respectively whereas the highest average and least deviations belong to SVR (rbf) and GRNN with mean test sets  $R^2$  of 0.97 and 0.94 and deviation of 0.07 and 0.11, respectively.

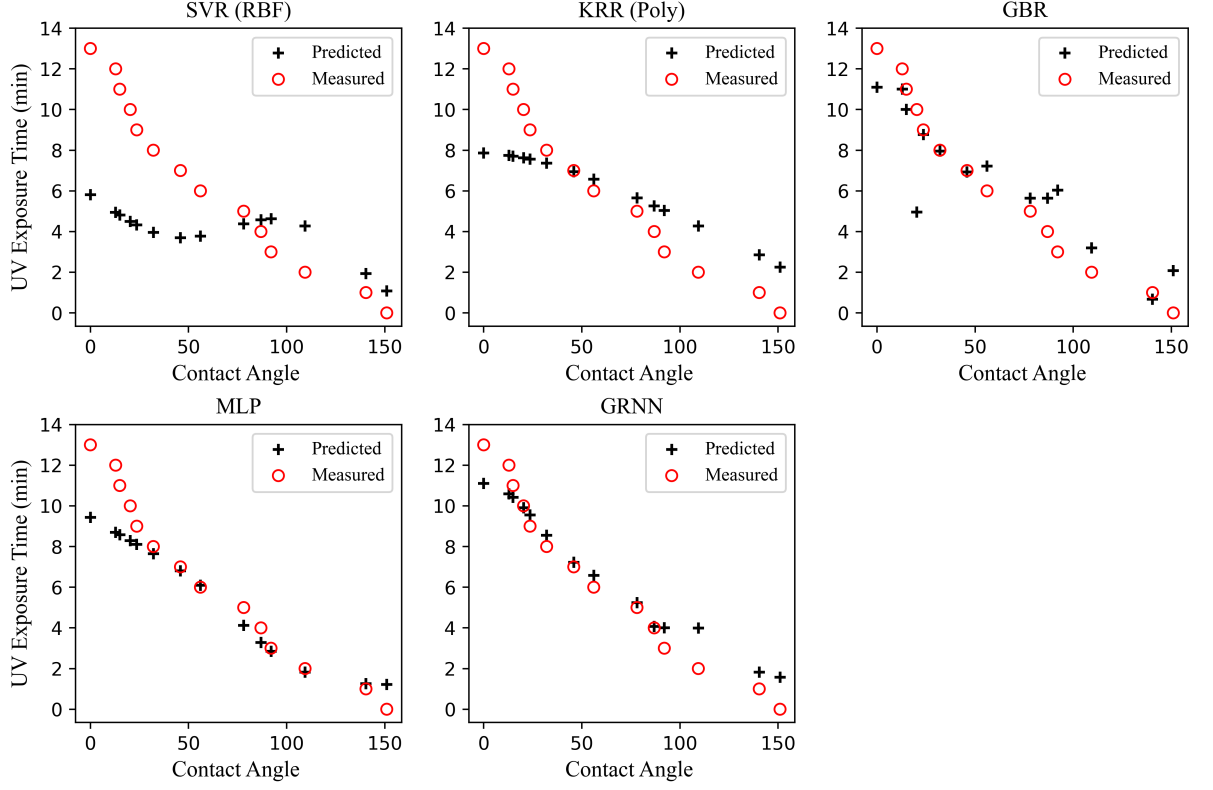


Figure 14: Prediction of UV exposure time for  $\phi = 0.5$  by all models.

On the other hand, the train sets  $R^2$ s, as expected, are generally close and above 0.96 with maximum deviation of 0.03. As observed, the test sets  $R^2$  can be a proper measure to compare models, since larger differences among the models are noticeable. Overall, the high variation of KRR (Poly), GBR, and MLP in test set  $R^2$  is an indication of instability in these methods with respect to the train and test data sets. In contrast, SVR (RBF) and GRNN show a relatively stable behavior.

TABLE IV: Evaluation of non-parametric models on unseen data ( $\phi = 0.5$ ). MAE and RMSE are calculated on the non-scaled data.

Method	$R^2$	MAE	RMSE
SVR (RBF)	-0.03	3.38	4.10
KRR (Poly)	0.63	2.00	2.44
MLP	0.84	1.14	1.61
GBR	0.78	1.39	1.91
GRNN	0.93	0.83	1.04

To further investigate the universality of each model, a new set of unseen data was examined. As mentioned earlier, the data for  $\phi = 0.5$  was kept aside from the beginning for gauging future prediction by the models. Figure 14 shows the re-scaled predicted versus measured UV irradiation time for all methods. Table IV shows the corresponding metrics values of the same figure. Here, contrary to Figure 13, SVR (RBF) performs poorly on the unseen data, suggesting over-fitting. KRR (Poly) shows average performance, while MLP, GBR and GRNN with overall  $R^2 > 0.78$  predict the required UV exposure time with relative high accuracy. Following Figure 14, GRNN has been consistent obtaining the maximum  $R^2$  ( $>0.93$ ) and minimum MAE of 0.83 on the unseen data, which shows its capability to successfully capture the pattern and extend it for the unseen data.

## 2.4 Conclusion

The present work investigated the wettability of  $\text{TiO}_2$  formulation-coated surfaces and how it can be tuned with UV irradiation. In total, 8 different  $\text{TiO}_2$  suspensions were made, sprayed on a glass slide, and dried to form a thin photocatalytic coating. Contact angle measurements quantified the intrinsic wettability of each resulting coating. Each coated slide was then exposed

to UV irradiation for gradually rising periods until the surface attained the superhydrophilic property. The data was subsequently split into two categories, input and output. The input data consisted of two features, namely, mass ratio ( $\phi$ ) of  $\text{TiO}_2$  particles in the dry coating, and intrinsic contact angle (the property that quantifies wettability), while the output data consisted of the corresponding UV exposure time required to attain a certain contact angle (lower than or equal to the initial value). To model UV exposure time, 6 different techniques were assessed. For this purpose, a set of data was set aside to compare the final models on future predictions. The rest of the data was scaled from 0 to 1, and 80% of the data was employed for training each model, with the remaining 20% used for testing. The overall performance of each model was evaluated by examining 50 different train and test sets. Poor performance of the parametric models revealed the non-linear nature of the data. On the other hand, all non-parametric methods obtained a high accuracy (above  $\sim 0.9$ ) in both train and test sets. The results reveal a non-linear relationship between the input and output variables, substantiating the need for non-parametric methods. GRNN showed a stable performance with lowest variation in all accuracy metrics and highest accuracy of 0.93 on the unseen data set, which supports employment of this method for future designs and applications. The study identified a reliable predictive learning-based model based on experimental data to predict a process parameter (UV exposure time) required for a desired outcome (coating wettability). The present approach offers a methodology that can be followed for other technological problems and can be used to facilitate design decisions.

## CHAPTER 3

### APPLICATION OF WETTABILITY CONFINEMENT IN AN ISOTHERMAL SYSTEM, STUDY OF SPREADING OF A GAS BUBBLE SUBMERGED IN A LIQUID

*”This chapter is reprinted with permission from M. Jafari Gukeh, T. Roy, U. Sen, R. Ganguly, and C. M. Megaridis. Lateral spreading of gas bubbles on submerged wettability-confined tracks. Langmuir 36, no. 40 (2020): 11829-11835. Copyright 2020, American Chemical Society” (see Appendix E)*

#### **3.1 Background and Motivation**

The advancement of surface engineering techniques has facilitated scalable approaches for fabricating wettable and non-wettable surfaces, on which a variety of liquids can be manipulated. Distinctly, different behaviors of liquid spreading on wettable and non-wettable surfaces enable one to effectively confine liquid volumes on surfaces which possess spatially juxtaposed wettable and non-wettable domains separated by a sharp wettability-contrast line (409; 410; 16; 411; 23). The scientific literature from the last two decades bears testimony to the applicability of wettability-patterned surfaces in open-surface microfluidics (364), pool boiling (412), condensation (363; 413), and electronics cooling (360; 414). A superhydrophobic (water-repelling) surface behaves as a superaerophilic (air-attracting) one when submerged in water, and vice

versa for a superhydrophilic surface (415; 416). A review of the various fabrication techniques for obtaining superaerophobic and superaerophilic surfaces was recently presented by George et al. (417). Numerous studies have shown possible applications of such surfaces in gas harvesting (418; 419; 420; 365), wastewater remediation (421), catalytic action (422), drag reduction (423), etc.

The dynamics of liquid-droplet spreading on wettability-patterned tracks has been the subject of numerous studies (410; 16; 23). A typical design of such tracks includes spatially-juxtaposed regions of contrasting wettability (e.g. a narrow superhydrophilic patch surrounded by a superhydrophobic area (410; 411; 16; 23)). The spreading of a liquid droplet on such tracks is primarily dictated by the interplay between the capillary pressure and the viscous resistance (410; 23). On the other hand, a multitude of surface textures (424; 425) and wettability patterns have been used to manipulate underwater gas bubbles, with corresponding geometric optimization of the patterns being performed using phenomenological approaches.

Prior works on wettability patterning have often used surface textures and geometric shapes of patterns inspired by nature (30; 426; 427). Ma et al. (428) achieved directional and continuous underwater transport of gas bubbles on superaerophilic shape-gradient tracks laid on a superaerophobic background, and reported that larger bubble volumes and smaller apex angles favoured faster transport. They identified the driving force to originate from the difference of the contact angles in the front and rear side of the bubble, whereas the resisting force was the inertia of the ambient liquid. Liu et al. (418) characterized the movement of underwater bubbles on superaerophilic wedge-shaped tracks presuffused with a pre-existing air film, which



enhanced the velocity of the bubbles. The directional transport was attributed to the Laplace pressure difference along the track. Song et al. (429) further explored the continuous transport of gas bubbles on wedge-shaped wettability-patterned tracks immersed in water and arranged in series. They reported that continuous transport was possible when the width of the narrow end of the track exceeded a critical value. The driving force was attributed to the Laplace pressure gradient, whereas the resisting force was attributed to the inertial drag and contact angle hysteresis. Duan et al. (430) employed hierarchical micro-structured superaerophilic polytetrafluoroethylene cones for transporting gas bubbles underwater from the tip to the cone base. They identified the Laplace pressure as the driving factor and contact angle hysteresis to be the resisting factor. Apart from the bare superaerophilic surfaces, lubricant-infused nanoporous structures have also been used for manipulating gas bubbles in water (431; 426; 432; 433). Although the dynamics of spreading of a liquid droplet on a wettability-confined track has been well characterized (410; 16; 23), there is a dearth of knowledge on the spreading of gas bubbles on such tracks in a submerged condition.

For the spreading of a liquid droplet, surface tension,  $\gamma$ , drives the spreading in order to minimize its surface energy (434). However, above the capillary length  $l_c$  (2), gravity also influences spreading (435). This capillarity-driven spreading is usually resisted by viscosity (436), which manifests itself as viscous dissipation close to the contact line (437). The viscous effect is highly pronounced for liquid droplets, since the viscosity of the liquid is much higher than that of the surrounding medium (usually air). However, that is not the case for a gas bubble spreading on a submerged, wettability-confined track, where the viscosity of the surrounding

medium is much higher. In the present work, the dynamics of spreading of such gas bubbles is investigated experimentally, and quantified using high-speed imaging. The spreading behavior is studied for liquids of different viscosities, surface tensions, and densities, and a scaling law is derived that accurately describes the experimentally-observed motion of the gas bubbles. The results are generalized in terms of the fluid properties, such that they can be applied to any liquid/gas pair.

### **3.2 Materials and Methods**

A facile and scalable fabrication method was employed to create the desired wettability pattern on rectangular aluminum plates of dimensions 75 mm  $\times$  15 mm (mirror-finish 6061 aluminum, 2 mm thick, McMaster-Carr). After peeling off the protective polymer layer from the surface of the as-received substrate, the metal surface was rinsed with ethanol (200 proof, Decon Labs) and DI water, and subsequently dried. A Yb-laser (100% power, 10 kHz frequency, 200 mm/s traverse speed, Scorpion Rapide, EMS400, Tykma Electrox) was then used to selectively etch the substrate outside the designated region of the track, thus leaving a track elevated above the surrounding surface ( Figure 15a). The track elevation was maintained at 500  $\mu$ m, while the track length was 30 mm, and the track width was varied in different designs, as explained in the next section. The same laser marking system (50% power, 20 kHz frequency, 200 mm/s traverse speed) was utilized further to lay longitudinal microgrooves (40  $\mu$ m wide, 70  $\mu$ m deep, and 100  $\mu$ m apart) on the elevated track itself ( Figure 15b-i). Thus, a uniform microtexture was imparted on the surface. The sample was then passivated in boiling water for 1 h ( Figure 15c-i), resulting in the creation of broccoli-like hierarchical structures on the

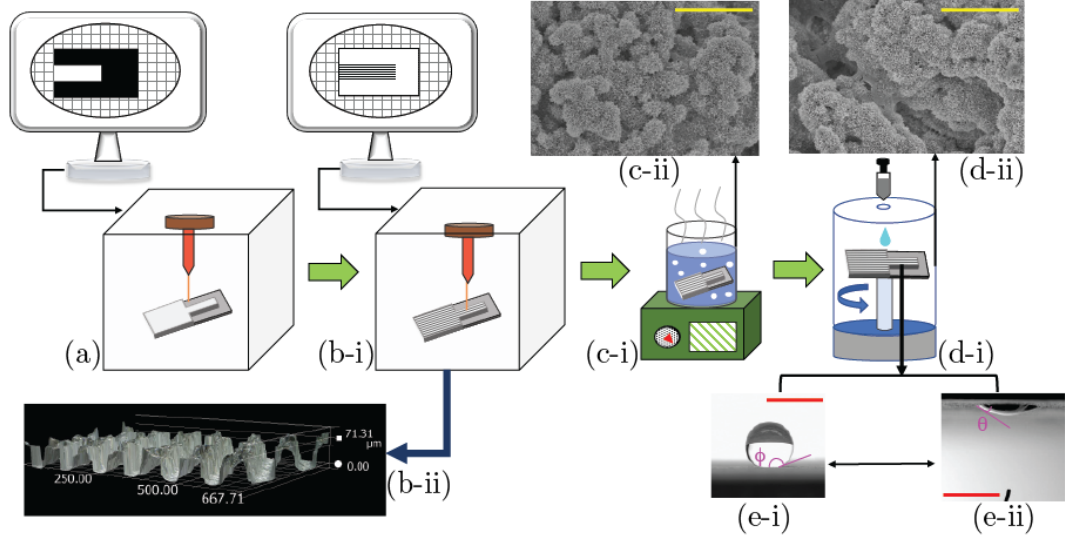


Figure 15: Schematic of the sample fabrication procedure: (a) Laser etching of aluminum sample creates the elevated track; (b-i) laser engraving of microgrooves along the elevated track; (b-ii) cross-sectional depth profile of the microgrooves on the track (all dimensions are in  $\mu\text{m}$ ); (c-i) passivating sample in boiling water for 1 h; (c-ii) scanning electron micrograph of sample after passivation (scale bar denotes 1  $\mu\text{m}$ ); (d-i) spin-coating Teflon on the substrate; (d-ii) scanning electron micrograph of Teflon-coated substrate (scale bar denotes 1  $\mu\text{m}$ ); (e-i) sessile water droplet contact angle  $\phi = 155.6 \pm 5.6^\circ$  (scale bar denotes 3 mm); (e-ii) captive air bubble contact angle  $\theta = 25.5 \pm 2.3^\circ$  for superhydrophobic substrate submerged under water (scale bar denotes 3 mm).

surface ( Figure 15c-ii). These structures were created due to the formation of an aluminum oxide hydroxide ( $\text{Al}(\text{O})\text{OH}$ ), or böhmite (438; 439), layer on the surface. Subsequently, a thin layer of Teflon AF (1 wt. % in Fluorinert FC-40, Chemours AF 2400) was spin-coated (2000 rpm for 20 s, WS-400-6NPP-LITE Spin Processor) on the micro/nano-textured surface ( Figure 15d-i), and then cured on a laboratory hot plate (at  $80^\circ\text{C}$  for 15 min, then at  $180^\circ\text{C}$  for 12 min, and finally at  $260^\circ\text{C}$  for 7 min, UX-03405-31, Cole-Parmer, StableTemp). The Teflon coating was

conformal to the textured substrate, and resulted in a thin air layer being trapped within the microtexture once the surface was submerged in water. Therefore, the dispensed bubble spreads on a thin layer of air and does not ‘see’ the microgrooves. Hence, the static and dynamic contact angles do not differ much with roughness  $R_a$  above  $1\text{ }\mu\text{m}$ (440). Therefore, it is expected that the dimensions of the microgrooves do not have a significant effect on the spreading behavior of the gas bubble. Finally, the Teflon layer from the substrate around the track was scraped-off with sharp tweezers to reveal the underlying micro/nano-textured aluminum, leaving only the elevated track covered in Teflon.

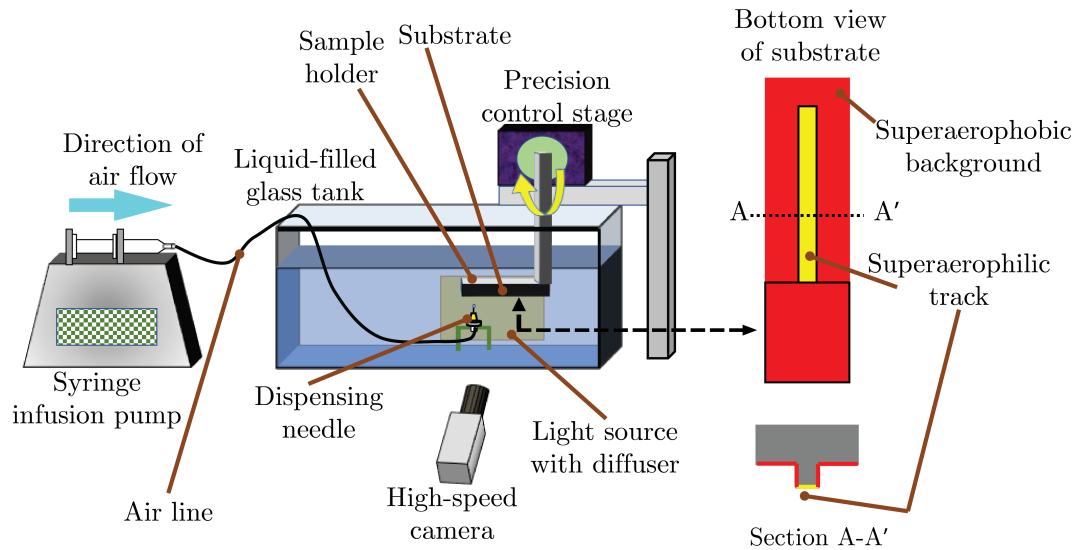


Figure 16: Schematic of the experimental setup.

It is important to note that the vertical faces of the elevated track were also scraped during this process. This rendered the track's top surface superhydrophobic (414) (likewise, super-aerophobic), while the rest of the surrounding substrate was superhydrophilic (likewise, super-aerophilic). It is noted that at the edge of the track where the bubble was dispensed, the superaerophobic and superaerophilic domains were at the same elevation. The contact angle of sessile water droplets on the superhydrophobic domain was  $\phi = 155.6 \pm 1.6^\circ$  (Figure 15e-i), while the corresponding captive air bubble contact angle was  $\theta = 25.5 \pm 2.3^\circ$  (Figure 15e-ii). On the superhydrophilic (scraped) domain, a water droplet was observed to spread instantaneously with a contact angle  $< 5^\circ$ , while the captive air bubble contact angle was  $\simeq 180^\circ$ . Scanning electron micrographs (Figure 15c-ii and Figure 15d-ii) were obtained using the imaging module of a Raith 100 eLINE electron beam lithography system, while the texture-depth image (Figure 15b-ii, showing a cross-sectional depth profile), which clearly depicts the microgrooves, was captured using a Keyence VHX6000 optical microscope.

A schematic of the experimental setup used in the present work is shown in Figure 37. Air bubbles of different diameters (1.64 mm, 2.06 mm, and 2.22 mm) were dispensed from below the horizontal sample onto the wettability-confined track using a syringe infusion pump (PHD ULTRA, Harvard Apparatus) through three different needles (Nordson EFD) with 100, 200, and 250  $\mu\text{m}$  inner diameters, respectively. A precision control stage (Newport) was used to submerge the sample in a liquid-filled glass tank, and a spirit level was used to ensure that the substrate was horizontal at all times. In order to avoid any buoyancy effects, a slightly negative tilt (about  $-1^\circ$  with the horizontal) was maintained before dispensing the air bubble. The

substrate was kept at a depth of 3 cm below the free surface of the liquid for all experiments. Each air bubble was dispensed so that it first came into contact with the superaerophobic part, which forced it to gently roll onto the superaerophilic track with the help of a superaerophobic wire, whereupon the bubble underwent further spreading. This ensured that the bubble came into contact with the track with negligible horizontal momentum. Each bubble spreading event on the superaerophilic track was imaged at 3200 frames-per-second (fps) using a high-speed camera (Phantom Miro 310, Vision Research AMETEK, mounted with a TOYO Optics TV Zoom Lens 12.5-75 mm F1.8 Japan). A portable LED light source (VidPro) was used to back-illuminate the sample through a rectangular diffuser sheet (Lumen XT LT LW7, Makrolon). Sequential time-lapsed images obtained from the high-speed camera were further analyzed using the image processing feature of MATLAB, where the instantaneous position of the spreading front was identified by a sharp jump in the pixel B/W intensity.

### **3.3 Results and Discussion**

Deionized water was chosen as the primary ambient fluid in which the wettability-patterned sample was submerged. To extend the analysis, four other ambient fluids were also used: pure ethylene glycol (99+%, Alfa Aesar), 50% wt. solution of ethylene glycol in deionized water, 50% wt. solution of glycerol (99+%, Alfa Aesar) in deionized water, and 80% wt. solution of glycerol in deionized water. The salient properties of the aforementioned liquids – surface tension ( $\gamma$ ), density ( $\rho$ ), and dynamic viscosity ( $\eta$ ) – are listed in Table V. As each sample was carefully submerged, a uniform air layer remained in the micro/nano-texture of the superaerophilic track. The uniformity of the air layer was assessed visually, with the absence of any distinct gas bulge

confirming a spatially-uniform entrapment. As mentioned in the previous section, each air bubble was dispensed in such a way that it first touched the superaerophobic part of the substrate. The stationary captive bubble was then gently guided onto the superaerophilic track by means of a superaerophobic aluminum wire. The track length was kept fixed at 30 mm throughout the present work, while the bubble transport occurred on four different track widths ( $w$ ) of 1.1 mm, 1.4 mm, 1.7 mm, and 2 mm. The dispensed air-bubble diameter was varied (1.64 mm, 2.06 mm, and 2.22 mm).

TABLE V: Salient properties of the different ambient liquids (at 25°C) (441; 442; 443; 444; 445).

Liquid	$\gamma$ (mN/m)	$\rho$ (kg/m <sup>3</sup> )	$\eta$ (mPa.s)
Deionized water	72.4	997	0.9
Ethylene glycol	47.5	1115	19.8
50% ethylene glycol*	54	1080	3.6
80% glycerol*	68	1206	51.5
50% glycerol*	68.6	1125	5.1

\* in water

### 3.3.1 Spreading Morphologies

A time-lapsed image sequence of the typical spreading of a 2.06 mm air bubble on a  $w = 1.4$  mm track is shown in Figure 17a-i - Figure 17a-vi. The initially-spherical bubble comes into contact with the track with negligible initial velocity (Figure 17a-i, left end). The lateral spread of the bubble is confined on the track by the wettability-contrast lines, while the bubble

is initially pinned at the left edge of the track. Hence, the bubble undergoes confined spreading in the left-to-right direction in Figure 17a-i - Figure 17a-vi. The bubble initially has a spherical bead shape ( Figure 17a-i), but within a few ms, it undergoes shape deformation, as seen in Figure 17a-ii. As the bubble deforms, two distinct regions – a ‘front’ and a ‘bulge’ – appear on the spreading bubble volume (as seen in Figure 17a-iii, and highlighted in Figure 17b for a typical spreading configuration). The bulge continuously supplies the spreading front with air, while decreasing in thickness as it remains pinned at the two lateral wettability-contrast lines bounding the track. The front, on the other hand, does not undergo such a drastic change of morphology; it rather continues spreading along the track with a nearly constant cross-sectional area. This is confirmed by measuring the height of the spreading front,  $h$ , at the sections along the dotted vertical red lines in Figure 17a-iv and Figure 17a-v, which are magnified in Figure 17a-vii and Figure 17a-viii, respectively, for clarity. The heights, as measured from the snapshots, vary between a narrow range of 0.45 mm to 0.49 mm over the entire stretch of the spreading; hence, the front height can be considered constant within the limit of the experimental error. Since the bubble front spreads transversely across the entire width  $w$  of the track (which is constant), this implies that the cross-sectional area of the spreading front remains constant. This is readily evident from Figure 18, where the variation of the height ( $h$ ) of the spreading bubble front with the lengthwise coordinate ( $x_c$ ) along the track (for spatial locations downstream of the bulge) is presented for a bubble diameter  $D = 2.06$  mm. It can be observed from Figure 18 that  $h$  remains fairly constant with  $x_c$ , and is only dependent on the track width ( $w$ ). The inset of Figure 18 shows a plot of the spatial average (averaged along



$x_c$ ) of the height ( $h_{\text{avg}}$ ), which is approximately equal to  $h$ , since  $h$  remains constant against the track width for cases run with different initial diameter ( $D$ ) of the dispensed bubbles. The data points collapse on a straight line, implying that  $h$  is independent of the bubble diameter ( $D$ ), and scales linearly with the track width ( $w$ ). The spreading continues until the front has reached the end of the track (Figure 17a-vi), and a uniform air layer covers the entire length of the track; the average air film height after spreading ceases  $\simeq 0.46$  mm for the case depicted in Figure 17. The spreading behavior for a bubble of diameter 2.06 mm on a track of  $w = 1.4$  mm is shown in Figure 17. The spreading behavior for other track widths and different bubble diameters is presented in movies S1 and S2 of the appendix B.

Although the qualitative bubble-spreading behavior resembles a liquid spreading on a rectangular wettability-confined track (410), a quantitative investigation reveals a distinction. The temporal evolution of the spreading air front ( $x$ ) is plotted in Figure 17c for different track widths ( $w$ ), all submerged in water. The shaded region around each plot represents the error bars computed from 10 runs with fixed conditions. For a liquid droplet spreading on a similar wettability-patterned track, the spreading front follows the well-known Washburn equation (410; 23):  $x \sim t^{1/2}$ . However, in the present work, the spreading air front clearly follows a linear relationship with time,  $x \sim t$  (Figure 17c). This translates to constant spreading velocity during the process; these spreading velocities were  $O(500 \text{ mm/s})$  for bubbles placed on the present tracks submerged in water. Nonetheless, Figure 17c also reveals the effect of  $w$  – smaller track widths result in faster spreading for given dispensed bubble volume. Qualitatively, this can be understood from the fact that for the same displaced volume, a higher  $w$  leads to

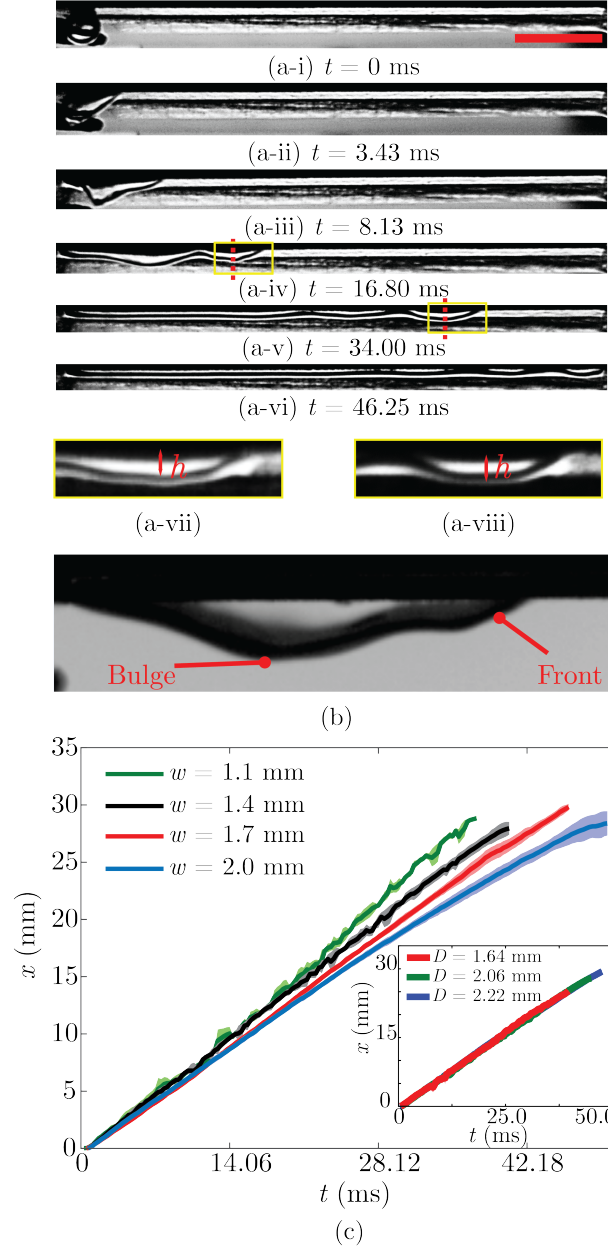


Figure 17: (a-i) – (a-vi) Time-lapsed images of an air bubble (2.06 mm diameter) spreading on a rectangular track of  $w = 1.4$  mm (scale bar denotes 5 mm); (a-vii) and (a-viii) zoomed-in view of the spreading fronts of Figure 17a-iv and Figure 17a-v, respectively, where the heights of the front,  $h$ , are, respectively, 0.49 mm and 0.45 mm (axial locations where the heights are measured are shown by the red dashed lines in a-iii and a-iv); (b) definition of bulge and bubble front in a typical spreading configuration; (c) temporal evolution of the spreading air front ( $x$ ) on wettability-confined tracks of different widths ( $w$ ) submerged in water for bubble diameter,  $D = 2.06$  mm; inset shows the temporal evolution of the spreading front  $x$  for different bubble diameters on a track with  $w = 1.4$  mm.

a smaller incremental spreading of the front, resulting in a slower spreading rate (as seen in Figure 17c). To further strengthen this argument, a quantitative relationship is derived in the following subsection. Moreover, the effect of the variation of the bubble volume is also studied. The temporal variation of the spreading front for bubbles of different initial diameters spreading on a track of width 1.4 mm (inset of Figure 17c) shows that the spreading is insensitive to the initial bubble volume. This is explained quantitatively in the following section.

### 3.3.2 Dynamics of Bubble Spreading

The spreading of a bubble on the wettability-confined track may be explained by the energy minimization principle. In all cases, the bubble diameter is below the capillary length of water. Since the track is superaerophilic (likewise, superhydrophobic), energetically it favors coverage by an air layer rather than ambient water. Therefore, and as mentioned previously, a thin, uniform layer of air gets trapped within the micro/nano-textures of the surface as the substrate is immersed in the ambient liquid. This implies that the substrate is pre-suffused with air in all experiments in the present work, and the air bubble is, in fact, spreading on a thin layer of air attached to the track. This results in a slip condition on the basal footprint of the spreading bubble, resulting in lower frictional resistance to its motion. As the bubble spreads, the gas pushes out the liquid ahead of it in its immediate vicinity, similar to an expanding hole in a liquid sheet (446). Since the bubble spreads with constant velocity (Figure 17b), the velocity of the liquid in its immediate vicinity also stays constant, and scales with the velocity of the spreading bubble (447). The viscosity of air ( $\simeq 0.02$  mPa.s) is significantly lower than that of any of the liquids used here (Table V). Therefore, the viscous loss inside

the bubble is negligible, and the resistance to the spreading of the bubble occurs due to the ambient liquid; this resistance manifests itself as pressure drag against the forward movement of the bubble. A schematic showing two orthogonal views of the spreading air bubble is shown in Figure 19a, which depicts the primary forces on the bubble front. Downstream of the bulge, the spreading bubble front has a nearly cylindrical shape, with the cross-section being that of a circular sector. Therefore, only the transverse curvature of the meniscus is relevant here. Since the cross-section is bounded by the track width  $w$ , the radius of curvature of the spreading bubble,  $R \sim w$ , resulting in a capillary pressure  $p_{\text{cap}} \sim \gamma/w$ . The cross-sectional area ( $A_{\text{cs}}$ ) of the spreading bubble can be written as  $A_{\text{cs}} \sim hw$ . Now from Figure 18, it can be inferred that  $h \sim w$ , which leads to  $A_{\text{cs}} \sim w^2$ .

The driving force is capillarity-driven, and can be written as

$$F_c \sim \gamma w \quad (3.1)$$

as the pressure difference is  $p_{\text{cap}} \sim \gamma/w$  (since radius of curvature,  $R \sim w$ ) and  $F_c \sim p_{\text{cap}} A_{\text{cs}}$ . The Reynolds number [ $\text{Re} = \rho v w / \eta$ , where  $v$  is the spreading velocity, which is  $O(500 \text{ mm/s})$ ] is  $O(10^3)$ , which means that the spreading is in the inertial regime (448). Therefore, the pressure drag,  $F_d$  (Figure 19a), is the resisting force and can be expressed as

$$F_d \sim \rho v^2 A_{\text{cs}} \sim \rho v^2 w^2 \quad (3.2)$$

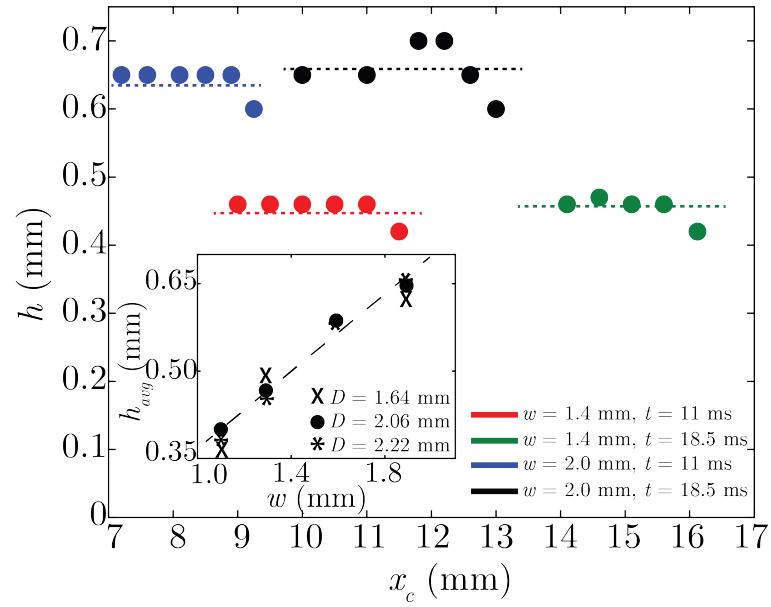


Figure 18: Variation of the height ( $h$ ) of the spreading bubble front with the lengthwise coordinate ( $x_c$ ) at two different time instants ( $t$ ) for two different track widths ( $w$ ) while keeping the diameter of the bubble constant ( $D = 2.06$  mm); inset shows the variation of the spatially-averaged height ( $h_{avg}$ ) of the bubble front with the track width ( $w$ ) for different bubble diameters ( $D$ ). The dashed lines serve as guides for the eyes.

A balance between driving and resisting forces ( $F_c \sim F_d$ ), produces the following expression for the bubble spreading velocity

$$v \sim \left( \frac{\gamma}{\rho w} \right)^{1/2} \quad (3.3)$$

which results in  $v \sim w^{-0.5}$  for a given liquid (constant  $\gamma$  and  $\rho$ ). It is interesting to note that the form of Equation 3.3, expectedly, bears a strong resemblance to the expression of the classical Taylor-Culick velocity (449), which also arises from an inertio-capillary balance. Indeed, the scaling relationship is reflected in the experimental measurements, as shown in Figure 19b, where the spreading velocity,  $v$ , is plotted against the inverse of the square root of track width,  $w^{-0.5}$ , revealing a linear behavior with positive slope. Moreover, Equation 3.3 suggests that the spreading velocity is independent of the initial diameter of the bubble ( $D$ ), as also observed experimentally in the inset of Figure 17c and in movie S2 of the appendix B, where bubbles of different initial diameters spread on the identical wettability-confined tracks with the same velocity.

It is interesting to note that Equation 3.3 does not include the viscosity ( $\eta$ ) of the ambient liquid. Therefore, the scaling law, if accurate, should predict the experimentally-observed velocities. To test this, the bubble spreading behavior was observed in other ambient liquids mentioned in Table V (where the viscosity  $\eta$  of the liquid, among other properties, changes significantly), and the spreading velocity,  $v_{\text{exp}}$ , was measured from the experiments. The qualitative spreading behavior in such liquids is shown in movie S3 of the appendix B.

We note that, even for the liquid with the highest  $\eta$  tested in the present study (80% glycerol in water,  $\eta = 51.5$  mPa.s),  $Re$  was still  $O(10)$ , which indicates that the spreading is

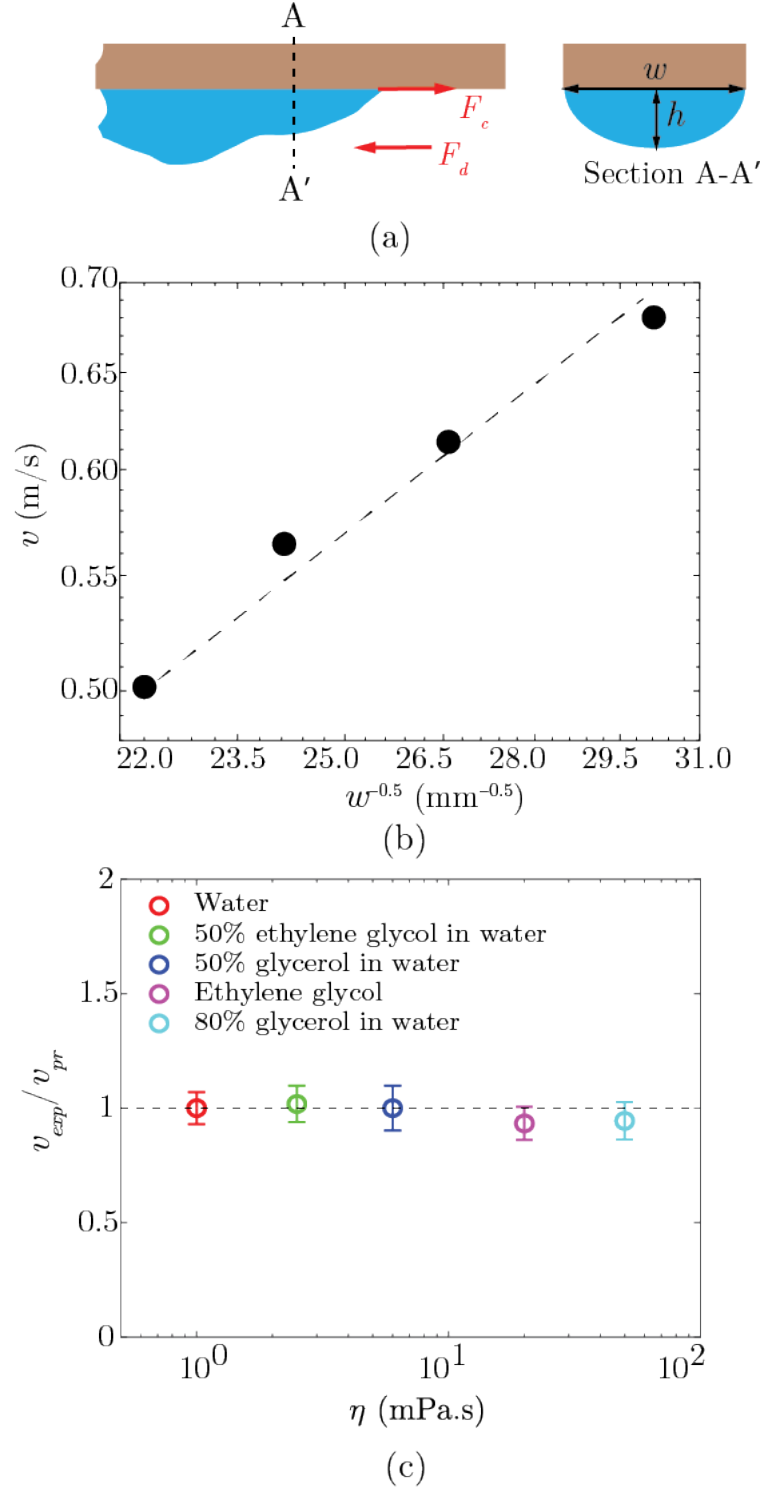


Figure 19: (a) Schematic of an air bubble spreading on a wettability-confined track showing the salient forces; (b) variation of experimentally-measured spreading velocity  $v$  with  $w^{-0.5}$  ( $w$  being the track width) when the substrate is submerged under water (the dashed line is a straight guide); (c) ratio of the experimentally measured ( $v_{exp}$ ) and scaling-predicted ( $v_{pr}$ ) spreading velocities for ambient liquids of different viscosities ( $\eta$ ) for track width and bubble size of  $w = 1.4$  mm and  $D = 2.06$  mm, respectively.

still in the inertial regime, and the scaling relationship (Equation 3.3) should still hold. Knowing the properties of the liquids (Table V), a spreading velocity ( $v_{pr}$ ) for a given track width was predicted from Equation 3.3 as

$$v_{pr} \sim v_0 \left( \frac{\gamma_l \rho_0}{\gamma_0 \rho_l} \right)^{1/2} \quad (3.4)$$

where the subscript ‘l’ denotes the liquid being tested, and ‘0’ denotes water. The ratio of the experimental to predicted velocities,  $v_{exp}/v_{pr}$ , with the viscosity of the ambient fluid,  $\eta$ , is shown in Figure 19c for a  $D = 2.06$  mm bubble and  $w = 1.4$  mm track. It is observed that, over almost two decades of viscosity tested in the present work, the ratio  $v_{exp}/v_{pr}$  remains constant at a value close to 1, which indicates that the scaling relationship derived in Equation 3.3 accurately describes the experimentally-observed phenomenon and is valid for inertio-capillary spreading, where the effect of viscosity ( $\eta$ ) is negligible. It is expected that at lower Reynolds numbers ( $Re$ ), viscosity will dominate the spreading behavior. However, viscous effects in spreading of the bubble are beyond the scope of the present study, and will be left for future work.

### 3.4 Conclusion

The present study investigated the spreading of millimeter-sized air bubbles released one-at-a-time on a submerged, constant-width, wettability-confined track. The substrate consisted of a superaerophilic track on a superaerophobic background; both track width and bubble diameter were varied in the experiments. High-speed imaging revealed that the spreading bubble morphology comprises of a spreading front and a trailing air bulge, the latter feeding into the former as the spreading progressed. It was identified that the bulge had a gradually decreasing cross-sectional area, while that of the front remained constant during spreading. The temporal



evolution of the spreading front revealed a linear relationship, which translates to a constant spreading velocity. A scaling relationship between the driving and resisting forces reveal that, for a constant bubble diameter and a given ambient fluid, the spreading velocity arises from an inertio-capillary force balance, and varies as the inverse of the square root of the track width. This scaling relationship was further confirmed by experimental measurements. Furthermore, the scaling relationship was found to accurately predict the experimentally-observed spreading velocities when the viscosity of the ambient fluid was changed over two decades. The study reveals the fundamental principle governing the spreading of gas volumes on wettability-confined horizontal tracks, and its outcomes can be used to facilitate design decisions.

## CHAPTER 4

# APPLICATION OF WETTABILITY ENGINEERING IN A NON-ISOTHERMAL SYSTEM, A REVISIT OF CONDENSATION HEAT TRANSFER ENHANCEMENT

*” Copyright 2022 IEEE. To be published in the 21st Intersociety Conference on Thermal and Thermomechanical Phenomena in Electronic Systems (ITherm 2022). Reprinted, with permission, from M. Jafari Gukeh, G. Damoulakis, and C. M. Megaridis. Exploring the Design Features of Wettability-Patterned Surfaces for Condensation Heat Transfer, 2022.”* (450) IEEE does not require individuals working on a thesis to obtain a formal reuse license.

### 4.1 Background and Motivation

Condensation is a classic physical phenomenon, and omnipresent in nature, in which vapor turns to liquid on a subcooled surface whose temperature is lower than the vapor saturation temperature at its partial pressure. Condensation is an effective heat transfer mode in industries, such as electrolyte fuel cells (451), heat exchangers (452), harvesting from air-borne moisture (453), seawater desalination (454), power generation from natural gas (455), water harvesting via dewing (456), electric power generation (457), thermal management of electronics, e.g. vapor chambers (278) and heat pipes (458), and air-conditioning (459). When vapor releases its latent heat upon contact with a subcooled dry surface, it condenses to liquid forming droplets, i.e. Dropwise Condensation (DWC). The nucleation density is highly dependant

on the wettability of the solid surface, vapor density, and subcooling temperature (460). The condensate droplets may coalesce and form a liquid film (Filmwise Condensation, FWC) on the surface, causing a transition from DWC to FWC, which, in turn, reduces the heat transfer rate by one to two orders of magnitude due to the low thermal conductivity of the film (461). Therefore, wettability of the solid plays an important role on condensation heat transfer rate. There are two primary factors in determining the condensation heat transfer rate on a surface, namely, nucleation density and drainage mechanism. Simultaneous enhancement in both factors leads to higher heat transfer rates; but achieving this condition requires precise engineering of the surface morphology and wettability. The drainage mechanism on vertical surfaces is mostly gravity-dependent and the shedding is a function of droplet mobility on the surface (i.e. low contact angle hysteresis) or correspondingly the maximum droplet radius ( $r_{\max}$ ) departing from the nucleation site. As shown earlier (462; 463), heat transfer rate decreases with increasing  $r_{\max}$ . In the past two decades, scientists have taken several approaches to control  $r_{\max}$  and drainage rate on a surface; such approaches include gradient surfaces (148; 464), superhydrophobic surfaces (465; 466), grooved surfaces (467; 468), and wettability-patterned surfaces (469; 470; 471; 362).

Uniform superhydrophobic surfaces could be effectively used to adjust  $r_{\max}$  and droplet mobility on the surface. Droplet jumping -a phenomenon induced by coalescence of smaller droplets during DWC- on superhydrophobic surfaces significantly reduces  $r_{\max}$ , since the jumping droplets are only tens of micrometers in diameter (466; 121; 128). However, self-propelled jumping droplets from superhydrophobic surfaces are seen only at low surface subcooling,

whereas at higher surface subcooling, surface-flooding occurs, hindering performance. This makes DWC on hydrophobic surfaces better than on superhydrophobic surfaces (472; 466; 120). In addition, more wettable surfaces have lower thermodynamic barrier to nucleation, thus leading to greater DWC performance for the hydrophobic surfaces compared to their superhydrophobic counterparts (473; 128; 64).

To overcome the above balancing issues, multi-wettability (a.k.a. wettability-patterned) surfaces have been developed and implemented in the literature to control  $r_{\max}$  and enhance drainage of the condensate (163; 159; 152; 474; 153; 475; 476; 162). Peng et al. (469) enhanced the condensation collection rate by 23% compared to uniform DWC via vertically striped pattern in the absence of non-condensable gases. Chatterjee et al. (471) achieved 8% improvement in heat transfer via a hydrophilic pattern on a superhydrophobic background, when compared to a uniformly superhydrophobic surface. Wang et al. (477) improved heat flux by 73% using superhydrophilic islands on a superhydrophobic background. Hou et al. (478) exploited a hydrophilic/hydrophobic pattern to enhance DWC. Their pattern showed  $\sim 63\%$  improvement in heat transfer coefficient of the hybrid surfaces compared to a conventional flat hydrophobic silicon surface. Ghosh et al. (363) utilized bioinspired wettability-patterned superhydrophilic wedge-shape tracks on a hydrophilic background to promote capillary-driven condensate drainage and enhanced DWC heat transfer by reducing  $r_{\max}$  on the hydrophilic regions (DWC) of the condenser plate. The patterned surface exhibited 19% performance improvement compared to the uniform DWC case in a NCG+vapor environment.

Although Ghosh et al. (363) reported heat transfer coefficient (HTC) enhancement and attributed it to the optimized  $r_{\max}$ , their study did not examine the relative role of potentially influential parameters, such as FWC-to-total area ratio, superhydrophilic wedge-shape track length, wedge angle, and superhydrophilic straight track width. Consequently, the underlying reason behind the HTC improvement was not quantified. In a follow-up study, Mahapatra et al. (362) used the same configuration as (363) with an inter-digitated arrangement of superhydrophilic wedge-shape tracks with long wettability contrast lines and capillary-driven condensate removal for rapid drainage of the condensate from the surface. In two cases of the study, they used a range of fractional area (FWC to total surface, denoted as  $\phi$ ) designs and demonstrated a maximum improvement of 30% in water collection rate and 34.4% in HTC for  $\phi = 35\%$ . It was revealed that with increasing vapor mass content in the environment the optimum  $\phi$  value was also increased. Compared against uniformly superhydrophobic surface examined under the same ambient condition, a maximum of 75.8% and 95.1% improvement in HTC and water collection rate was reported, respectively.

Mahapatra et al. (362) showcased the influence of FWC to total area ( $\phi$ ) by changing the wedge-shape track's spacing, which modulated  $r_{\max}$ , but the role of other potential factors, such as superhydrophilic wedge geometry and main drainage vein width size are yet to be examined. Moreover, the experiments were done in the presence of NCGs and the pattern was designed for gravity-driven scenario, where the straight superhydrophilic tracks just acted as a drain with no preferential collection point. A similar mechanism is also used in closed thermal-management devices with wickless components, such as vapor chambers and heat pipes (278; 458; 323) where

operation takes place in a low-pressure non-NCG environment and generally, against gravity. Condensation of vapor in passive heat spreaders is a major heat transfer mechanism and directly controls heat rejection efficiency and working fluid circulation in these devices. There, the vapor is condensed on a wettability-patterned hydrophobic/superhydrophilic surface; a similar method as in (362; 363) is used to collect the condensate along the main straight superhydrophilic drainage tracks with a difference of directing the condensate to certain low-pressure domains to create a capillary-bridge acting to return the condensate to the heated area (evaporator). The efficiency of this process is a function of surface wettability,  $\phi$  ratio, wedge and straight tracks shapes and geometries, number and shape of condensate collection points, capillary-bridge length, and the vapor load.

Nevertheless, previous studies (278; 323) examined the condenser performance enhancement by changing the superhydrophilic-to-total area ratio without any particular constrain on wedge-shape track geometry or  $r_{\max}$ , but yet the source of this enhancement remains unknown. Inspired by this dearth of knowledge, in this follow-up study, all the aforementioned factors are isolated and the sole influence of the superhydrophilic wedge-shape tracks is investigated with the same substrate and surface engineering procedure but in a vapor+NCG environment.

## **4.2 Materials and Methods**

### **4.2.1 Experimental Setup**

Figure 20 shows a photograph of the present experimental setup. An environmental chamber (ESPEC, SH-641) at a fixed condition (40°C dry bulb temperature and 80% RH) was used for testing different surfaces.

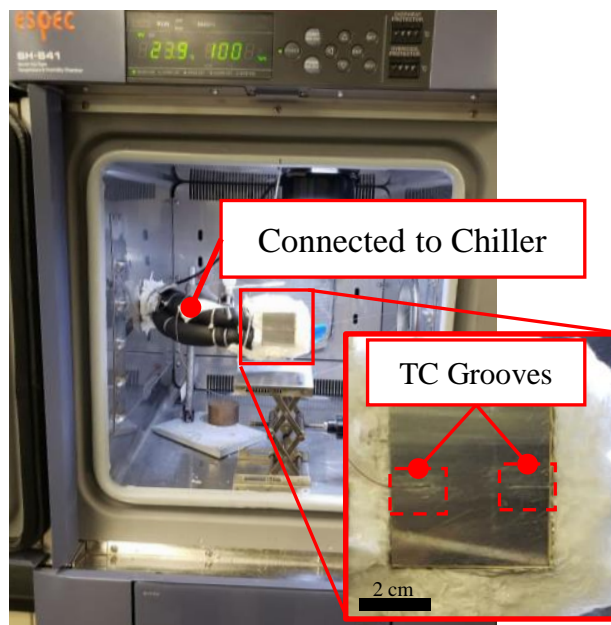


Figure 20: The environmental chamber (with open door) used in this study for the experimental setup. The inset shows the insulated bare cold plate with two grooves for thermocouples to measure the condensation-surface temperature during the tests.

Each sample was mounted on a cold plate (40 mm  $\times$  40 mm  $\times$  12 mm (DIYhz)) via a thermally conductive adhesive tape (McMaster Carr, 6838A11). A chiller (Neslab RTE-110) working at 10°C with a flow rate of 0.112 kg/s of pure ethylene glycol (Alfa Aesar, 99%) was used to remove heat from the cold plate. Two thermocouples (Omega, T-type, bead diameter 0.05 mm) were placed into 500  $\mu$ m diameter holes milled on the cold plate. A data acquisition system (Omega, USB 2400 series) with a sampling frequency of 1 Hz was used to record the temperatures. Condensate that drained from each surface was collected over 15 minutes, and weighed in a digital micro-balance (FX-3000i WP, A & D Company Limited). 2 samples were

fabricated for each wettability design and 4 runs for each design were performed to collect sufficient data for each case.

A mirror-finish copper plate with dimensions 40 mm  $\times$  42 mm  $\times$  1 mm (110 mirror-finish copper, McMaster-Carr) was employed as the condenser surface. First, the surface was cleaned via water and soap, ethanol, DI water, and dried with nitrogen. Next, a thin layer of Teflon AF (Chemours AF 2400, 1% solution Fluorinert FC-40, Chemours AF 2400) was spin coated on the surface at 2000 rpm for 20 s. The sample was then cured in a furnace (Lindberg, Blue-M-HTF55322c) with a step-wise heating protocol, 160°C for 10 min, 240°C for 5 min, and 330°C for 15 min under a reduced atmosphere of Argon and Hydrogen, to avoid copper oxidation. This process renders a mildly hydrophobic surface (sessile contact angle was 118°). To reduce heat losses to the environment, the piping to/from the chiller was insulated (McMaster-Carr, Pipe Condensation-Reducing Vinyl Foam) and only the designated condensation area was exposed to the vapor+NCG mixture. An extra 2 mm length protruding from the sample's plate bottom facilitated the condensate departure from the lower area of the copper plate, and prevented interference from the insulation around the plate.

A laser marking system (EMS400, TYKMAElectrox®), 40% power, 20 kHz frequency, 200 mm/s traverse speed) was used to apply the patterns. Through this process, the Teflon coating was selectively removed, rendering the underlying area superhydrophilic (albeit susceptible to oxidation, thus requiring passivation). An aqueous solution of 0.1 mol/L ammonium persulfate (Alfa Aesar) and 2.5 mol/L sodium hydroxide was used to passivate the laser-etched plate via a wet-etching process for 5 minutes. This procedure grew nanohairs on the laser-etched domains,



creating a hierarchical micro-nano structured surface with a contact angle of  $\sim 0^\circ$ , while the Teflon-coated areas remained unchanged with contact angle of  $\sim 118^\circ$ . This process created superhydrophilic domains laid in a hydrophobic background. The contact angles were measured by depositing a  $4.7\mu\text{L}$  DI water droplet and imaging with a camera (1080 HD MINTRON).

#### 4.2.2 Data Reduction

The overall heat transfer during condensation in vapor+NCG environment has two components, sensible and latent heat. The latter component can be calculated from the measured condensation rate (38):

$$\text{HTC} = \frac{\dot{m}_w h_{fg}}{T_{\text{dew}} - T_s} \quad (4.1)$$

driven by the substrate temperature ( $T_s$ ) and the dew-point temperature ( $T_{\text{dew}}$ ) of the environment. The former part (driven by the difference between the ambient  $40^\circ\text{C}$  and  $T_s$ ) remains more or less the same for all surfaces explored in this work. Thus, the sensible part of the overall HTC is not considered in the current study. The error analysis was performed for each metric following a Gaussian Error Propagation (479; 278) as follows:

$$\Sigma_\alpha = \sqrt{\frac{\partial \alpha}{\partial \beta} \sigma_\beta^2 + \frac{\partial \alpha}{\partial \gamma} \sigma_\gamma^2 + \dots} \quad (4.2)$$

where  $\Sigma$  is the error for a random performance metric, here as  $\alpha$ , which is a function of  $\beta$  and  $\gamma$ , etc. The standard deviation of the experimental measurements due to each instrument was  $\pm 0.25^\circ\text{C}$  for the thermocouples and  $\pm 0.01\text{g}$  for the micro-balance scale.

### 4.3 Results and Discussion

#### 4.3.1 Working Principle and Factors

In the interdigitated and staggered wedge-shape superhydrophilic pattern laid on the hydrophobic surroundings, the hydrophobic regions promote DWC, whilst the superhydrophilic tracks facilitate condensate fluid drainage. As more vapor condenses on the surface, small droplets start to form on the hydrophobic areas and a thin layer of water forms on the superhydrophilic areas.

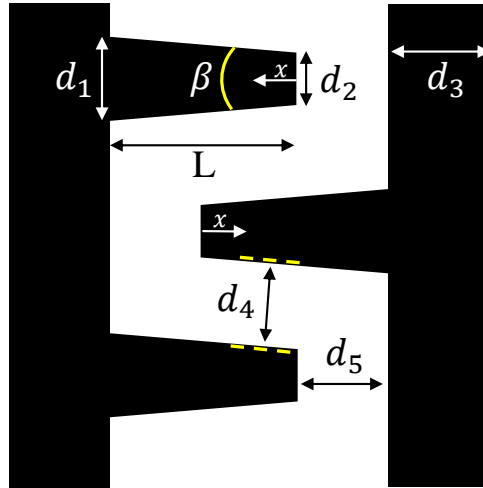


Figure 21: Schematic of the wettability pattern features used in this study. Black and white denote superhydrophilic and hydrophobic domains, respectively. This quantum cell shows the design parameters.  $d_1$  wide portion of the wedge track,  $\beta$  opening angle,  $d_2$  narrow end of the wedge track,  $d_3$  central vein width,  $L$  wedge track length,  $d_4$  &  $d_5$  distances between two adjacent superhydrophilic domains.

Small droplets gradually grow by condensation and their size increases due to coalescence events with other droplets that are growing in the vicinity. When the enlarged droplets come into contact with the superhydrophilic track edge, they merge with the liquid film, leaving a pristine space on the hydrophobic area for renewed droplet formation. The wedge-shape track promotes pumpless and rapid transport of the condensates to the central vertical vein tracks (16) and the staggered pattern promotes faster removal of droplets through the main track by reducing the viscous loss caused by the condensate flows from opposite wedge-shape tracks (362). Low-curvature well domains towards the plate's bottom are connected to the main tracks, and are specifically engineered to operate as low-pressure accumulation areas where condensate is collected by the Laplace-pressure difference along the track. These wells also improve the shedding action of the collected liquid.

#### **4.3.2 Influence of Wedge-Shape Track**

Figure 21 depicts a quantum cell of the wettability patterns in this study. As shown in our previous studies (362; 363),  $d_4$  &  $d_5$  practically control  $r_{\max}$  on the DWC region of the pattern; lower values of these two lengths result in lower  $r_{\max}$  and thus, in higher HTC. However, the influence of  $d_1, d_2, d_3$  and  $L$  is yet unclear. In principle, a superhydrophilic region on the surface provides a permanent, stable, and quick path to drain the condensate, thus providing more free surface for new vapor condensation. Since there is always a liquid film covering the superhydrophilic region during the condensation period, the transport velocity of a droplet from any point on the wedge-shaped track to the drainage points at the plate's bottom edge is a function of two pressures gradients: One is caused by the tapering curvature of the liquid

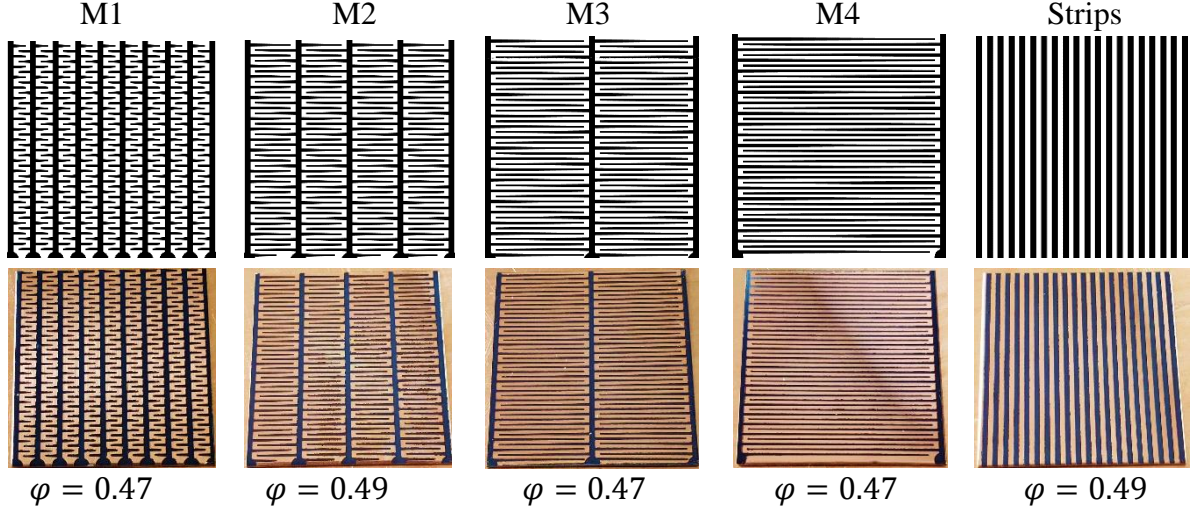


Figure 22: Five distinct wettability patterns used in this study. In each column, from top to bottom: Name of the design, wettability-pattern design, fabricated sample used in experiments, and corresponding  $\phi$  ratio. Superhydrophilic areas are denoted with black, while hydrophobic domains are in white or copper color.  $\phi$  denotes the superhydrophilic-to-total area ratio. The value of  $\phi$  remains practically constant for all five cases. Scale bar denotes 2 cm.

film on the wedge-shape track (16) (affected by  $d_1, d_2$ , and  $L$ ), and the other is due to the liquid surface curvature difference between the wide end of the wedge-shape track and the main drainage vein (i.e  $d_1/d_3$  ratio). The impact of the former pressure gradient is studied in this work by focusing on the wedge-shape track geometry while fixing the latter, i.e. the  $d_1/d_3$  ratio remains constant.

The maximum droplet size  $r_{\max}$  on a surface with uniform wettability could be found by (480):

$$r_{\max} = \left[ \frac{3\gamma(\cos\theta_r - \cos\theta_a)\sin\theta}{\rho_w g \sin\alpha (2 - 3\cos\theta + \cos^3\theta)} \right]^{0.5} \quad (4.3)$$

where  $\gamma$  is the liquid surface tension,  $\theta_r$  and  $\theta_a$  are the liquid droplet receding and advancing contact angles, respectively,  $\alpha$  the surface tilt angle, and  $\theta$  the static contact angle. For the hydrophobic surface in our study,  $\theta_r$ ,  $\theta_a$ ,  $\theta$ , and  $\alpha$  were measured as  $110^\circ$ ,  $123^\circ$ ,  $118^\circ$ , and  $90^\circ$ , respectively. This renders a theoretical  $r_{\max}$  of  $\sim 1.2$  mm from Eq. 3, while from the experiment, a maximum of  $\sim 1$  mm was measured for the hydrophobic surface. For the patterned surface with  $d_4 = d_5 = 1$  mm, the width of the DWC region is kept constant all along the plate, rendering a maximum droplet size  $r_{\max} = 0.5$  mm for all cases. Thus, the wettability patterns are expected to enhance the overall HTC of the surface by reducing and constraining the  $r_{\max}$  compared to the uniformly hydrophobic surface.

As originally shown by Ghosh et al. (16) the pressure gradient along a wedge-shape wettability confined track scales as

$$\frac{\partial P}{\partial x} \sim \gamma \sin(\theta_{\text{avg}}) \beta / \delta(x)^2 \quad (4.4)$$

where  $\theta_{\text{avg}}$  is the average angle of a liquid bulge confined in the track,  $\beta$  is the wedge angle, and  $\delta(x)$  is the local width of the track at position  $x$  from the narrow end. For a track of length  $L$  and covered with a liquid film, one may rewrite this equation as

$$\frac{\partial P}{\partial L} \sim \gamma \sin(\theta_{\text{avg}}) / \beta L^2 \quad (4.5)$$

To meet the aforementioned constraints and to explore solely the influence of the wedge pressure gradient on the overall HTC of the surface, one should minimize changes in some parameters while varying others. To that end, since  $\theta_{\text{avg}}$  is highly dependent of  $\delta(x)$ , we keep the wide

and narrow ends of the track constant ( $d_2 = 0.23$  mm &  $d_1 = 0.44$  mm in Figure 21) for all cases to fix the maximum and minimum width of the track, and thus cause minimum changes on  $\theta_{\text{avg}}$  along the track. Accordingly, to keep the  $d_1/d_3$  ratio constant,  $d_3 = 1$  mm was fixed for all cases. Using the chosen values for  $\sin(\theta_{\text{avg}})$  and  $\gamma$ , which are constant for all cases, and since for small wedge angles it is

$$\beta \approx \frac{d_1 - d_2}{L} \quad (4.6)$$

Eq. 5 can be written as

$$\frac{\partial P}{\partial L} \sim \frac{1}{L} \quad (4.7)$$

So, with the current wettability design (fixed values of  $d_1$  and  $d_2$ ), the pressure gradient along the wedge-shape track can change only via the length  $L$ . To cover a wide range of pressure gradients, 4 different values of  $L$  were examined. Figure 22 shows 4 types of wettability patterns where the superhydrophilic/total area ( $\phi$ ) is kept essentially fixed, while  $L$  is 2.3 mm, 7.7 mm, 17.5 mm, and 37.5 mm, for cases M1 to M4, respectively. To further illuminate the influence of a wettability pattern with wedge-shape tracks, a simple case with 1 mm superhydrophilic vertical strips spaced 1 mm apart and similar  $\phi$  was also fabricated and tested to provide a control case.

### 4.3.3 Main Results

Figure 23 and Figure 24 show the water collection rate and HTC for all five cases. As seen, the hydrophobic (HPB) surface as the benchmark case with uniform dropwise condensation has the lowest water collection rate and HTC with average of  $1.90 \pm 0.02$  L/m<sup>2</sup>h and  $0.0568 \pm$

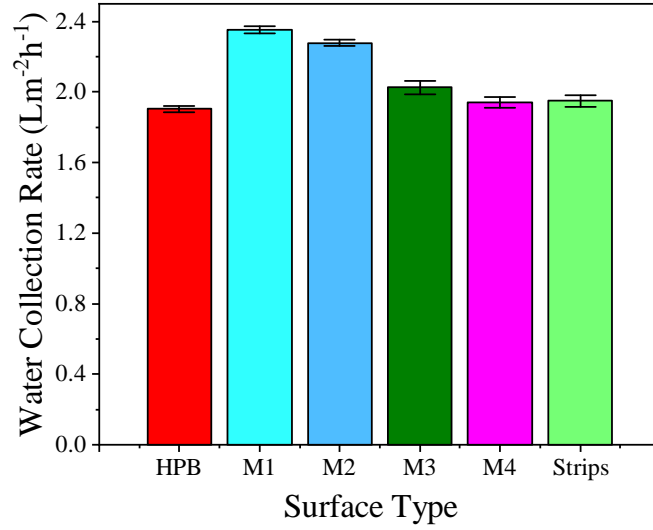


Figure 23: Water condensate collection rate for all surfaces in an environment of 40°C and 80% RH.

0.0005 kW/m<sup>2</sup>K, respectively. Among the four wettability-patterned cases, M1 and M2 show higher HTC and water collection rate with  $0.0706 \pm 0.0006$  kW/m<sup>2</sup>K and  $2.35 \pm 0.02$  L/m<sup>2</sup>h for M1, and  $0.0691 \pm 0.0005$  kW/m<sup>2</sup>K and  $2.29 \pm 0.02$  L/m<sup>2</sup>h for M2. These results show an average 24% enhancement in both HTC and water collection rate for M1 compared to HPB case. As shown in our previous works (363; 362), a wettability patterned surface enhanced the HTC up 75.8% and 34.4% compared to a superhydrophobic and a uniform hydrophilic case (where  $r_{\max}$  was  $\sim 1.5$  times of the hydrophobic case in the current study). However the experimental setup and the wettability pattern design parameters were different in those earlier studies. The present design clearly shows the robustness of the pattern that can surpass any uniform wettability surface in condensation heat transfer.

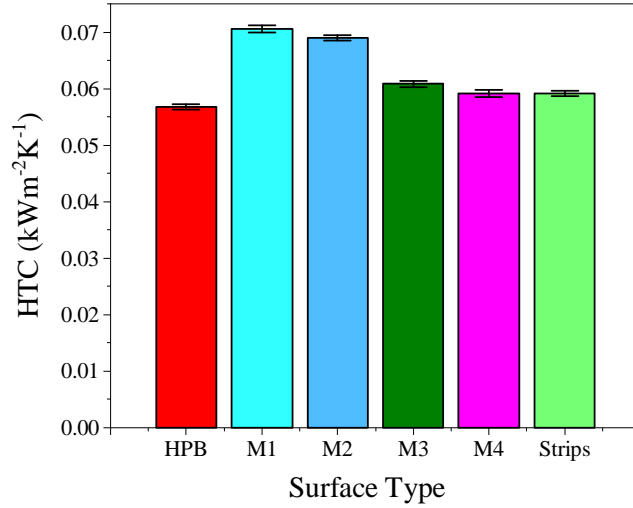


Figure 24: Overall heat transfer coefficient for all surfaces in an environment of 40°C and 80% RH.

Cases M3 and M4 showed lower HTC and water collection rate with  $0.0608 \pm 0.0006$  kW/m<sup>2</sup>K and  $2.03 \pm 0.04$  L/m<sup>2</sup>h for M3, and  $0.0591 \pm 0.0007$  kW/m<sup>2</sup>K and  $1.94 \pm 0.03$  L/m<sup>2</sup>h for M4. Comparing M1-M4 and using M1 as the base patterned case, from Eq. 7 we can deduce that the pressure gradient for the wedge-shape track is reduced by 3.3, 7.6, and 16.3 times from M2-M4, respectively. This result shows a direct impact of the wedge-shape track pumping power on the overall HTC of a surface. As mentioned above, the main role of FWC area in these types of wettability patterns is a quick drainage path of the condensate. Generally, different patterns are referred with their  $\phi$  value (362; 278; 323), however,  $\phi$  alone does not accurately represent all wettability pattern characteristics and, as shown here, the same  $\phi$  value but different wedge dimensions cause highly different performances. Similarly, the striped case



shows a close performance to M3 and M4 with  $0.0591 \pm 0.0005$  kW/m<sup>2</sup>K and  $1.95 \pm 0.03$  L/m<sup>2</sup>h in HTC and water collection rate, respectively. Comparing M1-M4 to the uniform vertical striped surface shows that wedge-shape track influence could be eliminated when its pressure gradient is reduced by almost one order magnitude. The striped case performs very similarly to the M3 and M4 cases due to its capability to control the  $r_{\max}$ , however, the trade-off between controlling  $r_{\max}$  and replacing the DWC area by FWC domains, does not allow the surface to surpass the HPB surface.

#### 4.4 Conclusion

An experimental evaluation of condensation heat transfer on wettability-patterned surfaces in a vapor+NCG atmosphere was carried out in this work. A parametric analysis was used to create several designs where the maximum condensate droplet size ( $r_{\max}$ ), drainage-vein width, and narrow and wide end widths of the wedge-shape tracks were maintained constant, while the wedge length  $L$ , and accordingly the wedge opening angle ( $\beta$ ), were modified. Five different patterns were designed and manufactured on copper plates, and their heat-transfer performance was evaluated. The performance was compared to a uniform hydrophobic case acting as benchmark. On the wedge-shaped tracks, the patterns were created to provide various pressure gradients spanning a range where the lowest to highest gradient varied by a factor of  $15\times$ . The findings revealed a clear relationship between the total surface HTC and the pressure gradient on the wedge-shape tracks, with the  $L = 2.3$  mm surface achieving the highest HTC of  $0.0706 \pm 0.0006$  kW/m<sup>2</sup>K and water collection rate of  $2.35 \pm 0.02$  L/m<sup>2</sup>h. Although the combined

effect of wedge-shape track length and opening angle was explored in this work, a more complete examination of the effects of each individual parameter is left for future research.

## CHAPTER 5

### APPLICATION OF WETTABILITY ENGINEERING IN THERMAL MANAGEMENT; A HYBRID VAPOR CHAMBER

*” Copyright 2022 IEEE. An earlier and more limited version of this chapter is to be published in the 21st Intersociety Conference on Thermal and Thermomechanical Phenomena in Electronic Systems (ITherm 2022). Reprinted, with permission, from G. Damoulakis, C. Bao, M. Jafari Gukeh, A. Mukhopadhyay, S.K. Mazumder, and C. M. Megaridis. Hybrid Vapor Chamber-based Cooling System for Power Electronics, 2022.”* (481) IEEE does not require individuals working on a thesis to obtain a formal reuse license.

#### **5.1 Background and Motivation**

”According to MarketsandMarkets, the power electronics market is projected to grow from USD 37.4 billion in 2021 to USD 46.3 billion by 2026; it is expected to grow at a compound annual growth rate (CAGR) of 4.4% from 2021 to 2026” (482). Expanding incorporation of high-frequency power electronics in various applications, such as electric vehicles, renewable energy sectors, power grids, biomedical electronics, wireless transmission, etc. (483; 484; 485; 486; 487), has been the key driving force for this growth in the past decade. Concurrently, with developing market in each sector, demands for thinner, lighter, and miniaturized electronic devices with higher power density and compacted size have been rapidly increasing. To achieve that, nowadays, switching frequency of semiconductor devices in power electronics reaches hundreds

of kHz or MHz level and shows a promise for additional growth (488; 489; 490). However, an increasingly more compact electronic device with higher power density and reduced size or volume also handles greater heat fluxes. Hence, these advancements impose difficult challenges to thermal management technologies to maintain safe and reliable operation of these devices. As reported by the US Air Force Avionics Integrity Program (491), approximately 55% of electronic equipment failures originate from temperature problems. Moreover, Black's equation (492) also shows that the temperature increase accelerates the failure process of electronic devices. These challenges highlight the importance of more efficient and cost-effective thermal management solutions to improve performance and reliability of high-power electronic devices.

In general, electronics cooling methods can be divided into two categories; active and passive (213). The passive cooling approach mostly relies on natural convection, whereas in active cooling, an extra source, usually electricity, is required to remove heat. Active cooling could be performed by either direct or indirect contact of the heat transfer medium. Vapor chambers and heat pipes are the most commonly used devices for indirect cooling. These devices, which are essentially passive heat spreaders, are designed to spread heat more uniformly and efficiently to a larger area from where the heat could be removed by the active medium e.g., forced air or the circulating liquid in a cold plate. These devices remove heat more efficiently via phase change where the latent heat of the working fluid is absorbed by evaporation on the heat source and is released by condensation on the condenser side (attached to a heat sink) of the device. Next, the condensed liquid returns to the evaporator via wick capillary action either via wicking posts or capillary bridges (493) and the thermodynamic cycle is completed.

By repeating this process, the heat is dissipated from a local spot to a larger area efficiently and eventually removed by a heat sink from the condenser (cooled) side.

As mentioned above, VCs are consisted of evaporation and condensation sections. The evaporation usually takes place on a metal wick (or a fine micro/nano structure) where the thin-film evaporation and boiling promotes heat removal and plays the major role in a VC thermal performance (494; 177). The wick's physical properties including the porosity, permeability, and effective thermal conductivity designate the critical/maximum heat load that can be removed by the device without dry-out (495). Numerous studies have been conducted to enhance the evaporation/boiling performance in a vapor chamber. Chen et al. (307) combined the copper mesh with a micropillar structure and fabricated a novel ultra-thin vapor chamber (UTVC). The results showed that the UTVC can have up to 30 times higher thermal conductivity compared to pure copper. Moreover, the maximum heat transfer reduction was reported as less than 11% while this device worked against gravity. Liu et al. (300; 301) suggested a biomimetic leaf-vein-like porous structure for the wick of the vapor chamber. The results showed that the leaf-vein porous network could reduce the thermal resistance with great temperature uniformity on the condenser side. Velardo et al. (309) fabricated a hybrid wick structure, combining screen mesh and sintered powder, which was shown to enhance the heat transfer performance of a vapor chamber (257). Li et al. (308) experimentally investigated the influence of the foam and sintered copper powder wick structures on a vapor chamber's thermal performance. They found that the copper foam enhanced temperature uniformity on the condenser side, but the copper powder reduced thermal resistance. Although numerous studies have been

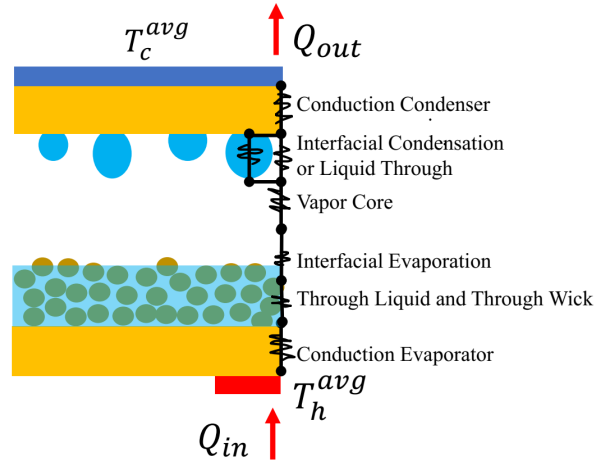


Figure 25: Major thermal resistances in a vapor chamber as the heat moves from the hot side (bottom) to the cool side (top).

performed and investigated the role of wick structure on evaporation and boiling in vapor chambers (496; 272; 497; 498; 499; 303), heat transfer enhancement of vapor chambers through the condensation section has not been explored as much. Most of the literature has focused on the contribution of boiling and evaporation heat transfer on the evaporator side of the VC to its thermal performance. However, evaporation/boiling and condensation phase change occur at the same time inside a closed chamber, and thus the interactions directly influence the heat transfer characteristics of the chamber (500).

Figure 25 shows a schematic diagram of a vapor chamber's thermal resistance network. The major hurdles in the heat transfer path are imposed by the bulk wick (micro/nano structure), interfacial resistance of the evaporation, and condensation. While the first two factors are governed by the wick structure, the latter one can be controlled independently. In the conven-

tional fully wick-lined vapor chambers, the condensation occurs on a metal wick and in a porous material. A range of studies have been conducted to enhance condensation and temperature uniformity on the metal wicks. Patankar et al. (280) proposed a biporous condenser-side wick that could provide a wider vapor core and the condenser surface peak-to-mean temperature difference reduced by 37% compared to a uniform wick structure. Li et al. (281) performed a numerical design optimization and proposed a grooved condenser wick structure to ensure temperature uniformity. Wu et al. (501) implemented numerical analysis to illuminate the role of condenser wettability on the boiling performance of a vapor chamber. They concluded that there is an optimal uniform wettability where the thermal resistance and evaporator temperature are minimal. In a recent study, Zhang et al. (502) showed that the condensation mode in a VC could be the governing factor in the overall thermal performance of the device. Wiedenheft et al. (320) also conducted an experimental study with a vapor chamber featuring a superhydrophobic surface that promoted jumping-droplet condensation mode and achieved significant heat transfer enhancement compared to a copper plate.

As extensively discussed in chapters 1 and 4, wettability patterning has been shown to be the most effective approach to enhance condensation heat transfer. In a particular case, Mahapatra et al. (362) developed a wettability-engineered surface where a juxtaposed hydrophilic (DWC) and superhydrophilic (FWC) wedge-shape track network enhanced the HTC via confining the droplets on the DWC domains and quickly draining the condensate via the superhydrophilic tracks. On the same premise, Koukoravas et al. (493) successfully developed a hybrid vapor chamber in which similar wettability-patterned surface was used as the condenser and achieved

minimum thermal resistance of 0.24 K/W at 87 W. Featuring similar technology, a vapor chamber-thermal diode (323) and a heat pipe (458) were later fabricated and showed thermal performance enhancement over uniform hydrophilic or hydrophobic wickless condenser surfaces.

In this follow-up study, as a real-life application of electronics cooling with this technology, a hybrid vapor chamber with a uniform wick-lined evaporator and a wickless wettability-engineered condenser for cooling two high-power metal-oxide-semiconductor field-effect transistors (MOSFET)s is fabricated and tested. As opposed to our previous studies (493; 329) where a liquid cooling heat sink method was used, in this work, forced air convection cooling via a simple aluminum plate heat sink was used to further illustrate the performance capabilities of wettability patterning on the condenser side of a vapor chamber in a harsher environment.

## 5.2 Materials and Methods

Figure 26 and Figure 27 show all the components of the experimental setup and the details of the vapor chamber test rig, respectively. As shown in Figure 26, the heat generation by the MOSFETs was controlled by the following equipment: a DC power supply HY10010EX with output from 10 to 60 V; a logic power supply (Agilent E3646A) set at 20 V to operate the printed circuit board (PCB); a Wavetek Model 395 wave generator set at 100KHz to control the switching frequency of the MOSFETs; and a Tektronix TPS2024B digital oscilloscope to monitor the electrical signals. As shown in Figure 27, the VC is clamped between 152.4 mm  $\times$  101.6 mm  $\times$  10 mm aluminum 6061 (McMaster-Carr) plate and a table via 4 screws and nuts. The pressure applied on the system was controlled via a torque screwdriver (Neiko 10573B) set at 30 Nm. The aluminum plate provides sufficient pressure for sealing the VC via the gasket



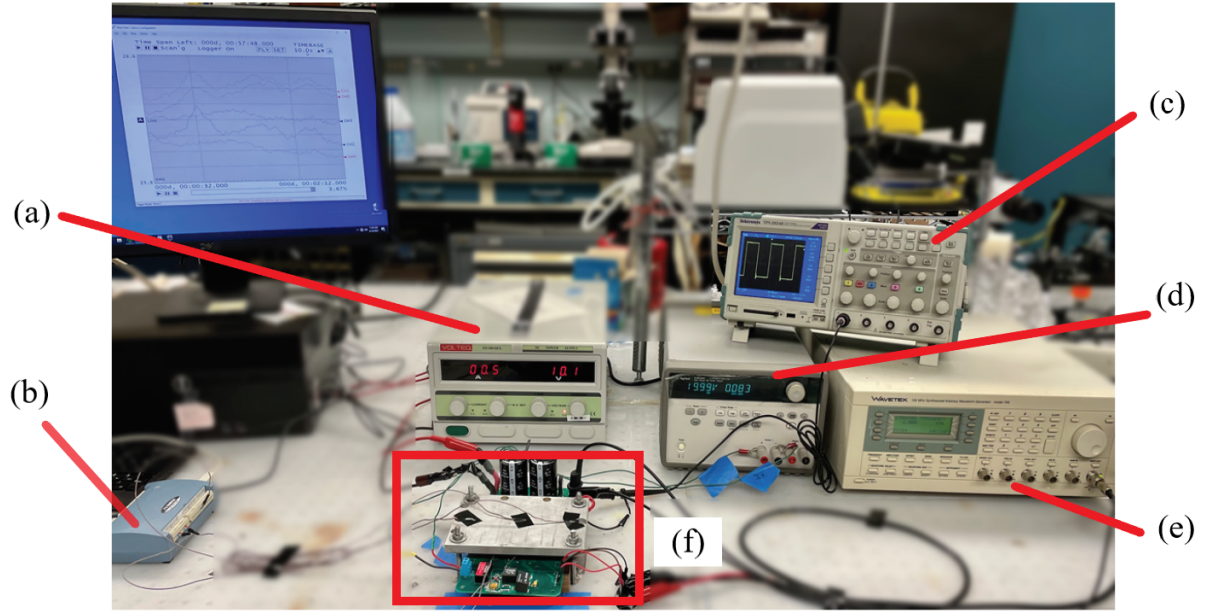


Figure 26: Experimental setup components: (a) DC Power Supply, (b) DAQ, (c) oscilloscope, (d) logic power supply, (e) wave generator, (f) board/VC assembly.

mechanism (will be discussed in the next subsection) and also acts as the heat sink for the system.

The VC is in contact with the aluminum plate and the MOSFETs through a thermally conductive and electrically insulating pad (thermal conductivity  $3.5 \text{ W/m-K}$ , 951-GP3500ULMG20-12, Mouser). A 5 mm Teflon plate with two identical ( $45 \text{ mm} \times 16 \text{ mm}$ ) pockets (Appendix C: Figure 49) was placed on the PCB to provide a uniform seating area for the VC and insulate the evaporator plate from the bottom side. Temperatures were recorded via 6 thermocouples (Omega, T-type, bead diameter  $0.05 \text{ mm}$ ) in which four were distributed on the condenser plate and the rest on the MOSFETs. The temperature recordings were performed via a data

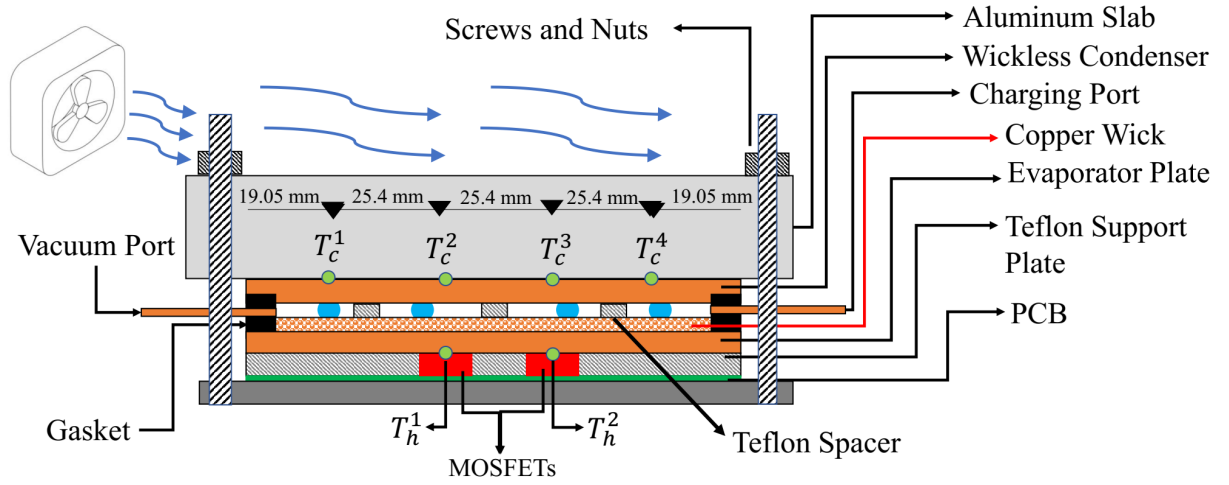


Figure 27: Schematic of the experimental setup rig and thermocouple arrangement

acquisition device (Omega DAQ, USB 2400 series) set at 1 Hz sampling frequency. More pieces of equipment -not shown here- utilized in the experiments included: a vacuum pump (Alcatel Annecy 2008A) to evacuate the VC from the NCGs and set the pressure at  $\sim 7$  KPa. This pump was connected to the VC via a copper tube through the gasket with an on-off valve and a precise flow-control valve connected in series. The on-off valve was located right before the VC and a vacuum gauge was connected between the two valves to control the pressure during the evacuation stage. Also, a  $12\text{ cm} \times 12\text{ cm}$  electrical fan (Sunon, SP101A, 115 V, 0.21 A) was placed near the aluminum heat sink to remove the heat in the lateral direction, as shown in Figure 27.

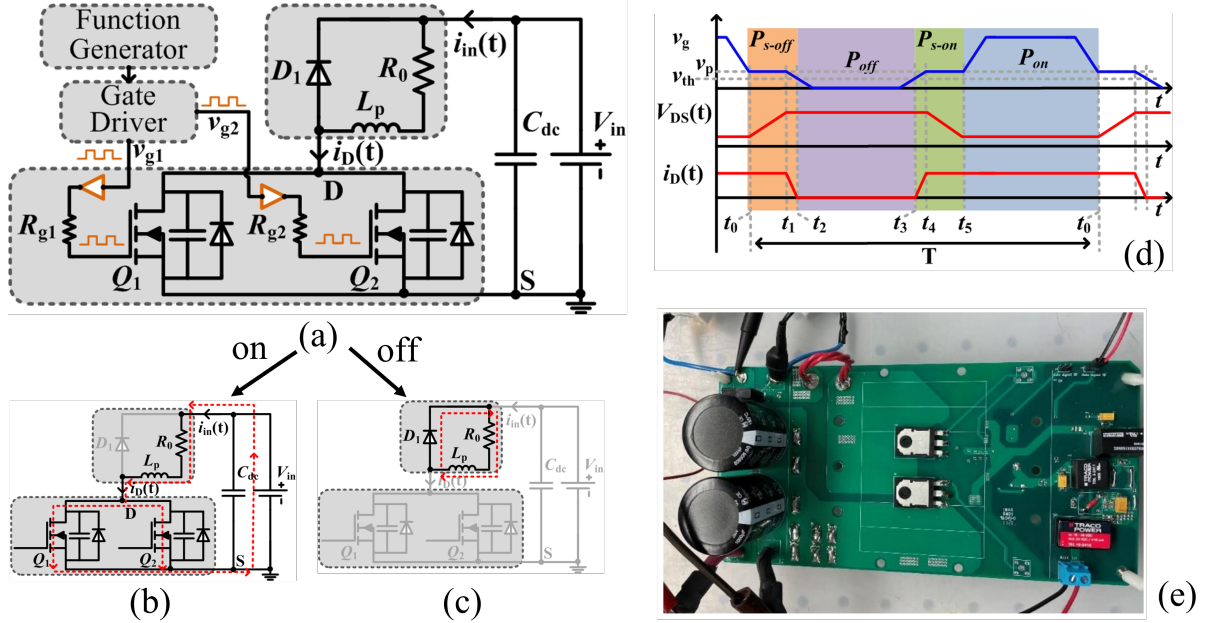


Figure 28: (a) Detailed circuitry used as controllable heat source. (b)  $Q_1$  and  $Q_2$  are on. (c)  $Q_1$  and  $Q_2$  are off. (d) Simplified gate signal and loss generation mechanism. (e) Photograph of the assembled experimental prototype.

### 5.2.1 Power Electronics Design and Thermal Cooling

Figure 28(a) illustrates the detailed circuitry used here as a controllable heat source; the circuitry is modified from the standardized double pulse test circuit typically employed in Power Electronics. An experimental prototype of the circuitry was implemented, as shown in Figure 28(e), to demonstrate the efficacy of the proposed cooling system. The experimental settings and equipment used are tabulated in Table VI. The circuitry mainly consists of a DC power supply ( $V_{in}$ ), a DC-link capacitor ( $C_{dc}$ ), the fixed resistive load ( $R_0$ ), a freewheeling diode ( $D_1$ ), semiconductor devices ( $Q_1$  and  $Q_2$ ), a gate driver and a function generator. The number

of semiconductor devices in parallel can be expanded to enlarge heat generation capability. The function generator launches digital signals that are amplified by the gate driver circuit to the voltage level suitable for triggering semiconductor devices in parallel. Upon receiving the amplified gate signals, the semiconductor devices are turned on and off separately through gate resistors ( $R_{g1}$  and  $R_{g2}$ ). This design enables flexible control on the amount of generated heat.

#### **5.2.1.1 Circuitry Operation**

The current from the DC power supply flows through load  $R_0$  and the semiconductor devices when any of  $Q_1$  and  $Q_2$  is on, as shown in Figure 28(b). However, when both power devices  $Q_1$  and  $Q_2$  are turned off, then, no energy is extracted from the power supply and the current is stored inside the parasitic inductor  $L_p$ , freewheels through diode  $D_1$  and gradually dissipates the magnetic energy by load resistor  $R_0$ , as illustrated in Figure 28(c). The turn-on loss, turn-off loss and conducting loss are generated as semiconductor devices are periodically turned on and off. Those electrical losses are further converted into heat. Without proper and sufficient cooling, the device temperature will exceed the maximum tolerable limitation ( $\sim 120^\circ\text{C}$ ) and lead to permanent damage.

#### **5.2.1.2 Loss (Heat) Generation Mechanism**

To elaborate on the loss generation mechanism, the simplified turn-on and turn-off transients together with on/off of the semiconductor devices over one switching period ( $T$ ) are shown in Figure 28(d). The voltage across drain and source of  $Q_1$  and  $Q_2$  is denoted as  $V_{DS}$  and it starts to increase whenever the gate voltage decreases to plateau level  $V_p$ , as indicated from  $t_0$  to  $t_1$ . After that, the device current  $i_D$  decreases to zero when the gate voltage is reduced to

TABLE VI: Experimental settings and equipment.

Name	Value
$f_s$	100 kHz
$R_0$	3 $\Omega$
$v_{g1}$ and $v_{g2}$	15 V
$Q_1$ and $Q_2$	STFW4N150
DC Supply	HY10010EX
Auxiliary Supply	Agilent E3646A
Function Generator	Wavetek Model 395

the threshold level  $V_{th}$ , between  $t_1$  and  $t_2$ . The device is fully turned off between  $t_2$  and  $t_3$ , and the loss ( $P_{off}$ ) within this period is negligible. The time interval between  $t_3$  and  $t_5$  follows the reverse process from  $t_0$  to  $t_1$ . Both time intervals induce significant loss (denoted as  $P_{s-off}$  and  $P_{s-on}$ ) due to large overlap between  $V_{DS}$  and  $i_D$ . It is worth mentioning that the induced loss can be further controlled by varying the switching frequency  $f_s$  and gate resistances  $R_{g1}$  and  $R_{g2}$ . The time interval between  $t_5$  and  $t_0$  represents the device conduction period and usually does not induce much loss ( $P_{on}$ ) due to low on-state resistance of up-to-date devices. However, the dated Si-based MOSFETs of TO-247-3 package (each 25 mm x 16 mm x 5 mm total dimension including terminals, 1.55 cm<sup>2</sup> effective heat dissipation area) with typical 5  $\Omega$  on-state resistance is intentionally selected here to generate considerable loss, and thus, emulate high-power application cases with a low-power and low-cost experimental setup.

Nowadays, Si-based semiconductor devices of different packaging are widely manufactured and used in both industry and academia due to their many merits, such as low cost, high

reliability and availability, and adequate supportive circuits. The TO-247-3 package is one of the most common Si-based MOSFETs; this type of package is usually used for relative low power applications due to thermal constraints posted on it. The losses generated from device switching events heat up the device and the loss becomes larger as the switching frequency or system power level increases. Consequently, it is hard for the semiconductor device of the TO-247-3 package to handle the generated heat under such circumstance without proper cooling. The conventional heat sink with forced air cooling is bulky with limited cooling performance, therefore, the hybrid VC-based cooling is proposed here as a novel and advanced cooling method for high power application in the area of Power Electronics that requires efficient cooling.

### **5.2.2 Wick-lined Evaporator**

Figure 29(a) shows a photograph of the evaporator used in this study. The evaporator is made of a 114.3 mm  $\times$  63.5 mm  $\times$  2 mm conductive 101 copper plate (thermal conductivity 390.88 W/m.K, McMaster-Carr). A 1 mm deep trench-cut was milled around the MOSFETs on the back of the plate to minimize the lateral conduction through the copper plate ( Figure 30(a)). Therefore, the thickness of the evaporator plate at this point was reduced to 1 mm. Two 31.75  $\times$  1 mm  $\times$  1 mm grooves were milled onto the copper plate to accommodate the thermocouples. To fabricate the wick structure, a 1 mm thick copper frame (with uniform 6.35 mm width) was placed on the evaporator plate and filled with a fine copper powder (35-40  $\mu$ m, 90% purity, Metal Powder USA). Then, the frame was removed and the sample was transferred to a single-zone tube furnace (Lindberg, Blue-M-HTF55322c) where the copper powder was sintered at

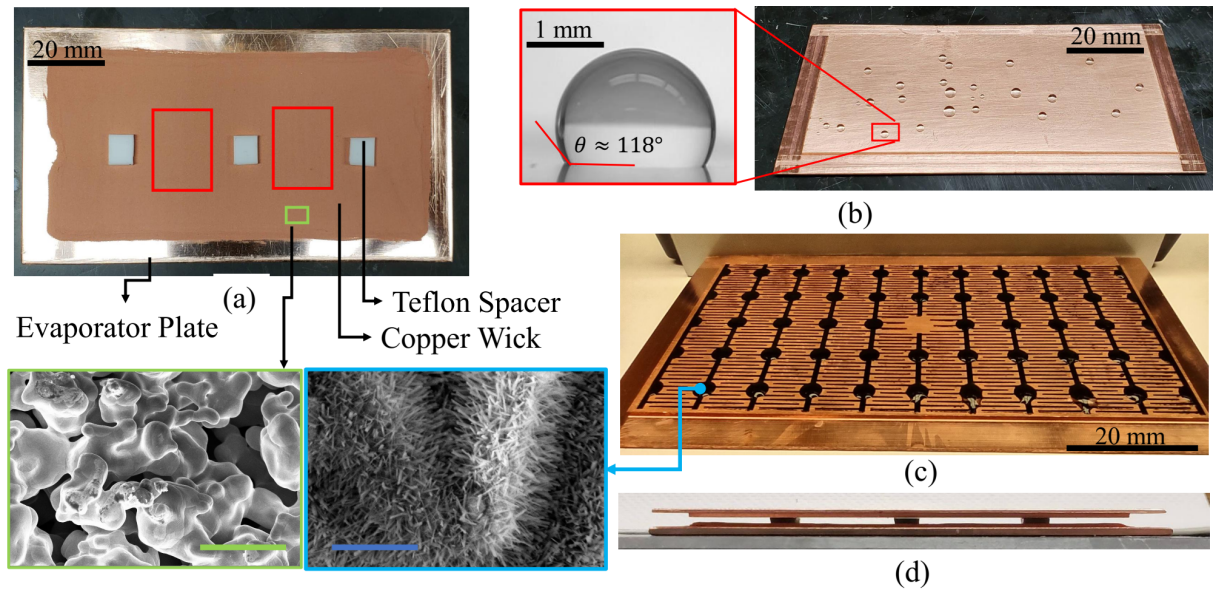


Figure 29: (a) Fabricated evaporator plate with elevated sintered copper powder layer on top and 3 Teflon spacers. The two red boxes indicate the MOSFET positions under the plate. (b) Fabricated uniform hydrophobic condenser plate. (c) Fabricated wettability-patterned condenser plate with wet superhydrophilic domains for contrast. Black and copper indicate superhydrophilic and hydrophobic domains, respectively. (d) Side view of the VC assembly without the sealing gasket. Bottom left: SEM images of the sintered copper powder and the superhydrophilic region of the wettability-patterned condenser. Green and blue scale bar denote 10  $\mu\text{m}$  and 1  $\mu\text{m}$ , respectively.

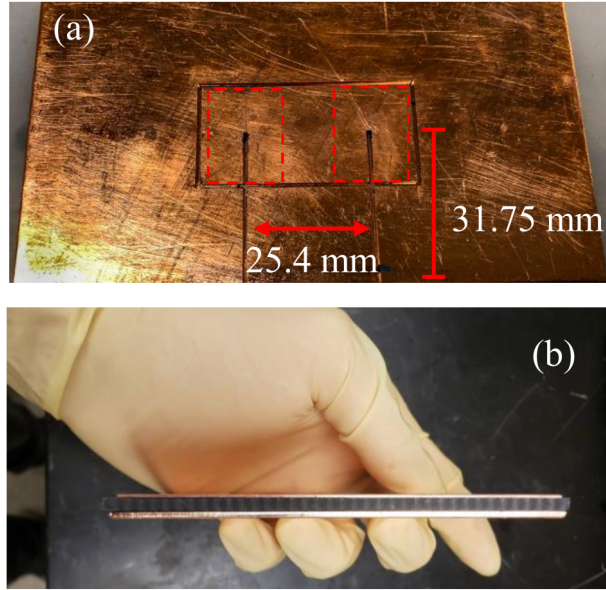


Figure 30: a) Back of the evaporator plate showing a 1 mm deep trench around the MOSFETs and 2 thermocouple grooves. The dashed lines indicate the approximate position of the MOSFETs. b) Side view of the assembled VC.

a temperature of  $950^{\circ}\text{C}$  for 15 min in a controlled atmosphere in Hydrogen and Argon. SEM images of the sintered copper powder microstructure are shown at bottom left of Figure 29.

### 5.2.3 Wickless Plate

Figure 29(b) and (c) show photographs of the condensers used in this study. The condenser plate is made of a  $114.3\text{ mm} \times 63.5\text{ mm} \times 2\text{ mm}$  conductive 101 copper plate (thermal conductivity  $390.88\text{ W/m.K}$ , McMaster-Carr). A  $6.35\text{ mm}$  wide and  $1\text{ mm}$  deep rim was milled out from the plate border to place the gasket and also provide the essential interior gap for the VC. To prepare a hydrophobic condenser, Teflon AF (AF 2400, Amorphous Fluoroplastics Solution, Chemours Co.) solution was spin coated on the plate (2000 rpm for 20 s, WS-400-6NPP-



LITE Spin Processor) and then cured in the aforementioned furnace in the following stages: 80 °C, 240 °C, and 330 °C for 10 minute intervals. The cured Teflon layer has a thickness below 100nm (493) and renders a hydrophobic surface (CA  $\sim$  118°). For the wettability-patterned condenser ( Figure 29c), a fiber-laser marking system (EMS400, TYKMAElectrox®), 40% power, 20 kHz frequency, 200 mm/s traverse speed) was employed to selectively remove the Teflon layer alongside a thin copper layer, resulting in shallow superhydrophilic etched domains as shown in the contact profilometry images in Appendix C (Figure 50 and Figure 51). Next, a chemical etching approach was used to passivate the etched domains. In this process the plate was immersed in an aqueous solution of 2.5 mol/L sodium hydroxide and 0.1 mol/L ammonium persulfate (Alfa Aesar) at room temperature for 6 min. This process grew copper hydroxide nano hairs on the laser-etched domains, creating a nanostructured surface (503) with water contact angle of  $\sim$  0°, while the Teflon-coated mirror-finish regions retained their hydrophobicity with contact angle of  $\sim$  118°. Figure 29(c) shows the final biphilic condenser and the SEM photos of the nanostructures on the superhydrophilic domains. This technique created a wettability-patterned surface with superhydrophilic regions laid on a hydrophobic background.

#### 5.2.4 Gasket

To seal the device during the experiment and provide the required interior gap between evaporator and condenser plates, as shown in Figure 27 and Figure 30(b), a 3.175 mm thick and 6.35 mm wide gasket sheet (Viton® Fluoroelastomer Rubber Sheet Chemical-Resistant, McMaster-Carr) was placed on the borders of the device. Two identical holes, each 1.5 mm in diameter, were made into two opposite sides of the gasket to accommodate the evacuation and

charging ports. Two 1.64 mm OD and 60 mm-long copper tubes connected to a syringe filled with DI water and the vacuum pump, respectively, were press-fitted into these holes. The gasket in addition to three 5 mm x 5 mm x 1 mm Teflon pieces ( Figure 29(a)) maintained a fixed distance between the two plates, creating the 1 mm-wide vapor space needed for implementing the thermal cycle. Teflon was chosen for the spacers to minimize the conduction heat transfer across the device.

### 5.2.5 Experimental Procedure

After assembling the device and clamping it via the torque screwdriver, the device was evacuated. Next, the vacuum line was closed and a designated amount of DI water was charged into the device through the charging port. Next, the device was preheated to 50 °C for 20 minutes to release any dissolved NCGs from the DI water. This process was shown to be adequate for ridding the device of NCGs (493; 458; 329). After that, the device was set back to room temperature and was ready for the final tests. Next, a step-wise heating protocol was performed. Due to the low heat removal capability by the heat sink, the device reached steady-state in 9 minutes and the last 60 seconds from this point were used for the analysis. Two shut-down criteria were implemented in this study; the first was when the measured temperatures of the MOSFETs ( $T_h^1$  and  $T_h^2$ ) reached 100°C, while the second one was when the device reached a dry-out state, which was indicated by a sharp increase in the above temperatures.

## 5.2.6 Performance Metrics and Error Analysis

### 5.2.6.1 Metrics

The heat input was calculated as

$$Q = VI - R_0 I^2 \quad (5.1)$$

where  $V$  is the input DC voltage,  $R_0$  the  $3\ \Omega$  resistive load, and  $I$  the input current.

The thermal resistance of the device was calculated by

$$R_{VC} = \frac{\Delta T}{Q} \quad (5.2)$$

where, based on Figure 27,

$$\Delta T = T_h - T_c = \frac{T_h^1 + T_h^2}{2} - \frac{T_c^1 + T_c^2 + T_c^3 + T_c^4}{4} \quad (5.3)$$

To account for the occupied space with the working fluid in the VC, the charging ratio (CR) is as follows

$$CR = \frac{\text{Liquid volume}}{\text{Available free space}} \quad (5.4)$$

In this study three CRs were tested; 25% (CR1), 35% (CR2), and 45% (CR3).

### 5.2.6.2 Error Propagation

To determine experimental errors, a Gaussian error propagation rule (493; 458) was performed on each metric as follows

$$\Sigma_{\phi} = \sqrt{\left(\frac{\partial \phi}{\partial \alpha}\right)^2 \sigma_{\alpha}^2 + \left(\frac{\partial \phi}{\partial \beta}\right)^2 \sigma_{\beta}^2 + \dots} \quad (5.5)$$

where  $\phi$  is a defined metric, which is a function of  $\alpha, \beta$ , etc. The standard deviation of each variable  $x$  is calculated by

$$\sigma_x = \sqrt{\sigma_x^{2\text{exp}} + \sigma_x^{2\text{instr}}} \quad (5.6)$$

with  $\sigma_x^{\text{exp}}$  and  $\sigma_x^{\text{instr}}$  being the standard deviation of the experimental measurements and instrument accuracy for each variable ( $V, I, T_h, T_c$ ), respectively. The latter is considered constant for each instrument, while the values for  $\sigma_I^{\text{instr}}$ ,  $\sigma_V^{\text{instr}}$ , and  $\sigma_T^{\text{instr}}$  were 0.005  $\Omega$ , 0.005 V, and 0.25 K, respectively. For each case, two runs were performed and the final error was calculated by

$$\Sigma_{\bar{\phi}} = \frac{\Sigma_{\phi}}{\sqrt{2}} \quad (5.7)$$

Considering  $Q = f(V, I)$ , the heat input error can be found as

$$\Sigma_Q = \sqrt{\left(\frac{\partial Q}{\partial V}\right)^2 \sigma_V^2 + \left(\frac{\partial Q}{\partial I}\right)^2 \sigma_I^2} \quad (5.8)$$

Also, since  $R_{VC} = R_{VC}(T_h, T_c, V, I)$ , the thermal resistance error can be calculated by

$$\Sigma_{R_{VC}} = \sqrt{\left(\frac{\partial R_{VC}}{\partial V}\right)^2 \sigma_V^2 + \left(\frac{\partial R_{VC}}{\partial I}\right)^2 \sigma_I^2 + \left(\frac{\partial R_{VC}}{\partial T_h}\right)^2 \sigma_{T_h}^2 + \left(\frac{\partial R_{VC}}{\partial T_c}\right)^2 \sigma_{T_c}^2} \quad (5.9)$$

### 5.3 Results and Discussion

The working principle in this study follows prior work (493; 329). As shown in Figure 31, the wettability pattern consists of an interdigitated design in which superhydrophilic wedge-shape tracks are spaced 1 mm apart and connected to a main stem, which features a large circular area along its path. As shown earlier (362; 363), the pattern of Figure 31(b) can enhance the condensation heat transfer by controlling the maximum condensate diameter on the DWC (hydrophobic) regions (by fixing the spacing between superhydrophilic wedge-shape tracks, 1 mm in this study) in addition to enhancing condensate removal and drainage. The enhanced drainage originates from liquid curvature difference (and thus capillary pressure) along the wedge-shape tracks, due to their diverging angle, which enables a high transport and pumping velocity  $O(10 \text{ cm/s})$  from the narrow towards the wider end of the track (16).

In an operational mode, as soon as the pattern is exposed to vapor, a film covers the superhydrophilic regions, whilst dropwise condensation takes place on the DWC (hydrophobic) domains. The condensate droplets on the DWC region grow either by further condensation or coalescence and, after getting large enough ( $D > 1 \text{ mm}$ ), they touch the superhydrophilic (FWC) regions and, again due to capillary action, are quickly drained to provide a fresh surface for renewed condensation. The FWC domains possess a unique quality due to having low curvature

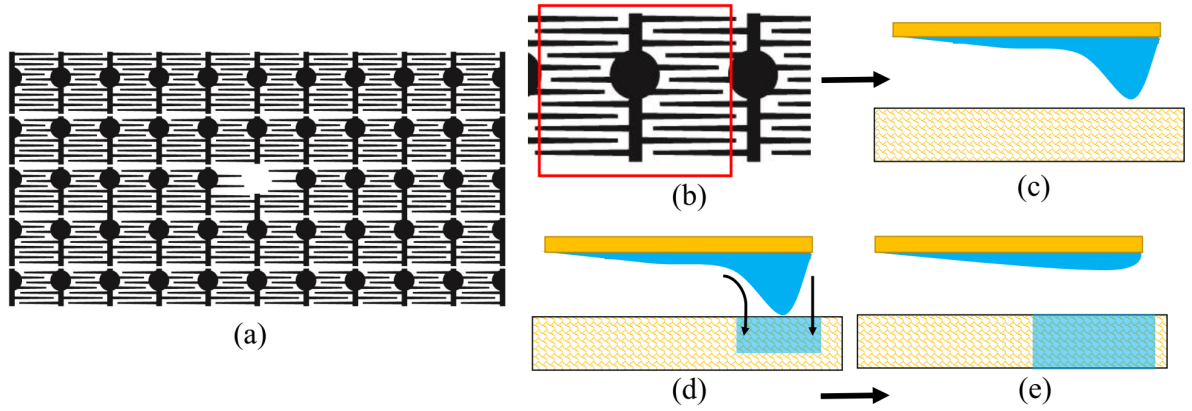
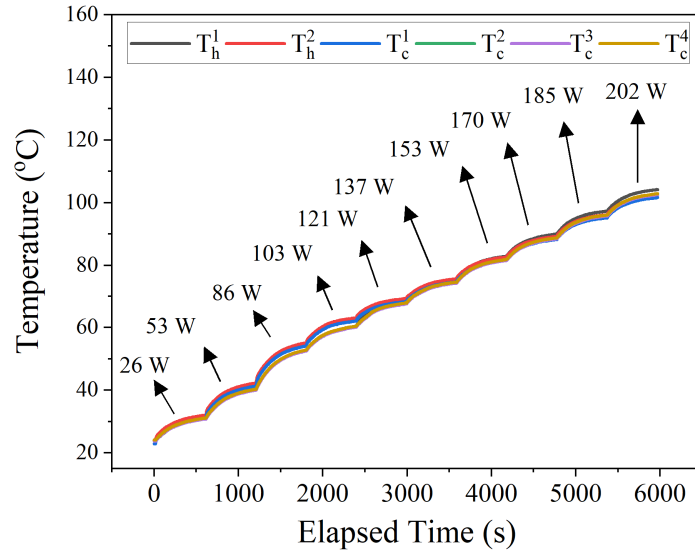
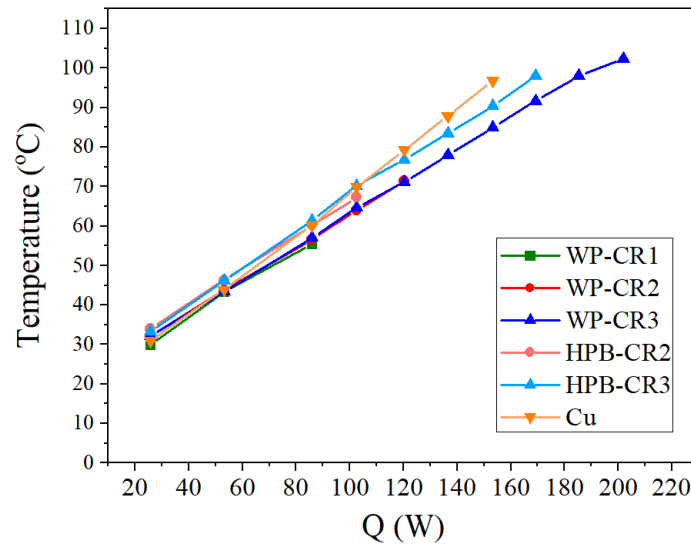


Figure 31: (a) Wettability pattern used in this study (black: superhydrophilic; white: hydrophobic). (b) A single unit of the pattern with a low pressure site. (c) Growing bulge facing the wick. (d) The bulge eventually touches the wick structure and forms a capillary bridge. (e) Fluid drainage after snapping of the capillary bridge.

circular domains, in which by creating a low-pressure site, can naturally collect the condensate at the designated points by capillary action. As more vapor gets condensed, a bulge starts to grow at these low-pressure sites (Figure 31(c)) and after growing large enough, reaches the wick on the other side of the device (Figure 31(d)). At this point, a capillary bridge is formed and the liquid bulge is transferred to the wick-lined evaporator due to capillary pressure difference. This capillary bridge is eventually fully drained and snaps due to loss of liquid (Figure 31(e)). The liquid is transferred back to restart the thermal cycle. The capillary bridge frequency of formation/snapping is a critical part of the thermodynamic cycle of the device and is a function of the wettability pattern, the interior-gap distance, charging ratio, and the heat load.



(a)



(b)

Figure 32: a) Raw thermocouple measurements vs. heating power over elapsed time for a WP-VC, (b) temperature rise of the MOSFETs as heating input increases for all VCs and the copper plate.

### 5.3.1 Results

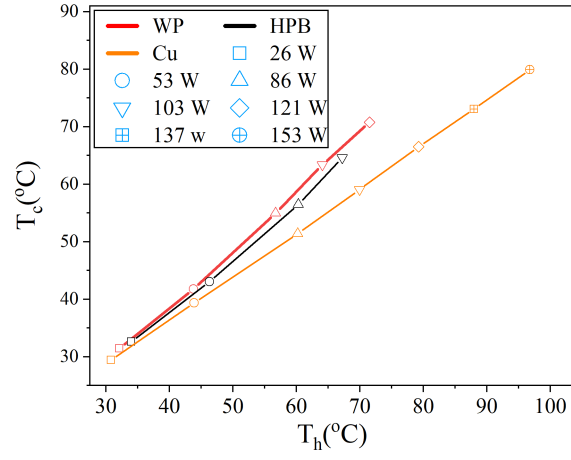
Figure 32(a) showcases the temperature rise of the best performing vapor chamber with a wettability-patterned condenser (VC-WP) at CR3 as the heating input increases up to 202 W. As seen, when the heating input increases, all temperatures rise in sync with small differences, hinting to a small thermal resistance. A larger temperature-rise slope is seen up to 86 W followed by a lower rise slope at each step from 86 W to 202 W. At low heat fluxes, conduction heat transfer through the wick and liquid bulk, which imposes a high thermal resistance, prevails and thin-film evaporation from the top of the wick structure is initiated. By increasing the heat load, the liquid meniscus recedes into the wick and gradually the conduction thermal resistance declines (504). Moreover, close temperatures on the condenser side point out to the temperature uniformity and heat spreading capability of the current device. In this case, the device removed 202 W without dry-out, while keeping the MOSFETs below 105 °C. Figure 32(b) shows the average temperature of the MOSFETs for all cases in this study. For benchmarking purposes, a copper plate with the exact dimension of the VC was used to provide a better insight on the VC's performance. As seen, the copper plate reached 97°C at 153 W where the experiment was shut down to protect the MOSFETs from overheating. The copper plate shows competitive performance to both VCs at low heat loads. This was expected since conduction at low heat loads and with a large surface area (50 cm<sup>2</sup>) is able to remove the heat efficiently. However, as the heat flux increased, the discrepancy between the copper plate and the VCs was magnified. Temperatures of the MOSFETs for the copper plate started to rise above the vapor chamber with hydrophobic condenser (HPB-VC) with CR2 and CR3 at 103 W and 137 W, respectively.



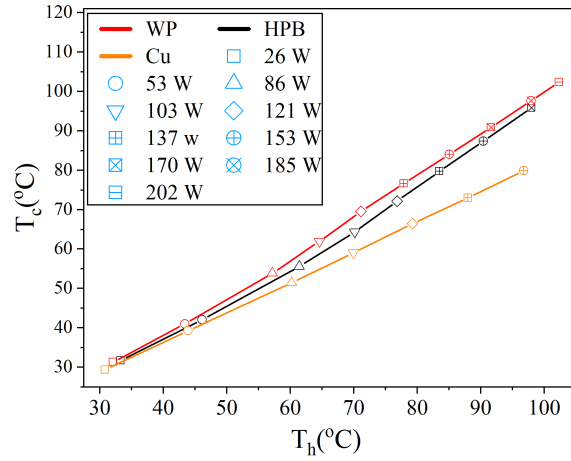
While the overall differences are small, the copper plate reached 8 °C above HPB-VC (91°C) at 153 W. Compared to the VC-WP, the copper plate shows a higher MOSFET temperature after 53 W. This shows that the WP-VC has good heat dissipation capability even at lower heat fluxes. By increasing the heat input, the copper plate at its maximum heat input, has 15 °C higher temperature compared to the WP-VC (82°C).

Figure 32(b) also shows the role of the charging ratio on each device's performance. As seen, the HPB-VC and WP-VC at two and three charging ratios tested in this study show identical temperature rise, pointing to the VC's robustness. However, the WP-VC holds a lower temperature at each charging ratio compared to the HPB-VC. This is a result of a uniform and controlled distribution of the condensation on the condenser, which in turn, provides a uniform and continuous supply of working liquid to the heating zones. The structured liquid circulation by the WP condenser avoids random blockage on the heated areas as opposed to the VC-HPB, where random condensation and pooling on the surface would cause higher resistance to the vapor passage by reducing the internal vapor space, which imposes higher evaporation resistance at the evaporator (191; 505), and as a result, higher temperatures of the heaters.

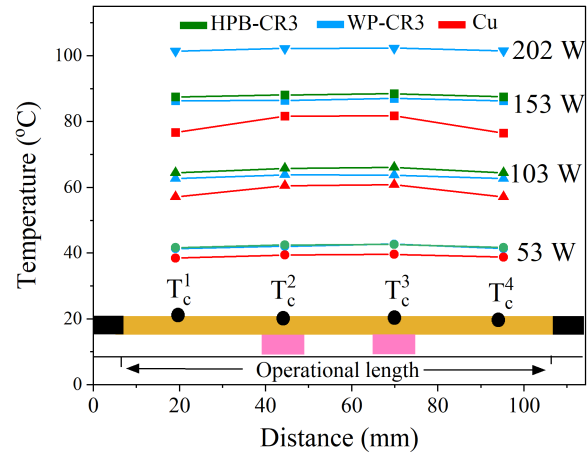
In a multi-phase closed system where evaporation, boiling, condensation, and liquid transfer are taking place simultaneously, deciphering the role of each element is a complicated task. However, one way to demonstrate the differences is to compare the temperature on the cooled side of the system ( $T_c^{avg}$ ) at the same heater temperature ( $T_h^{avg}$ ). Figure 33(a) and 33(b) present the average condenser temperature ( $T_c^{avg}$ ) as a function of heater temperature ( $T_h^{avg}$ ) at each heat input for both VCs at CR2 and CR3 in addition to the copper plate. As seen,



(a)



(b)



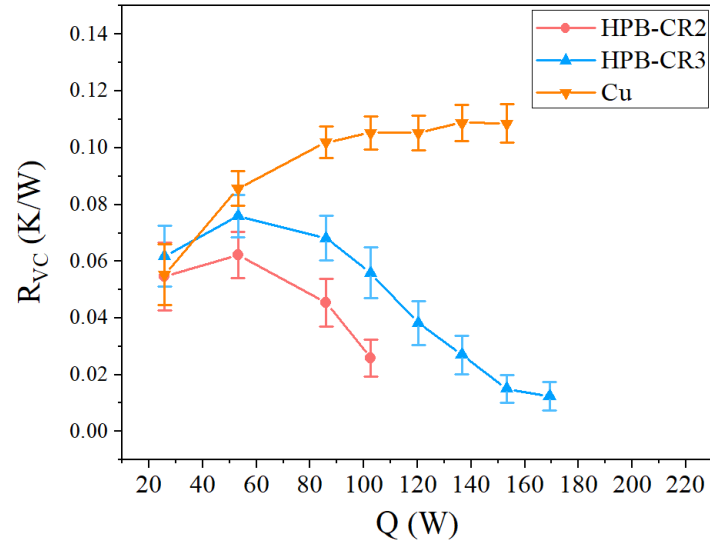
(c)

Figure 33: Temperature rise of the condenser plate vs. MOSFET temperature as heating input increases for the copper plate and two VCs with charge ratio CR2 (a), and CR3 (b). Similar markers indicate same heat input. c) Spatial condenser temperature distributions at four heating inputs.

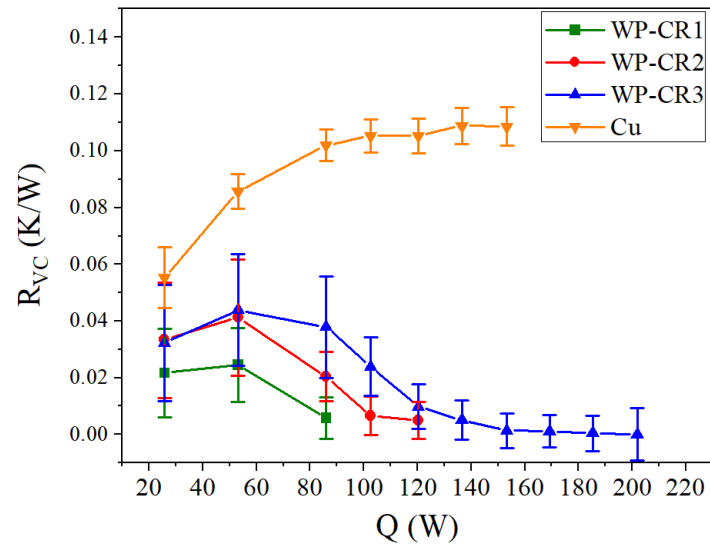
there is a minimal  $T_c^{\text{avg}}$  difference between HPB-VC and WP-VC at a  $T_h^{\text{avg}}$  for both charging ratios. However, for both CR2 and CR3, at the same  $T_h^{\text{avg}}$ , the HPB condenser shows a lower average temperature compared to the WP one, which is consistent with having lower heat transfer rate compared to the WP condenser (458; 323; 362). Nevertheless, due to the convection cooling method, the overall high working temperature of the device has minimized the differences between the two VC cases. Moreover, the copper plate for all cases shows a lower average cooled side temperature at a similar average heaters' temperature. This is expected since conduction is the main heat transfer mechanism, i.e. higher thermal resistance, as compared to two-phase (convection) heat transfer (494). To further compare the VCs' versus copper plate's performance, Figure 33(c) shows spatial temperature distribution on the cooled side for four heat inputs. As seen, the VCs have a great temperature uniformity along the condenser. However, the copper plate shows overall lower temperatures and has an almost uniform temperature on the cooled side at the low heat inputs while, by increasing the heat load, temperatures above the MOSFETs ( $T_c^2$  and  $T_c^3$ ) increase more and create a non-uniform temperature profile along the heat sink due to the inefficiency of the pure conduction to spread the heat laterally, as reported before (249). As established in the literature (258; 506; 308; 507; 326; 508; 509), having a low heat removal rate (i.e., natural convection vs. liquid cooled plate) naturally creates a more uniform temperature profile on the condenser side, albeit with a higher temperature for the same heat input. That said, even though in this study a forced convection method is used for the cooling method, having an aluminum plate without a finned structure reduces the heat removal rate and as a result, the system operates in higher temperature and is

prone to having a more uniform temperature on the condenser side. Furthermore, having two heat sources, with a relatively large surface area compared to the VC's heat dissipation area, enhances the heat dissipation and temperature uniformity along the heat sink too. Considering the above, the copper plate forms a non-uniform profile at the higher heat fluxes, highlighting the effectiveness of the VCs' thermal performance.

Figure 34(a) and 34(b) show the thermal resistance variation of HPB-VC and WP-VC versus heat input, respectively. For clarity, each device is compared to the copper plate and shown separately. As seen, both HPB-VC and WP-VC show a typical characteristic of a vapor chamber where the thermal resistance declines with rising heat load, as opposed to the copper plate whose thermal resistance increases and reaches a plateau. Also, each VC with lower CR shows a lower thermal resistance at the same heat load; when the amount of working liquid increases in the device, conduction heat transfer plays a greater role and hence, causes higher thermal resistance for the device. However, as the heat input increases this effect is minimized. On the other hand, having more working liquid delays the dry-out or critical heat flux, enabling the device to reach higher heat fluxes and operate more efficiently. This trend is consistent for both VCs, although the WP-VC overall has a lower average thermal resistance at each charging ratio and the same heat input. At CR2, the HPB-VC reaches dry-out at 103 W with thermal resistance of  $0.025 \pm 0.0065$  K/W, while the WP-VC tolerates 121 W with thermal resistance of  $0.0049 \pm 0.0061$  K/W. The WP-VC is able to tolerate even higher heat loads due to the wettability-patterned condenser's role, which can consistently return the working fluid to the wick structure in an organized fashion. This is observed for CR3, where



(a)



(b)

Figure 34: Comparison of copper plate thermal resistance with a) HPB-VC, and b) WP-VC at different charging ratios and several heat loads.

the HPB-VC dries-out at 170 W with thermal resistance of  $0.012 \pm 0.005$  K/W, as opposed to the WP-VC which could reach 202 W without dry-out at thermal resistance of  $0.001 \pm 0.009$  K/W. At that point, the test was terminated because the MOSFETs reached  $> 100^\circ\text{C}$ . The overall low thermal resistance shows the VCs' greater thermal performance, which is consistent with prior studies (326; 284; 508; 509; 510), where natural or forced convection was the primary cooling technique.

#### **5.4 Conclusion**

In this study, a hybrid vapor chamber consisting of a wick-lined evaporator and wettability-engineered condenser was fabricated and investigated. The vapor chamber was designed for cooling two high-power MOSFETs on a custom-made PCB. This VC is the first apparatus applying wettability-patterning technique to manage more than one heat sources, simultaneously. A fan-cooling approach with a simple aluminum plate heat sink was chosen to provide a comprehensive image of the VC's performance under lower heat removal conditions. Two condenser types, hydrophobic and wettability-patterned, were implemented in the VC and the thermal performances were compared with that of a solid copper plate. For different charging ratios tested for HPB-VC and WP-VC, the devices showed a consistent and repeatable thermal performance. It was shown that larger charge ratios lead to a larger critical heat flux but lower thermal resistance. The WP-VC was shown to have an overall lower thermal resistance compared to the HPB-VC at the same charge ratio and heating input. Minimum thermal resistance of  $< \sim 0.01$  K/W was recorded for the WP-VC. A maximum heat load of 202 W, among all cases, was removed by the WP-VC while keeping the MOSFETs  $< 105^\circ\text{C}$ . The low thermal resistance

values originate from the low heat removal cooling approach (fan cooling) in addition to low VC-to-heaters' area ratio. Further tests with a liquid-cooling method and a thinner device with lower heater-to-VC heat dissipation area ratio could illuminate the performance differences and efficiency of the current device for high power electronics cooling applications.

## CHAPTER 6

### APPLICATION OF WETTABILITY ENGINEERING IN THERMAL MANAGEMENT; A HYBRID HEAT PIPE

*"This chapter is reprinted with permission from M. Jafari Gukeh, G. Damoulakis, and C. M. Megaridis. Low-profile heat pipe consisting of wick-lined and non-adiabatic wickless wettability-patterned surfaces." Applied Thermal Engineering 211 (2022): 118433." (see Appendix E)*

#### 6.1 Background and Motivation

Recent technological developments in computers and communications equipment have resulted in miniaturized sizes, high-power, and high-heat flux integrated circuits (ICs) with heat-extraction demands that outrun traditional approaches (511). One of the most interesting and trustworthy technologies that are commonly used to transfer heat from localized areas in different heat-extracting cases are Heat Pipes (HPs) (512). The most significant advantages of HPs are their high effective thermal conductivity and heat-dissipation capabilities, which are paired with geometrical flexibility. Heat pipes generally feature an evaporation section, an adiabatic section, and a condensation section. The heat from the source is absorbed by the working fluid, which changes phase in the evaporator section of a typical thermal cycle. The vapor then passes via the adiabatic section to the distant condensation zone, where it condenses and releases its



latent heat. Further, this condensed liquid is drawn back to the evaporator by capillary action, thus completing the thermal cycle and perpetuating the process. Flat or low-profile HPs, the forefathers of the vapor-chamber systems, are the latest generation of heat pipes that have been employed to assist in the thermal management of high-power electronic components, such as automotive LED lighting, GPUs, and high-performance PC components throughout the previous two decade (513; 514; 515; 516; 517; 518; 519).

Heat pipes are distinguished by their thermal resistance, power dissipation capabilities, and dry-out tolerance. The capillary wick structure governs the evaporator section, which has the largest influence on the system's performance. The evaporation resistance, which accounts for a significant portion of the heat pipe's thermal resistance, is controlled by factors such as heat load, wick porosity, permeability, and thickness, as well as the kind and amount of working fluid. Conduction and convection dominate heat transmission at low heat fluxes, whereas evaporation occurs from capillary menisci at the solid–liquid interface on the copper wick. Evaporation becomes more vigorous as the heat flux increases, and the menisci withdraw into the wick (516; 519). An increase in heat flow may lead in nucleate boiling around the heated part (520; 521).

Wicks are essential on the evaporator side, but they have their own drawbacks. Fine-wick structures are widely recognized for having decreased evaporation resistance due to their extremely small pore sizes, but they also have large hydraulic losses (pressure drop) (522). In a flat HP, where the liquid has to travel distances of 10 cm or more, the hydraulic loss can be significant, posing a major hurdle when handling high heat fluxes that require continuous

resupply of the heating spot from the condensation section (522; 523). Researchers have tried to overcome this issue via incorporating different wick pore sizes over the heat source, where the maximum heat transfer occurs, than the rest of the heat pipe. Pounds and Bonner (517) utilized a well-engineered wick structure with thick axial feeder wick and a thin, fine pore mono-layer wick near the heater that can reduce the evaporation thermal resistance, in turn lowering the total thermal resistance of the system by 45% for a typical metal core PCB. Tang et al (524) incorporated a graded wick structure in a cylindrical heat pipe that outperformed a heat pipe with homogeneous wick when placed at different orientations. It was shown that increasing the thickness of the coarse wick can significantly improve the heat transfer capacity of the heat pipe. North (525) showed numerically that an axially variable wick had optimal performance when the pore size of the evaporator wick was almost 100 times smaller than the pore size on the condenser.

A common method to evaluate heat pipe performance, particularly with flat heat pipes, relies on insulating the entire device except the heating and cooling surface area (522; 523; 526; 527; 528; 529; 530; 346; 531). But under real-world conditions (532; 533; 534; 535; 536; 537; 538; 539) either side of the condensation section could be exposed to a heat sink. For example, in an active cooling method, such as with a fan or a liquid-cooled plate, the heat is removed from one portion of the condensation section while another portion could be exposed to the ambient medium either actively or passively, thus creating a non-adiabatic condition on the plate. Although this condition might not create a major difference in the performance of some heat pipes, flat heat pipes with a relatively thick vapor space (2–5 mm) could be influenced, thus causing a

non-isothermal condition on the wickless metal plate. The exposure of the condenser to an active/passive heat sink could be used effectively to improve heat removal from the device through engaging the wickless side to the thermal cycle of the HP. Inspired by this scenario, the heat transfer performance of a flat heat pipe with partially insulated wickless plate opposing a wick-lined, locally heated plate is investigated.

There have been numerous studies to enhance performance of heat pipes via different wick structures (522; 540; 259; 264) and the realm of investigating wickless heat pipes has remained unexplored. It has been shown that wettability patterns could offer relief to the wick's high pressure drop problem (493; 323; 329). Through using free surface, wettability-patterned surfaces may transport liquids at high velocity ( $V > 0.1$  m/s) and with minimal pressure loss. They can be manufactured to control droplets on the surface, to increase condensation and collect condensate fluid at precise spots (493; 541; 329).

The flat HP structure in this study was inspired by the vapor chamber system of Koukoravas et al. (493). Under the same premise, the present HP system benefits from a wickless, biphilic wettability-patterned (WP) (541) plate component, which has been shown to enhance the heat transfer coefficient of condensation (541). A wick-lined plate component is on the other side of the system, and between the two plates, there is a vapor space where the device can take advantage of the latent heat of vaporization and condensation of the working fluid. The wickless WP plate could practically control DwC and FwC through its specific wettability pattern. The flat HP uses water as working fluid, an axially graded wick-lined evaporator and a wickless wettability-patterned surface. The heat is added at a localized area at one end of the wick-

lined evaporator, while condensation occurs on remote portions of the wick-lined evaporator as well as on the opposing wickless surface. The specially designed hydrophobic/superhydrophilic wettability patterns on the wickless surface provide a return mechanism for the condensate to the wick-lined plate. This technique enhances the liquid-return flow to the heated area thus decreasing the HP's total thermal resistance.

## **6.2 Materials and Methods**

### **6.2.1 Heat Pipe Design**

Figure 35 shows a detailed schematic of the heat pipe designed and investigated herein. The fabrication process for each component is as follows:

#### **6.2.1.1 Wick-lined Evaporator**

A 110 mm  $\times$  30 mm  $\times$  3 mm conductive 101 copper plate (thermal conductivity 390.88 W/m.K, McMaster-Carr) was used as the evaporator casing. A 100 mm  $\times$  20 mm  $\times$  1 mm pocket was milled onto the copper plate to accommodate the required space for the copper wick. As shown in Figure 35b, a 5 mm gap on the border seated the gasket. As shown in Figure 35a, to reduce lateral conduction through the solid plate, a 1-mm deep channel was created under the evaporator plate near the heater surface. Therefore, the thickness of the evaporator plate at this point was reduced to 1 mm. Two identical holes, each 1.64 mm in diameter, were drilled into the pocket of the evaporator plate to accommodate evacuation and charging ports. Two 1.64 mm OD and 50 mm-long copper tubes were fitted into these holes and sealed with epoxy to avert leakage. Three types of copper wicks were fabricated and evaluated in this study; two uniform and one axially graded. For the uniform porosity cases, the pocket was filled

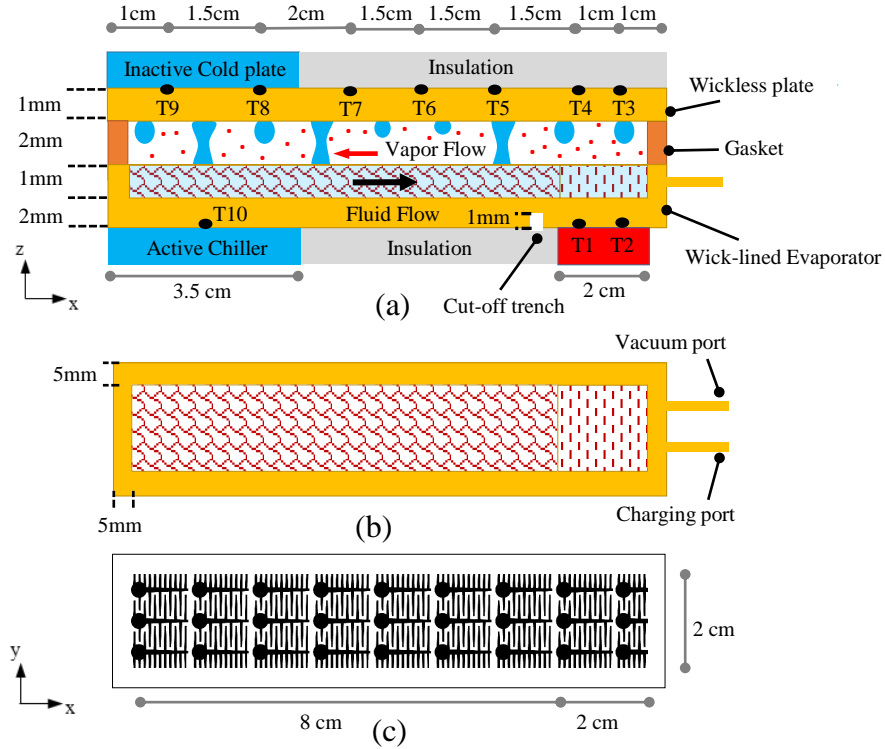


Figure 35: a) Cross section of the heat pipe showing the heater (red), the heat sinks (blue), insulation (grey), the thermocouple positions TX, and thickness of each component (disproportionate scales are used to show detail) b) Top view of the axially graded wick-lined evaporator. c) Top view of the wickless WP surface with superhydrophilic domains (black) laid on a hydrophobic background (white).

with either a fine copper powder size (35–40 m, 90% purity, Metal Powder USA) or a coarse powder size (average 300 m, 90% purity, Chemical Store Inc.). For the axially graded case, an area 20 mm  $\times$  20 mm at one end of the evaporator's pocket was filled with the fine copper powder, while the rest of the pocket was filled with the coarse powder. Finally, and for all cases, the copper powder was sintered at a temperature of 950°C for 15 min in a single-zone tube furnace (Lindberg, Blue-M-HTF55322c) in a controlled atmosphere of Hydrogen and Argon.

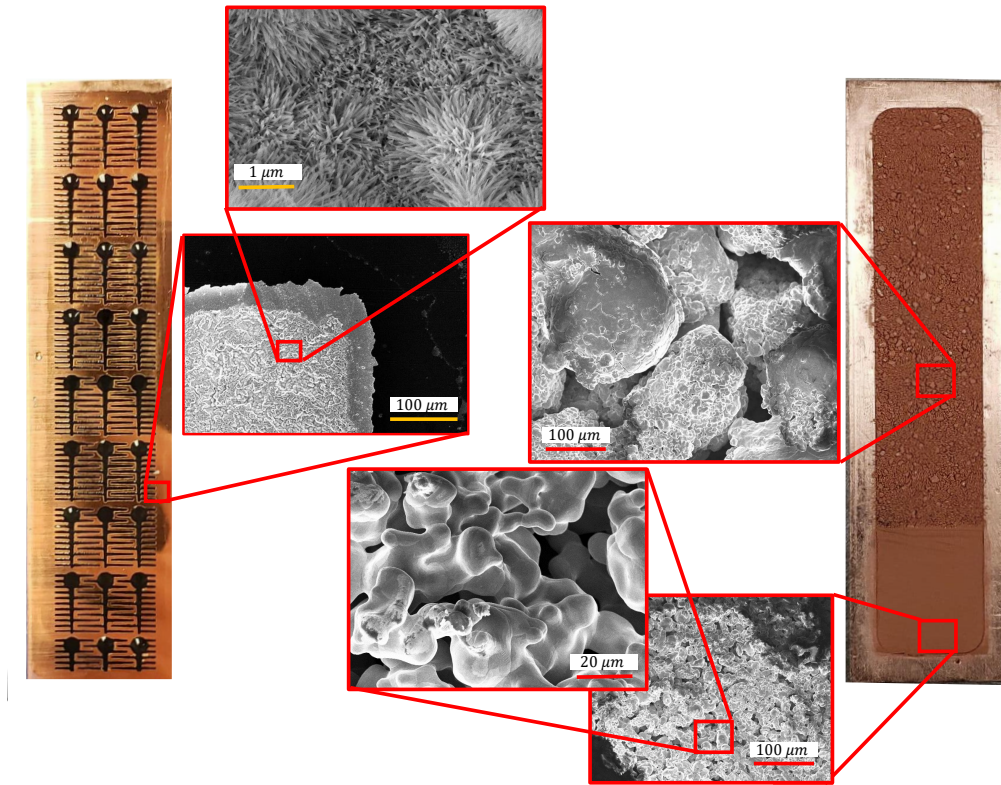


Figure 36: Left: Wickless wettability-patterned plate with partially wetted superhydrophilic regions. Black and copper domains denote superhydrophilic and hydrophobic areas, respectively. Right: Axially graded wick-lined evaporator plate. Middle top to bottom: SEM images of the micro/nanostructure on the laser/chemical-etched domains on the wickless plate, coarse and finer wick structures on the wick-lined plate.

The porosity of the coarse and fine wicks were calculated as 0.55 and 0.33, respectively. The right portion of Figure 36 shows a fabricated axially graded wick-lined plate with corresponding SEM details.

#### 6.2.1.2 Wickless Plate

A 110 mm  $\times$  30 mm  $\times$  1 mm mirror-finished 110 copper plate (thermal conductivity 390.88 W/m.K, McMaster-Carr) with contact angle (CA) of  $\sim 80^\circ$  was used as the wickless side of the heat pipe. Three different wettabilities, including uniform hydrophilic (HPL) (mirror-finish copper), uniform hydrophobic (HPB) copper, and WP wickless copper were tested. To create a hydrophobic surface, the mirror-finish copper plate was spin-coated (2000 rpm for 20 s, WS-400-6NPP-LITE Spin Processor) with Teflon AF (AF 2400, Amorphous Fluoroplastics Solution, Chemours Co.). Afterward, the film was cured in the above mentioned furnace in the following stages: 160°C, 240°C, and 330°C, each stage lasted 10 min, creating a Teflon film with thickness below 100 nm (estimate based on Teflon films applied by spin-coating on a smooth silicon substrate under identical conditions (493)). To create the desired wettability pattern, a laser etching workstation (EMS400, TYKMAElectrox®), with 40traverse speed) was used to selectively remove the Teflon layer, resulting in superhydrophilic etched domains. After that, the plate was submerged in an aqueous solution of 2.5 mol/L sodium hydroxide and 0.1 mol/L ammonium persulfate (Alfa Aesar) at room temperature for 5 min. This process grew nano hairs on the laser-etched domains, rendering a nanostructured surfac (503) with water contact angle of  $< 5^\circ$ , while the Teflon-coated mirror-finish regions retained their hydrophobic property with contact angle of  $\sim 120^\circ$ . This method produced a wettability-patterned surface with superhydrophilic domains laid in a hydrophobic background. Figure 35c shows a fully patterned surface used in this study. The left portion of Figure 36 showcases a wettability-patterned wickless plate with corresponding SEM images of its micro/nano structures.

### 6.2.1.3 Gasket

To seal the device during the experiment, as shown in Figure 35a, a 2-mm thick silicone rubber (Tensile strength: 700 psi, Temperature range: -70 to 260 °C, McMaster-Carr) sheet was placed on the edge borders of the device. The gasket maintained a fixed distance between the two plates, creating the vapor space needed for implementing the thermal cycle. The interior gap between the two plates is maintained by the gasket without any spacers, as the plate deflection caused by the pressure differential is quite low (see appendix D).

### 6.2.2 Experimental Setup

Figure 37 shows a schematic exploded view of the experimental setup. A 40 mm  $\times$  50 mm  $\times$  125 mm Teflon block (rated for temperatures from 350° to 500°F, McMaster-Carr) was used to house the cooling and the heating block, and provided the seating space for the heat pipe. The evaporator plate's adiabatic part was insulated by the Teflon block. A 30 mm  $\times$  125 mm  $\times$  1 mm pocket was created on top of the block to secure the evaporator plate. A 20 mm  $\times$  20 mm  $\times$  40 mm pocket was created to host the heating block on one side. Another 40 mm  $\times$  40 mm  $\times$  12 mm pocket was created inside the Teflon block to provide enough space for the cold plate on the other side. A copper block 20 mm  $\times$  20 mm  $\times$  40 mm (McMaster-Carr) was drilled with two cylindrical holes on the bottom (6.25 mm  $\times$  25 mm) to accommodate two 100 W high-density cartridge heaters (Omega). To maximize the insulation for the heating block, five 1.5-mm thick ultra-high-temperature alumina pieces (conductivity 7 W/m.K, maximum temperature rating 1648°C) were secured between the heating and the Teflon block. A 40 mm  $\times$  40 mm  $\times$  12 mm CPU cooling block (DIYhz) was connected to a chiller (Neslab RTE-110),



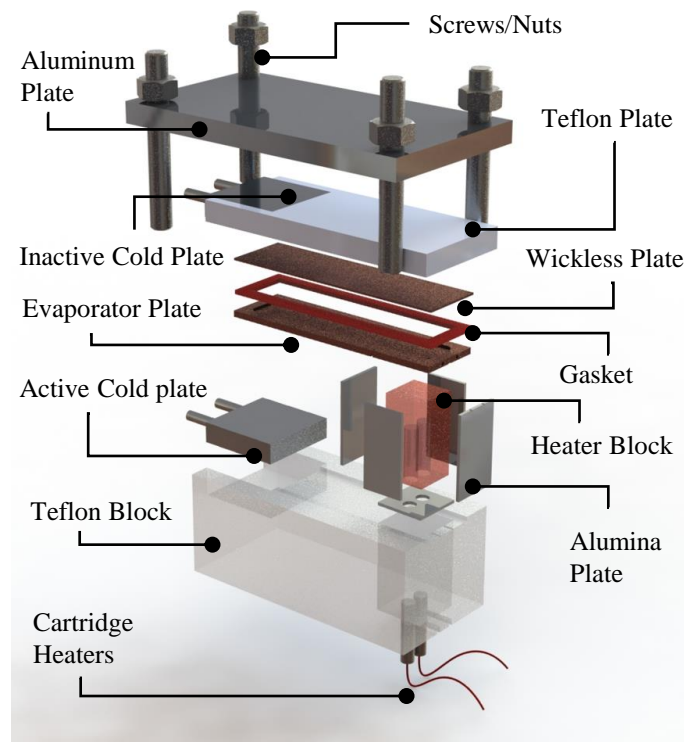


Figure 37: Exploded view of the experimental setup, displaying the assembly of various employed components. The Teflon Block is displayed transparent to expose the nested parts.

with the temperature set at 20 °C using a flow rate of 0.11 kg/s of pure ethylene glycol (Alfa Aesar, 99%).

As shown in Figure 37, a 12 mm thick aluminum plate (McMaster- Carr) mounted on 4 long screws and nuts was utilized to clamp the entire system onto a laboratory table. This design was used for two purposes; first, to properly seal the device, and second, to maximize the thermal contact between the evaporator plate with the cold plate and the heating block. Moreover, this design provided proper insulation for 7.5 cm of the wickless plate length by

employing another 12 mm-thick Teflon block, while the rest 3.5 cm was in contact with another similar cold plate that was also connected to the chiller but was shut off during the experiment, thus creating a non-isothermal top-plate condition and emulating an indirect heat sink to the environment.

Ten thermocouples (Omega, T-type, bead diameter 0.05 mm) connected to two data acquisition systems (Omega DAQ, USB 2400 series) were secured at designated spots in the milled grooves on the heater block, cold plates, and top Teflon block, and distributed as shown in Figure 35(a), to monitor and record the temperature of the system. A thin layer of thermal paste (Omegatherm 201, Omega) was applied on all non-insulated interfaces to maximize the thermal contact between components. Thermocouple locations, heat pipe, and test setup component placement are shown in Figure 52 and Figure 53 in appendix D.

### **6.2.3 Experimental Procedure**

A torque screwdriver (Neiko 10573B) was set at 35 N m and used to ensure uniform pressure on the system. After sealing the device, the heat pipe was evacuated from non-condensable gases (NCGs). Next, a designated amount of DI water was charged into the device through the charging port. Overall, four charging ratios were tested on the WP-equipped heat pipes. Next, to release the NCGs dissolved in the DI water, the device was preheated to 50 °C for 25 min and a secondary evacuation (degassing) process was performed. It has been demonstrated that this technique is adequate for removing the NCGs from the device interior (493; 323). The negligible role of NCGs in this device's performance is further discussed in the appendix D. Lastly, the HP could achieve a steady state condition after 4 min and the data for 90 s in

steady state was utilized for thermal characterization. Two shut-down threshold criteria were implemented in this work; the first one was when the measured temperatures T1 or T2 reached 100 °C. The second one was when the device reached a dry-out state, see Section 6.3.2.

## 6.2.4 Performance Metrics and Error Analysis

### 6.2.4.1 Metrics

The heat input was calculated as:

$$Q = \frac{V^2}{R_{\text{heater}}} \quad (6.1)$$

where  $V$  is the input voltage and  $R_{\text{heater}}$  is the heaters' electrical resistance.

The thermal resistance of the heat pipe was found by (522; 526)

$$R = \frac{\Delta T}{Q} \quad (6.2)$$

where, based on Figure 35a,

$$\Delta T = T_e - T_c \quad (6.3)$$

and

$$T_e = \frac{T1 + T2}{2} \quad (6.4)$$

and for consistency, (see section 6.3.1)

$$T_c = \frac{T8 + T9 + T10}{3} \quad (6.5)$$

The corresponding effective thermal conductivity was found by (522; 526)

$$K = \frac{Q L_{\text{eff}}}{A \Delta T} \quad (6.6)$$

where  $A$  denotes the cross sectional area of the HP, and  $L_{\text{eff}}$  the operating length of the device (10 cm in this case). To account for the occupied space with the working liquid in the HP and provide a better comparison among different configurations, the charging ratio (CR) is introduced

$$\text{CR} = \frac{\text{Liquid volume}}{\text{Available free space}} \quad (6.7)$$

#### 6.2.4.2 Error Propagation

To determine experimental errors, a Gaussian error propagation rule (493; 542) was performed on each metric as follows

$$\Sigma_{\phi} = \sqrt{\left(\frac{\partial \phi}{\partial \alpha}\right)^2 \sigma_{\alpha}^2 + \left(\frac{\partial \phi}{\partial \beta}\right)^2 \sigma_{\beta}^2 + \dots} \quad (6.8)$$

where  $\phi$  is a defined metric, which is a function of  $\alpha, \beta$ , etc. The standard deviation of each variable  $x$  is calculated by

$$\sigma_x = \sqrt{\sigma_x^{\text{exp}} + \sigma_x^{\text{instr}}} \quad (6.9)$$

with  $\sigma_x^{\text{exp}}$  and  $\sigma_x^{\text{instr}}$  being the standard deviation of the experimental measurements and instrument accuracy for variable  $x$ , respectively. The latter is considered constant for each instrument,

while the values for  $\sigma_{R_{\text{heater}}}^{\text{instr}}$ ,  $\sigma_V^{\text{instr}}$ , and  $\sigma_T^{\text{instr}}$  were 0.005  $\Omega$ , 0.005 V, and 0.25 K, respectively.

For each case, two runs were performed and the final error was calculated as:

$$\Sigma_{\bar{\phi}} = \frac{\Sigma_{\phi}}{\sqrt{2}} \quad (6.10)$$

Considering  $Q = f(R_{\text{heater}}, V)$ , the heat input error can be found as:

$$\Sigma_Q = \sqrt{\left(\frac{\partial Q}{\partial V}\right)^2 \sigma_V^2 + \left(\frac{\partial Q}{\partial R_{\text{heater}}}\right)^2 \sigma_{R_{\text{heater}}}^2} \quad (6.11)$$

Also, since  $R = R(T_e, T_c, V, R_{\text{heater}})$ , the thermal resistance error can be calculated as:

$$\Sigma_R = \sqrt{\left(\frac{\partial R}{\partial V}\right)^2 \sigma_V^2 + \left(\frac{\partial R}{\partial R_{\text{heater}}}\right)^2 \sigma_{R_{\text{heater}}}^2 + \left(\frac{\partial R}{\partial T_e}\right)^2 \sigma_{T_e}^2 + \left(\frac{\partial R}{\partial T_c}\right)^2 \sigma_{T_c}^2} \quad (6.12)$$

Similarly,  $K = K(V, R_{\text{heater}}, T_e, T_c)$  so the device thermal conductivity error is as follows

$$\Sigma_k = \sqrt{\left(\frac{\partial k}{\partial V}\right)^2 \sigma_V^2 + \left(\frac{\partial k}{\partial R_{\text{heater}}}\right)^2 \sigma_{R_{\text{heater}}}^2 + \left(\frac{\partial k}{\partial T_e}\right)^2 \sigma_{T_e}^2 + \left(\frac{\partial k}{\partial T_c}\right)^2 \sigma_{T_c}^2} \quad (6.13)$$

The final errors for heat input, effective thermal conductivity and thermal resistance were determined to be in the 3 to 5 percent range.

### 6.3 Results and Discussion

#### 6.3.1 Working Principle

The thermal cycle of a wick-lined heat pipe consists of evaporation at the heated zone, condensation on the cold side, and lastly, conveyance of the condensate back to the heated zone. In the current hybrid design, a new condensation and return mechanism through the wickless WP-plate is superposed on this cycle. In this design, the wickless plate placed opposite to the wick-lined plate also transfers heat due to its contact with an external heat sink (Figure 35a). The saturated vapor comes in contact with the wickless surface and depending on this surface temperature, the vapor temperature and the internal pressure of the device, the vapor could condense on all or parts of the wickless surface. For consistency, only T8, T9 and T10, which are in direct contact with the heat sinks (top and bottom, respectively in Figure 35a), are used for the calculations. The rejected heat gets transferred through lateral conduction in the wickless plate, where insulated, and directly to the heat sink where not insulated, thus facilitating condensation there. Condensation on the wickless surface is tailored to enhance heat removal and reduce the overall thermal resistance of the device. This is achieved by efficiently returning the condensate from the wickless surface to the opposing wick using a patterned wettability mechanism. The transport rate in the present device depends on different factors, including wick thickness, wick shape, working-fluid mass, and wettability pattern of the wickless plate. As opposed to the conventional flat heat pipes, where the vapor condenses mainly on the wick, and the condensate returns through it, here, the WP plate assists the heat dissipation along the length of the device by spreading the condensate over the entire wickless WP plate. Additionally,

the WP plate improves the working fluid circulation by facilitating liquid movement in the absence of a wick.

The heat transfer enhancement is achieved by incorporating a superhydrophilic/hydrophobic pattern on the wickless plate where FWC occurs on the superhydrophilic domains (black areas in Figure 35c), while DWC occurs on the hydrophobic background (white areas Figure 35c) (493; 541). The pattern repeats identical design units (Figure 35c), with each consisting of lateral wedges emanating from a main stem wedge terminating at a circular end-well. Every wedge track passively and rapidly transports droplets from its narrow to its wider end, as established in (16). The lateral wedges are intended to gather condensate droplets from the surrounding areas and transport them to the main stem wedge, which collects the condensate and transports it to the adjoining end-well. Because of its reduced curvature, the end-well is a low-pressure site and is specifically intended as a fluid collecting point, where the condensate is passively carried by the Laplace pressure difference along the wedge tracks.

As additional vapor is produced over the heated zone, condensation proceeds, and small droplets on the hydrophobic sections become larger and merge with one another until they reach the pattern's interdigitated superhydrophilic tracks. When a droplet (due to its growth) reaches the superhydrophilic area, it merges with the existing liquid on the film and then gets carried horizontally to a lower-pressure site, driven by Laplace-pressure differences. As additional condensate accumulates on an end-well, a bulge forms and grows until reaching the opposing wick. At this point, a capillary bridge is formed, which draws liquid to the wick via capillary action, eventually snapping due to water volume loss into the wick. The condensate

is eventually drawn to the heater zone (again due to capillary action) and the thermodynamic cycle is repeated.

The capillary bridge frequency of formation/snapping is an essential part of the cycle, which depends on the wettability pattern, the interior gap height, the amount (mass) of the working fluid, and the applied heat flux. The performance of the device is considerably decreased if the capillary bridges do not form or snap cyclically. The former happens when a device is undercharged; lacking enough working fluid to form the bulge and return the fluid back to the heater before dry-out. The latter occurs when the device is overcharged; large amounts of working fluid prevent the capillary bridge to snap and may cause a permanent vapor-flow blockage in the device

As mentioned earlier, an axially-graded wick structure was also incorporated to facilitate and enhance the return mechanism of the condensate to the heated zone. Using the fine wick structure only over the heated area increases the thin-film evaporation rate (262) and results in greater capillary pressure due to the wick's small pore size. The coarse wick on the rest of the heat pipe significantly reduces the pressure drop, due to the bigger pore size, and amplifies the condensate-return flow rate from the cold to the hot side of the wick-lined plate.

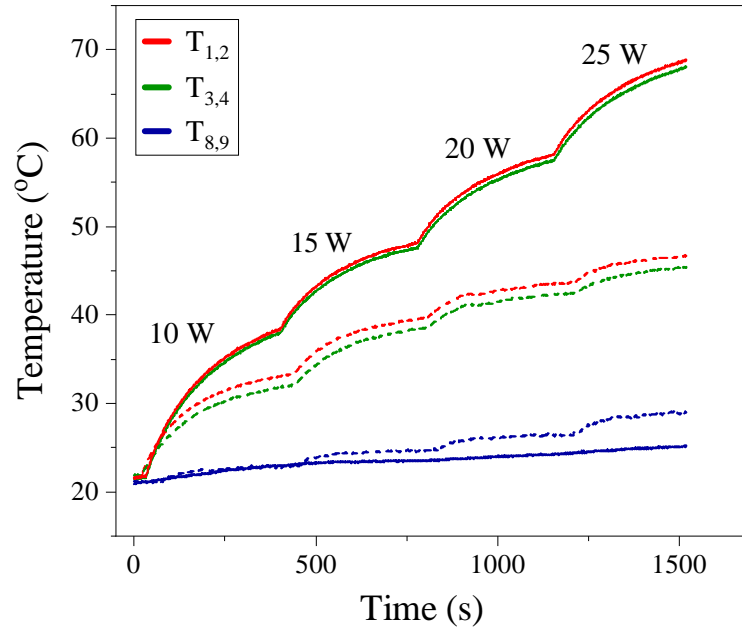
### **6.3.2 Main Results**

A Cu plate (30 mm  $\times$  110 mm  $\times$  2 mm) was evaluated for benchmarking purposes for heat dissipation. This plate occupied the space of the evaporator plate in Figure 37, with thermocouples T1, T2 and T10 placed at its bottom, and T3 to T9 at its top (placing shown in Figure 35). All other components shown in Figure 37, including the Teflon and Aluminum holding plates at

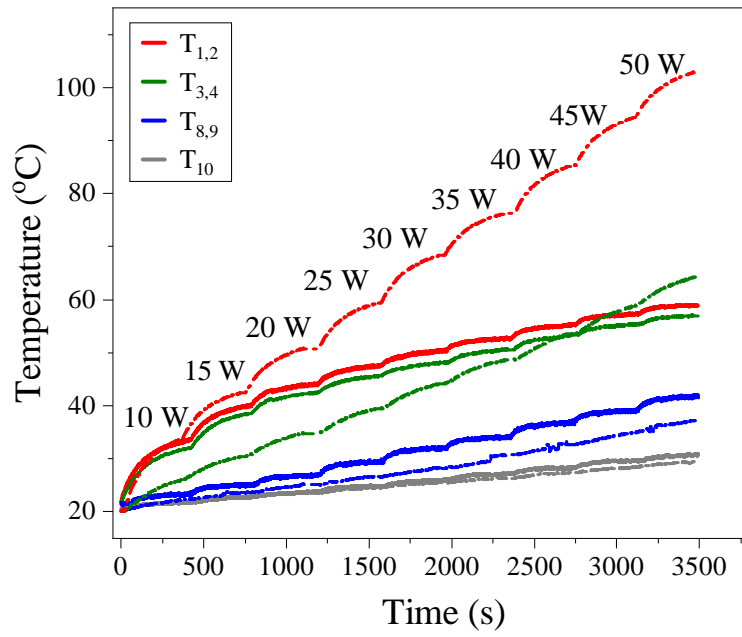


top, remained the same as with the HP. 38(a) presents the temporal temperature rise of the Cu plate (solid lines) versus a HP with wickless WP component (dashed lines) with 25% CR and subjected to heat inputs from 10W to 25W. In 38(a) and for clarity, the average temperature of T1 and T2 ( $T_{1,2}$ ) is plotted (in red), along with the average of T3 and T4 ( $T_{3,4}$ ) (in green), and the average of T8 and T9 ( $T_{8,9}$ ) (in blue).

Heat transfer in the Cu plate is driven only by conduction; in the HP, heat transfer is driven mostly by convection and phase change of water. Naturally, the solid copper plate showed a slower response to heat input variation than the HP. The temperature averages  $T_{1,2} = (T1 + T2)/2$  and  $T_{3,4} = (T3 + T4)/2$  increased in unison, but  $T_{8,9} = (T8 + T9)/2$  remained almost constant and equal to T10 (not shown here) during the entire test period. The heater temperature rose rapidly over the copper plate, showing that heat transfer with the solid plate is less efficient than with the HP. For the 6-minute time intervals of the experimental runs with the copper plate, the heater temperature progressively rose, while the HP temperature reached steady state within that short period. At the end of the experiment, the solid copper plate had reached 70°C, while the HP was only at 45°C. At the same time, the temperature difference  $T_{3,4} - T_{8,9}$  for the HP was 17°C, while for the solid copper plate it was 42°C, confirming that the copper plate poses greater resistance for thermal transport than the HP. As Figure 38(a) reveals, the HP has a thermal response that differs from the solid copper plate, as the HP's working medium evaporates, thus keeping the heated side cooler. The vapor releases heat at the condenser end, as indicated by the rising  $T_{8,9}$ . As more vapor occupies the inner space at rising heating power,



(a)

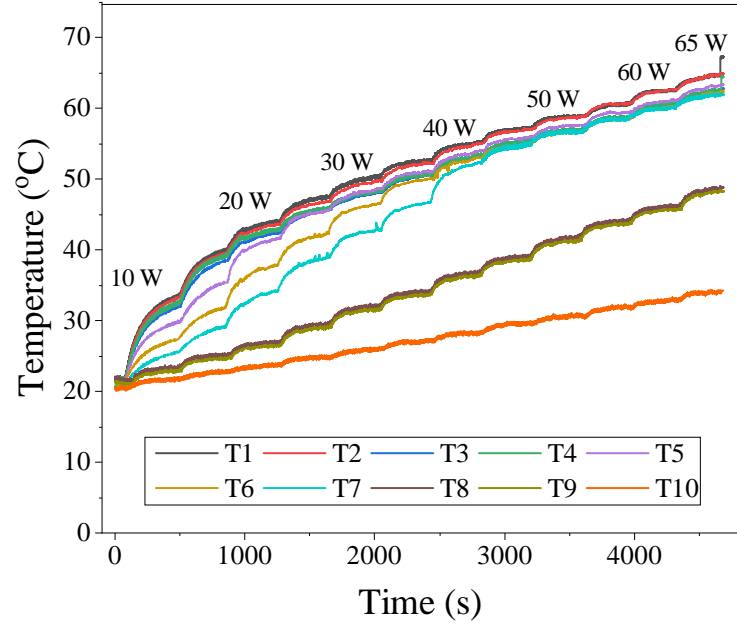


(b)

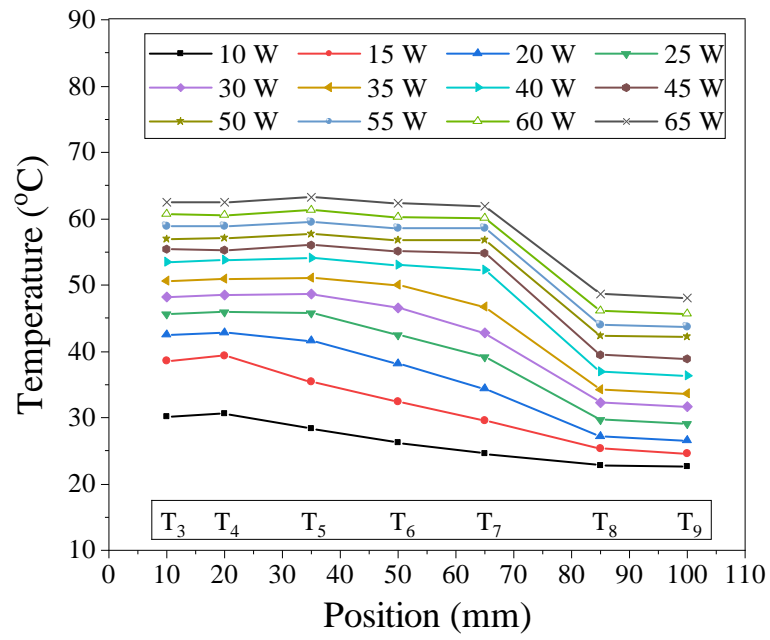
Figure 38: Raw thermocouple measurements for: (a) a flat copper plate (solid lines) and a HP charged with 25% CR (dashed lines), and (b) an empty HP (dashed lines) and the same HP charged with 25% CR (solid lines) as heat input power increased. Temperature measurement error  $\pm 0.25^{\circ}\text{C}$ .

more condensation occurs on the wickless plate, and as a result, its temperature increases in tandem.

Figure 38(b) shows the temperature rise of the same heat pipe at the heater zone ( $T_{1,2}$  and  $T_{3,4}$ ) and condensation zone ( $T_{8,9}$ ,  $T_{10}$ ) with  $CR = 25\%$  (solid lines) and  $CR = 0\%$  (empty) (dashed lines) as a function of heat input in the range 10W to 50W. The thermal behavior of the empty HP is similar to the Cu plate where the temperatures rose steadily in each time step. At 10W, the  $T_{1,2}$  curves for the empty and charged HPs show similar rising trend, indicating that conduction through the wick-lined plate prevails at this low heat flux. As the heat flux increases, the discrepancy between the empty and charged HP is magnified; at 50W,  $T_{1,2}$  for the empty and charged devices reaches  $102^\circ\text{C}$  and  $58.8^\circ\text{C}$ , respectively. On the other side,  $T_{3,4}$  for the empty HP reaches  $64^\circ\text{C}$ , while for the charged device this temperature is only  $1.5^\circ\text{C}$  below  $T_{1,2}$ . The difference between  $T_{1,2}$  and  $T_{3,4}$  for the empty HP rises due to the absence of phase change, but the high value of  $T_{3,4}$  points to a possible influence of conduction heat transfer through the gasket in the heat pipe thermal performance. In real-life applications, for a closed and sealed HP, this effect could be mitigated through a modified design where the conducted heat is channeled toward phase change by thin side walls. On the other hand, at 50W,  $T_{8,9}$  reaches  $37^\circ\text{C}$  for the empty device, and  $42^\circ\text{C}$  for the charged device. This translates to a  $27^\circ\text{C}$  and  $15.3^\circ\text{C}$  temperature difference along the wickless plate for the empty and 25% charged HP, respectively, at a heat load of 50W. In summary, the present hybrid design demonstrates all of the characteristics of a HP whose performance could be further analyzed at greater heat loads.



(a)



(b)

Figure 39: Raw thermocouple measurements vs. heating power over time (a), and (b) over placement distribution for a flat heat pipe with 25% CR.

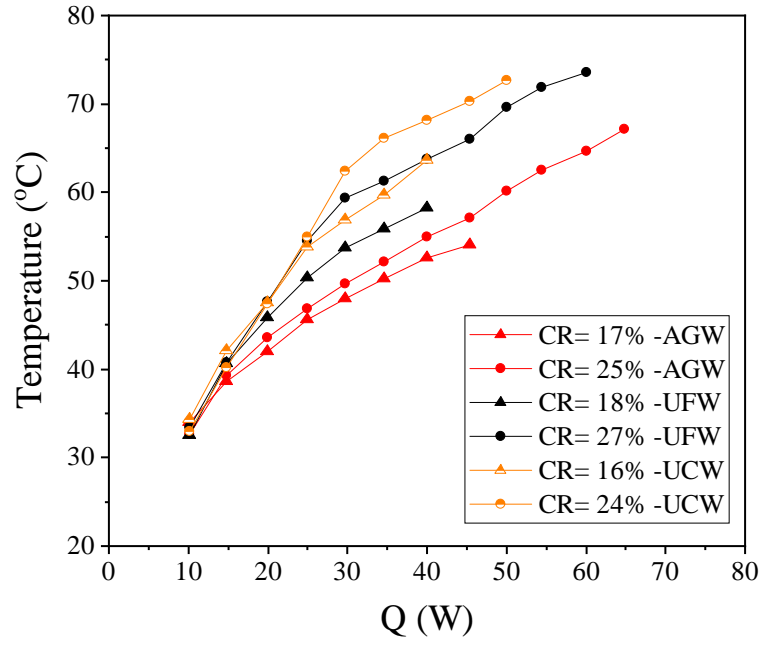
Figure 39(a) plots the temperature rise of a HP with axially-graded wick-lined evaporator and 25% CR, when the heat input varied from 10 W to 65 W in 5 W increments. As seen, the overall temperature of the device increases in sync with the heat input. From 10 W to 15 W, the temperatures near the heater (T1 to T4) rise together, indicating a low evaporation resistance; the large slope indicates the major role of conduction through the solid/porous metal and the working fluid. Initially, evaporation is taking place from the top of the wick and the temperatures T5 to T7 rise slower, but remain below T1 to T4. At 15 W, T1 to T4 start to rise with a much slower rate, which hints the beginning of the thin-film evaporation where most of the heat is transferred through phase change (494; 543). Temperatures T5 to T7 increase swiftly from 15 W to 35 W, and at 40 W, the WP-plate achieves a fairly uniform temperature, except for the condensation section, which is most impacted by the adjacent heat sink. It is worth mentioning the all thermocouples are placed on the outer side of the wickless and wick-lined plates, measuring the outer solid surface temperatures. As discussed earlier, the metal block (heat sink) in contact with the wickless plate induces condensation on the surface, creating a temperature gradient with the lowest temperature recorded on the heat sink. For each heat load up to 65 W, the device reaches a steady state condition. T1 and T2 rise quickly after this time (not depicted), indicating that the wick begins to partially dry up. At this point, the experiment was purposely terminated to prevent damage to the heaters.

Figure 39(b) shows the temperature distribution of the WP plate of the same HP for different heat inputs (see Figure 35 for thermocouple placement). The temperature difference between the evaporation and the condensation sections increases up to 20 W and subsequently remains

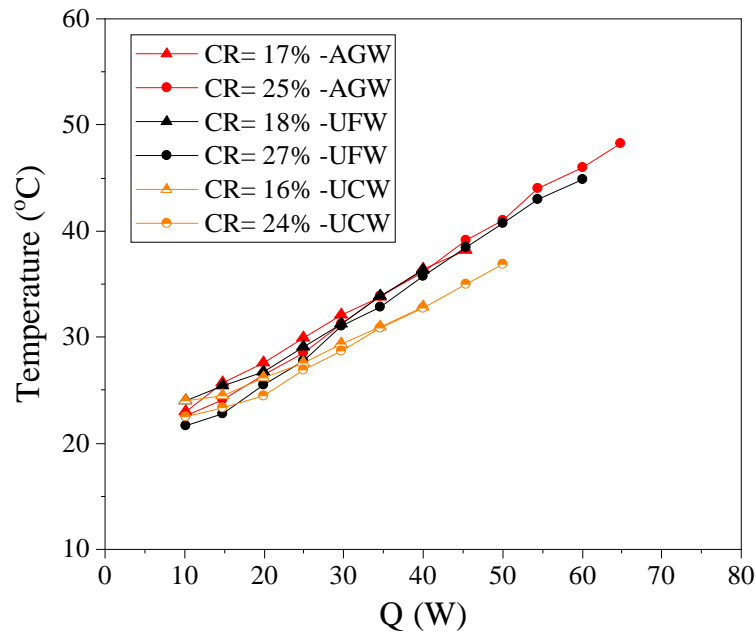
relatively constant up to 65 W. The temperature distributions show that the device performs best at higher heat inputs, where the temperature remains uniform along the HP up to the condensation section, indicating effective heat transport.

### 6.3.2.1 Effect of Wick Structure

Figures 40(a) and 40(b) show average evaporation and condensation temperatures ( $T_{1,2}$  and  $T_{8,9}$ ) on the wickless plate vs. heat input for heat pipes with uniform fine wick structure (UFW), uniform coarse wick structure (UCW), and axially graded wick structure (AGW) on the evaporator plate. As shown in Figure 55 in appendix D, no significant variation of  $T_{10}$  was observed for all cases in this study. Here, all devices featured the same wickless WP component and were filled with two different charging ratios. As seen, the AGW-HP has better performance (lower evaporator temperature) at both charging ratios, while the UFW and UCW-HPs behave differently on the evaporator side. The evaporation temperature for the UCW-HP is slightly higher than the UFW, as also reported in the literature (543). Generally, the coarse wick structure has a higher evaporation resistance compared to the fine wick due to its lower thin-film evaporation area (544). Besides, the former has a higher porosity and permeability. While higher permeability is preferred for transferring the condensate, higher porosity is insufficient to create the required Laplace pressure to drive the liquid. On the other hand, the fine wick structure has lower porosity and permeability. The former enables this structure to create larger Laplace pressure to drive the liquid, while lower permeability causes a larger pressure drop for the liquid, hence, making the evaporator prone to earlier dry out (522). However, taking advantage of the wickless WP plate, the UFW reached a higher critical heat

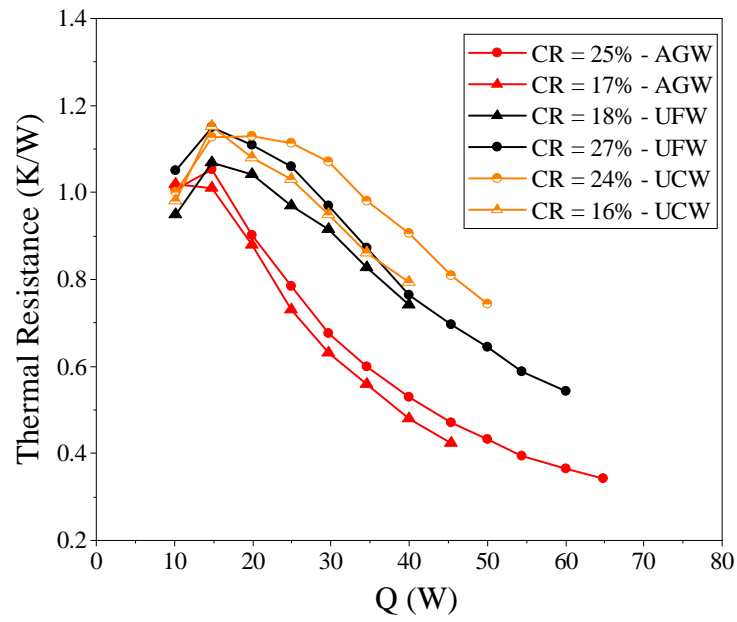


(a)

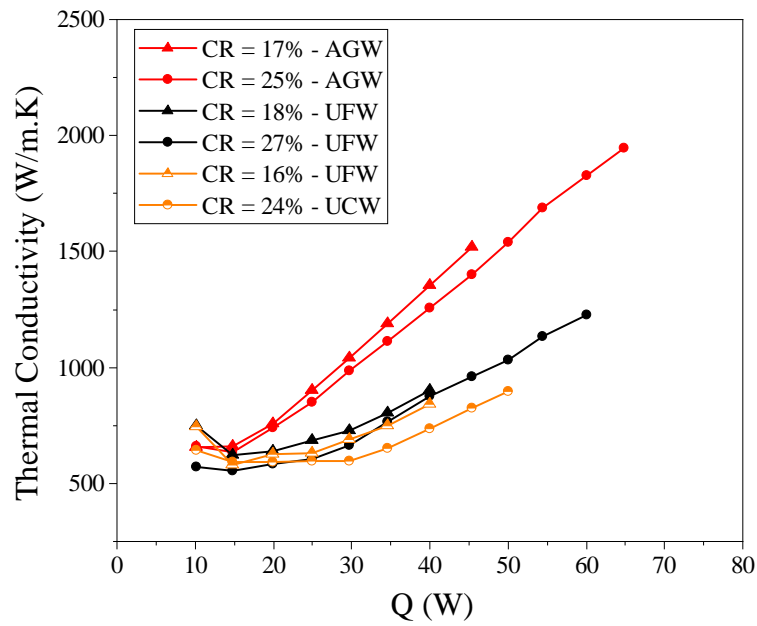


(b)

Figure 40: (a) Average evaporator temperature ( $T_{1,2}$ ), and (b) average condensation temperature ( $T_{8,9}$ ) on the wickless plate of flat heat pipes for two fluid charging ratios (CR) and three distinct wick structures; AGW: axially graded, UFW: uniform fine, and UCW: uniform coarse.



(a)



(b)

Figure 41: (a) Thermal resistance, and (b) Effective thermal conductivity of the flat heat pipes with three distinct wick structures (AGW: axially graded, UFW: uniform fine, and UCW: uniform coarse) at two charging ratios.



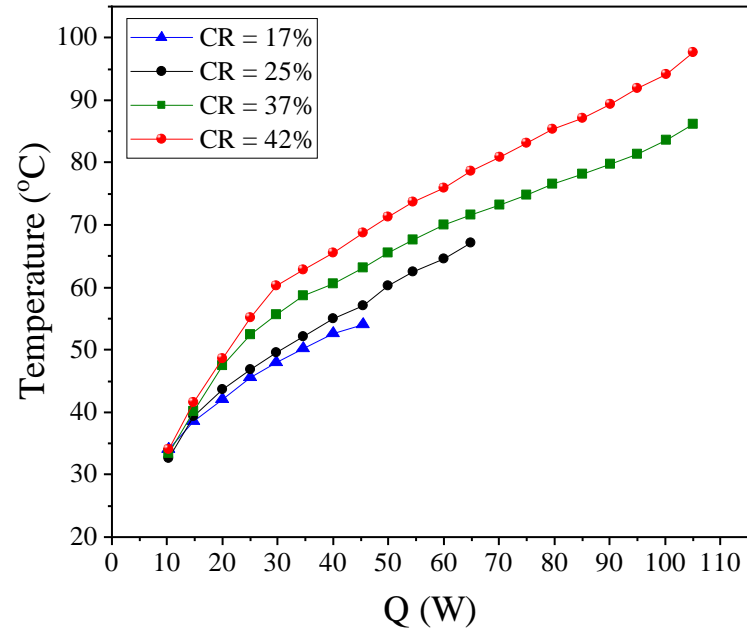
load than the UCW-HP, since the WP component could enhance the resupply of the condensate. Benefiting from both fine and coarse wick structures, the AGW-HP shows a lower evaporation temperature in both charging ratios, since the coarse wick structure can rapidly transfer the cooled liquid to the fine wick structure over the heater, where intense evaporation takes place. As a result, the AGW-HP was able to reach a higher critical heat flux in both charging ratios compared to other HPs. Due to having the same WP plates, the condensation temperatures are close however, the condenser temperatures for the UCW-HP are lower at high heat fluxes, which suggests lower evaporation rates (544; 177; 545). When less vapor is present, less phase change takes place at the condensation section, thus eventually causing lower temperatures there. As shown in a prior study (262), smaller copper-particle sizes for the wick provide a larger percentage of thin-film area. As a result, the proportion of mass evaporating from the identified thin-film area vs. total mass evaporating from the whole meniscus was shown to be a direct function of particle size. This improvement is attributed to the increased meniscus area as well as to the increased solid–liquid contact per unit volume. As shown in (262), smaller pore sizes provide larger thin-film region. Accordingly, the proportion of thin-film evaporation to the entire meniscus evaporation is a direct function of the pore size. As a result, with a smaller pore size, the evaporation rate increases due to the increased meniscus area and the increased solid–liquid contact per unit volume.

Figures 41(a) and Figure 41(b) show the thermal resistance and effective thermal conductivity of the above three HPs. The similar profiles suggest a repeatable behavior even with different wick structure. As expected, the AGW outperformed the other two HPs at either

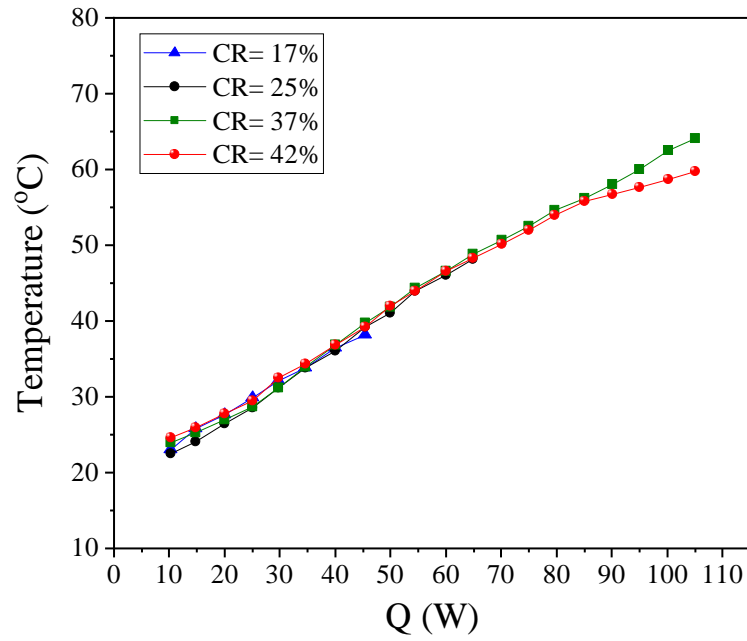
charging ratio, in terms of both thermal resistance and thermal conductivity. The UFW-HP shows a lower thermal resistance than the UCW-HP, in agreement with prior studies (522; 546). The minimum thermal resistances with 18% CR for UFW and 16% CR for UCW (0.74 K/W and 0.79 K/W, respectively) were achieved at 40 W. For 27% CR and 24% CR, the minimum thermal resistance (0.54 K/W) for UFW was achieved at 60 W, and for UCW (0.74 K/W) at 50 W. The AGW-HP achieved the lowest thermal resistance of 0.42 K/W with 17% CR, and 0.34 K/W with 25% CR at 45 W and 65 W, respectively.

### **6.3.2.2 Effect of Fluid Charging Ratio**

Although similar thermal characteristics are observed for the HPs with a wickless WP plate and an axially-graded wick-lined evaporator, there are performance differences as well. Figure 42(a) shows average evaporation temperature ( $T_{1,2}$ ) and Figure 42(b) shows the average condensation temperature ( $T_{8,9}$ ) for the same HP charged with different amounts of water. Initially the evaporation temperatures rise at the same rate. As the charging ratio increases, so do the evaporator temperatures. Since at low heat fluxes conduction prevails, a greater amount of working fluid will absorb more heat and as a result, the onset of thin-film evaporation is further delayed. Based on the knowledge that thin-film evaporation facilitates heat removal, for the devices with 17%, 25%, 37%, and 42% CR, thin-film evaporation starts at 10 W, 15 W, 25 W, and 30 W respectively. A device filled with greater amounts of water retains higher temperatures at lower heat fluxes, because it takes more energy to get the apparatus into the thin-film evaporation regime. Thus, for the same heat input, the HP with a reduced charging ratio performs better. For instance, at 45 W the evaporator temperatures of the

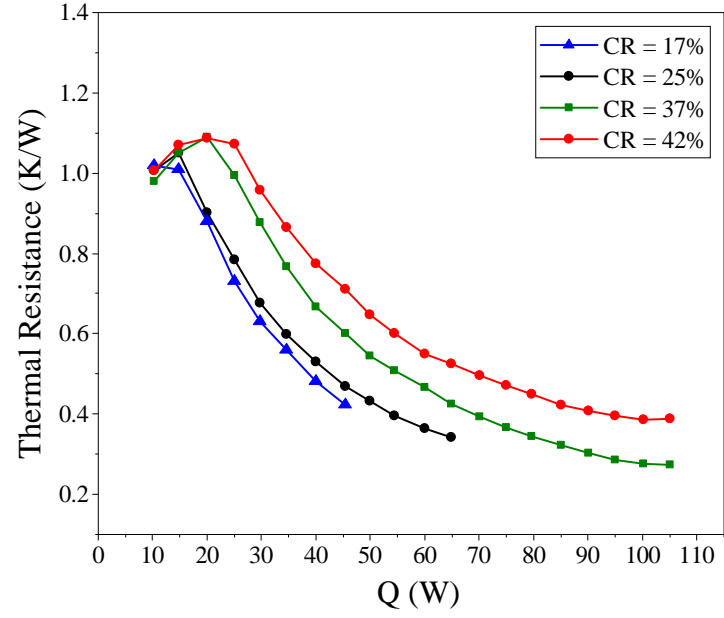


(a)

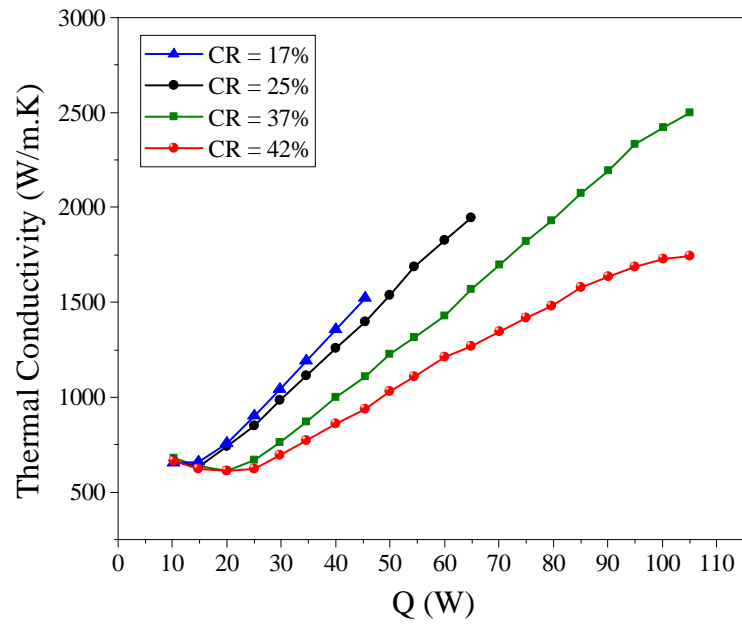


(b)

Figure 42: (a) Average evaporator temperature ( $T_{1,2}$ ), and (b) average condenser temperature ( $T_{8,9}$ ) on the wickless plate with respect to heat input for four identical AGW-WP HPs filled with different charging ratios.



(a)



(b)

Figure 43: (a) Thermal resistance, and (b) Effective thermal conductivity vs. heat input for AGW-WP HPs filled with different charging ratios.

lowest to highest CR devices stand at 54.3 °C, 57.1°C, 63.4°C, 68.7°C , respectively. These differences are attributed to the initial temperature rise when conduction still influences the device performance and thin-film evaporation has not been initiated yet. Besides, the condenser temperatures are nearly identical, implying independence of the charging ratio. This is likely due to the surface wettability pattern, where the surface never saturates and DWC region is always available for the upcoming vapor, as opposed to the metal wicks, which at increased heat flux encounter thicker liquid films on the condensation side, thus saturating these wicks and causing FWC to dominate the heat transfer in this region (547; 548; 353; 549). Figure 42(b) shows a deviation at 90 W for the 42% CR, where the condenser temperature slope changes. This can be attributed to the comparatively larger amount of liquid accumulating there, thus reducing the condensation rate on the wickless WP plate, in turn causing the temperature in that vicinity to rise slower than in the less-charged cases. Furthermore, because additional water allows the device to endure larger heat-input powers, the devices with 37% CR and 42% CR handled 105 W of maximum heat input, compared to 65 W and 45 W for the devices with 25% and 17% CR. As seen, the HP with 37% CR could handle 105W while maintaining an evaporator temperature of 86.2°C, compared to 97.6°C for 42% CR, in turn suggesting that 42% CR was over-saturated and as a result, conduction through the working fluid became an impediment for heat transfer along the device.

Figure 43(a) shows the measured thermal resistance vs. heat input for the same four CRs. A general trend can be observed for all charging ratios, indicating a repeatable behavior for this device. At low heat fluxes, where conduction is predominant, the thermal resistance increases

up to the point where thin-film evaporation takes place (543). From that point on, as the heat flux increases, thermal resistance declines consistently. As mentioned earlier, following Figure 42(a), the break point is directly related to the amount of working fluid where the thermal resistance starts to drop. The corresponding powers where this break occurs, i.e. beginning of thin-film evaporation, are 10 W, 15 W, 25 W, and 30 W, in excellent agreement with 42(a). At the same heat input, the thermal resistance increases with charging ratio. This is anticipated as the temperature difference along the device rises with charging ratio. The minimum thermal resistance for each charge was found at the maximum heat load; 0.42 K/W, 0.34 K/W, 0.27 K/W, and 0.39 K/W respectively, from the lowest to the highest-charged device. The HP with 42% CR, as mentioned earlier, is overcharged, resulting in its thermal resistance leveling off at 90 W, where the liquid thickness is too high at the condenser section where phase change is impeded.

Figure 43(b) shows the effective thermal conductivity of the same four HPs vs. heat input. A similar trend is observed, as is in Figure 43(a), where at the same heat load, the conductivity of the device declines with charging ratio. As seen, the effective conductivity decreases at low heat inputs, where heat transfer by conduction prevails. The thermal conductivity then starts to increase when thin-film evaporation starts. The maximum thermal conductivity of 1520 W/m.K, 1944 W/m.K, 2499 W/m.K, and 1745 W/m.K was recorded from the lowest to highest charged device. Similar to Figure 43(a), a change in the slope of the 42% CR case was seen at 90 W, and reveals the adverse impact of the liquid thickness in the condensation section.

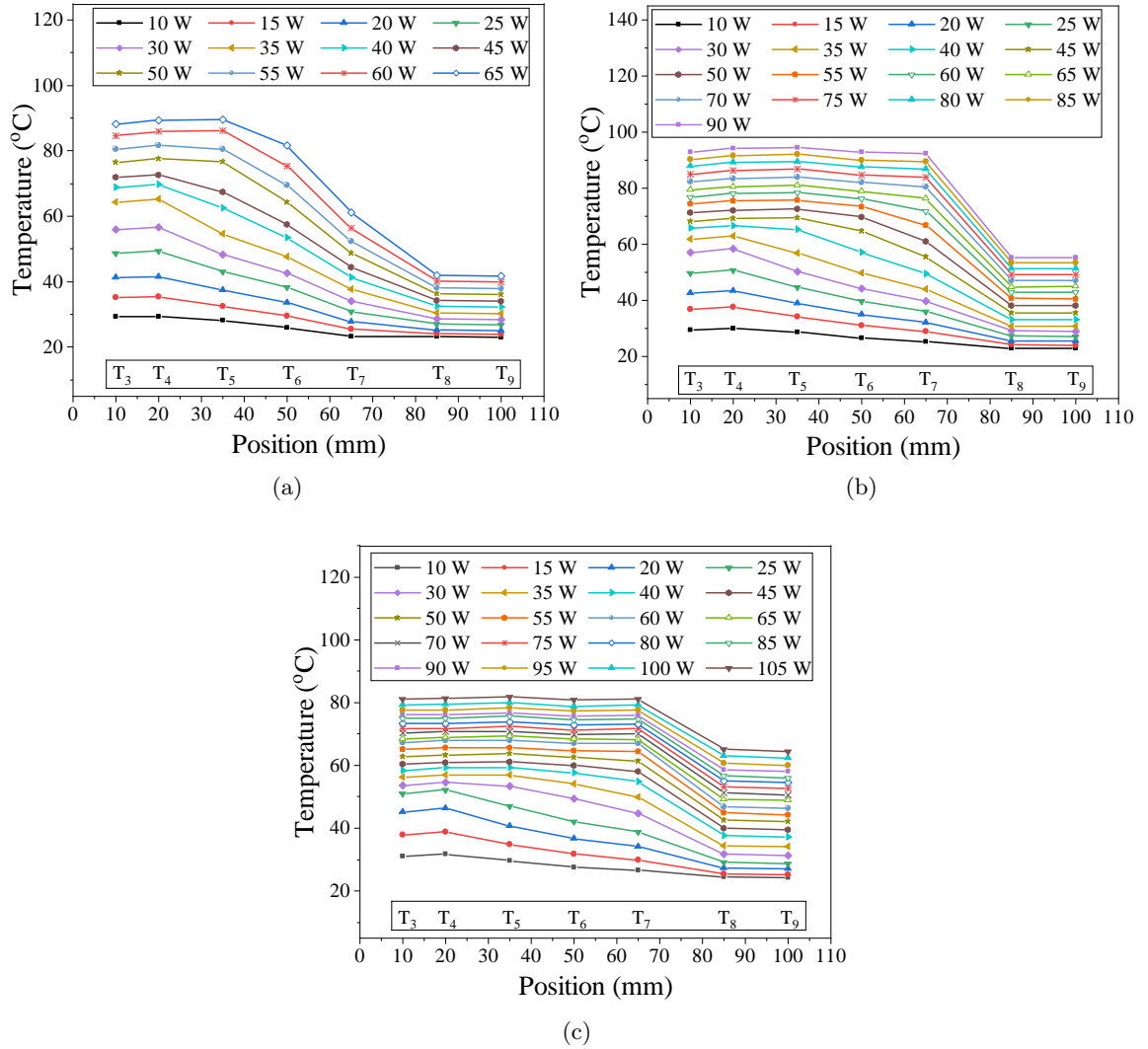


Figure 44: Raw thermocouple readings for locations along three flat heat pipes with the same charging ratio (37%), wick-lined evaporator, and (a) uniform wickless hydrophilic (HPL) plate, (b) uniform wickless hydrophobic (HPB) plate, and (c) wickless wettability-patterned (WP) plate.

### 6.3.2.3 Effect of Wickless-Plate Wettability

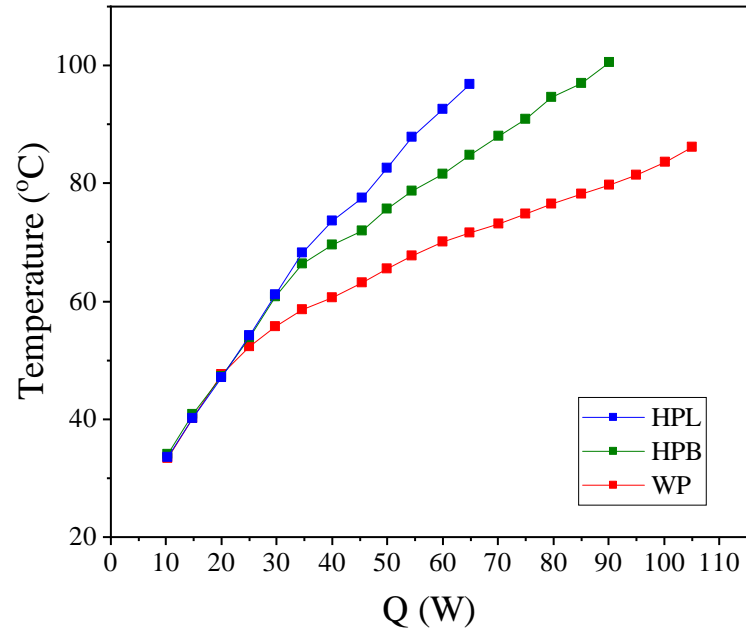
The temperature distribution on the wickless plate vs. heat input is now examined to provide a better understanding of the influence of the wickless component of the device. Figure 44(a) shows results for a heat pipe featuring a uniform hydrophilic (HPL) wickless plate with and 37% CR. As expected, by increasing the heat input, the temperatures of the whole system increase as well. However, the temperature changes are lower near the condensation section, so that T6 and T7 never catch up to T3 and T4. Hence, the wickless plate never reaches a uniform temperature even at 65 W, where the experiment was terminated to avert damage (heater temperature had reached 96°C). As anticipated, the hydrophilic plate would be covered with a liquid film quickly after exposure to vapor (due to FWC), which significantly influences the heat transfer capability of the device. This uniform film can reenter the thermodynamic cycle in two ways. First, when the thickness of the film increases and reaches the wick on the opposite side, thus being sucked in. Second, when its temperature is elevated to evaporate the liquid. Because of the hydrophilic nature of the plate, a thinner liquid film will be left behind in both cases. Having a homogeneous layer without an adequate return mechanism prevents condensate from returning to the wick, thus hindering the cyclical process. As a result, the inability to remove vapor raises the device's internal pressure. This pressure increase suppresses the evaporation rate (505; 191) and raises the temperature over the heater for the HPL and uniform hydrophobic (HPB) cases. Compared to the WP case in Figure 44(c), T5 to T7 as well as T8 and T9, are supposed to increase as the heat load increases, however due to the wickless



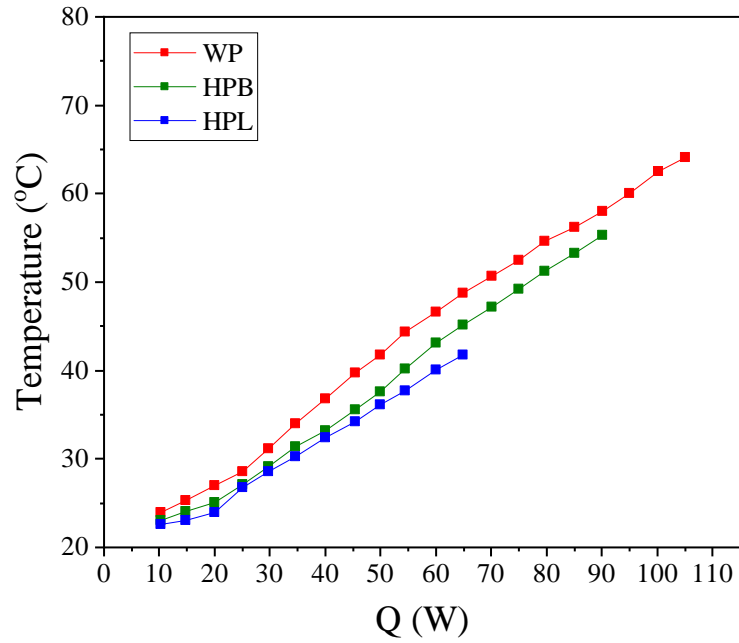
HPL plate's under-performance, T6 and T7 do not rise at the same pace as T5, and thus T8 and T9 remain well below the corresponding temperatures of the WP case.

Figure 44(b) shows the temperature distribution of a HP with a uniform hydrophobic (HPB) wickless component at the same charging ratio (37%). Here, the experiment was shut down at 90 W when the heater reached 100°C. A similar behavior as the HPL case can be observed here as well, where T6 and T7 reach T5 at 70 W, which is higher compared to the WP case. This implies formation of random droplets on the HPB plate. But the main difference with the HPL plate is that the hydrophobic plate has a higher static contact angle and a lower contact angle hysteresis. As more vapor is generated, small droplets form on the surface and start to grow individually or coalesce with each other and eventually form random large droplets on the entire surface. These larger droplets can bead up, due to hydrophobic property of the surface, and create new space for continued condensation on the plate. Furthermore, if these droplets get large enough, they can bridge the gap and reach the wick on the other side, thus draining quickly without leaving a footprint behind, creating more space for renewed condensation on the wickless plate. Thus, the severe problem of vapor space and interior pressure for the HPL case is mitigated, and the HPB-equipped HP operates at a lower heater temperature compared to the HPL case.

Figure 44(c) shows the temperature distribution of a HP with a wickless WP component at CR=37%. Compared to the HPB and HPL devices, the WP system attains lower overall temperature for each heat load. The wettability pattern, due to its specific design, controls the droplets size and distribution uniformly on the entire plate and prevents random condensation

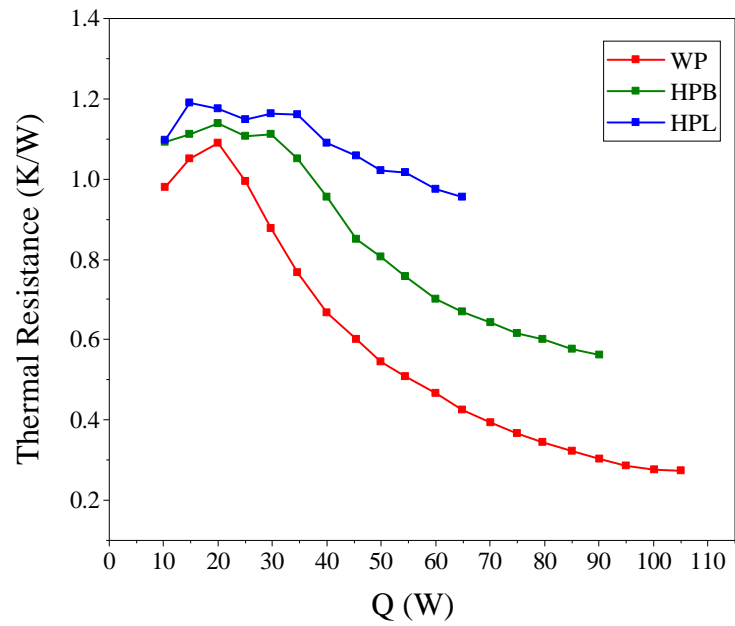


(a)

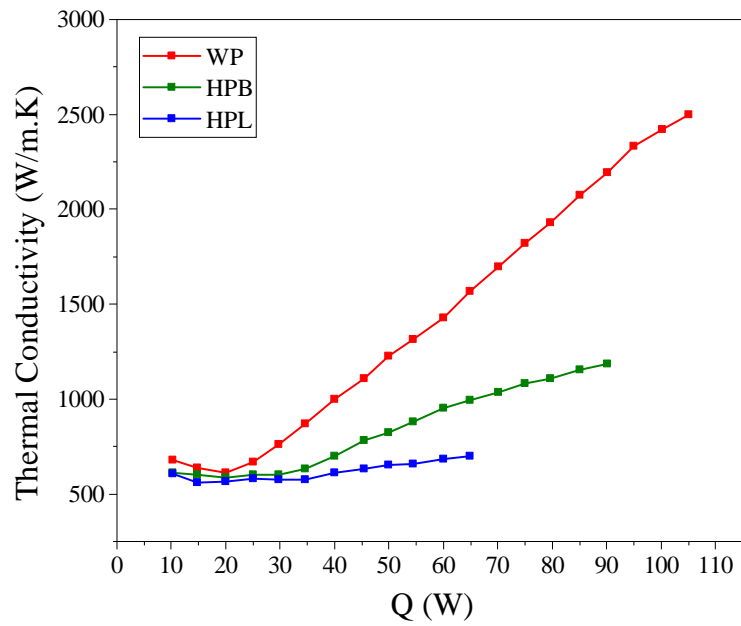


(b)

Figure 45: (a) Average evaporator temperature ( $T_{1,2}$ ), and (b) Average condenser temperature ( $T_{8,9}$ ) on the wickless plate for flat heat pipes with 37% CR and three distinct wickless components (WP: wettability-patterned, HPB: uniform hydrophobic, and HPL: uniform hydrophilic).



(a)



(b)

Figure 46: (a) Thermal resistance, and (b) Effective thermal conductivity of three heat pipes charged with 37% CR, and each equipped with a distinct wickless surfaces (WP: wettability-patterned, HPB: uniform hydrophobic, and HPL: uniform hydrophilic).

or pooling on it. Therefore, this device is set to a nearly uniform temperature at 40 W, except over the condensation section which is affected by the adjacent heat sink. These results show that wettability patterning can allow a HP to spread the heat more quickly and uniformly.

Figure 45(a) compares the evaporation temperatures of HPs with different wickless plate wettability at a fixed charging ratio of 37%. Following the temperature distribution results, the WP attains the lowest evaporator temperature compared to the HPB and HPL cases. Also, the WP case enters the thin-film evaporation regime at 25 W, while the corresponding power is 35W for the HPL and HPB devices. The respective evaporator temperatures are 52.3 °C for WP, 66.4 °C for HPB, and 68.2°C for the HPL system. As mentioned, the HPB case performs slightly better than the HPL case at higher heat loads due to its hydrophobic nature.

Figure 45(b) shows the condensation temperatures for the same HPs. In the WP case, the thin-film evaporation phase starts at lower heating powers, therefore, the condenser temperature rises above the corresponding temperatures for HPL and HPB, showing increased condensation. A similar behavior is observed for the HPB case, but the slope is lower than the WP case since the drop formation and distribution on the former is random and unregulated (due to its uniform wettability). As expected, the HPL case retains the lowest temperature at similar heat load, indicating weak phase change due to reduced evaporation rate and vapor space.

Finally, Figure 46(a) shows the thermal resistance of the three HP with different wickless plates at the same charging ratio (37%). The WP device performs best with the lowest thermal resistance of 0.27 K/W at 105 W. As expected, the HPL case has the maximum thermal resistance (0.95 K/W) at its critical heat load (65W). Figure 46(b) shows the corresponding

effective thermal conductivity for these devices. The WP case reached 2499 W/m.K at 105W, while the HPB case reached 1184 W/m.K at 90 W. This improvement in HP performance underlines the need of directing condensate back to the heater in an efficient way, which can be accomplished via wettability patterning.

#### **6.4 Conclusion**

In this work, a case study of a low-profile heat pipe with partially adiabatic wickless plate was performed. The partially adiabatic element was incorporated to emulate practical situations where the presence of external heat sinks force temperature non uniformities. A prototype heat pipe with a wickless wettability-patterned component and an axially graded copper-wick evaporator was assembled and tested. The wick-lined evaporator was designed to improve evaporation from the heater zone as well as transfer the condensed liquid to the device's hot side, whereas the wettability-patterned component was meant to improve condensation efficiency and provide a new conduit for condensate to return to the heater. The performance of the HP was studied using four different charging ratios of DI water and compared to the performance of HP with different uniform wick architectures and wickless plate wettability. Thermal resistance and effective thermal conductivity were the two primary performance metrics used for comparisons. It was discovered that the HP with an axially graded wick structure and a WP component had the lowest thermal resistance and greatest thermal conductivity. For the same heat input, the device with a greater fluid charge ratio (CR) could withstand higher heat loads while exhibiting higher thermal resistance and lower effective thermal conductivity. The HP at 37% CR could reach 105 W without dry-out. At its critical heat load, this device had thermal resistance of

0.27 K/W and effective thermal conductivity of 2499 W/m.K. Although the current design, the first of its kind, has demonstrated the ability to efficiently transfer heat and protect sensitive high-heat-power devices featuring limited surface area for heat dissipation, additional research on the wettability patterns, charging ratio, wick structure and thickness, interior gap thickness, and minimization of conduction heat transfer through the wick-lined solid plate can help to improve its performance to handle higher heat loads even more efficiently. The current design can be of value for a variety of applications, such as thermal management, electronics cooling, batteries, etc.

## CHAPTER 7

### CONCLUSION AND OUTLOOK

#### 7.1 Thesis Conclusion

Surface wettability engineering is a robust technique for manipulating liquids and gases on various open solid surfaces in isothermal and non-isothermal conditions. In this work, five different applications of wettability-engineered surfaces have been presented. In isothermal cases, it was shown that it is possible to reach a prescribed wettability using a  $\text{TiO}_2$  nanoparticle coating compound. The present approach provides a powerful tool for designing surface patterns with precise wettabilities, in this case for water, with contact angles in the range  $\sim 0 - 170^\circ$ . Wettability patterning is not only well suited for manipulating liquids; as shown, it could be efficiently used to confine and control gas bubbles submerged in liquids as well. The work provided a parametric study of spreading of mm-size gas bubbles on wettability-confined tracks, which led to deriving a scaling law governing the transport of bubbles on immersed superaerophilic tracks. To further investigate the potential of wettability engineering in non-isothermal cases, condensation heat transfer was also studied. In a follow-up study of works performed in the same lab, we showed the role of pressure gradient created by the superhydrophilic wedge-shape tracks on the overall condensate removal capacity and rate. As predicted by theory, the experiments revealed higher pressure gradient removed the condensate faster when the superhydrophilic/hydrophobic area ratio was fixed for all cases. The condensation heat transfer enhancement has

been incorporated in passive heat spreaders, with the goal to reduce the overall thermal resistance of such systems. A wettability-patterned copper surface was implemented in a vapor chamber to reduce the condensation thermal resistance in addition to enhancing water circulation by removing the copper wick structure. Moreover, the same concept was applied in a heat pipe, where it was shown that similar enhancement in thermal performance could be achieved via a surface-engineered component. All of the above studies showcased the robustness and versatility of wettability engineering technology where handling small liquid volumes is a critical task. As discussed, it is crucial to choose the proper surface-treatment technique and design parameters to reveal the advantage and applicability of wettability patterning. Although this work presented some case studies, further research into the individual cases is needed for forming a complete picture of the different aspects and functionality factors affecting particular applications.

## **7.2    Research Outlook**

Surface treatment and wettability engineering have become an integrated part of our daily lives. From the recent COVID-19 rapid test kits, harvesting fog from the atmosphere, desalinating sea water, separating water and oil, separating oil and gas, to cooling batteries in electric vehicles and microchips in our cellphones and laptops, all require precise handling of liquids to maximize the efficiency of each individual system. Surface engineering offers a facile and cost-effective approach to address technological problems where managing micro liquid/gas volumes is a matter of importance.



By increasing the industrial-scale implementation of surface-engineered surfaces, further research is required to develop durable and ready-for-market devices. With a rising demand for developing multi-functional surfaces, such as in biology, biomedical, and ink-jet printing industries, further research toward creating domains of specific wettability for different liquids would be required. Moreover, raising demand in the complementary case, where manipulating gases in liquids is a critical task, has also created an extensive research topic. Collecting and extracting the gas bubbles from a solution, such as biological samples, electrodes, boiling surfaces, etc, is a complex venture and requires further experimental and theoretical research to better understand the efficiency of engineering wetting forces in such circumstances.

Beside isothermal systems, skyrocketing demand in cooling high-power electronics and batteries has become one of the hottest topic in recent years. As shown, surface engineering incorporation in thermal management systems is a viable solution toward more efficient heat removal systems. Although the present work investigated a vapor chamber and a heat pipe with a wettability-patterned surface, more research should be pursued to create thinner and more effective devices to meet the miniaturization path in the electronics industry, where ever higher heat fluxes are required to be removed at smaller sizes/thicknesses.

### **7.3 Recommendation for Future Work**

To further comprehend, develop and fine-tune the surface energy patterning technology for different applications, more extensive research is required in this area. Following the presented  $\text{TiO}_2$  study in chapter 2, further evaluation of various coatings will provide better image of its wettability behavior. The current study focused on the static contact angle of various  $\text{TiO}_2$

coatings and even though the employed machine learning model showed great accuracy and generalized attributes, more data on dynamic contact angle (receding and advancing), adhesion force measurements, and coating durability tests could provide a more comprehensive picture.

Following the work in chapter 3, understanding gas bubble spreading dynamics was a major step toward designing more complex systems. Nevertheless, more research is needed to cover all aspects of these phenomena. Factors, such as larger bubble size (above capillary length), a wider range of wettability-confined tracks, larger variation in liquid properties (e.g. surface tension, density, and viscosity), and non-uniform tracks are factors that have not been studied in the current work and investigating them could be a valuable step towards understanding gas/liquid interactions in confined spaces.

In chapter 4, a parametric study showed the role of superhydrophilic wedge-shape tracks in overall condensation performance of a cooled surface. However, this study varied only one variable while keeping all other parameters constant, and of course, thermal performance of the entire surface is a function of all factors. Therefore, to further explore the role of wettability patterning in condensation heat transfer enhancement, one should explore and conduct an extensive study while keeping all the variables in play, which is a time-consuming and expensive task. To this end, a collaboration with the University of California-Irvine was formed to take advantage of powerful machine learning and artificial intelligence tools in this application. In the ongoing research, high resolution videos of different patterns in the condensation rig are fed to image detection algorithms to automate droplet nucleation, growth, and drainage rate monitoring. By tracking individual droplets and using the experimental data (heat flux,

subcooling, and HTC), a correlation between the pattern and its condensation performance is derived, providing a solid modeling base towards optimizing the wettability pattern for various applications and conditions.

Chapter 5 presented the application of wettability engineering in a hybrid (made of wick-lined and wickless components) vapor chamber. The rising demand for cooling high-power and high-density microchips and batteries in the booming electronics and electric vehicle industry will continue to require more efficient and cost-effective cooling solutions. Everyday life usage of electronics components requires reliable, low-cost, light-weight and highly efficient cooling techniques. As shown, wettability patterning could be a viable approach for these purposes. However, hybrid and wickless vapor chambers are relatively new and very young compared to the conventional fully wick-lined devices and require further studies to reach mass production and implementation. To this end, the idea of surface energy patterning incorporation inside a vapor chamber could be pursued in two ways:

- **Hybrid vapor chambers:** The power-electronics setup explored in this work was intentionally made of low-efficiency MOSFETs to generate high heat losses. The maximum 200 W drawn from this system could be further enhanced by switching to active liquid-cooling method (cold plates). In this approach, the MOSFET temperatures will reach 100°C at much higher heat loads and therefore, the cooling capacity of the hybrid vapor chamber could be tested further. In addition, using more spacers would resist the plates' deflection and enable thinner vapor chambers, which in turn, will reduce thermal resistance.

- **Fully wickless vapor chambers:** Another approach for the power electronics cooling application features a fully wickless system. As shown by our group (329), fully wickless vapor chambers are more light-weight, easy to fabricate, and also allow examining various patterns for different heaters' configurations. For this case, a wickless and wettability-patterned evaporator plate could be fabricated to accommodate two heat sources and accordingly, the pattern on the condenser could be further adjusted to return the condensed liquid to the surface over the two MOSFETs. In collaboration with The University of Nebraska-Lincoln, femtosecond laser surface processing (FLSP) could be applied on the evaporator side to enhance evaporation and boiling occurring over the hot spots.

Moreover, following our latest work with wick-free vapor chambers (329), a new robust setup was fabricated and tested. The new vapor chamber setup was designed for  $1\text{ cm} \times 1\text{ cm}$  heat source and a  $5\text{ cm} \times 5\text{ cm}$  vapor chamber. The setup rig was specifically designed with the aim of reducing the vapor chamber thickness  $< 2\text{ mm}$  and the thermal resistance to drop  $< 0.1\text{ K/W}$  even when reaching higher heat fluxes. A thin wick-free and FLSP treated vapor chamber will be investigated and built to be tested with this setup.

Finally, in chapter 6, we introduced wettability patterning on a wickless component of a flat-plate heat pipe. The results showed the superiority of wettability patterning over uniform wettability on the condenser side. Replacing the wick also on the evaporator side with a wickless wettability-patterned surface could further enhance the device's thermal performance and reduce its thermal resistance. Due to the robustness of wettability patterning and its

high liquid transport velocity on wettability-confined superhydrophilic wedge-shape tracks, it is expected that a fully wickless system could tolerate much higher heat loads since the liquid could travel with least resistance from the cooled to the heated side of the heat pipe. Moreover, implementing FLSP-treated domains on the heater zone could further enhance the phase-change process with lowest evaporation resistance, and overall, reduce the total thermal resistance of the heat pipe. Furthermore, for a better understanding of the evaporation/condensation and transport of the condensate inside the device, a new setup with transparent top could be made to allow visualization study of the heat pipe's interior.

## CHAPTER 8

### APPENDICES

#### 8.1 Appendix A: Supplementary Materials for Chapter 2

##### 8.1.1 Titanium Dioxide Formulation Composition

Each  $\text{TiO}_2$  formulation (liquid dispersion of mass  $M$ ) has three main components: polymer solution (mass  $p$ ), filler (mass  $f$ ) and solvent (mass  $s$ ). The value of  $M$  for all formulations prepared is kept constant at 15 g which is then coated on four  $75\text{mm} \times 25\text{ mm}$  microscope slides. There are infinite combinations of  $\text{TiO}_2$ -polymer-solvent, which differ in the mass of each constituent. Therefore, it is essential to define a unique feature (property), which designates a unique  $\text{TiO}_2$  formulation and combines certain values of  $p$ ,  $f$  and  $s$ , respectively. That feature is the filler mass fraction and is denoted by  $\phi$ ; it is defined as the mass ratio of filler ( $\text{TiO}_2$ ) particles in the dried coating

$$\phi = \frac{f}{f + cp} \quad (8.1)$$

where  $c$  is the weight percent of the polymer in the PMC water solution which in our case is 0.2.

Consequently, two more equations are needed to determine the values of  $p$ ,  $f$  and  $s$  for any known value of  $\phi$ . Equation 8.1 can be rewritten as

$$(\phi - 1)f + \phi cp = 0 \quad (8.2)$$

The total mass,  $M$  can be found from

$$f + p + s = M \quad (8.3)$$

Another parameter,  $d$  is defined as the mass ratio of the solid components ( $f+cp$ ) to the total mass ( $f + p + s$ ) of the dispersion

$$(d - 1)f + (d - c)p + ds = 0 \quad (8.4)$$

Equation 8.2, Equation 8.3, and Equation 8.4 could be arranged as

$$\begin{bmatrix} d-1 & d-c & d \\ 1 & 1 & 1 \\ \phi-1 & c\phi & 0 \end{bmatrix} \begin{bmatrix} f \\ p \\ s \end{bmatrix} = \begin{bmatrix} 0 \\ M \\ 0 \end{bmatrix} \quad (8.5)$$

Solving the system of (Equation 8.5), the values of  $f$ ,  $p$  and  $s$  are determined with  $c$ ,  $M$  and  $d$  being known constants with values 0.2, 15 g, and 0.08, respectively. The 15 g mass was chosen for each batch and fixed for all  $\phi$  values to provide sufficient amount of material for spraying. The mass fraction,  $\phi$ , was set to each of the values listed in the following section.

### 8.1.2 Data

$\phi$	UV time (min)	Contact Angle ( $\pm 1.1^\circ$ )
0.2	0	114.13
	3	93.36
	6	90.57
	9	85.29
	12	65.9
	15	62.94
	18	62.96
	21	62.91
	24	62.05
	27	60.32
	30	58.25
	33	47.92
	36	42.21
	39	33.04
	42	31.41
	45	22.3
	48	19.56
	51	14.11
	54	0

$\phi$	UV time (min)	Contact Angle ( $\pm 2.50^\circ$ )
0.42	0	148.64
	1	149.65
	2	146.05
	3	144.61
	4	94.8
	5	75.97
	6	63.57
	7	50.57
	8	41.06
	9	24.77
	10	17.57
	11	13.67
	12	0

$\phi$	UV time (min)	Contact Angle ( $\pm 1.30^\circ$ )
0.6	0	172.87
	1	166.46
	2	157.13
	3	124.31
	4	49.04
	5	0

$\phi$	UV time (min)	Contact Angle ( $\pm 1.25^\circ$ )
0.68	0	163.08
	1	159.73
	2	155.19
	3	119.66
	4	85.46
	5	56.44
	6	26.06
	7	20.11
	8	9.75
	9	0

$\phi$	UV time (min)	Contact Angle ( $\pm 2.80^\circ$ )
0.5	0	151.03
	1	140.44
	2	109.4
	3	92.06
	4	86.92
	5	78.13
	6	56.09
	7	45.91
	8	32.09
	9	23.64
	10	20.33
	11	14.98
	12	12.89
	13	0

$\phi$	UV time (min)	Contact Angle ( $\pm 1.45^\circ$ )
0.75	0	161.1
	0.5	125.52
	1	57.57
	1.5	15
	2	0

$\phi$	UV time (min)	Contact Angle ( $\pm 1.35^\circ$ )
0.8	0	159.94
	0.5	90.41
	1	77.18
	1.5	56.58
	2	0

$\phi$	UV time (min)	Contact Angle ( $\pm 2.10^\circ$ )
0.35	0	132.41
	2	124.58
	4	101.76
	6	81.95
	8	74.27
	10	62.75
	12	51.3
	14	51.11
	16	40.65
	18	41.08
	20	21.22
	22	14.31
	24	0

Figure 47: Contact angle variation of different TiO<sub>2</sub> formulations with respect to UV exposure time. Contact angles below 10° are considered zero due to hemi-wicking phenomena that make contact angle measurement impossible.



### 8.1.3 Parametric Models

#### 8.1.3.1 Linear Regression Model

Linear regression intends to find the connection between the independent variable column ( $\mathbf{x}$ ) and the dependent variable column ( $\mathbf{y}$ ) based on a linear function, as described in

$$\mathbf{y} = f(\mathbf{x}) = \beta_0 + \sum_{j=1}^p \beta_j \mathbf{x}_j \quad (8.6)$$

where  $\mathbf{x}_j$  represents the vector for the  $j^{\text{th}}$  independent variable, whereas  $\beta_0$  and  $\beta_j$ , respectively, represent the intercept and slope (unknowns) in the straight-line equation. It is possible to estimate the values of the linear equation constants by minimizing the Sum of Squared Errors (SSE) between  $\mathbf{x}$  and  $\mathbf{y}$  in Equation 8.6. This method is referred to as the standard OLS (Ordinary Least Squares) regression.

#### 8.1.3.2 Modified Ridge Regression: Kernel Ridge Regression

Ridge Regression can be coupled with a kernel function, in this case, a  $L_2$  error is used

$$\text{SSE}_{L_2} = \sum_{i=1}^N (y_i - f(\varphi_i))^2 + \lambda \sum_{j=1}^p \beta_j^2 \quad (8.7)$$

where  $\varphi$  is the kernel function and  $\lambda$ , which is tuned through a validation process, controls the amount of shrinkage. Larger values of  $\lambda$  lead to more shrinkage and therefore the coefficients,  $\beta_j$ , become more robust to collinearity. This equation is the Kernel Ridge Regressor (KRR) and uses the Ridge Regression loss function.

### 8.1.4 Non-Parametric Models

#### 8.1.4.1 Gradient Boosting Regression

Ensemble-based algorithms comprise numerous base models, each giving an alternative solution to the problem whose predictions are consolidated in some way (typically by weighted or unweighted voting or averaging) to create the final model output. Combining forecasts of a gathering of individual base models frequently creates more stable and accurate prediction than by any of the individual base models in the ensemble (550). The ensemble methods are commonly favored in light of the fact that they can reduce the variance (551; 552). There are several ways to ensemble models, such as bagging in Random Forest (553) or boosting in Gradient Boosting (552) algorithms. While in bagging multiple trees are used for prediction, in boosting, the weight of each tree is determined by rough estimates from previous trees.

Gradient Boosting Regression (GBR) is an ensemble, tree-based ML technique. Conceptually, GBR trains a sequence of simple decision trees (as weak learners), each boosting the accuracy of the previous tree. The procedure used in GBR is as follows:

1. Set the number of trees (estimators) and number of splits (tree depth).
2. Set the dependent variable  $f(\hat{x})$  to zero, and assume the residual ( $r_i$ ) and dependent variables ( $y_i$ ) to be equal for trial  $i$ .
3. The boosting process for each tree estimator ( $N$  number of trees) follows the next steps repeatedly and sequentially for  $t = 1, 2, \dots, T$ :

- (a) Grow a tree and calculate the residual for each dependent variable (computing negative gradient  $r$ ).
- (b) Fit an estimator (regression tree)  $\hat{f}^t$  to the training data  $(x, r)$ , where  $t$  denotes a single tree.

- (c) Calculate a new target variable  $\hat{f}$  by adding in a regularized new tree

$$f(\hat{x}) \leftarrow f(\hat{x}) + \lambda \hat{f}^t(x)$$

- (d) Update the residuals

$$r_i \leftarrow r_i - \lambda \hat{f}^t(x_i)$$

- 4. Derive the boosted model by summing all sequential trees; predicting  $y$  from  $x$

$$f(\hat{x}) = \sum_{t=1}^T \lambda \hat{f}^t(x)$$

GBR is commonly used due to its high accuracy.

#### 8.1.4.2 Support Vector Machine

Support Vector Machine (SVM) is a kernel-based classification model used mostly to locate the optimum fit of  $y$  into its best match of class based on  $x$ . Support Vector Regression (SVR) employs similar features to the classification SVM algorithm. SVR is equipped with different kernel functions ( $\psi$ ) to perform the best prediction. Equation 8.8 below describes the predicted value of  $y(x)$  based on SVR, as it adopts a suitable kernel function (also known as basis function) as follows:

$$y(x) = \sum_{m=1}^N \beta_m \psi_m(x) + \beta_0 \quad (8.8)$$

where  $N$  represents the number of kernel functions. The values of  $\beta$  and  $\beta_o$  are estimated by minimizing  $\psi$  as follows:

$$\begin{aligned}
 \min \psi(\beta, \beta_o) &= \sum_{i=1}^N V_{\epsilon}^r + \frac{1}{2} \|\beta\|^2 \\
 &= \sum_{i=1}^N V(y_i - f(x_i)) + \frac{\lambda}{2} \sum_{m=1}^N \beta_m^2 \\
 V_{\epsilon}^r &= \begin{cases} 0, & \text{if } |r| \leq \epsilon \\ |r| - \epsilon, & \text{otherwise} \end{cases}
 \end{aligned} \tag{8.9}$$

where  $V_{\epsilon}^r$  are the total errors of selected vectors. The optimal bound can be found from managing the number of support vectors by using  $\epsilon$  as the threshold. Also,  $\lambda$ , the penalty parameter, determines how flexible the model is. By adjusting the values of  $\lambda$  and  $\epsilon$ , one can balance the bias-variance influence.

#### 8.1.4.3 Artificial Neural Networks Models: MLP and GRNN

Artificial neural networks are designed to find a relationship between input and output data through a network of neurons that simulate the human neural system. The Multi-Layer Perceptron (MLP) neural system, also known as Back Propagation Neural Network (BPNN), is one of the most popular algorithms employed by scientists. Based on three layers, namely, input, hidden, and output, MLP finds the most complex relationships between  $x$  (input layer) and  $y$  (output layer) thorough the hidden layer. MLP regressor takes in  $x$  as the input and calculates the output  $y$  using assigned weights ( $w$ ) from the activation function,  $f$ . The activation function is an internal function that transforms input to the output data. Typical activation functions

include the sigmoid, tanh, step, identity function, and rectified linear unit (ReLU) (406). The weights are specific values assigned to each neuron, and are tuned with the activation function. The MLP algorithm can predict the output  $y$  from input  $x$  as follows:

$$y(x, w) = w_o + f\left(\sum_{i=1}^n w_i \phi_i(x)\right) = w_o + f\left(\sum_{i=1}^n w_i x_i\right) \quad (8.10)$$

where  $x$  is an input vector;  $w$  a vector of assigned weights; and  $\phi_x$  the basis function. To find the weights  $w_i$ , a back propagation approach is taken in MLP so that the loss function (SSE) is minimized using different methods (e.g., gradient decent method (GDM)).

In contrast, GRNN is a feed-forward network structured in a similar way to MLP. As a neural network algorithm, GRNN consists of an input layer, a hidden layer (Radial Basis Function (RBF)), and an output layer. GRNN predicts  $y$  from  $x$  according to the following equation

$$y = \frac{\sum_{i=1}^n y_i g_i(x)}{\sum_{i=1}^n g_i(x)} \quad (8.11)$$

where  $y_i$  denotes the output corresponding to input training vector  $x_i$ . The basis function in equations Equation 8.10 and Equation 8.11 is the major difference between MLP and GRNN;  $\phi_x$  is linear in MLP and Gaussian in GRNN. The basis function  $g_i(x)$  is obtained by computing the distance between two vectors based on the Gaussian function:

$$g_i(x) = \exp\left(-\frac{\|x - k_i\|^2}{2\sigma^2}\right) \quad i = 1, 2, 3, \dots, n \quad (8.12)$$

where  $\sigma$  is the smoothing factor and  $n$  is the number of neurons in the input layer, which is equal to the dimension of the input vector in the learning sample. This equation computes the geometric distance between the new input vector  $x$  and the training vector  $k_i$ .

### 8.1.5 Hyperparameters

Table VII shows different values and functions used for each hyperparameter in different machine learning techniques.

TABLE VII: Hyperparameters used in different ML techniques

Method	Hyper-parameter	Function/Values
SVR	Kernel	linear, poly, rbf,
	degree	1-20
	epsilon	0, 0.02, 0.05, 0.1
MLP	hidden layer sizes	(1,1), (2,2), (2,2,1)
	activation function	logistic, tanh, relu
	solver	lbfgs, adam
	learning rate	constant, invscaling, adaptive
GBR	loss function	ls, lad, huber, quantile
	number of estimators	3, 5, 6, 8
	criterion	friedman mse, mse, mae
	max depth	3, 4, 5, 6
KRR	kernel	linear, rbf, laplacian, polynomial, exponential
	degree	1-20
GRNN	sigma	0.01-1

### 8.1.6 Parametric Model Results

Figure 48 shows that the simple parametric models are unable to capture the patterns in the data; note the low average and high deviation in all scoring metrics.

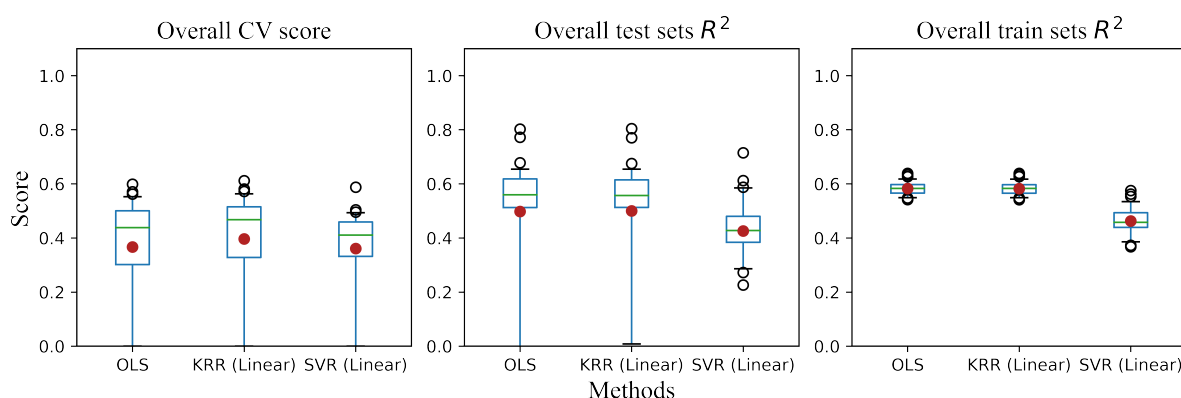


Figure 48: Overall performance evaluation of OLS (Ordinary Least Square), Kernel Ridge with a Linear function, and SVR with a linear kernel model. Red circles indicate the mean value for each model. Green lines mark the median.

## 8.2 Appendix B: Supplementary Materials for Chapter 3

Supplementary movies for: 1- Spreading of air bubbles on wettability-confined tracks of different widths, 2- Spreading of air bubbles of different initial diameters, and 3- Spreading on tracks submerged in different liquids could be found online (369).

### 8.3 Appendix C: Supplementary Materials for Chapter 5

#### 8.3.1 VC Seat

Figure 49 shows the Teflon plate with two pockets for accommodation the MOSFETs and providing a flat seating area for the vapor chamber. Blue tapes are used to hold the Teflon plate in its place.

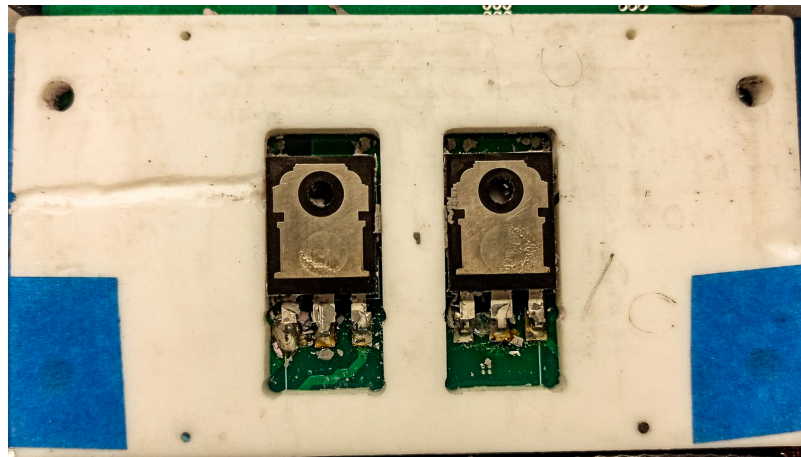


Figure 49: Teflon plate placing on the MOSFETs to provide a flat seat for the hybrid VC

#### 8.3.2 Profilometry

Figure 50 and Figure 51 show the contact profilometry images of the wedge-shape track and the low pressure circular well of the wettability-patterned condenser. As seen, the laser ablation creates a shallow microstructure with an average  $2\mu\text{m}$  high peaks and  $6\mu\text{m}$  deep valleys.



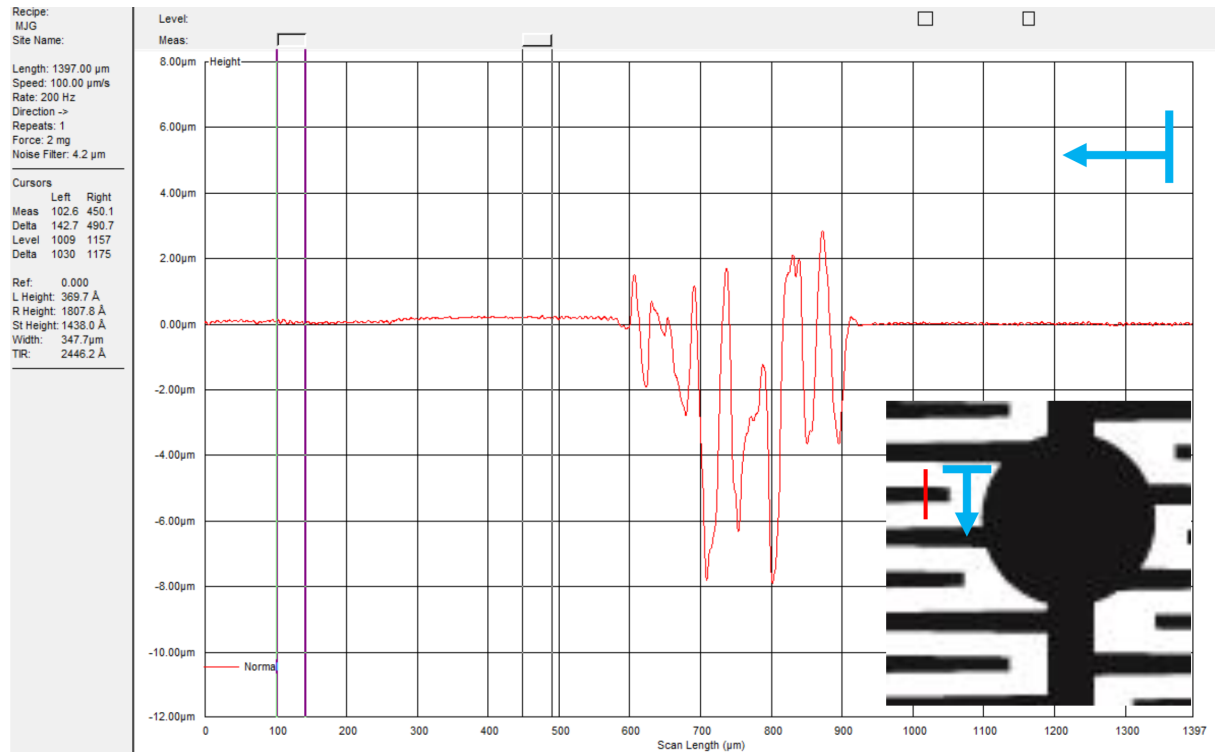


Figure 50: 2D profile of the superhydrophilic wedge-shape track. Blue arrow indicates the scanning direction. Red line denotes the scanned line.

## 8.4 Appendix D: Supplementary Materials for Chapter 6

### 8.4.1 Maximum Deflection of Wall Plate

Using the approach described in (554), the maximum deflection of the wickless plate (thinner of the two HP plates) at the minimum evacuation pressure of  $\approx 7$  kPa was calculated. Considering the physical properties of the copper plate (110 mirror-finish copper, McMaster-Carr, ASTM B152), namely, Young's modulus  $1.21 \times 10^{11}$  N/m<sup>2</sup>, Poisson's ratio 0.34, unsupported width 0.02 m, unsupported length 0.1 m, and thickness 0.001 m, we estimated that the maxi-

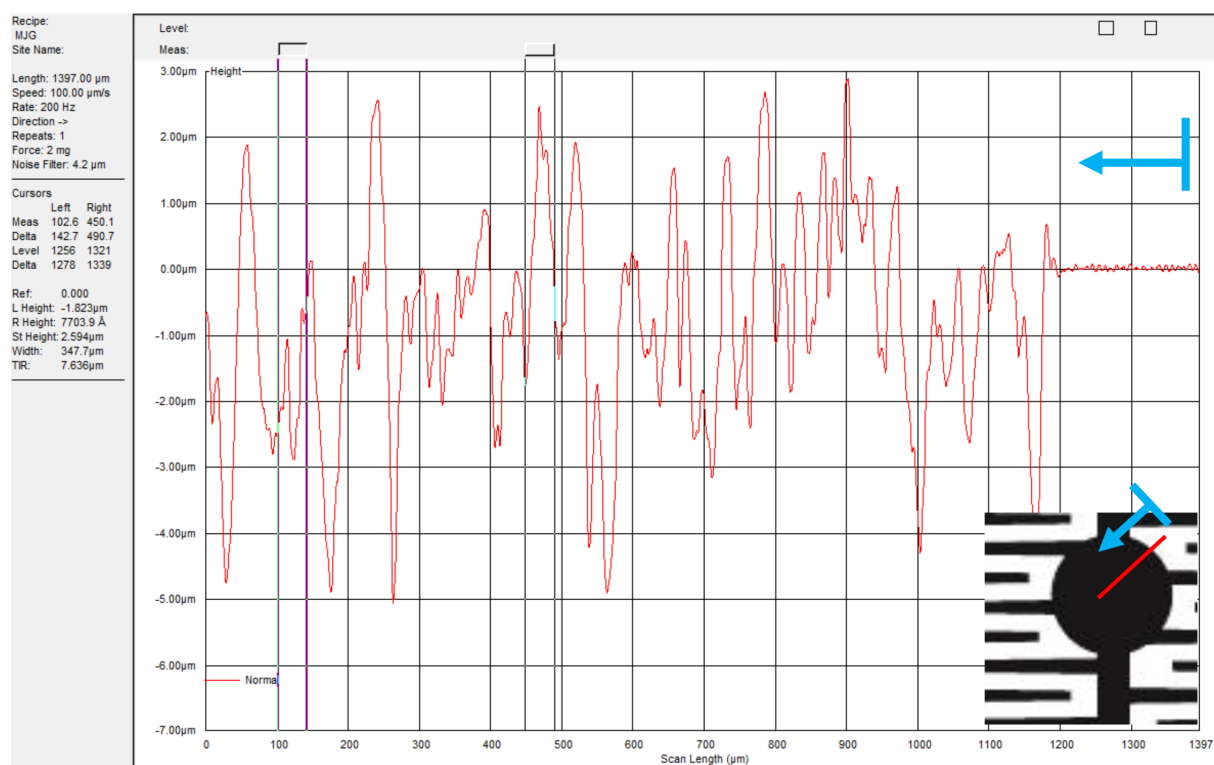


Figure 51: 2D profile of the superhydrophilic circular domain. Blue arrow indicates the scanning direction. Red line denotes the scanned line.

mum deflection at the geometric center of the condenser plate would be 0.018 mm. This estimate suggests that the wickless plate deflection at the maximum pressure difference between its two sides is negligible ( $< 1\%$ ) as compared to the initial gap distance of 2 mm from the top to bottom plate of the HP. So the gap is maintained without spacers for support.

#### **8.4.2 Heat Pipe System Details**

Figure 52 shows top-view photographs of the thermocouples, the heat pipe layered components and their relative placement. Figure 53 shows side views of two HP systems: (a) One with a Teflon insulating plate covering the entire wickless plate, and (b) another with the inactive cold plate, which allows thermal communication of the device with the environment. Figure 53(c) shows a photograph of the entire experimental apparatus.

#### **8.4.3 Role of NCGs**

Leakage of NCGs in HP systems is a major challenge. In the present study, we ensured that this problem was averted. Through a pressure gauge connected to the heat pipe via an on-off valve, the pressure before and after the experiment (system cooled down to room temperature and internal vapor pressure returned to initial condition) was monitored. Any observed pressure increase after an experiment was attributed to leakage and thus nullified the result. A typical experimental run took up to 2 hours (depending on the HP type and charging ratio). For all reported cases, there was no pressure increase after the experiment. Moreover, any leakage to the system would not only appear as a temperature drop on the condensation section, but would also influence the overall performance of the HP. For example, a leakage would progressively increase the temperature difference between  $T_{1,2}$  and  $T_{3,4}$ , as observed in

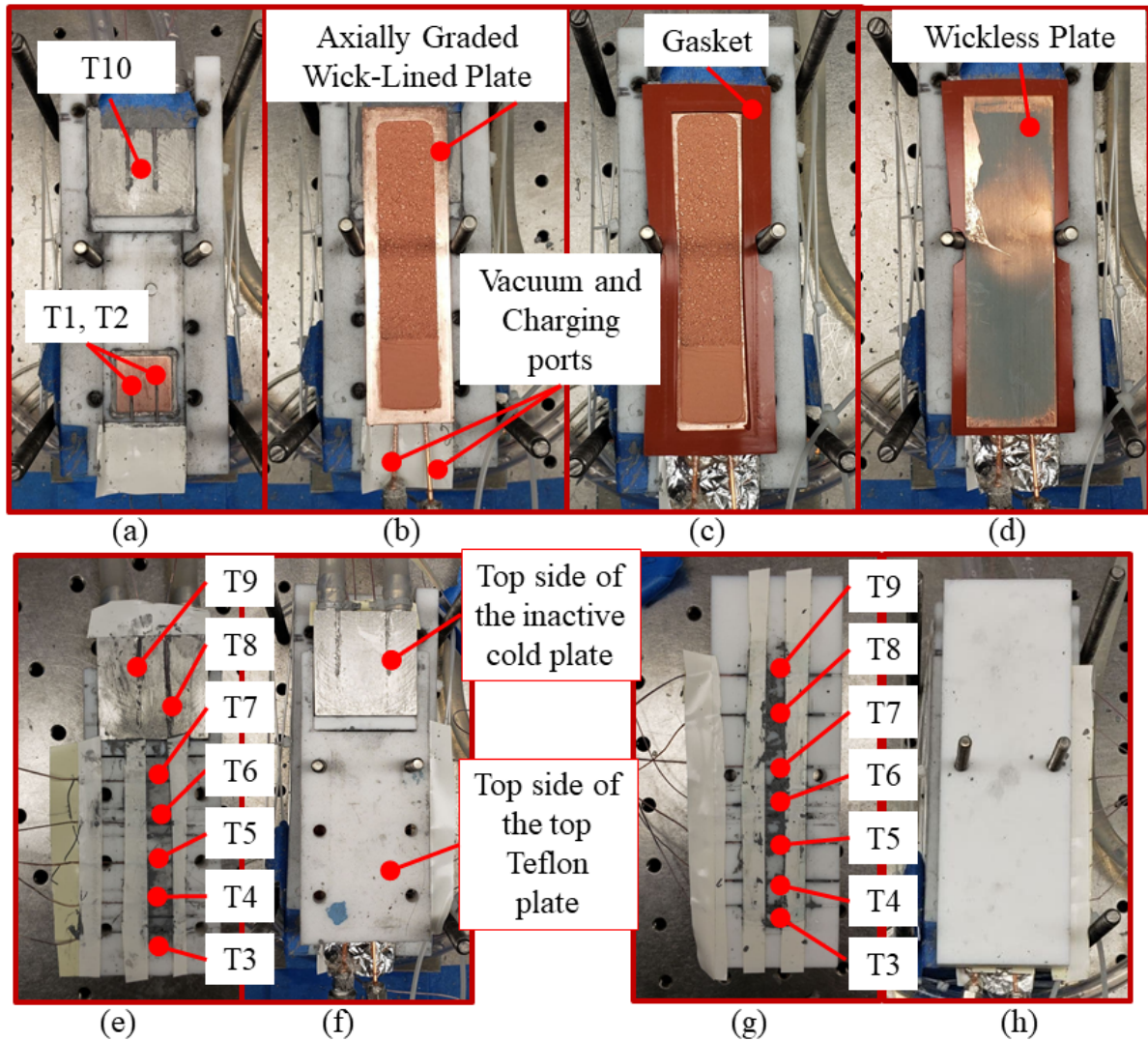


Figure 52: Bottom-to-top layer assembly of the HP. Thermocouple placement is also shown. (a) Thermocouples on the heater and active cold plate; (b) Wick-lined evaporator placement; (c) Gasket addition; (d) Wickless plate placement; (e) Thermocouple arrangement on the underside of the top Teflon plate and inactive cold plate; (f) Top Teflon plate has been inverted with the thermocouples now placed on its underside (not visible) and the TC wires at right hidden by the tape; (g) Thermocouple arrangement on the underside of the uniform top Teflon plate (no inactive cold plate present); (h) Top Teflon plate has been inverted with the thermocouples now placed on its underside (not visible) and the TC wires at right hidden by the tape.

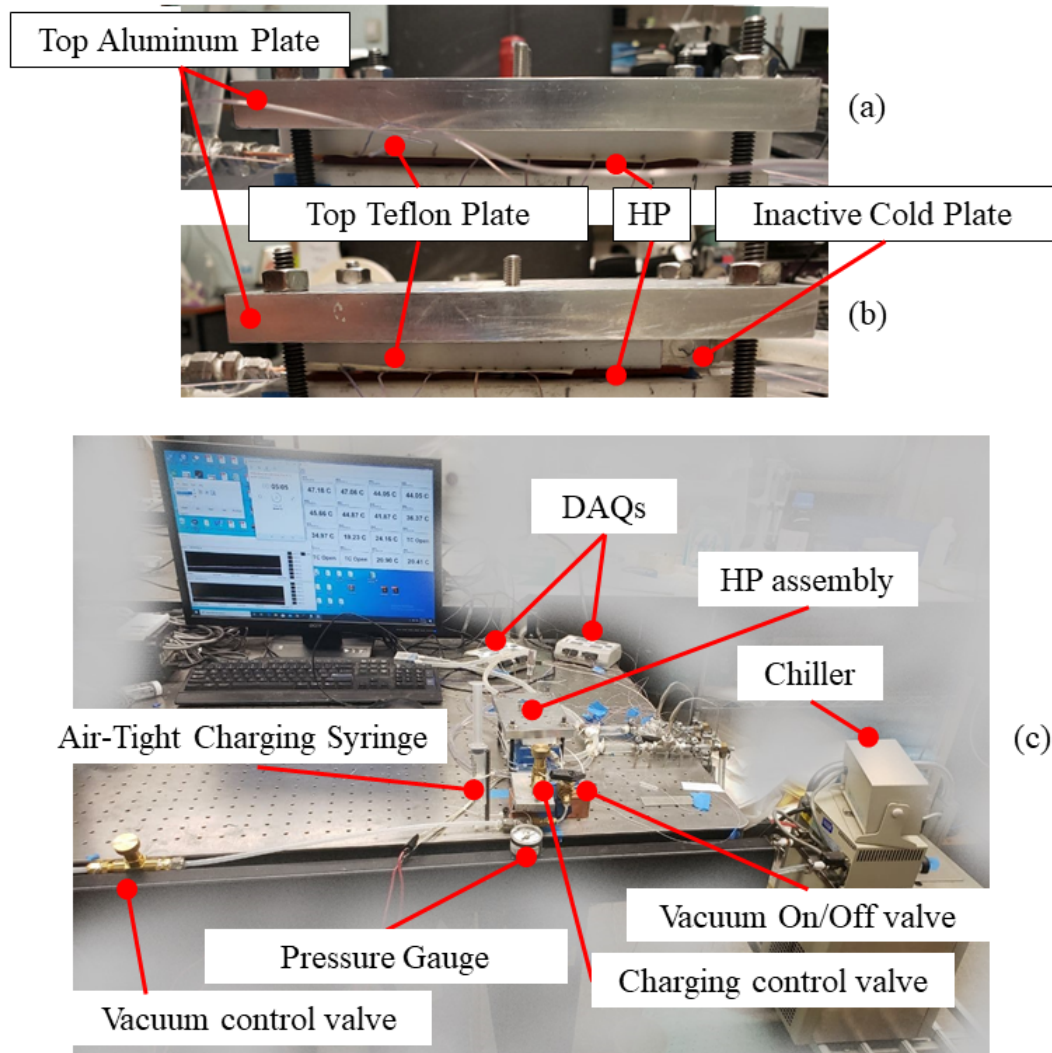


Figure 53: Fully assembled test setup. (a) Side view of the HP with fully-insulated wickless plate. (b) Side view of the HP with partially-insulated wickless plate and the inactive cold plate. (c) Full test setup apparatus.

all discarded experiments. To confirm the negligible role of NCGs in the present device's performance, a HP with a fully-insulated wickless side was fabricated and tested. As known from the literature (555), the NCG effect -if present- would appear as a vapor temperature difference along the device, so by creating an adiabatic condition on the wickless plate, the temperature difference as a result of the heat sink was eliminated. In the current study, T3-T9 were placed on the outer side of the plate and measure the plate's temperature. This is an important point, since the wickless plate is in contact with the gasket and, as shown in Figure 38(b), conduction heat transfer through the gasket from the wick-lined to the wickless plate is not negligible and thus could play a role. Nevertheless, in the case of the fully-insulated wickless plate, the temperature gradient should be minimized. We tested a AGW-WP HP with 25% CR and fully-insulated wickless plate for 1 hour under steady state condition at 30W.

Figure 54 shows the temperature rise of the HP when the heat load is raised from 10W to 30W in 5W increments. For the fully adiabatic wickless plate, the readings T1-T5 (thermocouples closest to the heater) increase in sync with minimal differences. Moreover, T7-T8 also rise and eventually catch up to T1-T5 at 25W. However, T8-T9 (condenser section), stay 4-6°C cooler than T3-T5 at 30W. Although this temperature difference is moderate compared to the non-adiabatic wickless plate case ( $\sim 15^\circ\text{C}$ ), it does not necessarily imply NCG presence. As shown in Figure 38(b), conduction heat transfer through the gasket, majorly between the wick-lined and wickless plate, is not negligible and could account for this phenomenon by transferring heat from the wickless plate (top) to the cold plate. As mentioned earlier, the thermocouples

are located on the outer side of the plate, thus recording the temperature of the plate rather than the vapor.

The system was allowed to run for 1 hour at a fixed heat input (30W) to further explore the possibility of NCG leakage over time. Appearance of any temperature difference, particularly between T5-T9, could indicate NCG leakage. As shown in Figure 54, the steady state temperatures remained unchanged during this period. Besides, another vacuum draw was performed after 1 hour to check a possible leakage. A low charging ratio was chosen for this test to minimize working fluid losses in the in-run vacuuming step. As seen in Figure 54, a temperature drop is observed for all thermocouples right after the evacuation, following the internal pressure

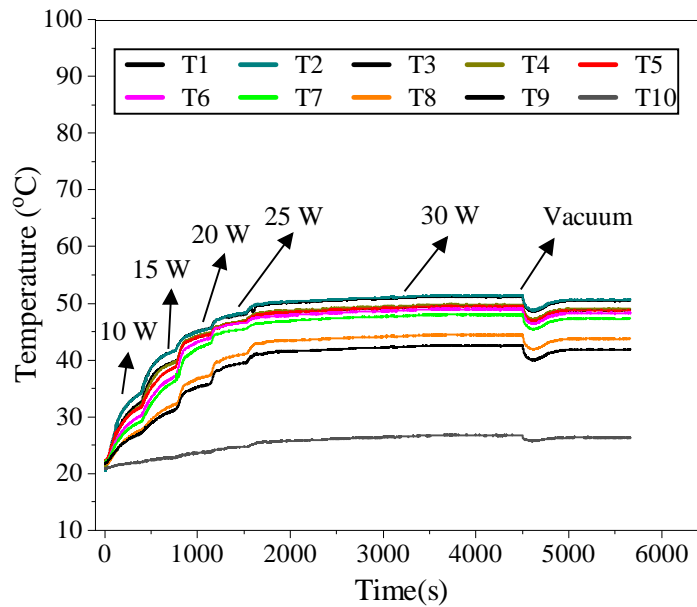


Figure 54: Raw thermocouple measurements vs. heating power over time for a HP with an insulated wickless plate.

drop and removal of some hot vapor. However, after approximately 4 minutes, all temperatures rose back to within  $\sim 0.5^{\circ}\text{C}$  of their pre-vacuum values and continued at steady state. This outcome testifies that the lower temperatures T8-T9 are not caused by leakage or accumulation of NCGs, since after 1 hour of running and subsequent evacuation, this difference remained unchanged. This also explains the temperature difference from T5 to T9 at lower heat fluxes as well. Due to the unavailability of the thermal conductivity of the gasket which was used for all HPs in this study, the amount of heat transferred through the gasket was not accounted in the calculations.

Based on the above, it is concluded that NCGs are not present to influence in the HP performance, and the temperature difference along the wickless plate arises from conduction heat transfer through the plate and the gasket. The larger temperature difference in the device with non-adiabatic boundary condition arises from heat rejection to the inactive heat sink (top in Figure 53(a)).

#### **8.4.4 Temperature on the Wick-lined Plate**

Figure 55 shows the variation of T10 vs. heat input for all cases examined in this study. As seen, the temperature rise at this location follows the same trend without significant differences among all cases. This is attributed to the high condensation thermal resistance on the wick structure (due to FwC).



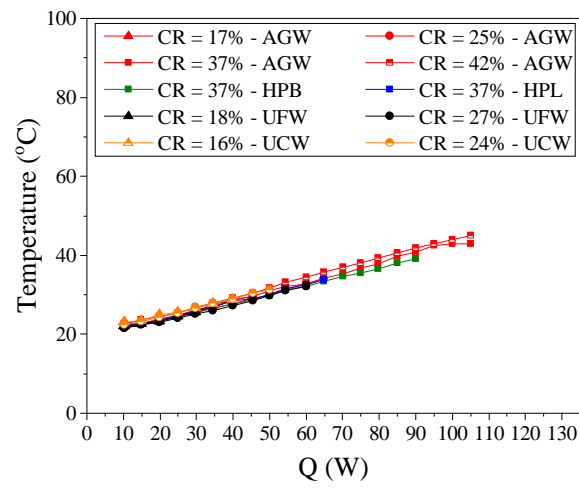


Figure 55: Thermocouple T10 temperature readings of flat heat pipes for all cases considered in this study.

## **8.5    Appendix E - Copyright and Permissions**

### **8.5.1    Copyright Form for Chapter 2**

Chapter 2 is subject to copyright. This chapter and its associated Appendix A: M. Jafari Gukeh, S. Moitra, A. N. Ibrahim, S. Derrible, and C. M. Megaridis. "Machine learning prediction of TiO<sub>2</sub>-coating wettability tuned via UV exposure". ACS Applied Materials Interfaces 13, no. 38 (2021): 46171-46179 (556). Permission to reproduce the whole article in a third-party publication was allowed only in the case of a thesis or dissertation (see Figure 56).

### **8.5.2    Copyright Form for Chapter 3**

Chapter 3 is subject to copyright. This chapter and its associated Appendix B: M. Jafari Gukeh, T. Roy, U. Sen, R. Ganguly, and C. M. Megaridis. "Lateral spreading of gas bubbles on submerged wettability-confined tracks." Langmuir 36, no. 40 (2020): 11829-11835 (369). Permission to reproduce the whole article in a third-party publication was allowed only in the case of a thesis or dissertation (see Figure 57).

### **8.5.3    Copyright Form for Chapter 6**

Chapter 6 is subject to copyright. This chapter and its associated Appendix B: Gukeh, Mohamad Jafari, G. Damoulakis, and C. M. Megaridis. "Experimental investigation of low-profile heat pipe with wickless wettability-patterned condenser." In 2021 20th IEEE Intersociety Conference on Thermal and Thermomechanical Phenomena in Electronic Systems (iTherm), pp. 271-279. IEEE, 2021. (361)

M. Jafari Gukeh, G. Damoulakis, and C. M. Megaridis. Low-profile heat pipe consisting of wick-lined and non-adiabatic wickless wettability-patterned surfaces." Applied Thermal Engineering

211, 118433, 2022. (458). Permission to reproduce the whole article in a third-party publication was allowed only in the case of a thesis or dissertation (see Figure 58 and Figure 59).

#### **8.5.4    Copyright Form for Figure 3**

Permission to reproduce a figure was allowed in this dissertation (see Figure 60 and Figure 61)

#### **8.5.5    Copyright Form for Figure 4**

Permission to reproduce a figure was allowed in this dissertation (see Figure 62)

8/1/22, 1:15 PM

Rightslink® by Copyright Clearance Center



Home

Help ▾

Live Chat

Sign in

Create Account



### Machine Learning Prediction of TiO<sub>2</sub>-Coating Wettability Tuned via UV Exposure

**Author:** Mohamad Jafari Gukeh, Shashwata Moitra, Ali Noaman Ibrahim, et al

**Publication:** Applied Materials

**Publisher:** American Chemical Society

**Date:** Sep 1, 2021

*Copyright © 2021, American Chemical Society*

#### PERMISSION/LICENSE IS GRANTED FOR YOUR ORDER AT NO CHARGE

This type of permission/license, instead of the standard Terms and Conditions, is sent to you because no fee is being charged for your order. Please note the following:

- Permission is granted for your request in both print and electronic formats, and translations.
- If figures and/or tables were requested, they may be adapted or used in part.
- Please print this page for your records and send a copy of it to your publisher/graduate school.
- Appropriate credit for the requested material should be given as follows: "Reprinted (adapted) with permission from {COMPLETE REFERENCE CITATION}. Copyright {YEAR} American Chemical Society." Insert appropriate information in place of the capitalized words.
- One-time permission is granted only for the use specified in your RightsLink request. No additional uses are granted (such as derivative works or other editions). For any uses, please submit a new request.

If credit is given to another source for the material you requested from RightsLink, permission must be obtained from that source.

[BACK](#)
[CLOSE WINDOW](#)

© 2022 Copyright - All Rights Reserved | [Copyright Clearance Center, Inc.](#) | [Privacy statement](#) | [Data Security and Privacy](#)  
 | [For California Residents](#) | [Terms and Conditions](#) Comments? We would like to hear from you. E-mail us at  
[customercare@copyright.com](mailto:customercare@copyright.com)

Figure 56: Copyright information for Chapter 2

8/1/22, 1:17 PM

Rightslink® by Copyright Clearance Center



Home



Help ▾



Live Chat



Sign in



Create Account



Most Trusted. Most Cited. Most Read.

### Lateral Spreading of Gas Bubbles on Submerged Wettability-Confining Tracks

**Author:** Mohamad Jafari Gukeh, Tamal Roy, Uddalok Sen, et al

**Publication:** Langmuir

**Publisher:** American Chemical Society

**Date:** Oct 1, 2020

Copyright © 2020, American Chemical Society

#### PERMISSION/LICENSE IS GRANTED FOR YOUR ORDER AT NO CHARGE

This type of permission/license, instead of the standard Terms and Conditions, is sent to you because no fee is being charged for your order. Please note the following:

- Permission is granted for your request in both print and electronic formats, and translations.
- If figures and/or tables were requested, they may be adapted or used in part.
- Please print this page for your records and send a copy of it to your publisher/graduate school.
- Appropriate credit for the requested material should be given as follows: "Reprinted (adapted) with permission from {COMPLETE REFERENCE CITATION}. Copyright {YEAR} American Chemical Society." Insert appropriate information in place of the capitalized words.
- One-time permission is granted only for the use specified in your RightsLink request. No additional uses are granted (such as derivative works or other editions). For any uses, please submit a new request.

If credit is given to another source for the material you requested from RightsLink, permission must be obtained from that source.

[BACK](#)
[CLOSE WINDOW](#)

© 2022 Copyright - All Rights Reserved | [Copyright Clearance Center, Inc.](#) | [Privacy statement](#) | [Data Security and Privacy](#)  
 | [For California Residents](#) | [Terms and Conditions](#) Comments? We would like to hear from you. E-mail us at  
[customercare@copyright.com](mailto:customercare@copyright.com)

Figure 57: Copyright information for Chapter 3

8/1/22, 1:19 PM

Rightslink® by Copyright Clearance Center



Home

Help ▾

Live Chat

Sign in

Create Account



### Low-profile heat pipe consisting of wick-lined and non-adiabatic wickless wettability-patterned surfaces

**Author:** Mohamad Jafari Gukeh, George Damoulakis, Constantine M. Megaridis

**Publication:** Applied Thermal Engineering

**Publisher:** Elsevier

**Date:** 5 July 2022

© 2022 Elsevier Ltd. All rights reserved.

#### Journal Author Rights

Please note that, as the author of this Elsevier article, you retain the right to include it in a thesis or dissertation, provided it is not published commercially. Permission is not required, but please ensure that you reference the journal as the original source. For more information on this and on your other retained rights, please visit: <https://www.elsevier.com/about/our-business/policies/copyright#Author-rights>

BACK

CLOSE WINDOW

© 2022 Copyright - All Rights Reserved | [Copyright Clearance Center, Inc.](#) | [Privacy statement](#) | [Data Security and Privacy](#)  
 | [For California Residents](#) | [Terms and Conditions](#) Comments? We would like to hear from you. E-mail us at [customercare@copyright.com](mailto:customercare@copyright.com)

Figure 58: Copyright information for Chapter 6

9/9/22, 5:30 PM

Rightslink® by Copyright Clearance Center

[Home](#)
[Help](#)
[Email Support](#)
[Sign in](#)
[Create Account](#)

Requesting permission to reuse content from an IEEE publication

**Experimental investigation of low-profile heat pipe with wickless wettability-patterned condenser**

Conference Proceedings:  
2021 20th IEEE Intersociety Conference on Thermal and Thermomechanical Phenomena in Electronic Systems (iTherm)

Author: Mohamad Jafari Gukeh

Publisher: IEEE

Date: 01 June 2021

*Copyright © 2021, IEEE*

**Thesis / Dissertation Reuse**

The IEEE does not require individuals working on a thesis to obtain a formal reuse license, however, you may print out this statement to be used as a permission grant:

*Requirements to be followed when using any portion (e.g., figure, graph, table, or textual material) of an IEEE copyrighted paper in a thesis:*

- 1) In the case of textual material (e.g., using short quotes or referring to the work within these papers) users must give full credit to the original source (author, paper, publication) followed by the IEEE copyright line © 2011 IEEE.
- 2) In the case of illustrations or tabular material, we require that the copyright line © [Year of original publication] IEEE appear prominently with each reprinted figure and/or table.
- 3) If a substantial portion of the original paper is to be used, and if you are not the senior author, also obtain the senior author's approval.

*Requirements to be followed when using an entire IEEE copyrighted paper in a thesis:*

- 1) The following IEEE copyright/ credit notice should be placed prominently in the references: © [year of original publication] IEEE. Reprinted, with permission, from [author names, paper title, IEEE publication title, and month/year of publication]
- 2) Only the accepted version of an IEEE copyrighted paper can be used when posting the paper or your thesis on-line.
- 3) In placing the thesis on the author's university website, please display the following message in a prominent place on the website: In reference to IEEE copyrighted material which is used with permission in this thesis, the IEEE does not endorse any of [university/educational entity's name goes here]'s products or services. Internal or personal use of this material is permitted. If interested in reprinting/republishing IEEE copyrighted material for advertising or promotional purposes or for creating new collective works for resale or redistribution, please go to [http://www.ieee.org/publications\\_standards/publications/rights/rights\\_link.html](http://www.ieee.org/publications_standards/publications/rights/rights_link.html) to learn how to obtain a License from RightsLink.

If applicable, University Microfilms and/or ProQuest Library, or the Archives of Canada may supply single copies of the dissertation.

[BACK](#)
[CLOSE WINDOW](#)

© 2022 Copyright - All Rights Reserved | Copyright Clearance Center, Inc. | Privacy statement | Data Security and Privacy

| For California Residents | Terms and Conditions Comments? We would like to hear from you. E-mail us at [customer-care@copyright.com](mailto:customer-care@copyright.com)

https://s100.copyright.com/AppDispatchServlet#formTop

1/1

Figure 59: Copyright information for Chapter 6

## License Details

This Agreement between university of Illinois at Chicago -- Mohamad Jafari Gukeh ("You") and Elsevier ("Elsevier") consists of your license details and the terms and conditions provided by Elsevier and Copyright Clearance Center.

[Print](#)
[Copy](#)

License Number	5360390418366
License date	Aug 01, 2022
Licensed Content Publisher	Elsevier
Licensed Content Publication	Applied Thermal Engineering
Licensed Content Title	Recent advances in the optimization of evaporator wicks of vapor chambers: From mechanism to fabrication technologies
Licensed Content Author	Xin Cheng,Guang Yang,Jingyi Wu
Licensed Content Date	Apr 1, 2021
Licensed Content Volume	188
Licensed Content Issue	n/a
Licensed Content Pages	1
Type of Use	reuse in a thesis/dissertation
Portion	figures/tables/illustrations
Number of figures/tables/illustrations	1
Format	electronic
Are you the author of this Elsevier article?	No
Will you be translating?	No
Title	Case Studies of Surface Engineering Applications in Thermo/Fluidic Systems
Institution name	University of Illinois at Chicago
Expected presentation date	Jan 2023
Order reference number	10001
Portions	Fig. 3
Requestor Location	university of Illinois at Chicago 842 West Taylor street  Chicago, IL 60607 United States Attn: university of Illinois at Chicago 98-0397604
Publisher Tax ID	98-0397604
Total	<b>0.00 USD</b>

Figure 60: Copyright information for Figure 3



8/1/22, 4:28 PM

Rightslink® by Copyright Clearance Center



Home



Help ▾



Email Support



Mohamad Jafari Gukeh ▾

**Nano- and Microstructures for Thin-Film Evaporation—A Review**

Author: J. L. Plawsky, , A. G. Fedorov, et al

Publication: Nanoscale &amp; Microscale Thermophysical Engineering

Publisher: Taylor &amp; Francis

Date: Jul 3, 2014

*Rights managed by Taylor & Francis***Thesis/Dissertation Reuse Request**

Taylor & Francis is pleased to offer reuses of its content for a thesis or dissertation free of charge contingent on resubmission of permission request if work is published.

BACK

CLOSE

© 2022 Copyright - All Rights Reserved | [Copyright Clearance Center, Inc.](#) | [Privacy statement](#) | [Data Security and Privacy](#)  
 | [For California Residents](#) | [Terms and Conditions](#) Comments? We would like to hear from you. E-mail us at  
[customercare@copyright.com](mailto:customercare@copyright.com)

Figure 61: Copyright information for Figure 4

8/4/22, 9:09 AM

Rightslink® by Copyright Clearance Center



Help

Live Chat

Mohamad Jafari Gukeh



**Chapter:**  
Chapter Four Recent Advances in Vapor Chamber Transport Characterization for High-Heat-Flux Applications

**Book:** Advances in Heat Transfer

**Author:** Justin A. Weibel, Suresh V. Garimella

**Publisher:** Elsevier

**Date:** Jan 1, 2013

Copyright © 2013 Elsevier Inc. All rights reserved.

### Order Completed

Thank you for your order.

This Agreement between Mohamad Jafari Gukeh ("You") and Elsevier ("Elsevier") consists of your order details and the terms and conditions provided by Elsevier and Copyright Clearance Center.

License number      Reference confirmation email for license number

License date      Aug, 04 2022

#### Licensed Content

Licensed Content Publisher	Elsevier
Licensed Content Publication	Elsevier Books
Licensed Content Title	Advances in Heat Transfer
Licensed Content Author	Justin A. Weibel, Suresh V. Garimella
Licensed Content Date	2013
Licensed Content Volume	45
Licensed Content Issue	n/a
Licensed Content Pages	93

#### Order Details

Type of Use	reuse in a thesis/dissertation
Portion	figures/tables/illustrations
Number of figures/tables/illustrations	1
Format	electronic
Are you the author of this Elsevier chapter?	No
Will you be translating?	No

#### About Your Work

Title	Case Studies of Surface Engineering Applications in Thermo/Fluidic Systems
Institution name	University of Illinois at Chicago
Expected presentation date	Jan 2023

#### Additional Data

Order reference number	10002
Portions	Figure 4.2

<https://s100.copyright.com/AppDispatchServlet>

1/2

Figure 62: Copyright information for Figure 4

## CITED LITERATURE

1. Bouasse, H.: Capillarite: phenomenes superficiels. Delagrave, 1924.
2. De Gennes, P.-G., Brochard-Wyart, F., and Quéré, D.: Capillarity and wetting phenomena: drops, bubbles, pearls, waves. Springer Science & Business Media, 2013.
3. Wenzel, R. N.: Resistance of solid surfaces to wetting by water. Industrial & Engineering Chemistry, 28(8):988–994, 1936.
4. Cassie, A. and Baxter, S.: Wettability of porous surfaces. Transactions of the Faraday society, 40:546–551, 1944.
5. Cassie, A.: Contact angles. Discussions of the Faraday society, 3:11–16, 1948.
6. Otitoju, T., Ahmad, A., and Ooi, B.: Superhydrophilic (superwetting) surfaces: A review on fabrication and application. Journal of industrial and engineering chemistry, 47:19–40, 2017.
7. Zhang, L., Zhao, N., and Xu, J.: Fabrication and application of superhydrophilic surfaces: a review. Journal of Adhesion Science and Technology, 28(8-9):769–790, 2014.
8. Ma, M. and Hill, R. M.: Superhydrophobic surfaces. Current opinion in colloid & interface science, 11(4):193–202, 2006.
9. Jeevahan, J., Chandrasekaran, M., Britto Joseph, G., Durairaj, R., and Mageshwaran, G.: Superhydrophobic surfaces: a review on fundamentals, applications, and challenges. Journal of Coatings Technology and Research, 15(2):231–250, 2018.
10. Yan, X., Qin, Y., Chen, F., Zhao, G., Sett, S., Hoque, M. J., Rabbi, K. F., Zhang, X., Wang, Z., Li, L., et al.: Laplace pressure driven single-droplet jumping on structured surfaces. ACS nano, 14(10):12796–12809, 2020.
11. Simon, M. G., Lin, R., Fisher, J. S., and Lee, A. P.: A laplace pressure based microfluidic trap for passive droplet trapping and controlled release. Biomicrofluidics, 6(1):014110, 2012.

12. Wu, L., Dong, Z., Li, F., and Song, Y.: Designing laplace pressure pattern for microdroplet manipulation. Langmuir, 34(2):639–645, 2018.
13. Choi, C.-H., Jeong, J.-M., Kang, S.-M., Lee, C.-S., and Lee, J.: Synthesis of monodispersed microspheres from laplace pressure induced droplets in micromolds. Advanced Materials, 24(37):5078–5082, 2012.
14. Finn, R.: Capillary surface interfaces. Notices of the AMS, 46(7):770–781, 1999.
15. Chen, H., Zhang, P., Zhang, L., Liu, H., Jiang, Y., Zhang, D., Han, Z., and Jiang, L.: Continuous directional water transport on the peristome surface of nepenthes alata. Nature, 532(7597):85–89, 2016.
16. Ghosh, A., Ganguly, R., Schutzius, T. M., and Megaridis, C. M.: Wettability patterning for high-rate, pumpless fluid transport on open, non-planar microfluidic platforms. Lab on a Chip, 14(9):1538–1550, 2014.
17. Alheshibri, M., Rogers, N., Sommers, A., and Eid, K.: Spontaneous movement of water droplets on patterned cu and al surfaces with wedge-shaped gradients. Applied Physics Letters, 102(17):174103, 2013.
18. Tan, X., Zhu, Y., Shi, T., Tang, Z., and Liao, G.: Patterned gradient surface for spontaneous droplet transportation and water collection: simulation and experiment. Journal of Micromechanics and Microengineering, 26(11):115009, 2016.
19. Guan, J. H., Ruiz-Gutiérrez, É., Xu, B. B., Wood, D., McHale, G., Ledesma-Aguilar, R., and Wells, G. G.: Drop transport and positioning on lubricant-impregnated surfaces. Soft Matter, 13(18):3404–3410, 2017.
20. Song, Y.-y., Liu, Y., Jiang, H.-b., Li, S.-y., Kaya, C., Stegmaier, T., Han, Z.-w., and Ren, L.-q.: Temperature-tunable wettability on a bioinspired structured graphene surface for fog collection and unidirectional transport. Nanoscale, 10(8):3813–3822, 2018.
21. Zhang, J. and Han, Y.: Shape-gradient composite surfaces: water droplets move uphill. Langmuir, 23(11):6136–6141, 2007.
22. Zheng, Y., Cheng, J., Zhou, C., Xing, H., Wen, X., Pi, P., and Xu, S.: Droplet motion on a shape gradient surface. Langmuir, 33(17):4172–4177, 2017.

23. Sen, U., Chatterjee, S., Ganguly, R., Dodge, R., Yu, L., and Megaridis, C. M.: Scaling laws in directional spreading of droplets on wettability-confined diverging tracks. Langmuir, 34(5):1899–1907, 2018.
24. Elsharkawy, M., Schutzius, T. M., and Megaridis, C. M.: Inkjet patterned superhydrophobic paper for open-air surface microfluidic devices. Lab on a Chip, 14(6):1168–1175, 2014.
25. Liang, Y.-E., Tsao, H.-K., and Sheng, Y.-J.: Drops on hydrophilic conical fibers: gravity effect and coexistent states. Langmuir, 31(5):1704–1710, 2015.
26. Ju, J., Xiao, K., Yao, X., Bai, H., and Jiang, L.: Bioinspired conical copper wire with gradient wettability for continuous and efficient fog collection. Advanced Materials, 25(41):5937–5942, 2013.
27. Khoo, H. and Tseng, F.-G.: Self-directed movements of droplets on radially patterned surfaces based on self-assembled monolayers. In 2006 International Conference on Microtechnologies in Medicine and Biology, pages 273–276. IEEE, 2006.
28. Bliznyuk, O., Seddon, J. R., Veligura, V., Kooij, E. S., Zandvliet, H. J., and Poelsema, B.: Directional liquid spreading over chemically defined radial wettability gradients. ACS applied materials & interfaces, 4(8):4141–4148, 2012.
29. Li, J., Tian, X., Perros, A. P., Franssila, S., and Jokinen, V.: Self-propelling and positioning of droplets using continuous topography gradient surface. Advanced Materials Interfaces, 1(3):1400001, 2014.
30. Zhang, C., Zhang, B., Ma, H., Li, Z., Xiao, X., Zhang, Y. and Cui, X., Yu, C., Cao, M., and Jiang, L.: Bioinspired pressure-tolerant asymmetric slippery surface for continuous self-transport of gas bubbles in aqueous environment. ACS Nano, 12(2):2048–2055, 2018.
31. Liu, G., Zhang, C., Liu, M., Guo, Z., Wang, X., Yu, C., and Cao, M.: Smart manipulation of gas bubbles in harsh environments via a fluorinert-infused shape-gradient slippery surface. Transactions of Tianjin University, 26(6):441–449, 2020.
32. Feng, W. and Bhushan, B.: Spontaneous transport of air bubbles on bioinspired superhydrophilic triangular patterns. Journal of colloid and interface science, 575:399–405, 2020.

33. Xue, X., Yu, C., Wang, J., and Jiang, L.: Superhydrophobic cones for continuous collection and directional transportation of co<sub>2</sub> microbubbles in co<sub>2</sub> supersaturated solutions. ACS nano, 10(12):10887–10893, 2016.
34. Zhou, J., Qi, B., Zhang, Y., and Wei, J.: Pool boiling heat transfer and bubble behavior on the treelike networks with wedge-shaped channels. International Communications in Heat and Mass Transfer, 118:104811, 2020.
35. Incropera, F. P., DeWitt, D. P., Bergman, T. L., Lavine, A. S., et al.: Fundamentals of heat and mass transfer, volume 6. Wiley New York, 1996.
36. Bergman, T. L., Lavine, A. S., Incropera, F. P., and DeWitt, D. P.: Introduction to heat transfer. John Wiley & Sons, 2011.
37. Bejan, A. and Kraus, A. D.: Heat transfer handbook, volume 1. John Wiley & Sons, 2003.
38. Bergman, T. L., Incropera, F. P., DeWitt, D. P., and Lavine, A. S.: Fundamentals of heat and mass transfer. John Wiley & Sons, 2011.
39. Perrot, P.: A to Z of Thermodynamics. Oxford University Press on Demand, 1998.
40. Collier, J. G. and Thome, J. R.: Convective boiling and condensation. Clarendon Press, 1994.
41. Othmer, D. F.: The condensation of steam. Industrial & Engineering Chemistry, 21(6):576–583, 1929.
42. Meisenburg, S. J., Boarts, R. M., and Badger, W. L.: The influence of small concentrations of air in steam on the steam-film coefficient of heat transfer. University of Michigan, 1935.
43. Uchida, H., Oyama, A., and Togo, Y.: Evaluation of post-incident cooling systems of light water power reactors. Technical report, Tokyo Univ., 1964.
44. Kroger, D. G. and Rohsenow, W. M.: Condensation heat transfer in the presence of a non-condensable gas. International Journal of Heat and Mass Transfer, 11(1):15–26, 1968.

45. Al-Diwany, H. and Rose, J.: Free convection film condensation of steam in the presence of non-condensing gases. International Journal of Heat and Mass Transfer, 16(7):1359–1369, 1973.
46. Zheng, S., Eimann, F., Philipp, C., Fieback, T., and Gross, U.: Dropwise condensation in the presence of non-condensable gas: Interaction effects of the droplet array using the distributed point sink method. International Journal of Heat and Mass Transfer, 141:34–47, 2019.
47. Shen, L., Tang, G., Li, Q., and Shi, Y.: Hybrid wettability-induced heat transfer enhancement for condensation with noncondensable gas. Langmuir, 35(29):9430–9440, 2019.
48. Sigsbee, R.: Vapor to condensed-phase heterogeneous nucleation. In Nucleation, pages 151–224. Dekker New York, 1969.
49. Nusselt, W.: Die oberflächenkondensation des wasserdampfes. VDI-Zs, 60:541, 1916.
50. Yun, R., Heo, J., and Kim, Y.: Effects of surface roughness and tube materials on the filmwise condensation heat transfer coefficient at low heat transfer rates. International communications in heat and mass transfer, 33(4):445–450, 2006.
51. Liu, P., Ho, J. Y., Wong, T. N., and Toh, K. C.: Convective filmwise condensation on the outer surface of a vertical tube: A theoretical analysis. International Journal of Heat and Mass Transfer, 161:120266, 2020.
52. Liu, J. and Grigoriev, R. O.: Analytical solution for filmwise condensation in confined high-aspect ratio geometry. International Journal of Heat and Mass Transfer, 133:561–571, 2019.
53. Zhang, W., Wang, S., and Lianbo, M.: Analytical modeling for vapor condensation in the presence of noncondensable gas and experimental validation. Journal of Heat Transfer, 143(1), 2021.
54. Marchuk, I. and Kabov, O.: Model of filmwise vapor condensation on curved surfaces. In Doklady Physics, volume 61, pages 19–23. Springer, 2016.
55. Han, D. and Lee, K.-J.: Experimental study on condensation heat transfer enhancement and pressure drop penalty factors in four microfin tubes. International Journal of Heat and Mass Transfer, 48(18):3804–3816, 2005.

56. Olivier, J. A., Liebenberg, L., Thome, J. R., and Meyer, J. P.: Heat transfer, pressure drop, and flow pattern recognition during condensation inside smooth, helical micro-fin, and herringbone tubes. International Journal of Refrigeration, 30(4):609–623, 2007.
57. Ho, J. Y., Leong, K. C., and Wong, T. N.: Forced convection condensation of r134a in three-dimensional conical pin fin tubes. International Journal of Heat and Mass Transfer, 144:118599, 2019.
58. Ho, J. and Leong, K.: Effect of fin pitch on the filmwise condensation of steam on three-dimensional conical pin fin arrays: A comparative study. International Journal of Heat and Mass Transfer, 150:119328, 2020.
59. Ho, J. and Leong, K.: A critical review of filmwise natural and forced convection condensation on enhanced surfaces. Applied Thermal Engineering, 186:116437, 2021.
60. Ji, W.-T., Mao, S.-F., Chong, G.-H., Zhao, C.-Y., Zhang, H., and Tao, W.-Q.: Effect of fin structure on the condensation of r-134a, r-1234ze (e), and r-1233zd (e) outside the titanium tubes. Journal of Heat Transfer, 142(1):014502, 2020.
61. Bonneau, C., Josset, C., Melot, V., and Auvity, B.: Comprehensive review of pure vapour condensation outside of horizontal smooth tubes. Nuclear Engineering and Design, 349:92–108, 2019.
62. Rifert, V., Sereda, V., Gorin, V., Barabash, P., and Solomakha, A.: Heat transfer during film condensation inside plain tubes. review of experimental research. Heat and mass transfer, 56(3):691–713, 2020.
63. Rifert, V., Sereda, V., and Solomakha, A.: Heat transfer during film condensation inside plain tubes. review of theoretical research. Heat and Mass Transfer, 55(11):3041–3051, 2019.
64. Rose, J.: Dropwise condensation theory and experiment: a review. Proceedings of the Institution of Mechanical Engineers, Part A: Journal of Power and Energy, 216(2):115–128, 2002.
65. von Eucken, A.: Energy and material exchange at border areas. Nat. Sci., 25:209–218, 1937.



66. McCormick, J. L. and Baer, E.: On the mechanism of heat transfer in dropwise condensation. Journal of Colloid Science, 18(3):208–216, 1963.
67. Umur, A. and Griffith, P.: Mechanism of Dropwise Condensation. Journal of Heat Transfer, 87(2):275–282, 05 1965.
68. Jakob, M.: Mechanical engineering, heat transf. Evaporation Condens, 58:643, 1936.
69. Tsuruta, T. and Tanaka, H.: Microscopic study of dropwise condensation. Trans. Jap. Soc. Mech. Engrs, Ser. B, 49:2181–2189, 1983.
70. Le Fevre, E. and Rose, J.: An experimental study of heat transfer by dropwise condensation. International Journal of Heat and Mass Transfer, 8(8):1117–1133, 1965.
71. Citakoglu, E. and Rose, J.: Dropwise condensation—some factors influencing the validity of heat-transfer measurements. International Journal of Heat and Mass Transfer, 11(3):523–537, 1968.
72. Tanner, D., Pope, D., Potter, C., and West, D.: Heat transfer in dropwise condensation at low steam pressures in the absence and presence of non-condensable gas. International Journal of Heat and Mass Transfer, 11(2):181–190, 1968.
73. Abu-Orabi, M.: Modeling of heat transfer in dropwise condensation. International journal of heat and mass transfer, 41(1):81–87, 1998.
74. Qi, B., Wei, J., Zhang, L., and Xu, H.: A fractal dropwise condensation heat transfer model including the effects of contact angle and drop size distribution. International Journal of Heat and Mass Transfer, 83:259–272, 2015.
75. Niu, D., Guo, L., Hu, H., and Tang, G.: Dropwise condensation heat transfer model considering the liquid-solid interfacial thermal resistance. International Journal of Heat and Mass Transfer, 112:333–342, 2017.
76. Wang, J., Ma, Z., Li, G., Sundén, B., and Yan, J.: Improved modeling of heat transfer in dropwise condensation. International Journal of Heat and Mass Transfer, 155:119719, 2020.
77. Vemuri, S. and Kim, K.: An experimental and theoretical study on the concept of dropwise condensation. International journal of heat and mass transfer, 49(3-4):649–657, 2006.

78. Kim, S. and Kim, K. J.: Dropwise Condensation Modeling Suitable for Superhydrophobic Surfaces. Journal of Heat Transfer, 133(8), 05 2011.
79. Xu, W., Lan, Z., Liu, Q., Du, B., and Ma, X.: Numerical study on the detailed droplet size distributions in dropwise condensation with the consideration of droplet” overlapping” and multiple re-nucleation. In International Heat Transfer Conference Digital Library. Begel House Inc., 2018.
80. Stevens, K. A., Crockett, J., Maynes, D., and Iverson, B. D.: Simulation of drop-size distribution during dropwise and jumping drop condensation on a vertical surface: Implications for heat transfer modeling. Langmuir, 35(39):12858–12875, 2019.
81. Chavan, S., Cha, H., Orejon, D., Nawaz, K., Singla, N., Yeung, Y. F., Park, D., Kang, D. H., Chang, Y., Takata, Y., et al.: Heat transfer through a condensate droplet on hydrophobic and nanostructured superhydrophobic surfaces. Langmuir, 32(31):7774–7787, 2016.
82. El Fil, B., Kini, G., and Garimella, S.: A review of dropwise condensation: Theory, modeling, experiments, and applications. International Journal of Heat and Mass Transfer, 160:120172, 2020.
83. Graham, C.: The limiting heat transfer mechanisms of dropwise condensation. Doctoral dissertation, Massachusetts Institute of Technology, 1969.
84. Shigeo, H. and Hiroaki, T.: Dropwise condensation of steam at low pressures. International journal of heat and mass transfer, 30(3):497–507, 1987.
85. Wen, R., Xu, S., Ma, X., Lee, Y.-C., and Yang, R.: Three-dimensional superhydrophobic nanowire networks for enhancing condensation heat transfer. Joule, 2(2):269–279, 2018.
86. Sigsbee, R. and Pound, G.: Heterogeneous nucleation from the vapor. Advances in Colloid and Interface Science, 1(3):335–390, 1967.
87. Paxson, A. T., Yagüe, J. L., Gleason, K. K., and Varanasi, K. K.: Stable dropwise condensation for enhancing heat transfer via the initiated chemical vapor deposition (icvd) of grafted polymer films. Advanced Materials, 26(3):418–423, 2014.
88. Kakac, S., Liu, H., and Pramuanjaroenkij, A.: Heat exchangers: selection, rating, and thermal design. CRC press, 2002.

89. Hanford, W. and Joyce, R.: Polytetrafluoroethylene. Journal of the American Chemical Society, 68(10):2082–2085, 1946.
90. Marto, P., Looney, D., Rose, J., and Wanniarachchi, A.: Evaluation of organic coatings for the promotion of dropwise condensation of steam. International journal of heat and mass transfer, 29(8):1109–1117, 1986.
91. Tsuchiya, H., Manabe, K., Gaudalet, T., Moriya, T., Suwabe, K., Tenjimbayashi, M., Kyong, K.-H., Gillot, F., and Shiratori, S.: Improvement of heat transfer by promoting dropwise condensation using electrospun polytetrafluoroethylene thin films. New Journal of Chemistry, 41(3):982–991, 2017.
92. Holden, K. M., Wanniarachchi, A. S., Marto, P. J., Boone, D. H., and Rose, J. W.: The Use of Organic Coatings to Promote Dropwise Condensation of Steam. Journal of Heat Transfer, 109(3):768–774, 08 1987.
93. Edwards, J. and Doolittle, J.: Tetrafluoroethylene promoted dropwise condensation. International Journal of Heat and Mass Transfer, 8(4):663–666, 1965.
94. Ma, X.-H., Wang, B.-X., Xu, D.-Q., and Lin, J.-F.: Lifetime test of dropwise condensation on polymer-coated surfaces. Heat Transfer—Asian Research: Co-sponsored by the Society of Chemical Engineers of Japan and the Heat Transfer Division of ASME, 28(7):551–558, 1999.
95. Damle, V. G., Sun, X., and Rykaczewski, K.: Can metal matrix-hydrophobic nanoparticle composites enhance water condensation by promoting the dropwise mode? Advanced Materials Interfaces, 2(16):1500202, 2015.
96. Lixin, C. and Jiehui, Y.: A new treated surface for achieving dropwise condensation. Journal of Enhanced Heat Transfer, 5(1):1–8, 1998.
97. Lara, J. R. and Holtzapple, M. T.: Experimental investigation of dropwise condensation on hydrophobic heat exchangers. part ii: Effect of coatings and surface geometry. Desalination, 280(1-3):363–369, 2011.
98. Erb, R. A.: Wettability of metals under continuous condensing conditions. The Journal of Physical Chemistry, 69(4):1306–1309, 1965.
99. Erb, R. A.: Dropwise condensation on gold. Gold Bulletin, 6(1):2–6, 1973.

100. Wilkins, D. G., Bromley, L. A., and Read, S. M.: Dropwise and filmwise condensation of water vapor on gold. AICHE Journal, 19(1):119–123, 1973.
101. Smith, T.: The hydrophilic nature of a clean gold surface. Journal of Colloid and Interface Science, 75(1):51–55, 1980.
102. Woodruff, D. W. and Westwater, J. W.: Steam Condensation on Various Gold Surfaces. Journal of Heat Transfer, 103(4):685–692, 11 1981.
103. Ge, M., Wang, S., Zhao, J., Zhao, Y., and Liu, L.: Effects of extended surface and surface gold plating on condensation characteristics of steam with large amount of co2. Experimental Thermal and Fluid Science, 92:13–19, 2018.
104. Gore, G., Sali, N., and Ghodake, A.: Of dropwise condensation heat transfer enhancement on silver coated copper surface using n-heptane as surfactant additive. Int. Adv. Res. J. Sci. Eng. Technol, 3:291–294, 2016.
105. Khorsand, S., Raeissi, K., and Ashrafizadeh, F.: Corrosion resistance and long-term durability of super-hydrophobic nickel film prepared by electrodeposition process. Applied Surface Science, 305:498–505, 2014.
106. Alwazzan, M., Egab, K., Wang, P., Shang, Z., Liang, X., Li, C., et al.: Condensation heat transfer on nickel tubes: The role of atomic layer deposition of nickel oxide. International Journal of Heat and Mass Transfer, 133:487–493, 2019.
107. Bigelow, W., Pickett, D., and Zisman, W.: Oleophobic monolayers: I. films adsorbed from solution in non-polar liquids. Journal of Colloid Science, 1(6):513–538, 1946.
108. Yang, Q. and Gu, A.: Dropwise condensation on sam and electroless composite coating surfaces. Journal of chemical engineering of Japan, 39(8):826–830, 2006.
109. Das, A., Kilty, H. P., Marto, P. J., Kumar, A., and Andeen, G. B.: Dropwise condensation of steam on horizontal corrugated tubes using an organic self-assembled monolayer coating. Journal of Enhanced Heat Transfer, 7(2), 2000.
110. Das, A., Kilty, H., Marto, P., Andeen, G., and Kumar, A.: The use of an organic self-assembled monolayer coating to promote dropwise condensation of steam on horizontal tubes. J. Heat Transfer, 122(2):278–286, 2000.

111. Bonner III, R. W.: Dropwise condensation on surfaces with graded hydrophobicity. In Heat Transfer Summer Conference, volume 43581, pages 491–495, 2009.
112. Bonner III, R. W.: Dropwise condensation life testing of self assembled monolayers. In International Heat Transfer Conference, volume 49378, pages 221–226, 2010.
113. Yang, Q., Ding, J., and Shen, Z.: Investigation on fouling behaviors of low-energy surface and fouling fractal characteristics. Chemical engineering science, 55(4):797–805, 2000.
114. Zhang, B. J., Kuok, C., Kim, K. J., Hwang, T., and Yoon, H.: Dropwise steam condensation on various hydrophobic surfaces: Polyphenylene sulfide (pps), polytetrafluoroethylene (ptfe), and self-assembled micro/nano silver (sams). International Journal of Heat and Mass Transfer, 89:353–358, 2015.
115. Ishino, C., Okumura, K., and Quéré, D.: Wetting transitions on rough surfaces. EPL (Europhysics Letters), 68(3):419, 2004.
116. Nosonovsky, M. and Bhushan, B.: Biomimetic superhydrophobic surfaces: multiscale approach. Nano letters, 7(9):2633–2637, 2007.
117. Goswami, A., Pillai, S. C., and McGranaghan, G.: Surface modifications to enhance dropwise condensation. Surfaces and Interfaces, 25:101143, 2021.
118. Wier, K. A. and McCarthy, T. J.: Condensation on ultrahydrophobic surfaces and its effect on droplet mobility: ultrahydrophobic surfaces are not always water repellant. Langmuir, 22(6):2433–2436, 2006.
119. Khandekar, S. and Muralidhar, K.: Dropwise condensation on inclined textured surfaces. Springer, 2014.
120. Zhong, L., Xuehu, M., Sifang, W., Mingzhe, W., and Xiaonan, L.: Effects of surface free energy and nanostructures on dropwise condensation. Chemical engineering journal, 156(3):546–552, 2010.
121. Chen, C.-H., Cai, Q., Tsai, C., Chen, C.-L., Xiong, G., Yu, Y., and Ren, Z.: Dropwise condensation on superhydrophobic surfaces with two-tier roughness. Applied physics letters, 90(17):173108, 2007.

122. Sharma, C. S., Stamatopoulos, C., Suter, R., von Rohr, P. R., and Poulikakos, D.: Rationally 3d-textured copper surfaces for laplace pressure imbalance-induced enhancement in dropwise condensation. ACS applied materials & interfaces, 10(34):29127–29135, 2018.
123. Parin, R., Martucci, A., Sturaro, M., Bortolin, S., Bersani, M., Carraro, F., and Del Col, D.: Nano-structured aluminum surfaces for dropwise condensation. Surface and Coatings Technology, 348:1–12, 2018.
124. Zhu, J., Luo, Y., Tian, J., Li, J., and Gao, X.: Clustered ribbed-nanoneedle structured copper surfaces with high-efficiency dropwise condensation heat transfer performance. ACS applied materials & interfaces, 7(20):10660–10665, 2015.
125. Wang, R., Wu, F., Xing, D., Yu, F., and Gao, X.: Density maximization of one-step electrodeposited copper nanocones and dropwise condensation heat-transfer performance evaluation. ACS applied materials & interfaces, 12(21):24512–24520, 2020.
126. Zhao, Y., Luo, Y., Zhu, J., Li, J., and Gao, X.: Copper-based ultrathin nickel nancone films with high-efficiency dropwise condensation heat transfer performance. ACS applied materials & interfaces, 7(22):11719–11723, 2015.
127. Kim, H. and Nam, Y.: Condensation behaviors and resulting heat transfer performance of nano-engineered copper surfaces. International journal of heat and mass transfer, 93:286–292, 2016.
128. Boreyko, J. B. and Chen, C.-H.: Self-propelled dropwise condensate on superhydrophobic surfaces. Physical review letters, 103(18):184501, 2009.
129. Enright, R., Miljkovic, N., Sprittles, J., Nolan, K., Mitchell, R., and Wang, E. N.: How coalescing droplets jump. ACS nano, 8(10):10352–10362, 2014.
130. Lu, D., Zhao, M., Zhang, H., Yang, Y., and Zheng, Y.: Self-enhancement of coalescence-induced droplet jumping on superhydrophobic surfaces with an asymmetric v-groove. Langmuir, 36(19):5444–5453, 2020.
131. Li, J., Zhang, W., Luo, Y., Zhu, J., and Gao, X.: Facile fabrication of anodic alumina rod-capped nanopore films with condensate microdrop self-propelling function. ACS applied materials & interfaces, 7(33):18206–18210, 2015.

132. Wang, R., Wu, F., Yu, F., Zhu, J., Gao, X., and Jiang, L.: Anti-vapor-penetration and condensate microdrop self-transport of superhydrophobic oblique nanowire surface under high subcooling. Nano Research, 14(5):1429–1434, 2021.
133. Qi, Z., Dongchang, Z., and Jifang, L.: Surface materials with dropwise condensation made by ion implantation technology. International journal of heat and mass transfer, 34(11):2833–2835, 1991.
134. Rausch, M., Fröba, A., and Leipertz, A.: Dropwise condensation heat transfer on ion implanted aluminum surfaces. International Journal of heat and Mass transfer, 51(5-6):1061–1070, 2008.
135. Kim, K., Lee, Y., and Jeong, J. H.: Dropwise condensation induced on chromium ion implanted aluminum surface. Nuclear Engineering and Technology, 51(1):84–94, 2019.
136. Rafiee, J., Mi, X., Gullapalli, H., Thomas, A. V., Yavari, F., Shi, Y., Ajayan, P. M., and Koratkar, N. A.: Wetting transparency of graphene. Nature materials, 11(3):217–222, 2012.
137. Preston, D. J., Mafra, D. L., Miljkovic, N., Kong, J., and Wang, E. N.: Scalable graphene coatings for enhanced condensation heat transfer. Nano letters, 15(5):2902–2909, 2015.
138. Kim, M.-S., Ada, K. A. L., Kwon, O. K., and Park, C. W.: A comparison of condensation heat transfer performance of mwcnt/fe composite coatings on steel substrate. Journal of Mechanical Science and Technology, 28(4):1589–1596, 2014.
139. Krishnan, D. V., Kumar, G. U., Suresh, S., Jubal, M., Thansekhar, M., and Ramesh, R.: Wetting transition in laser-fabricated hierarchical surface structures and its impact on condensation heat transfer characteristics. International Journal of Heat and Mass Transfer, 140:886–896, 2019.
140. Rajkumar, M. R., Praveen, A., Krishnan, R. A., Asirvatham, L. G., and Wongwises, S.: Experimental study of condensation heat transfer on hydrophobic vertical tube. International Journal of Heat and Mass Transfer, 120:305–315, 2018.
141. Panuthara, J. P., Muttathara, J. P. M., Ramachandralal, R. M., Asirvatham, L. G., and Wongwises, S.: Experimental investigation of condensation heat transfer on

- chlorotriethylsilane coated grooved vertical tube. International Communications in Heat and Mass Transfer, 108:104312, 2019.
142. Anand, S., Paxson, A. T., Dhiman, R., Smith, J. D., and Varanasi, K. K.: Enhanced condensation on lubricant-impregnated nanotextured surfaces. ACS nano, 6(11):10122–10129, 2012.
  143. Ge, Q., Raza, A., Li, H., Sett, S., Miljkovic, N., and Zhang, T.: Condensation of satellite droplets on lubricant-cloaked droplets. ACS applied materials & interfaces, 12(19):22246–22255, 2020.
  144. Enright, R., Miljkovic, N., Alvarado, J. L., Kim, K., and Rose, J. W.: Dropwise condensation on micro-and nanostructured surfaces. Nanoscale and Microscale Thermophysical Engineering, 18(3):223–250, 2014.
  145. Garimella, M. M., Koppu, S., Kadlaskar, S. S., Pillutla, V., Choi, W., et al.: Difference in growth and coalescing patterns of droplets on bi-philic surfaces with varying spatial distribution. Journal of colloid and interface science, 505:1065–1073, 2017.
  146. Grooten, M. and Van Der Geld, C.: Surface property effects on dropwise condensation heat transfer from flowing air-steam mixtures to promote drainage. International Journal of Thermal Sciences, 54:220–229, 2012.
  147. Yamauchi, A., Kumagai, S., and Takeyama, T.: Condensation heat transfer on various dropwise-filmwise coexisting surface. Heat Transfer-Japanese Research, 15(5):50–64, 1986.
  148. Daniel, S., Chaudhury, M. K., and Chen, J. C.: Fast drop movements resulting from the phase change on a gradient surface. Science, 291(5504):633–636, 2001.
  149. Kumagai, S., Tanaka, S., Katsuda, H., and Shimada, R.: On the enhancement of filmwise condensation heat transfer by means of the coexistence with dropwise condensation sections. Experimental heat transfer an International Journal, 4(1):71–82, 1991.
  150. Varanasi, K. K., Hsu, M., Bhate, N., Yang, W., and Deng, T.: Spatial control in the heterogeneous nucleation of water. Applied Physics Letters, 95(9):094101, 2009.
  151. Varanasi, K. K. and Deng, T.: Controlling nucleation and growth of water using hybrid hydrophobic-hydrophilic surfaces. In 2010 12th IEEE Intersociety Conference



- on Thermal and Thermomechanical Phenomena in Electronic Systems, pages 1–5, 2010.
152. Alwazzan, M., Egab, K., Peng, B., Khan, J., et al.: Condensation on hybrid-patterned copper tubes (ii): Visualization study of droplet dynamics. International Journal of Heat and Mass Transfer, 112:950–958, 2017.
  153. Egab, K., Alwazzan, M., Peng, B., Oudah, S. K., Guo, Z., Dai, X., Khan, J., and Li, C.: Enhancing filmwise and dropwise condensation using a hybrid wettability contrast mechanism: Circular patterns. International Journal of Heat and Mass Transfer, 154:119640, 2020.
  154. Yang, K.-S., Lin, K.-H., Tu, C.-W., He, Y.-Z., and Wang, C.-C.: Experimental investigation of moist air condensation on hydrophilic, hydrophobic, superhydrophilic, and hybrid hydrophobic-hydrophilic surfaces. International Journal of Heat and Mass Transfer, 115:1032–1041, 2017.
  155. Shang, Y., Hou, Y., Yu, M., and Yao, S.: Modeling and optimization of condensation heat transfer at biphilic interface. International Journal of Heat and Mass Transfer, 122:117–127, 2018.
  156. Naseem, H. and Murthy, H.: A simple thermal diffusivity measurement technique for polymers and particulate composites. International Journal of Heat and Mass Transfer, 137:968–978, 2019.
  157. Chen, Z., Modak, S., Kaviany, M., and Bonner, R.: Direct simulations of biphilic-surface condensation: optimized size effects. Frontiers in Heat and Mass Transfer (FHMT), 14:1–11, 2020.
  158. Yao, C.-W., Alvarado, J. L., Marsh, C. P., Jones, B. G., and Collins, M. K.: Wetting behavior on hybrid surfaces with hydrophobic and hydrophilic properties. Applied Surface Science, 290:59–65, 2014.
  159. Lo, C.-W., Chu, Y.-C., Yen, M.-H., and Lu, M.-C.: Enhancing condensation heat transfer on three-dimensional hybrid surfaces. Joule, 3(11):2806–2823, 2019.
  160. Schmiesing, N. C., Corti, G., and Sommers, A. D.: Water condensation and droplet shedding behavior on silica-nanospring-coated tubes. ACS applied materials & interfaces, 12(14):17046–17054, 2020.

161. Mondal, B., Mac Giolla Eain, M., Xu, Q., Egan, V. M., Punch, J., and Lyons, A. M.: Design and fabrication of a hybrid superhydrophobic–hydrophilic surface that exhibits stable dropwise condensation. ACS applied materials & interfaces, 7(42):23575–23588, 2015.
162. Xing, D., Wang, R., Wu, F., and Gao, X.: Confined growth and controlled coalescence/self-removal of condensate microdrops on a spatially heterogeneously patterned superhydrophilic–superhydrophobic surface. ACS Applied Materials & Interfaces, 12(26):29946–29952, 2020.
163. Xing, D., Wu, F., Wang, R., Zhu, J., and Gao, X.: Microdrop-assisted microdomain hydrophilicization of superhydrophobic surfaces for high-efficiency nucleation and self-removal of condensate microdrops. ACS applied materials & interfaces, 11(7):7553–7558, 2019.
164. Orejon, D., Shardt, O., Gunda, N. S. K., Ikuta, T., Takahashi, K., Takata, Y., and Mitra, S. K.: Simultaneous dropwise and filmwise condensation on hydrophilic microstructured surfaces. International Journal of Heat and Mass Transfer, 114:187–197, 2017.
165. Klotz, C. E.: Evaporative cooling. The Journal of chemical physics, 83(11):5854–5860, 1985.
166. Rahimi, P. and Charles, W.: Kinetics of evaporation: statistical rate theory approach. International Journal of Thermodynamics, 8(1):1–14, 2005.
167. Fang, G. and Ward, C. A.: Examination of the statistical rate theory expression for liquid evaporation rates. Physical Review E, 59(1):441, 1999.
168. Duan, F., He, B., et al.: Evaporation of liquid droplet in nano and micro scales from statistical rate theory. Journal of Nanoscience and Nanotechnology, 15(4):3011–3016, 2015.
169. Deryagin, B., Nerpin, S., and Churaev, N.: To the theory of liquid evaporation from capillaries. Kolloidn. Zh, 26:301–307, 1964.
170. Kiseleva, O., Starov, V., and Churaev, N.: Calculations of film flow under action of a temperature-gradient in conical capillaries. COLLOID JOURNAL OF THE USSR, 39(6):1021–1024, 1977.

171. Schrage, R. W.: A theoretical study of interphase mass transfer. In A Theoretical Study of Interphase Mass Transfer. Columbia University Press, 1953.
172. Plawsky, J. L., Ojha, M., Chatterjee, A., and Wayner Jr, P. C.: Review of the effects of surface topography, surface chemistry, and fluid physics on evaporation at the contact line. Chemical Engineering Communications, 196(5):658–696, 2008.
173. Bergles, A. E.: Recent developments in enhanced heat transfer. Heat and mass transfer, 47(8):1001–1008, 2011.
174. Liu, W., Li, Y., Cai, Y., and Sekulic, D. P.: Capillary rise of liquids over a microstructured solid surface. Langmuir, 27(23):14260–14266, 2011.
175. Courbin, L., Denieul, E., Dressaire, E., Roper, M., Ajdari, A., and Stone, H. A.: Imbibition by polygonal spreading on microdecorated surfaces. Nature materials, 6(9):661–664, 2007.
176. Maroo, S. C. and Chung, J.: A possible role of nanostructured ridges on boiling heat transfer enhancement. Journal of Heat Transfer, 135(4), 2013.
177. Ranjan, R., Murthy, J. Y., and Garimella, S. V.: Analysis of the wicking and thin-film evaporation characteristics of microstructures. Journal of Heat Transfer, 131(10), 2009.
178. Quéré, D.: Wetting and roughness. Annual review of materials research, 38(1):71–99, 2008.
179. Ojha, M., Chatterjee, A., Dalakos, G., Wayner Jr, P. C., and Plawsky, J. L.: Role of solid surface structure on evaporative phase change from a completely wetting corner meniscus. Physics of Fluids, 22(5):052101, 2010.
180. Ranjan, R., Garimella, S. V., Murthy, J. Y., and Yazawa, K.: Assessment of nanostructured capillary wicks for passive two-phase heat transport. Nanoscale and microscale thermophysical engineering, 15(3):179–194, 2011.
181. Kamrin, K., Bazant, M. Z., and Stone, H. A.: Effective slip boundary conditions for arbitrary periodic surfaces: the surface mobility tensor. Journal of Fluid Mechanics, 658:409–437, 2010.

182. Rothstein, J. P.: Slip on superhydrophobic surfaces. Annual review of fluid mechanics, 42:89–109, 2010.
183. Barberis, F. and Capurro, M.: Wetting in the nanoscale: A continuum mechanics approach. Journal of colloid and interface science, 326(1):201–210, 2008.
184. Cheng, X., Yang, G., and Wu, J.: Recent advances in the optimization of evaporator wicks of vapor chambers: From mechanism to fabrication technologies. Applied Thermal Engineering, 188:116611, 2021.
185. Plawsky, J., Fedorov, A., Garimella, S., Ma, H., Maroo, S., Chen, L., and Nam, Y.: Nano- and microstructures for thin-film evaporation—a review. Nanoscale and microscale thermophysical engineering, 18(3):251–269, 2014.
186. Ibrahim, K., Abd Rabbo, M., Gambaryan-Roisman, T., and Stephan, P.: Experimental investigation of evaporative heat transfer characteristics at the 3-phase contact line. Experimental Thermal and Fluid Science, 34(8):1036–1041, 2010.
187. Sefiane, K. and Ward, C. A.: Recent advances on thermocapillary flows and interfacial conditions during the evaporation of liquids. Advances in colloid and interface science, 134:201–223, 2007.
188. Ma, H., Cheng, P., Borgmeyer, B., and Wang, Y.: Fluid flow and heat transfer in the evaporating thin film region. Microfluidics and Nanofluidics, 4(3):237–243, 2008.
189. Ajaev, V. S., Gambaryan-Roisman, T., and Stephan, P.: Static and dynamic contact angles of evaporating liquids on heated surfaces. Journal of colloid and interface science, 342(2):550–558, 2010.
190. Maroo, S. C. and Chung, J.: Heat transfer characteristics and pressure variation in a nanoscale evaporating meniscus. International Journal of Heat and Mass Transfer, 53(15-16):3335–3345, 2010.
191. Narayanan, S., Fedorov, A. G., and Joshi, Y. K.: Interfacial transport of evaporating water confined in nanopores. Langmuir, 27(17):10666–10676, 2011.
192. Carey, V. P.: Liquid-vapor phase-change phenomena: an introduction to the thermophysics of vaporization and condensation processes in heat transfer equipment. CRC Press, 2020.

193. Ajaev, V. S.: Instability and rupture of thin liquid films on solid substrates. Interfacial Phenomena and Heat Transfer, 1(1):81–92, 2013.
194. Benselama, A. M., Harmand, S., and Sefiane, K.: Thermocapillary effects on steadily evaporating contact line: A perturbative local analysis. Physics of Fluids, 24(7):072105, 2012.
195. Nam, Y., Sharratt, S., Byon, C., Kim, S. J., and Ju, Y. S.: Fabrication and characterization of the capillary performance of superhydrophilic cu micropost arrays. Journal of Microelectromechanical Systems, 19(3):581–588, 2010.
196. Bodla, K. K., Murthy, J. Y., and Garimella, S. V.: Direct simulation of thermal transport through sintered wick microstructures. Journal of heat transfer, 134(1), 2012.
197. Bodla, K. K., Weibel, J. A., and Garimella, S. V.: Advances in fluid and thermal transport property analysis and design of sintered porous wick microstructures. Journal of Heat Transfer, 135(6), 2013.
198. Ranjan, R., Murthy, J. Y., Garimella, S. V., and Vadakkan, U.: A numerical model for transport in flat heat pipes considering wick microstructure effects. International Journal of Heat and Mass Transfer, 54(1-3):153–168, 2011.
199. Nam, Y., Sharratt, S., Cha, G., and Ju, Y. S.: Characterization and Modeling of the Heat Transfer Performance of Nanostructured Cu Micropost Wicks. Journal of Heat Transfer, 133(10):101502, 08 2011.
200. Narayanan, S., Fedorov, A. G., and Joshi, Y. K.: Gas-assisted thin-film evaporation from confined spaces for dissipation of high heat fluxes. Nanoscale and Microscale Thermophysical Engineering, 13(1):30–53, 2009.
201. Weibel, J. A. and Garimella, S. V.: Recent advances in vapor chamber transport characterization for high-heat-flux applications. Advances in Heat Transfer, 45:209–301, 2013.
202. Kim, J., Oh, J., and Lee, H.: Review on battery thermal management system for electric vehicles. Applied thermal engineering, 149:192–212, 2019.
203. Zhu, L., Tan, H., and Yu, J.: Analysis on optimal heat exchanger size of thermoelectric cooler for electronic cooling applications. Energy conversion and management, 76:685–690, 2013.

204. Moore, A. L. and Shi, L.: Emerging challenges and materials for thermal management of electronics. Materials today, 17(4):163–174, 2014.
205. Moore, G. E.: Cramming more components onto integrated circuits, 1965.
206. Mattila, T. T., Li, J., and Kivilahti, J. K.: On the effects of temperature on the drop reliability of electronic component boards. Microelectronics Reliability, 52(1):165–179, 2012.
207. Yang, K.-S., Ding, W.-T., Yeh, C.-T., Lee, M.-T., and Wang, C.-C.: An experimental and analytical investigation of the photo-thermal-electro characteristics of a high power ingan led module. Applied Thermal Engineering, 98:756–765, 2016.
208. Tang, Y., Lin, L., Zhang, S., Zeng, J., Tang, K., Chen, G., and Yuan, W.: Thermal management of high-power leds based on integrated heat sink with vapor chamber. Energy conversion and management, 151:1–10, 2017.
209. Liu, D., Zhao, F.-Y., Yang, H.-X., and Tang, G.-F.: Thermoelectric mini cooler coupled with micro thermosiphon for cpu cooling system. Energy, 83:29–36, 2015.
210. Ramadass, P., Haran, B., White, R., and Popov, B. N.: Capacity fade of sony 18650 cells cycled at elevated temperatures: Part i. cycling performance. Journal of power sources, 112(2):606–613, 2002.
211. Wright, R., Christophersen, J., Motloch, C., Belt, J., Ho, C., Battaglia, V., Barnes, J., Duong, T., and Sutula, R.: Power fade and capacity fade resulting from cycle-life testing of advanced technology development program lithium-ion batteries. Journal of Power Sources, 119:865–869, 2003.
212. Naphon, P., Wongwises, S., and Wiriyaart, S.: On the thermal cooling of central processing unit of the pcs with vapor chamber. International Communications in Heat and Mass Transfer, 39(8):1165–1168, 2012.
213. Murshed, S. S.: Introductory chapter: electronics cooling—an overview. Electronics Cooling, pages 1–11, 2016.
214. Liang, G. and Mudawar, I.: Review of spray cooling—part 1: Single-phase and nucleate boiling regimes, and critical heat flux. International Journal of Heat and Mass Transfer, 115:1174–1205, 2017.

215. Arshad, A., Jabbar, M., and Yan, Y.: Synthetic jet actuators for heat transfer enhancement—a critical review. International Journal of Heat and Mass Transfer, 146:118815, 2020.
216. Kuncoro, I., Pambudi, N., Biddinika, M., Widiastuti, I., Hijriawan, M., and Wibowo, K.: Immersion cooling as the next technology for data center cooling: A review. In Journal of Physics: Conference Series, volume 1402, page 044057. IOP Publishing, 2019.
217. Wei, J.: Liquid cooling, opportunity & challenges toward effective and efficient scalabilities. In 2019 IEEE CPMT Symposium Japan (ICSJ), pages 83–84. IEEE, 2019.
218. Ahmad, I., Pathak, M., and Khan, M. K.: Electrowetting induced microdroplet oscillation over interdigitated electrodes for hotspot cooling applications. Experimental Thermal and Fluid Science, 125:110372, 2021.
219. Mohseni, K.: Effective cooling of integrated circuits using liquid alloy electrowetting. In Semiconductor Thermal Measurement and Management IEEE Twenty First Annual IEEE Symposium, 2005., pages 20–25. IEEE, 2005.
220. Zhang, Y., Ma, J., Wei, N., Yang, J., and Pei, Q.-X.: Recent progress in the development of thermal interface materials: a review. Physical Chemistry Chemical Physics, 23(2):753–776, 2021.
221. Wang, G., Qian, N., and Ding, G.: Heat transfer enhancement in microchannel heat sink with bidirectional rib. International Journal of Heat and Mass Transfer, 136:597–609, 2019.
222. Wang, G., Chen, T., Tian, M., and Ding, G.: Fluid and heat transfer characteristics of microchannel heat sink with truncated rib on sidewall. International Journal of Heat and Mass Transfer, 148:119142, 2020.
223. Van Erp, R., Soleimanzadeh, R., Nela, L., Kampitsis, G., and Matioli, E.: Co-designing electronics with microfluidics for more sustainable cooling. Nature, 585(7824):211–216, 2020.
224. Abdollahi, A., Sharma, R. N., and Vatani, A.: Fluid flow and heat transfer of liquid-liquid two phase flow in microchannels: A review. International Communications in Heat and Mass Transfer, 84:66–74, 2017.

225. Chamkha, A. J., Molana, M., Rahn timer, A., and Ghadami, F.: On the nanofluids applications in microchannels: a comprehensive review. Powder Technology, 332:287–322, 2018.
226. Alihosseini, Y., Targhi, M. Z., Heyhat, M. M., and Ghorbani, N.: Effect of a micro heat sink geometric design on thermo-hydraulic performance: A review. Applied Thermal Engineering, 170:114974, 2020.
227. Liang, G. and Mudawar, I.: Review of channel flow boiling enhancement by surface modification, and instability suppression schemes. International Journal of Heat and Mass Transfer, 146:118864, 2020.
228. O'Neill, L. E. and Mudawar, I.: Review of two-phase flow instabilities in macro-and micro-channel systems. International Journal of Heat and Mass Transfer, 157:119738, 2020.
229. Liu, T., Asheghi, M., and Goodson, K. E.: Performance and Manufacturing of Silicon-Based Vapor Chambers. Applied Mechanics Reviews, 73(1):010802, 2021.
230. Twaha, S., Zhu, J., Yan, Y., and Li, B.: A comprehensive review of thermoelectric technology: Materials, applications, modelling and performance improvement. Renewable and sustainable energy reviews, 65:698–726, 2016.
231. Zhang, S., Feng, D., Shi, L., Wang, L., Jin, Y., Tian, L., Li, Z., Wang, G., Zhao, L., and Yan, Y.: A review of phase change heat transfer in shape-stabilized phase change materials (ss-pcms) based on porous supports for thermal energy storage. Renewable and Sustainable Energy Reviews, 135:110127, 2021.
232. Arshad, A., Jabbal, M., Yan, Y., and Darkwa, J.: The micro-/nano-pcms for thermal energy storage systems: a state of art review. International Journal of Energy Research, 43(11):5572–5620, 2019.
233. Arshad, A., Jabbal, M., Sardari, P. T., Bashir, M. A., Faraji, H., and Yan, Y.: Transient simulation of finned heat sinks embedded with pcm for electronics cooling. Thermal Science and Engineering Progress, 18:100520, 2020.
234. Huang, K., Yan, Y., Wang, G., and Li, B.: Improving transient performance of thermoelectric generator by integrating phase change material. Energy, 219:119648, 2021.



235. Garimella, S. V., Persoons, T., Weibel, J. A., and Gektin, V.: Electronics thermal management in information and communications technologies: Challenges and future directions. IEEE Transactions on Components, Packaging and Manufacturing Technology, 7(8):1191–1205, 2016.
236. Barako, M. T., Gambin, V., and Tice, J.: Integrated nanomaterials for extreme thermal management: A perspective for aerospace applications. Nanotechnology, 29(15):154003, 2018.
237. Lasance, C. J. and Poppe, A.: Thermal management for LED applications, volume 2. Springer, 2014.
238. Bar-Cohen, A., Wang, P., and Rahim, E.: Thermal management of high heat flux nano-electronic chips. Microgravity Science and Technology, 19(3):48–52, 2007.
239. Bar-Cohen, A. and Wang, P.: Thermal management of on-chip hot spot. Journal of Heat Transfer, 134(5):051017, 2012.
240. Ali, H. M., Arshad, A., Jabbal, M., and Verdin, P. G.: Thermal management of electronics devices with pcms filled pin-fin heat sinks: a comparison. International Journal of Heat and Mass Transfer, 117:1199–1204, 2018.
241. Shang, B., Ma, Y., Hu, R., Yuan, C., Hu, J., and Luo, X.: Passive thermal management system for downhole electronics in harsh thermal environments. Applied Thermal Engineering, 118:593–599, 2017.
242. Radwan, A., Ookawara, S., and Ahmed, M.: Thermal management of concentrator photovoltaic systems using two-phase flow boiling in double-layer microchannel heat sinks. Applied Energy, 241:404–419, 2019.
243. Mudawar, I.: Recent advances in high-flux, two-phase thermal management. Journal of Thermal Science and Engineering Applications, 5(2):021012, 2013.
244. Velardo, J., Singh, R., Date, A., and Date, A.: An investigation into the effective thermal conductivity of vapour chamber heat spreaders. Energy Procedia, 110:256–261, 2017.
245. Sun, Z., Chen, X., and Qiu, H.: Experimental investigation of a novel asymmetric heat spreader with nanostructure surfaces. Experimental thermal and fluid science, 52:197–204, 2014.

246. Huang, C., Lin, W.-K., and Chen, J.-K.: Important factors affecting the thermal resistance and thermal diffusivity of vapor chambers. Applied Thermal Engineering, 126:1148–1155, 2017.
247. Mizuta, K., Fukunaga, R., Fukuda, K., Nishino, T., Goshima, T., Nii, S., and Asano, T.: Quasi one-dimensional approach to evaluate temperature dependent anisotropic thermal conductivity of a flat laminate vapor chamber. Applied Thermal Engineering, 146:843–853, 2019.
248. Tsai, M.-C., Kang, S.-W., and de Paiva, K. V.: Experimental studies of thermal resistance in a vapor chamber heat spreader. Applied Thermal Engineering, 56(1-2):38–44, 2013.
249. Ji, X., Xu, J., and Abanda, A. M.: Copper foam based vapor chamber for high heat flux dissipation. Experimental thermal and fluid Science, 40:93–102, 2012.
250. Bulut, M., Kandlikar, S. G., and Sozbir, N.: A review of vapor chambers. Heat Transfer Engineering, 40(19):1551–1573, 2019.
251. Mochizuki, M. and Nguyen, T.: Review of various thin heat spreader vapor chamber designs, performance, lifetime reliability and application. Frontiers in Heat and Mass Transfer (FHMT), 13, 2019.
252. Cai, Q., Chen, B.-c., and Tsai, C.: Design, development and tests of high-performance silicon vapor chamber. Journal of Micromechanics and Microengineering, 22(3):035009, 2012.
253. Chen, Y.-T., Kang, S.-W., Hung, Y.-H., Huang, C.-H., and Chien, K.-C.: Feasibility study of an aluminum vapor chamber with radial grooved and sintered powders wick structures. Applied Thermal Engineering, 51(1-2):864–870, 2013.
254. Wang, M., Cui, W., and Hou, Y.: Thermal spreading resistance of grooved vapor chamber heat spreader. Applied Thermal Engineering, 153:361–368, 2019.
255. Xu, S., Lewis, R. J., Liew, L.-A., Lee, Y.-C., and Yang, R.: Development of ultra-thin thermal ground planes by using stainless-steel mesh as wicking structure. Journal of Microelectromechanical Systems, 25(5):842–844, 2016.
256. Long, J., Chu, P., Li, Y., Lin, J., Cao, Z., Xu, M., Ren, Q., and Xie, X.: Dual-scale porous/grooved microstructures prepared by nanosecond laser surface texturing for

- high-performance vapor chambers. Journal of Manufacturing Processes, 73:914–923, 2022.
257. Wiriyasart, S. and Naphon, P.: Thermal performance enhancement of vapor chamber by coating mini-channel heat sink with porous sintering media. International Journal of Heat and Mass Transfer, 126:116–122, 2018.
  258. Mizuta, K., Fukunaga, R., Fukuda, K., Nii, S., and Asano, T.: Development and characterization of a flat laminate vapor chamber. Applied Thermal Engineering, 104:461–471, 2016.
  259. Zeng, J., Lin, L., Tang, Y., Sun, Y., and Yuan, W.: Fabrication and capillary characterization of micro-grooved wicks with reentrant cavity array. International Journal of Heat and Mass Transfer, 104:918–929, 2017.
  260. He, B., Wei, M., Somasundaram, S., Tan, C. S., and Wang, E. N.: Experiments on the ultrathin silicon vapor chamber for enhanced heat transfer performance. In 2016 15th IEEE Intersociety Conference on Thermal and Thermomechanical Phenomena in Electronic Systems (ITherm), pages 569–573. IEEE, 2016.
  261. Jafari, D., Wits, W. W., and Geurts, B. J.: Metal 3d-printed wick structures for heat pipe application: Capillary performance analysis. Applied thermal engineering, 143:403–414, 2018.
  262. Bodla, K. K., Murthy, J. Y., and Garimella, S. V.: Evaporation analysis in sintered wick microstructures. International Journal of Heat and Mass Transfer, 61:729–741, 2013.
  263. Adera, S., Antao, D., Raj, R., and Wang, E. N.: Design of micropillar wicks for thin-film evaporation. International Journal of Heat and Mass Transfer, 101:280–294, 2016.
  264. Tang, H., Tang, Y., Yuan, W., Peng, R., Lu, L., and Wan, Z.: Fabrication and capillary characterization of axially micro-grooved wicks for aluminium flat-plate heat pipes. Applied Thermal Engineering, 129:907–915, 2018.
  265. Lu, M., Mok, L., and Bezama, R.: A graphite foams based vapor chamber for chip heat spreading. 128:427–431, 2006.

266. Wen, R., Xu, S., Lee, Y.-C., and Yang, R.: Capillary-driven liquid film boiling heat transfer on hybrid mesh wicking structures. Nano Energy, 51:373–382, 2018.
267. Huang, G., Liu, W., Luo, Y., and Li, Y.: A novel ultra-thin vapor chamber for heat dissipation in ultra-thin portable electronic devices. Applied Thermal Engineering, 167:114726, 2020.
268. Chen, L., Deng, D., Huang, Q., Xu, X., and Xie, Y.: Development and thermal performance of a vapor chamber with multi-artery reentrant microchannels for high-power led. Applied Thermal Engineering, 166:114686, 2020.
269. Zhang, H., Pan, Q., and Zhang, H.: Multi-scale porous copper foams as wick structures. Materials letters, 106:360–362, 2013.
270. Ravi, S., Dharmarajan, R., and Moghaddam, S.: Physics of fluid transport in hybrid biporous capillary wicking microstructures. Langmuir, 32(33):8289–8297, 2016.
271. Li, Y., He, H.-f., and Zeng, Z.-x.: Evaporation and condensation heat transfer in a heat pipe with a sintered-grooved composite wick. Applied Thermal Engineering, 50(1):342–351, 2013.
272. Ryu, S., Han, J., Kim, J., Lee, C., and Nam, Y.: Enhanced heat transfer using metal foam liquid supply layers for micro heat spreaders. International journal of heat and mass transfer, 108:2338–2345, 2017.
273. Kim, S. S., Weibel, J. A., Fisher, T. S., and Garimella, S. V.: Thermal performance of carbon nanotube enhanced vapor chamber wicks. In International Heat Transfer Conference, volume 49408, pages 417–424, 2010.
274. Barako, M. T., Roy-Panzer, S., English, T. S., Kodama, T., Asheghi, M., Kenny, T. W., and Goodson, K. E.: Thermal conduction in vertically aligned copper nanowire arrays and composites. ACS applied materials & interfaces, 7(34):19251–19259, 2015.
275. Vaartstra, G., Lu, Z., and Wang, E. N.: Simultaneous prediction of dryout heat flux and local temperature for thin film evaporation in micropillar wicks. International Journal of Heat and Mass Transfer, 136:170–177, 2019.

276. Dai, X., Yang, F., Yang, R., Lee, Y.-C., and Li, C.: Micromembrane-enhanced capillary evaporation. International Journal of Heat and Mass Transfer, 64:1101–1108, 2013.
277. Damoulakis, G., Kaufman, G., Tsubaki, A., Gogos, G., Zuhlke, C., and Megaridis, C. M.: Vapor chamber thermal diode with laser-fabricated wickless components. In 2021 20th IEEE Intersociety Conference on Thermal and Thermomechanical Phenomena in Electronic Systems (iTherm), pages 246–253. IEEE, 2021.
278. Koukoravas, T. P., Damoulakis, G., and Megaridis, C. M.: Experimental investigation of a vapor chamber featuring wettability-patterned surfaces. Applied Thermal Engineering, 178:115522, 2020.
279. Boreyko, J. B. and Chen, C.-H.: Vapor chambers with jumping-drop liquid return from superhydrophobic condensers. International Journal of Heat and Mass Transfer, 61:409–418, 2013.
280. Patankar, G., Weibel, J. A., and Garimella, S. V.: Patterning the condenser-side wick in ultra-thin vapor chamber heat spreaders to improve skin temperature uniformity of mobile devices. International Journal of Heat and Mass Transfer, 101:927–936, 2016.
281. Li, B., Xu, J., Wang, Y., and Hong, J.: Optimization design of grooved condenser wick structures in a vapor chamber for electronic cooling applications. Structural and Multidisciplinary Optimization, 61(5):2001–2019, 2020.
282. Li, B., Chen, H., Xu, J., Yin, X., and Hong, J.: Topology optimization of vapor chamber internal structures consisting of evaporator and condenser. Applied Mathematical Modelling, 107:233–255, 2022.
283. Ji, X., Xu, J., Abanda, A. M., and Xue, Q.: A vapor chamber using extended condenser concept for ultra-high heat flux and large heater area. International Journal of Heat and Mass Transfer, 55(17-18):4908–4913, 2012.
284. Wong, S.-C., Hsieh, K.-C., Wu, J.-D., and Han, W.-L.: A novel vapor chamber and its performance. International Journal of Heat and Mass Transfer, 53(11-12):2377–2384, 2010.

285. Lu, Z., Bai, P., Huang, B., Henzen, A., Coehoorn, R., Liao, H., and Zhou, G.: Experimental investigation on the thermal performance of three-dimensional vapor chamber for led automotive headlamps. Applied Thermal Engineering, 157:113478, 2019.
286. Gupta, M., Singh, V., Kumar, R., and Said, Z.: A review on thermophysical properties of nanofluids and heat transfer applications. Renewable and Sustainable Energy Reviews, 74:638–670, 2017.
287. Huminic, G. and Huminic, A.: Hybrid nanofluids for heat transfer applications—a state-of-the-art review. International Journal of Heat and Mass Transfer, 125:82–103, 2018.
288. Du, K., Calautit, J., Wang, Z., Wu, Y., and Liu, H.: A review of the applications of phase change materials in cooling, heating and power generation in different temperature ranges. Applied energy, 220:242–273, 2018.
289. Tan, F. and Tso, C.: Cooling of mobile electronic devices using phase change materials. Applied thermal engineering, 24(2-3):159–169, 2004.
290. Zhang, S., Chen, C., Chen, G., Sun, Y., Tang, Y., and Wang, Z.: Capillary performance characterization of porous sintered stainless steel powder wicks for stainless steel heat pipes. International Communications in Heat and Mass Transfer, 116:104702, 2020.
291. Boomsma, K. and Poulikakos, D.: The effects of compression and pore size variations on the liquid flow characteristics in metal foams. J. Fluids Eng., 124(1):263–272, 2002.
292. Lee, J., Suh, Y., Dubey, P. P., Barako, M. T., and Won, Y.: Capillary wicking in hierarchically textured copper nanowire arrays. ACS applied materials & interfaces, 11(1):1546–1554, 2018.
293. Washburn, E. W.: The dynamics of capillary flow. Physical review, 17(3):273, 1921.
294. Byon, C. and Kim, S. J.: Capillary performance of bi-porous sintered metal wicks. International Journal of Heat and Mass Transfer, 55(15-16):4096–4103, 2012.
295. Chen, G., Fan, D., Zhang, S., Sun, Y., Zhong, G., Wang, Z., Wan, Z., and Tang, Y.: Wicking capability evaluation of multilayer composite micromesh wicks for ultra-thin two-phase heat transfer devices. Renewable Energy, 163:921–929, 2021.

296. Ryu, S., Lee, W., and Nam, Y.: Heat transfer and capillary performance of dual-height superhydrophilic micropost wicks. International Journal of Heat and Mass Transfer, 73:438–444, 2014.
297. Wei, M., He, B., Liang, Q., Somasundaram, S., Tan, C. S., and Wang, E. N.: Optimization and thermal characterization of uniform silicon micropillar based evaporators. International Journal of Heat and Mass Transfer, 127:51–60, 2018.
298. Wei, M., He, B., Somasundaram, S., Tan, C. S., and Wang, E. N.: Optimization and thermal characterization of uniform micropillar based silicon evaporator in advanced vapor chambers. In 2016 15th IEEE Intersociety Conference on Thermal and Thermomechanical Phenomena in Electronic Systems (ITherm), pages 1019–1023. IEEE, 2016.
299. Cho, S., Tummala, R., and Joshi, Y.: Capillary performance of micropillar arrays in different arrangements. Nanoscale and Microscale Thermophysical Engineering, 22(2):97–113, 2018.
300. Peng, Y., Liu, W., Liu, B., Liu, J., Huang, K., Wang, L., and Chen, W.: The performance of the novel vapor chamber based on the leaf vein system. International Journal of Heat and Mass Transfer, 86:656–666, 2015.
301. Liu, W., Peng, Y., Luo, T., Luo, Y., and Huang, K.: The performance of the vapor chamber based on the plant leaf. International Journal of Heat and Mass Transfer, 98:746–757, 2016.
302. Yao, F., Miao, S., Zhang, M., and Chen, Y.: An experimental study of an anti-gravity vapor chamber with a tree-shaped evaporator. Applied Thermal Engineering, 141:1000–1008, 2018.
303. Sudhakar, S., Weibel, J. A., and Garimella, S. V.: Design of an area-scalable two-layer evaporator wick for high-heat-flux vapor chambers. IEEE Transactions on Components, Packaging and Manufacturing Technology, 9(3):458–472, 2018.
304. Sudhakar, S., Weibel, J. A., Zhou, F., Dede, E. M., and Garimella, S. V.: Area-scalable high-heat-flux dissipation at low thermal resistance using a capillary-fed two-layer evaporator wick. International Journal of Heat and Mass Transfer, 135:1346–1356, 2019.

305. Sudhakar, S., Weibel, J. A., Zhou, F., Dede, E. M., and Garimella, S. V.: The role of vapor venting and liquid feeding on the dryout limit of two-layer evaporator wicks. International Journal of Heat and Mass Transfer, 148:119063, 2020.
306. Patel, A. K. and Zhao, W.: Heat transfer analysis of graphite foam embedded vapor chamber for cooling of power electronics in electric vehicles. In Heat Transfer Summer Conference, volume 57885, page V001T09A003. American Society of Mechanical Engineers, 2017.
307. Chen, Z., Li, Y., Zhou, W., Deng, L., and Yan, Y.: Design, fabrication and thermal performance of a novel ultra-thin vapour chamber for cooling electronic devices. Energy Conversion and Management, 187:221–231, 2019.
308. Li, Y., Li, Z., Zhou, W., Zeng, Z., Yan, Y., and Li, B.: Experimental investigation of vapor chambers with different wick structures at various parameters. Experimental Thermal and Fluid Science, 77:132–143, 2016.
309. Velardo, J., Date, A., Singh, R., Nihill, J., Date, A., Phan, T. L., and Takahashi, M.: Experimental investigation of a vapour chamber heat spreader with hybrid wick structure. International Journal of Thermal Sciences, 140:28–35, 2019.
310. Wang, Q.-H., Zhao, H., Xu, Z.-J., Li, J.-R., and Deng, D.-X.: Numerical analysis on the thermal hydraulic performance of a composite porous vapor chamber with uniform radial grooves. International Journal of Heat and Mass Transfer, 142:118458, 2019.
311. Weibel, J. A., Garimella, S. V., Murthy, J. Y., and Altman, D. H.: Design of integrated nanostructured wicks for high-performance vapor chambers. IEEE Transactions on Components, Packaging and Manufacturing Technology, 1(6):859–867, 2011.
312. Weibel, J. A. and Garimella, S. V.: Visualization of vapor formation regimes during capillary-fed boiling in sintered-powder heat pipe wicks. International Journal of Heat and Mass Transfer, 55(13-14):3498–3510, 2012.
313. Le, D. V., Pham, Q. N., Lee, J., Zhang, S., and Won, Y.: Evaporative wicking phenomena on nanotextured surfaces. Journal of Electronic Packaging, 141(3), 2019.
314. Jung, S. M., Preston, D. J., Jung, H. Y., Deng, Z., Wang, E. N., and Kong, J.: Porous cu nanowire aerosponges from one-step assembly and their applications in heat dissipation. Advanced Materials, 28(7):1413–1419, 2016.



315. Jung, S. M., Jung, H. Y., Dresselhaus, M. S., Jung, Y. J., and Kong, J.: A facile route for 3d aerogels from nanostructured 1d and 2d materials. Scientific reports, 2(1):1–6, 2012.
316. Boreyko, J. B., Zhao, Y., and Chen, C.-H.: Planar jumping-drop thermal diodes. Applied Physics Letters, 99(23):234105, 2011.
317. Hsieh, S.-S., Lee, R.-Y., Shyu, J.-C., and Chen, S.-W.: Thermal performance of flat vapor chamber heat spreader. Energy Conversion and Management, 49(6):1774–1784, 2008.
318. Zhao, Y., Boreyko, J. B., Chiang, M.-H., Baker, C. H., and Chen, C.-H.: Beetle inspired electrospray vapor chamber. In International Conference on Micro/Nanoscale Heat Transfer, volume 43918, pages 439–441, 2009.
319. Zhao, Y., Chen, T., Zhang, X., Zauscher, S., and Chen, C.-H.: Development of an adaptive vapor chamber with thermoresponsive polymer coating. In International Conference on Micro/Nanoscale Heat Transfer, volume 43918, pages 395–398, 2009.
320. Wiedenheft, K. F., Guo, H. A., Qu, X., Boreyko, J. B., Liu, F., Zhang, K., Eid, F., Choudhury, A., Li, Z., and Chen, C.-H.: Hotspot cooling with jumping-drop vapor chambers. Applied Physics Letters, 110(14):141601, 2017.
321. Shukla, K., Solomon, A., and Pillai, B.: Thermal performance of vapor chamber with nanofluids. Frontiers in Heat Pipes (FHP), 3(3), 2013.
322. Edalatpour, M., Murphy, K. R., Mukherjee, R., and Boreyko, J. B.: Bridging-droplet thermal diodes. Advanced Functional Materials, 30(43):2004451, 2020.
323. Damoulakis, G., Jafari-Gukeh, M., Koukoravas, T. P., and Megaridis, C.: High-Performance Planar Thermal Diode with Wickless Components. Journal of Electronic Packaging, 144:031004, 2022.
324. Shaeri, M. R., Attinger, D., and Bonner III, R. W.: Vapor chambers with hydrophobic and biphilic evaporators in moderate to high heat flux applications. Applied Thermal Engineering, 130:83–92, 2018.
325. Yuki, K., Fukushima, K., Takemura, A., and Suzuki, K.: Wettability and evaporation enhancement for heat transport devices by high performance oxide

- layer. In 2015 International Conference on Electronics Packaging and iMAPS All Asia Conference (ICEP-IAAC), pages 601–604. IEEE, 2015.
326. Yang, Y., Li, J., Liao, D., Ye, X., and Qiu, H.: A novel evaporator integrated with wettability pattern for improving thermal performance of an ultrathin vapor chamber. 2021.
  327. Liu, T., Yan, W., Yang, X., and Wang, S.: Thermal performance of wickless and orientation independent thin vapor chambers with wettability patterned micro structure. Thermal Science, (00):17–17, 2022.
  328. Yang, Y., Li, J., Wang, H., Liao, D., and Qiu, H.: Microstructured wettability pattern for enhancing thermal performance in an ultrathin vapor chamber. Case Studies in Thermal Engineering, 25:100906, 2021.
  329. Damoulakis, G. and Megaridis, C. M.: Wick-free paradigm for high-performance vapor-chamber heat spreaders. Energy Conversion and Management, 253:115138, 2022.
  330. Gaugler, R. S.: Heat transfer device. US Patent, 2, 1944.
  331. Tang, H., Tang, Y., Wan, Z., Li, J., Yuan, W., Lu, L., Li, Y., and Tang, K.: Review of applications and developments of ultra-thin micro heat pipes for electronic cooling. Applied energy, 223:383–400, 2018.
  332. Shiraishi, M., Kikuchi, K., and Yamanishi, T.: Investigation of heat transfer characteristics of a two-phase closed thermosyphon. In Advances in heat pipe technology, pages 95–104. 1982.
  333. Nikolayev, V. S.: Physical principles and state-of-the-art of modeling of the pulsating heat pipe: A review. Applied Thermal Engineering, 195:117111, 2021.
  334. Ji, X., Guo, H., and Xu, J.: Research and development of loop heat pipe—a review. Frontiers in Heat and Mass Transfer (FHMT), 14, 2020.
  335. Faghri, A.: Review and advances in heat pipe science and technology. Journal of heat transfer, 134(12), 2012.
  336. Shioga, T., Mizuno, Y., and Nagano, H.: Operating characteristics of a new ultra-thin loop heat pipe. International Journal of Heat and Mass Transfer, 151:119436, 2020.

337. Zhou, W., Li, Y., Chen, Z., Deng, L., and Gan, Y.: A novel ultra-thin flattened heat pipe with biporous spiral woven mesh wick for cooling electronic devices. Energy Conversion and Management, 180:769–783, 2019.
338. Zhou, W., Li, Y., Chen, Z., Deng, L., and Gan, Y.: Ultra-thin flattened heat pipe with a novel band-shape spiral woven mesh wick for cooling smartphones. International Journal of Heat and Mass Transfer, 146:118792, 2020.
339. Zhou, W., Xie, P., Li, Y., Yan, Y., and Li, B.: Thermal performance of ultra-thin flattened heat pipes. Applied Thermal Engineering, 117:773–781, 2017.
340. Chen, G., Tang, Y., Wan, Z., Zhong, G., Tang, H., and Zeng, J.: Heat transfer characteristic of an ultra-thin flat plate heat pipe with surface-functional wicks for cooling electronics. International Communications in Heat and Mass Transfer, 100:12–19, 2019.
341. Wang, Q., Hong, J., and Yan, Y.: Biomimetic capillary inspired heat pipe wicks. Journal of Bionic Engineering, 11(3):469–480, 2014.
342. Li, J., Lv, L., Zhou, G., and Li, X.: Mechanism of a microscale flat plate heat pipe with extremely high nominal thermal conductivity for cooling high-end smartphone chips. Energy conversion and management, 201:112202, 2019.
343. Tharayil, T., Godson Asirvatham, L., Rajesh, S., and Wongwises, S.: Effect of nanoparticle coating on the performance of a miniature loop heat pipe for electronics cooling applications. Journal of Heat Transfer, 140(2), 2018.
344. Zhang, S., Chen, J., Sun, Y., Li, J., Zeng, J., Yuan, W., and Tang, Y.: Experimental study on the thermal performance of a novel ultra-thin aluminum flat heat pipe. Renewable Energy, 135:1133–1143, 2019.
345. Yao, C., Dan, D., Zhang, Y., Wang, Y., Qian, Y., Yan, Y., and Zhuge, W.: Thermal performance of a micro heat pipe array for battery thermal management under special vehicle-operating conditions. Automotive Innovation, 3(4):317–327, 2020.
346. Li, Y., Zhou, W., He, J., Yan, Y., Li, B., and Zeng, Z.: Thermal performance of ultra-thin flattened heat pipes with composite wick structure. Applied Thermal Engineering, 102:487–499, 2016.

347. Sardarabadi, H., Heris, S. Z., Ahmadpour, A., and Passandideh-Fard, M.: Experimental investigation of a novel type of two-phase closed thermosyphon filled with functionalized carbon nanotubes/water nanofluids for electronic cooling application. Energy Conversion and Management, 188:321–332, 2019.
348. Xu, R., Zhang, C., Chen, H., Wu, Q., and Wang, R.: Heat transfer performance of pulsating heat pipe with zeotropic immiscible binary mixtures. International Journal of Heat and Mass Transfer, 137:31–41, 2019.
349. Ramkumar, P., Sivasubramanian, M., Raveendiran, P., and Kanna, P. R.: An experimental inquisition of waste heat recovery in electronic component system using concentric tube heat pipe heat exchanger with different working fluids under gravity assistance. Microprocessors and Microsystems, 83:104033, 2021.
350. Sun, X., Ling, L., Liao, S., Chu, Y., Fan, S., and Mo, Y.: A thermoelectric cooler coupled with a gravity-assisted heat pipe: An analysis from heat pipe perspective. Energy Conversion and Management, 155:230–242, 2018.
351. Lips, S., Lefèvre, F., and Bonjour, J.: Combined effects of the filling ratio and the vapour space thickness on the performance of a flat plate heat pipe. International Journal of Heat and Mass Transfer, 53(4):694–702, 2010.
352. Chen, J.-S. and Chou, J.-H.: Cooling performance of flat plate heat pipes with different liquid filling ratios. International Journal of Heat and Mass Transfer, 77:874–882, 2014.
353. Wong, S.-C., Cheng, H.-S., and Tu, C.-W.: Visualization experiments on the performance of mesh-wick heat pipes with differing wick wettability. International Journal of Heat and Mass Transfer, 114:1045–1053, 2017.
354. Singh, M., Kondaraju, S., and Bahga, S. S.: Enhancement of thermal performance of micro heat pipes using wettability gradients. International Journal of Heat and Mass Transfer, 104:400–408, 2017.
355. Singh, M., Datla, N. V., Kondaraju, S., and Bahga, S. S.: Enhanced thermal performance of micro heat pipes through optimization of wettability gradient. Applied Thermal Engineering, 143:350–357, 2018.

356. Liu, C., Li, Q., and Fan, D.: Fabrication and performance evaluation of flexible flat heat pipes for the thermal control of deployable structure. International Journal of Heat and Mass Transfer, 144:118661, 2019.
357. Xie, X., Weng, Q., Luo, Z., Long, J., and Wei, X.: Thermal performance of the flat micro-heat pipe with the wettability gradient surface by laser fabrication. International Journal of Heat and Mass Transfer, 125:658–669, 2018.
358. Lou, D., Li, T., Liang, E., Lu, G., Yang, S., Cheng, J., Yang, Q., Tao, Q., and Liu, D.: Superhydrophobic/superhydrophilic hybrid copper surface enhanced micro heat pipe by using laser selective texturing. ECS Journal of Solid State Science and Technology, 10(11):113005, 2021.
359. Li, J. and Guo, Z.: Spontaneous directional transportations of water droplets on surfaces driven by gradient structures. Nanoscale, 10(29):13814–13831, 2018.
360. Koukoravas, T. P., Ghosh, A., Mahapatra, P. S., Ganguly, R., and Megaridis, C. M.: Spatially-selective cooling by liquid jet impinging orthogonally on a wettability-patterned surface. International Journal of Heat and Mass Transfer, 95:142–152, 2016.
361. Gukeh, M. J., Damoulakis, G., and Megaridis, C. M.: Experimental investigation of low-profile heat pipe with wickless wettability-patterned condenser. In 2021 20th IEEE Intersociety Conference on Thermal and Thermomechanical Phenomena in Electronic Systems (iTherm), pages 271–279. IEEE, 2021.
362. Mahapatra, P. S., Ghosh, A., Ganguly, R., and Megaridis, C. M.: Key design and operating parameters for enhancing dropwise condensation through wettability patterning. International Journal of Heat and Mass Transfer, 92:877–883, 2016.
363. Ghosh, A., Beaini, S., Zhang, B. J., Ganguly, R., and Megaridis, C. M.: Enhancing dropwise condensation through bioinspired wettability patterning. Langmuir, 30(43):13103–13115, 2014.
364. Lam, P., Wynne, K. J., and Wnek, G. E.: Surface-tension-confined microfluidics. Langmuir, 18(3):948–951, 2002.
365. Bernardini, J., Sen, U., Jafari Gukeh, M., Asinari, P., and Megaridis, C. M.: Wettability-engineered meshes for gas microvolume precision handling in liquids. ACS Applied Materials & Interfaces, 12(15):18046–18055, 2020.

366. Sarkar, S., Roy, T., Roy, A., Moitra, S., Ganguly, R., and Megaridis, C. M.: Revisiting the supplementary relationship of dynamic contact angles measured by sessile-droplet and captive-bubble methods: Role of surface roughness. Journal of Colloid and Interface Science, 581:690–697, 2021.
367. Zhang, J., Li, J., and Han, Y.: Superhydrophobic ptfe surfaces by extension. Macromolecular Rapid Communications, 25(11):1105–1108, 2004.
368. Teshima, K., Sugimura, H., Inoue, Y., Takai, O., and Takano, A.: Transparent ultra water-repellent poly (ethylene terephthalate) substrates fabricated by oxygen plasma treatment and subsequent hydrophobic coating. Applied Surface Science, 244(1-4):619–622, 2005.
369. Jafari Gukeh, M., Roy, T., Sen, U., Ganguly, R., and Megaridis, C. M.: Lateral spreading of gas bubbles on submerged wettability-confined tracks. Langmuir, 36(40):11829–11835, 2020.
370. Moitra, S., Roy, T., Ganguly, R., and Megaridis, C. M.: Jet impact on superhydrophobic metal mesh. Langmuir, 37(9):2891–2899, 2021.
371. Fürstner, R., Barthlott, W., Neinhuis, C., and Walzel, P.: Wetting and self-cleaning properties of artificial superhydrophobic surfaces. Langmuir, 21(3):956–961, 2005.
372. Feng, X., Zhai, J., and Jiang, L.: The fabrication and switchable superhydrophobicity of tio2 nanorod films. Angewandte Chemie, 117(32):5245–5248, 2005.
373. Zhang, X., Shi, F., Yu, X., Liu, H., Fu, Y., Wang, Z., Jiang, L., and Li, X.: Polyelectrolyte multilayer as matrix for electrochemical deposition of gold clusters: toward superhydrophobic surface. Journal of the American Chemical Society, 126(10):3064–3065, 2004.
374. Shang, H. M., Wang, Y., Takahashi, K., Cao, G. Z., Li, D., and Xia, Y.: Nanostructured superhydrophobic surfaces. Journal of materials science, 40(13):3587–3591, 2005.
375. Sun, W., Zhou, S., Chen, P., and Peng, L.: Reversible switching on superhydrophobic tio2 nano-strawberry films fabricated at low temperature. Chemical Communications, 5(5):603–605, 2008.

376. Bauer, S., Park, J., von der Mark, K., and Schmuki, P.: Improved attachment of mesenchymal stem cells on super-hydrophobic  $\text{TiO}_2$  nanotubes. Acta Biomaterialia, 4(5):1576–1582, 2008.
377. Kwak, G., Lee, M., Senthil, K., and Yong, K.: Wettability control and water droplet dynamics on  $\text{Si-SiO}_2$  core-shell nanowires. Langmuir, 26(14):12273–12277, 2010.
378. Niu, J. J. and Wang, J. N.: A novel self-cleaning coating with silicon carbide nanowires. The Journal of Physical Chemistry B, 113(9):2909–2912, 2009.
379. Feng, X., Feng, L., Jin, M., Zhai, J., Jiang, L., and Zhu, D.: Reversible super-hydrophobicity to super-hydrophilicity transition of aligned  $\text{ZnO}$  nanorod films. Journal of the American Chemical Society, 126(1):62–63, 2004.
380. Pauporté, T., Bataille, G., Joulaud, L., and Vermersch, F.: Well-aligned  $\text{ZnO}$  nanowire arrays prepared by seed-layer-free electrodeposition and their Cassie–Wenzel transition after hydrophobization. The Journal of Physical Chemistry C, 114(1):194–202, 2010.
381. Lee, M., Kwak, G., and Yong, K.: Wettability control of  $\text{ZnO}$  nanoparticles for universal applications. ACS Applied Materials & Interfaces, 3(9):3350–3356, 2011.
382. Sethi, S. and Dhinojwala, A.: Superhydrophobic conductive carbon nanotube coatings for steel. Langmuir, 25(8):4311–4313, 2009.
383. Yildirim, A., Budunoglu, H., Daglar, B., Deniz, H., and Bayindir, M.: One-pot preparation of fluorinated mesoporous silica nanoparticles for liquid marble formation and superhydrophobic surfaces. ACS Applied Materials & Interfaces, 3(6):1804–1808, 2011.
384. Fujishima, A., Rao, T. N., and Tryk, D. A.: Titanium dioxide photocatalysis. Journal of Photochemistry and Photobiology C: Photochemistry Reviews, 1(1):1–21, 2000.
385. Tian, D., Song, Y., and Jiang, L.: Patterning of controllable surface wettability for printing techniques. Chemical Society Reviews, 42(12):5184–5209, 2013.
386. Chatterjee, S., Sinha Mahapatra, P., Ibrahim, A., Ganguly, R., Yu, L., Dodge, R., and Megaridis, C. M.: Precise liquid transport on and through thin porous materials. Langmuir, 34(8):2865–2875, 2018.

387. Sen, U., Chatterjee, S., Sinha Mahapatra, P., Ganguly, R., Dodge, R., Yu, L., and Megaridis, C. M.: Surface-wettability patterning for distributing high-momentum water jets on porous polymeric substrates. ACS Applied Materials & Interfaces, 10(5):5038–5049, 2018.
388. Schmidt, J., Marques, M. R., Botti, S., and Marques, M. A.: Recent advances and applications of machine learning in solid-state materials science. npj Computational Materials, 5(1):1–36, 2019.
389. Elton, D. C., Boukouvalas, Z., Butrico, M. S., Fuge, M. D., and Chung, P. W.: Applying machine learning techniques to predict the properties of energetic materials. Scientific Reports, 8(1):1–12, 2018.
390. Bélisle, E., Huang, Z., Le Digabel, S., and Gheribi, A. E.: Evaluation of machine learning interpolation techniques for prediction of physical properties. Computational Materials Science, 98:170–177, 2015.
391. Shandiz, M. A. and Gauvin, R.: Application of machine learning methods for the prediction of crystal system of cathode materials in lithium-ion batteries. Computational Materials Science, 117:270–278, 2016.
392. Evans, J. D. and Coudert, F.-X.: Predicting the mechanical properties of zeolite frameworks by machine learning. Chemistry of Materials, 29(18):7833–7839, 2017.
393. Gurgenc, T., Altay, O., Ulas, M., and Ozel, C.: Extreme learning machine and support vector regression wear loss predictions for magnesium alloys coated using various spray coating methods. Journal of Applied Physics, 127(18):185103, 2020.
394. Arisoy, Y. M. and Özel, T.: Machine learning based predictive modeling of machining induced microhardness and grain size in ti-6al-4v alloy. Materials and Manufacturing Processes, 30(4):425–433, 2015.
395. Altay, O., Gurgenc, T., Ulas, M., and Özel, C.: Prediction of wear loss quantities of ferroalloy coating using different machine learning algorithms. Friction, 8(1):107–114, 2020.
396. Morrisette, J. M., Mahapatra, P. S., Ghosh, A., Ganguly, R., and Megaridis, C. M.: Rapid, self-driven liquid mixing on open-surface microfluidic platforms. Scientific Reports, 7(1):1800, 2017.



397. Lee, D. and Derrible, S.: Predicting residential water demand with machine-based statistical learning. Journal of Water Resources Planning and Management, 146(1):04019067, 2020.
398. Asif, K., Zhang, L., Derrible, S., Indacochea, J. E., Ozevin, D., and Ziebart, B.: Machine learning model to predict welding quality using air-coupled acoustic emission and weld inputs. Journal of Intelligent Manufacturing, 33:881–895, 2020.
399. Dayeen, F. R., Sharma, A. S., and Derrible, S.: A text mining analysis of the climate change literature in industrial ecology. Journal of Industrial Ecology, 24(2):276–284, 2020.
400. Seyrfar, A., Ataei, H., Movahedi, A., and Derrible, S.: Data-driven approach for evaluating the energy efficiency in multifamily residential buildings. Practice Periodical on Structural Design and Construction, 26(2):04020074, 2021.
401. Kohavi, R.: A study of cross-validation and bootstrap for accuracy estimation and model selection. In Ijcai, volume 14, pages 1137–1145. Montreal, Canada, 1995.
402. Pedregosa, F., Varoquaux, G., Gramfort, A., Michel, V., Thirion, B., Grisel, O., Blondel, M., Prettenhofer, P., Weiss, R., Dubourg, V., Vanderpals, J., Passos, A., Cournapeau, D., Brucher, M., and Perrot, M.: Scikit-learn: Machine learning in python. Journal of Machine Learning Research, 12:2825–2830, 2011.
403. Vovk, V.: Kernel Ridge Regression, pages 105–116. Berlin, Heidelberg, Springer Berlin Heidelberg, 2013.
404. Cortes, C. and Vapnik, V.: Support-vector networks. Machine Learning, 20(3):273–297, 1995.
405. Specht, D. F.: A general regression neural network. IEEE Transactions on Neural Networks, 2(6):568–576, 1991.
406. Hornik, K., Stinchcombe, M., and White, H.: Multilayer feedforward networks are universal approximators. Neural Networks, 2(5):359–366, 1989.
407. Friedman, J. H.: Greedy function approximation: A gradient boosting machine. Annals of Statistics, 29:1189–1232, 2001.

408. Kaufman, S., Rosset, S., Perlich, C., and Stitelman, O.: Leakage in data mining: Formulation, detection, and avoidance. ACM Transactions on Knowledge Discovery from Data (TKDD), 6(4):1–21, 2012.
409. Gau, H., Herminghaus, S., Lenz, P., and Lipowsky, R.: Liquid morphologies on structured surfaces: from microchannels to microchips. Science, 46-49:283, 1999.
410. Schutzius, T. M., Elsharkawy, M., Tiwari, M. K., and Megaridis, C. M.: Surface tension confined (STC) tracks for capillary-driven transport of low surface tension liquids. Lab Chip, 12(24):5237–5242, 2012.
411. Elsharkawy, M., Schutzius, T. M., and Megaridis, C. M.: Inkjet patterned superhydrophobic paper for open-air surface microfluidic devices. Lab Chip, 14:1168–1175, 2014.
412. Jo, H. J., Kim, S. H., Park, H. S., and Kim, M. H.: Critical heat flux and nucleate boiling on several heterogeneous wetting surfaces: controlled hydrophobic patterns on a hydrophilic substrate. Int. J. Multiphase Fl., 62:101–109, 2014.
413. Sinha Mahapatra, P., Ghosh, A., Ganguly, R., and Megaridis, C. M.: Key design and operating parameters for enhancing dropwise condensation through wettability patterning. Int. J. Heat Mass Transf., 92:877–883, 2016.
414. Koukoravas, T. P., Sinha Mahapatra, P., Ganguly, R., and Megaridis, C. M.: Wettability-confined liquid-film convective cooling: parameter study. Int. J. Heat Mass Transf., 126:667–676, 2018.
415. Cao, M., Li, Z., Ma, H., Geng, H., Yu, C., and Jiang, L.: Is superhydrophobicity equal to underwater superaerophilicity: regulating the gas behavior on superaerophilic surface via hydrophilic defects. ACS Appl. Mater. Interfaces, 10(24):20995–21000, 2018.
416. Zhang, P., Zhang, J., Xue, Z., Wang, J., and Jiang, L.: Reliable manipulation of gas bubbles by regulating interfacial morphologies and chemical components. Mater. Horiz., 4(4):665–672, 2017.
417. George, J. E., Chidangil, S., and George, S. D.: Recent progress in fabricating superaerophobic and superaerophilic surfaces. Adv. Mater. Interfaces, 4:1601088, 2017.
418. Liu, Z., Zhang, H., Han, Y., Huang, L., Chen, Y., Liu, J., Wang, X., Liu, X., and Ling, S.: Superaerophilic wedge-shaped channels with precovered air film for efficient

- subaqueous bubbles/jet transportation and continuous oxygen supplementation. ACS Appl. Mater. Interfaces, 11(26):23808–23814, 2019.
419. Yu, C., Cao, M., Dong, Z., Li, K., Yu, C., Wang, J., and Jiang, L.: Aerophilic electrode with cone shape for continuous generation and efficient collection of  $\text{H}_2$  bubbles. Adv. Func. Mater., 26(37):6830–6835, 2016.
  420. Yu, C., Zhu, X., Li, K., Cao, M., and Jiang, L.: Manipulating bubbles in aqueous environment via a lubricant-infused slippery surface. Adv. Func. Mater., 27(29):1701605, 2017.
  421. Zhang, C., Cao, M., Ma, H., Yu, C., Li, K., Yu, C., and Jiang, L.: Morphology-control strategy of the superhydrophobic poly (methyl methacrylate) surface for efficient bubble adhesion and wastewater remediation. Adv. Func. Mater., 27(43):1702020, 2017.
  422. Christopher, P., Xin, H., and Linic, S.: Visible-light-enhanced catalytic oxidation reactions on plasmonic silver nanostructures. Nature Chem., 3(6):467, 2011.
  423. Hu, H. and Wen, J., Bao, L., Jia, L., Song, D., Song, B., Pan, G., Scaraggi, M., Dini, D., Xue, Q., and Feng, Z.: Significant and stable drag reduction with air rings confined by alternated superhydrophobic and hydrophilic strips. Sci. Adv., 3(9):1603288, 2017.
  424. Zhu, S., Li, J., Cai, S., Bian, Y., Chen, C., Xu, B., Su, Y., Hu, Y., Wu, D., and Chu, J.: Unidirectional transport and effective collection of underwater  $\text{CO}_2$  bubbles utilizing ultrafast-laser-ablated Janus foam. ACS Appl. Mater. Interfaces, 12:18110–18115, 2020.
  425. Chen, C., Huang, Z., Shi, L.-A., Jiao, Y., Zhu, S., Li, J., Hu, Y., Chu, J., Wu, D., and Jiang, L.: Remote photothermal actuation of underwater bubble toward arbitrary direction on planar slippery  $\text{Fe}_3\text{O}_4$ -doped surfaces. Adv. Func. Mater., 29:1904766, 2019.
  426. Tang, X., Xiong, H., Kong, T., Tian, Y., Li, W.-D., and Wang, L.: Bioinspired nanostructured surfaces for on-demand bubble transportation. ACS Appl. Mater. Interfaces, 10(3):3029–3038, 2018.

427. Long, Z., Zhao, Y., Zhang, C., Zhang, Y., Yu, C., Wu, Y., Ma, J., Cao, M., and Jiang, L.: A multi-bioinspired dual-gradient electrode for microbubble manipulation toward controllable water splitting. Adv. Mater., page 1908099, 2020.
428. Ma, H., Cao, M., Zhang, C., Bei, Z., Li, K., Yu, C., and Jiang, L.: Directional and continuous transport of gas bubbles on superaerophilic geometry-gradient surfaces in aqueous environments. Adv. Func. Mater., 28(7):1705091, 2018.
429. Song, J., Liu, Z., Wang, X., Liu, H., Lu, Y., Deng, X., Carmalt, C. J., and Parkin, I. P.: High-efficiency bubble transportation in an aqueous environment on a serial wedge-shaped wettability pattern. J. Mater. Chem. A, 7(22):13567–13576, 2019.
430. Duan, J.-A., Dong, X., Yin, K., Yang, S., and Chu, D.: A hierarchical superaerophilic cone: Robust spontaneous and directional transport of gas bubbles. Appl. Phys. Lett., 113(20):203704, 2018.
431. Li, J. and Guo, Z.: Patterned slippery surface for bubble directional transportation and collection fabricated via a facile method. Research, 2019:9139535, 2019.
432. Lv, X., Jiao, Y., Wu, S., Li, C., Zhang, Y., Li, J., Hu, Y., and Wu, D.: Anisotropic sliding of underwater bubbles on microgrooved slippery surfaces by one-step femtosecond laser scanning. ACS Appl. Mater. Interfaces, 11(22):20574–20580, 2019.
433. Li, J. and Guo, Z.: Bubble shapes and their changes on slippery surfaces during directional transportation. J. Colloid Interface Sci., 552:84–90, 2019.
434. Tanner, L. H.: The spreading of silicone oil drops on horizontal surfaces. J. Phys. D: Appl. Phys., 12(9):1473, 1979.
435. Huppert, H. E.: The propagation of two-dimensional and axisymmetric viscous gravity currents over a rigid horizontal surface. J. Fluid Mech., 121:43–58, 1982.
436. Snoeijer, J. H. and Andreotti, B.: Moving contact lines: scales, regimes, and dynamical transitions. Annu. Rev. Fluid Mech., 45:269–292, 2013.
437. Huh, C. and Scriven, L. E.: Hydrodynamic model of steady movement of a solid/liquid/fluid contact line. J. Colloid Interface Sci., 35(1):85–101, 1971.
438. Vedder, W. and Vermilyea, D. A.: Aluminum+ water reaction. Trans. Faraday Soc., 65:561–584, 1969.

439. He, M., Zhou, X., Zeng, X., Cui, D., Zhang, Q., Chen, J., Li, H., Wang, J., Cao, Z., Song, Y., and Jiang, L.: Hierarchically structured porous aluminum surfaces for high-efficient removal of condensed water. Soft Matter, 8(25):6680–6683, 2012.
440. Sarkar, S., Roy, T., Roy, A., Moitra, S., Ganguly, R., and Megaridis, C. M.: Revisiting the supplementary relationship of dynamic contact angles measured by sessile-droplet and captive-bubble methods: Role of surface roughness. Journal of Colloid and Interface Science, 581:690 – 697, 2021.
441. Khosharay, S., Tourang, S., and Tajfar, F.: Modeling surface tension and interface of (water+ methanol),(water+ ethanol),(water+ 1-propanol), and (water+ meg) mixtures. Fluid Phase Equilibria, 454:99–110, 2017.
442. Hoke Jr., B. C. and Chen, J. C.: Binary aqueous-organic surface tension temperature dependence. J. Chem. Eng. Data, 36:322–326, 1991.
443. Sun, T. and Teja, A. S.: Density, viscosity, and thermal conductivity of aqueous ethylene, diethylene, and triethylene glycol mixtures between 290 K and 450 K. J. Chem. Eng. Data, 48:198–202, 2003.
444. Segur, J. B. and Oberstar, H. E.: Viscosity of glycerol and its aqueous solutions. Ind. Eng. Chem. Res., 43(9):2117–2120, 1951.
445. Takamura, K., Fischer, H., and Morrow, N. R.: Physical properties of aqueous glycerol solutions. J. Pet. Sci. Eng., 98-99:50–60, 2012.
446. Taylor, G. I.: The dynamics of thin sheets of fluid. III. Disintegration of fluid sheets. Proc. R. Soc. Lond. A, 253(1274):313–321, 1959.
447. Liu, Z. and Zheng, Y.: PIV study of bubble rising behavior. Powder Technol., 168(1):10–20, 2006.
448. de Maleprade, H., Clanet, C., and Quéré, D.: Spreading of bubbles after contacting the lower side of an aerophilic slide immersed in water. Phys. Rev. Lett., 117(9):094501, 2016.
449. Savva, N. and Bush, J. W. M.: Viscous sheet retraction. J. Fluid Mech., 626:211–240, 2009.

450. Jafari Gukeh, M., Damoulakis, G., and Megaridis, C. M.: Exploring the design features of wettability-patterned surfaces for condensation heat transfer. In 2022 21st IEEE Intersociety Conference on Thermal and Thermomechanical Phenomena in Electronic Systems (iTherm). IEEE, 2022.
451. Zhang, F., Yang, X., and Wang, C.: Liquid water removal from a polymer electrolyte fuel cell. Journal of the Electrochemical Society, 153(2):A225, 2005.
452. Hong, K. and Webb, R. L.: Performance of Dehumidifying Heat Exchangers With and Without Wetting Coatings. Journal of Heat Transfer, 121(4):1018–1026, 1999.
453. Seo, D., Lee, C., and Nam, Y.: Influence of geometric patterns of microstructured superhydrophobic surfaces on water-harvesting performance via dewing. Langmuir, 30(51):15468–15476, 2014.
454. Khawaji, A. D., Kutubkhanah, I. K., and Wie, J.-M.: Advances in seawater desalination technologies. Desalination, 221(1-3):47–69, 2008.
455. Bao, J., Lin, Y., Zhang, R., Zhang, N., and He, G.: Strengthening power generation efficiency utilizing liquefied natural gas cold energy by a novel two-stage condensation rankine cycle (tcrc) system. Energy Conversion and Management, 143:312–325, 2017.
456. Lee, A., Moon, M.-W., Lim, H., Kim, W.-D., and Kim, H.-Y.: Water harvest via dewing. Langmuir, 28(27):10183–10191, 2012.
457. Beér, J. M.: High efficiency electric power generation: The environmental role. Progress in Energy and Combustion Science, 33(2):107–134, 2007.
458. Jafari Gukeh, M., Damoulakis, G., and Megaridis, C. M.: Low-profile heat pipe consisting of wick-lined and non-adiabatic wickless wettability-patterned surfaces. Applied Thermal Engineering, 211:118433, 2022.
459. Liu, L. and Jacobi, A. M.: The effects of hydrophilicity on water drainage and condensate retention on air-conditioning evaporators. 2006.
460. Attinger, D., Frankiewicz, C., Betz, A. R., Schutzius, T. M., Ganguly, R., Das, A., Kim, C.-J., and Megaridis, C. M.: Surface engineering for phase change heat transfer: A review. MRS Energy&Sustainability , 1:E4, 2014.

461. Cho, H. J., Preston, D. J., Zhu, Y., and Wang, E. N.: Nanoengineered materials for liquid–vapour phase-change heat transfer. Nature Reviews Materials, 2(2):1–17, 2016.
462. Sikarwar, B. S., Khandekar, S., and Muralidhar, K.: Mathematical modelling of dropwise condensation on textured surfaces. Sadhana, 38(6):1135–1171, 2013.
463. Tanasawa, I. and Ochiai, J.-i.: Expeimental study on dropwise condensatioin. Bulletin of JSME, 16(98):1184–1197, 1973.
464. Chaudhury, M. K. and Whitesides, G. M.: How to make water run uphill. Science, 256(5063):1539–1541, 1992.
465. Miljkovic, N., Enright, R., and Wang, E. N.: Effect of droplet morphology on growth dynamics and heat transfer during condensation on superhydrophobic nanostructured surfaces. ACS nano, 6(2):1776–1785, 2012.
466. Miljkovic, N., Enright, R., Nam, Y., Lopez, K., Dou, N., Sack, J., and Wang, E. N.: Jumping-droplet-enhanced condensation on scalable superhydrophobic nanostructured surfaces. Nano letters, 13(1):179–187, 2013.
467. Izumi, M., Kumagai, S., Shimada, R., and Yamakawa, N.: Heat transfer enhancement of dropwise condensation on a vertical surface with round shaped grooves. Experimental Thermal and Fluid Science, 28(2-3):243–248, 2004.
468. Narhe, R. and Beysens, D.: Nucleation and growth on a superhydrophobic grooved surface. Physical review letters, 93(7):076103, 2004.
469. Peng, B., Ma, X., Lan, Z., Xu, W., and Wen, R.: Experimental investigation on steam condensation heat transfer enhancement with vertically patterned hydrophobic–hydrophilic hybrid surfaces. International Journal of Heat and Mass Transfer, 58:27–38, 2015.
470. Chatterjee, A., Derby, M. M., Peles, Y., and Jensen, M. K.: Condensation heat transfer on patterned surfaces. International Journal of Heat and Mass Transfer, 56:889–897, 2013.
471. Chatterjee, A., Derby, M. M., Peles, Y., and K. Jensen, M.: Enhancement of condensation heat transfer with patterned surfaces. International Journal of Heat and Mass Transfer, 57:675–681, 2014.

472. Miljkovic, N. and Wang, E. N.: Condensation heat transfer on superhydrophobic surfaces. MRS bulletin, 38(5):397–406, 2013.
473. Bonner III, R. W.: Correlation for dropwise condensation heat transfer: Water, organic fluids, and inclination. International Journal of Heat and Mass Transfer, 61:245–253, 2013.
474. Song, Z., Lu, M., and Chen, X.: Investigation of dropwise condensation heat transfer on laser-ablated superhydrophobic/hydrophilic hybrid copper surfaces. ACS omega, 5(37):23588–23595, 2020.
475. Wang, H., Nguyen, Q., Kwon, J. W., and Ma, H.: Condensation and wetting behavior on hybrid superhydrophobic and superhydrophilic copper surfaces. Journal of Heat Transfer, 142(4):041601, 2020.
476. Xie, J., She, Q., Xu, J., Liang, C., and Li, W.: Mixed dropwise-filmwise condensation heat transfer on biphilic surface. International Journal of Heat and Mass Transfer, 150:119273, 2020.
477. Wang, H., Zhao, X., Wang, J., Wang, Z., Wang, D., and Tian, J.: Enhanced dropwise condensation on heterogeneously hybrid patterned surfaces. Case Studies in Thermal Engineering, 27:101319, 2021.
478. Hou, Y., Yu, M., Chen, X., Wang, Z., and Yao, S.: Recurrent filmwise and dropwise condensation on a beetle mimetic surface. ACS nano, 9(1):71–81, 2015.
479. Clifford, A. A.: Multivariate error analysis. 1973.
480. Quéré, D., Azzopardi, M.-J., and Delattre, L.: Drops at rest on a tilted plane. Langmuir, 14(8):2213–2216, 1998.
481. Damoulakis, G., Bao, C., Jafari Gukeh, M., Mukhopadhyay, A., Mazumder, S. k., , and Megaridis, C. M.: Hybrid vapor chamber-based cooling system for power electronics. In 2022 21st IEEE Intersociety Conference on Thermal and Thermomechanical Phenomena in Electronic Systems (iTherm). IEEE, 2022.
482. Power Electronics Market, <https://www.marketsandmarkets.com/Market-Reports/power-electronics-market-204729766.html>.



483. Mohamadi, M., Kumar, N., Mazumder, S. K., and Gupta, A.: High power design challenges for differential-mode ev universal battery supercharger. IEEE Transactions on Industry Applications, pages 1–1, 2022.
484. Li, L., Li, B., Wang, Z., Yang, M., and Xu, D.: Monopolar symmetrical dcx2013;dc converter for all dc offshore wind farms. IEEE Transactions on Power Electronics, 37(4):4275–4287, 2022.
485. Bao, C. and Mazumder, S. K.: Multiresonant-frequency filter for an electrosurgery inverter. IEEE Transactions on Power Electronics, 37(6):6242–6246, 2022.
486. Abbaszadeh, M. A., Monfared, M., and Heydari-doostabad, H.: High buck in buck and high boost in boost dual-mode inverter (hb2dmi). IEEE Transactions on Industrial Electronics, 68(6):4838–4847, 2021.
487. Li, H., Liu, M., Yang, Y., Song, Z., and Wang, Y.: A multi-mhz active clamp topology for high cost-performance wireless power transfer. IEEE Transactions on Power Electronics, 37(10):12828–12840, 2022.
488. Chatterjee, D. and Mazumder, S. K.: Switching transition control to improve efficiency of a dc/dc power electronic system. IEEE Access, 9:91104–91118, 2021.
489. Nabih, A., Ahmed, M. H., Li, Q., and Lee, F. C.: Transient control and soft start-up for 1-mhz llc converter with wide input voltage range using simplified optimal trajectory control. IEEE Journal of Emerging and Selected Topics in Power Electronics, 9(1):24–37, 2021.
490. Bao, C. and Mazumder, S. K.: Reduced collateral tissue damage using thermal-feedback-based power adaptation of an electrosurgery inverter. IEEE Transactions on Power Electronics, 37(10):11540–11545, 2022.
491. Tong, H.-M., Lai, Y.-S., and Wong, C.: Advanced flip chip packaging, volume 142. Springer, 2013.
492. Black, J. R.: Electromigration—a brief survey and some recent results. IEEE transactions on Electron devices, 16(4):338–347, 1969.
493. Koukoravas, T. P., Damoulakis, G., and Megaridis, C. M.: Experimental investigation of a vapor chamber featuring wettability-patterned surfaces. Applied Thermal Engineering, 178:115522, 2020.

494. Hanlon, M. A. and Ma, H. B.: Evaporation heat transfer in sintered porous media. J.Heat Transfer, 125(4):644–652, 2003.
495. Wang, Y. and Peterson, G.: Analytical model for capillary evaporation limitation in thin porous layers. Journal of thermophysics and heat transfer, 17(2):145–149, 2003.
496. Sudhakar, S., Weibel, J. A., and Garimella, S. V.: Experimental investigation of boiling regimes in a capillary-fed two-layer evaporator wick. International Journal of Heat and Mass Transfer, 135:1335–1345, 2019.
497. Ju, Y. S., Kaviani, M., Nam, Y., Sharratt, S., Hwang, G., Catton, I., Fleming, E., and Dussinger, P.: Planar vapor chamber with hybrid evaporator wicks for the thermal management of high-heat-flux and high-power optoelectronic devices. International Journal of Heat and Mass Transfer, 60:163–169, 2013.
498. Weibel, J., Kim, S., Fisher, T. S., and Garimella, S. V.: Carbon nanotube coatings for enhanced capillary-fed boiling from porous microstructures. Nanoscale and Microscale Thermophysical Engineering, 16(1):1–17, 2012.
499. Cai, Q. and Chen, Y.-C.: Investigations of biporous wick structure dryout. Journal of Heat Transfer, 134(2):021503, 2012.
500. Zhang, G., Liu, Z., and Wang, C.: An experimental study of boiling and condensation co-existing phase change heat transfer in small confined space. International Journal of Heat and Mass Transfer, 64:1082–1090, 2013.
501. Wu, S., Dai, H., Wang, H., Shen, C., and Liu, X.: Role of condensation on boiling heat transfer in a confined chamber. Applied Thermal Engineering, 185:116309, 2021.
502. Zhang, X., Liu, Z., and Li, Y.: Effects of the heating surface structure of phase change chamber on boiling-condensation coexisting phase change heat transfer. International Journal of Heat and Mass Transfer, 151:119437, 2020.
503. Zhang, W., Wen, X., Yang, S., Berta, Y., and Wang, Z. L.: Single-crystalline scroll-type nanotube arrays of copper hydroxide synthesized at room temperature. Advanced Materials, 15(10):822–825, 2003.
504. Weibel, J. A., Garimella, S. V., and North, M. T.: Characterization of evaporation and boiling from sintered powder wicks fed by capillary action. International Journal of Heat and Mass Transfer, 53(19-20):4204–4215, 2010.

505. Pati, S., Som, S., and Chakraborty, S.: Combined influences of electrostatic component of disjoining pressure and interfacial slip on thin film evaporation in nanopores. International Journal of Heat and Mass Transfer, 64:304–312, 2013.
506. Lv, L. and Li, J.: Managing high heat flux up to 500 w/cm<sup>2</sup> through an ultra-thin flat heat pipe with superhydrophilic wick. Applied Thermal Engineering, 122:593–600, 2017.
507. Li, Y.-C. and Wong, S.-C.: Effects of vapor duct thickness on the capillary blocking and thermal performance of ultra-thin vapor chambers under natural convection cooling. Applied Thermal Engineering, 195:117148, 2021.
508. Zhou, F., Zhou, G., Zhou, J., Huai, X., Jiang, Y., and Huang, Q.: Thermal performance evaluation of a novel ultra-thin vapor chamber with laval-like nozzle composite wick under different air cooling conditions. Case Studies in Thermal Engineering, 31:101845, 2022.
509. Li, H.-Y., Chiang, M.-H., Lee, C.-I., and Yang, W.-J.: Thermal performance of plate-fin vapor chamber heat sinks. International Communications in Heat and Mass Transfer, 37(7):731–738, 2010.
510. Wong, S.-C., Huang, S.-F., and Hsieh, K.-C.: Performance tests on a novel vapor chamber. Applied Thermal Engineering, 31(10):1757–1762, 2011.
511. Tavakkoli, F., Ebrahimi, S., Wang, S., and Vafai, K.: Analysis of critical thermal issues in 3d integrated circuits. International Journal of Heat and Mass Transfer, 97:337–352, 2016.
512. Tang, H., Tang, Y., Wan, Z., Li, J., Yuan, W., Lu, L., Li, Y., and Tang, K.: Review of applications and developments of ultra-thin micro heat pipes for electronic cooling. Applied Energy, 223:383–400, 2018.
513. Tang, Y., Lin, L., Zhang, S., Zeng, J., Tang, K., Chen, G., and Yuan, W.: Thermal management of high-power leds based on integrated heat sink with vapor chamber. Energy conversion and management, 151:1–10, 2017.
514. Moon, S. H., Hwang, G., Yun, H. G., Choy, T. G., and Kang, Y. I.: Improving thermal performance of miniature heat pipe for notebook pc cooling. Microelectronics Reliability, 42(1):135–140, 2002.

515. Naphon, P., Wongwises, S., and Wiriyaart, S.: Application of two-phase vapor chamber technique for hard disk drive cooling of pcs. International Communications in Heat and Mass Transfer, 40:32–35, 2013.
516. Faghri, A.: Heat pipe science and technology. Global Digital Press, 1995.
517. Pounds, D. and Bonner, R. W.: High heat flux heat pipes embedded in metal core printed circuit boards for led thermal management. In Fourteenth Intersociety Conference on Thermal and Thermomechanical Phenomena in Electronic Systems (ITherm), pages 267–271. IEEE, 2014.
518. Salem, T. K., Khosroshahi, F. S., Arik, M., Hamdan, M. O., and Budakli, M.: Numerical and experimental analysis of a heat-pipe-embedded printed circuit board for solid state lighting applications. Experimental Heat Transfer, 32(1):1–13, 2019.
519. Peterson, G. P.: An introduction to heat pipes. modeling, testing, and applications. Wiley Series in Thermal Management of Microelectronic and Electronic Systems, 1994.
520. Li, C., Peterson, G. P., and Wang, Y.: Evaporation/Boiling in Thin Capillary Wicks (I)—Wick Thickness Effects. Journal of Heat Transfer, 128(12):1312–1319, 2006.
521. Li, C. and Peterson, G. P.: Evaporation/Boiling in Thin Capillary Wicks (II)—Effects of Volumetric Porosity and Mesh Size. Journal of Heat Transfer, 128(12):1320–1328, 2006.
522. Zhu, M., Huang, J., Song, M., and Hu, Y.: Thermal performance of a thin flat heat pipe with grooved porous structure. Applied Thermal Engineering, 173:115215, 2020.
523. Liou, J.-H., Chang, C.-W., Chao, C., and Wong, S.-C.: Visualization and thermal resistance measurement for the sintered mesh-wick evaporator in operating flat-plate heat pipes. International Journal of Heat and Mass Transfer, 53(7-8):1498–1506, 2010.
524. Tang, H., Lian, L., Zhang, J., and Liu, Y.: Heat transfer performance of cylindrical heat pipes with axially graded wick at anti-gravity orientations. Applied Thermal Engineering, 163:114413, 2019.
525. North, M. T.: Optimization of heat pipe thermal transport using axially graded capillary wick structures. In ASME International Mechanical Engineering Congress and Exposition, volume 42215, pages 855–862, 2005.

526. Li, J. and Lv, L.: Experimental studies on a novel thin flat heat pipe heat spreader. Applied Thermal Engineering, 93:139–146, 2016.
527. Wong, S.-C., Lin, Y.-C., and Liou, J.-H.: Visualization and evaporator resistance measurement in heat pipes charged with water, methanol or acetone. International Journal of Thermal Sciences, 52:154–160, 2012.
528. Zu, S., Liao, X., Huang, Z., Li, D., and Jian, Q.: Visualization study on boiling heat transfer of ultra-thin flat heat pipe with single layer wire mesh wick. International Journal of Heat and Mass Transfer, 173:121239, 2021.
529. Wong, S.-C., Deng, M.-S., and Liu, M.-C.: Characterization of composite mesh-groove wick and its performance in a visualizable flat-plate heat pipe. International Journal of Heat and Mass Transfer, page 122259, 2021.
530. Chang, C., Han, Z., He, X., Wang, Z., and Ji, Y.: 3d printed aluminum flat heat pipes with micro grooves for efficient thermal management of high power leds. Scientific Reports, 11(1):1–8, 2021.
531. Gibbons, M. J., Marengo, M., and Persoons, T.: A review of heat pipe technology for foldable electronic devices. Applied Thermal Engineering, 194:117087, 2021.
532. Amethermasol company. Flat cool pipes/MHP serie.
533. Weng, Y.-C., Cho, H.-P., Chang, C.-C., and Chen, S.-L.: Heat pipe with pcm for electronic cooling. Applied Energy, 88(5):1825–1833, 2011.
534. Kim, K.-S., Won, M.-H., Kim, J.-W., and Back, B.-J.: Heat pipe cooling technology for desktop pc cpu. Applied thermal engineering, 23(9):1137–1144, 2003.
535. Moon, S. H., Hwang, G., Yun, H. G., Choy, T. G., and Kang, Y. I.: Improving thermal performance of miniature heat pipe for notebook pc cooling. Microelectronics Reliability, 42(1):135–140, 2002.
536. Yousefi, T., Mousavi, S., Farahbakhsh, B., and Saghir, M.: Experimental investigation on the performance of cpu coolers: Effect of heat pipe inclination angle and the use of nanofluids. Microelectronics Reliability, 53(12):1954–1961, 2013.

537. Elnaggar, M. H., Abdullah, M., and Mujeebu, M. A.: Experimental analysis and fem simulation of finned u-shape multi heat pipe for desktop pc cooling. Energy Conversion and Management, 52(8-9):2937–2944, 2011.
538. Elnaggar, M. H. and Edwan, E.: Heat pipes for computer cooling applications. Electronics Cooling, page 51, 2016.
539. Liang, J., Gan, Y., and Li, Y.: Investigation on the thermal performance of a battery thermal management system using heat pipe under different ambient temperatures. Energy conversion and management, 155:1–9, 2018.
540. Huang, X. and Franchi, G.: Design and fabrication of hybrid bi-modal wick structure for heat pipe application. Journal of Porous Materials, 15(6):635–642, 2008.
541. Mahapatra, P. S., Ghosh, A., Ganguly, R., and Megaridis, C. M.: Key design and operating parameters for enhancing dropwise condensation through wettability patterning. International Journal of Heat and Mass Transfer, 92:877–883, 2016.
542. Taylor, J. R.: An introduction to error analysis university science. Mill Valley, Calif, 1982.
543. Iverson, B. D., Davis, T. W., Garimella, S. V., North, M. T., and Kang, S. S.: Heat and mass transport in heat pipe wick structures. Journal of Thermophysics and Heat Transfer, 21(2):392–404, 2007.
544. Ranjan, R., Murthy, J. Y., and Garimella, S. V.: A microscale model for thin-film evaporation in capillary wick structures. International Journal of Heat and Mass Transfer, 54(1-3):169–179, 2011.
545. Ranjan, R., Patel, A., Garimella, S. V., and Murthy, J. Y.: Wicking and thermal characteristics of micropillared structures for use in passive heat spreaders. International Journal of Heat and Mass Transfer, 55(4):586–596, 2012.
546. Li, Y., He, J., He, H., Yan, Y., Zeng, Z., and Li, B.: Investigation of ultra-thin flattened heat pipes with sintered wick structure. Applied Thermal Engineering, 86:106–118, 2015.
547. Xu, P. and Li, Q.: Visualization study on the enhancement of heat transfer for the groove flat-plate heat pipe with nanoflower coated cuo layer. Applied Physics Letters, 111(14):141609, 2017.

548. Liao, X., Jian, Q., Zu, S., Li, D., and Huang, Z.: Visualization study and analysis on the heat transfer performance of an ultra-thin flat-plate heat pipe. International Communications in Heat and Mass Transfer, 126:105464, 2021.
549. Oshman, C., Shi, B., Li, C., Yang, R., Lee, Y. C., Peterson, G. P., and Bright, V. M.: The development of polymer-based flat heat pipes. Journal of Microelectromechanical Systems, 20(2):410–417, 2011.
550. Zhang, Y. and Haghani, A.: A gradient boosting method to improve travel time prediction. Transportation Research Part C: Emerging Technologies, 58:308–324, 2015.
551. Kuhn, M. and Johnson, K.: Applied predictive modeling, volume 26. Springer, New York, 2013.
552. James, G., Witten, D., Hastie, T., and Tibshirani, R.: An introduction to statistical learning, volume 112. Springer, New York, 2013.
553. Friedman, J., Hastie, T., and Tibshirani, R.: The elements of statistical learning, volume 1. Springer series in statistics New York, 2001.
554. Young, W. C., Budynas, R. G., and Sadegh, A. M.: Roark's formulas for stress and strain. McGraw-Hill Education, 2012.
555. Kempers, R., Robinson, A. J., Ewing, D. W., and Ching, C. Y.: Characterization of evaporator and condenser thermal resistances of a screen mesh wicked heat pipe. International Journal of Heat and Mass Transfer, 51(25-26):6039–6046, 2008.
556. Jafari Gukeh, M., Moitra, S., Ibrahim, A. N., Derrible, S., and Megaridis, C. M.: Machine learning prediction of tio2-coating wettability tuned via uv exposure. ACS Applied Materials & Interfaces, 13(38):46171–46179, 2021.

## VITA

# Mohamad Jafari Gukeh

Micro/Nanoscale Fluid Transport Laboratory (MNFTL)

Department of Mechanical and Industrial Engineering

University of Illinois at Chicago (UIC)

842 W Taylor St, Chicago, IL 60607

Office Phone: (312) 413-7601

## EDUCATION

- Doctor of Philosophy (Ph.D.) (2022)  
University of Illinois at Chicago  
Mechanical Engineering  
Ph.D. Thesis Title: “Case Studies of Surface Engineering Applications in Thermo/Fluidic Systems”
- Master of Science (M.Sc) (2020)  
University of Illinois at Chicago  
Mechanical Engineering
- Bachelor of Science (B.Sc) (2017)  
Sharif University of Technology  
Mechanical Engineering

## Experience

- R&D Intern (Summer 2022)  
Amica Systems- Irvine, CA.
- Research Assistant (Jan 2018 - Dec 2022)  
University of Illinois at Chicago- Chicago, IL.
- Teaching Assistant (Aug 2019 - May 2021)  
University of Illinois at Chicago- Chicago, IL.



## Journal Publications

- Mohamad Jafari Gukeh, George Damoulakis, and Constantine M. Megaridis. "Low-profile heat pipe consisting of wick-lined and non-adiabatic wickless wettability-patterned surfaces." *Applied Thermal Engineering* 211 (2022): 118433.
- George Damoulakis, Mohamad Jafari Gukeh, Theodore P. Koukoravas, and Constantine M. Megaridis. "High-Performance Planar Thermal Diode With Wickless Components." *ASME. J. Electron. Packag.* 2022; 144(3): 031004.
- Mohamad Jafari Gukeh, Shashwata Moitra, Ali Noaman Ibrahim, Sybil Derrible, and Constantine M. Megaridis. "Machine learning prediction of TiO<sub>2</sub>-coating wettability tuned via UV exposure." *ACS Applied Materials & Interfaces* 13, no. 38 (2021): 46171-46179.
- Mohamad Jafari Gukeh, Tamal Roy, Uddalok Sen, Ranjan Ganguly, and Constantine M. Megaridis. "Lateral spreading of gas bubbles on submerged wettability-confined tracks." *Langmuir* 36, no. 40 (2020): 11829-11835.
- Bernardini, Jacopo, Uddalok Sen, Mohamad Jafari Gukeh, Pietro Asinari, and Constantine M. Megaridis. "Wettability-Engineered Meshes for Gas Microvolume Precision Handling in Liquids." *ACS applied materials & interfaces* 12, no. 15 (2020): 18046-18055.

## Conference Publications

- Mohamad Jafari Gukeh, George Damoulakis, and Constantine M. Megaridis. "Experimental investigation of low-profile heat pipe with wickless wettability-patterned condenser." In *2021 20th IEEE Intersociety Conference on Thermal and Thermomechanical Phenomena in Electronic Systems (iTherm)*, pp. 271-279. IEEE, 2021.
- George Damoulakis, Mohamad Jafari Gukeh, Shashwata Moitra, and Constantine M. Megaridis. "Quantifying Steam Dropwise Condensation Heat Transfer via Experiment, Computer Vision and Machine Learning Algorithms." In *2021 20th IEEE Intersociety Conference on Thermal and Thermomechanical Phenomena in Electronic Systems (iTherm)*, pp. 1015-1023. IEEE, 2021.

- George Damoulakis, Mohamad Jafari Gukeh, Theodore P. Koukouravas, and Constantine M. Megaridis. "Vapor Chamber with Wickless Condenser-Thermal Diode." In 2020 19th IEEE International Conference on Thermal and Thermomechanical Phenomena in Electronic Systems (ITherm), pp. 104-112. IEEE, 2020.

### Conference Presentations

- Mohamad Jafari Gukeh, George Damoulakis, and Constantine Megaridis. "Experimental Investigation of a Low-Profile Heat Pipe with Wickless Wettability-Patterned Condenser." Bulletin of the American Physical Society (2022).
- Sreya Sarkar, Mohamad Jafari Gukeh, Tamal Roy, Ranjan Ganguly, George Damoulakis, and Constantine Megaridis. "An experimental procedure to quantify solid-liquid surface energy in wetting configurations." Bulletin of the American Physical Society (2022).
- George Damoulakis, Mohamad Jafari Gukeh, and Constantine Megaridis. "Condensation Experiments on Wettability-Patterned Surfaces in the Absence of Non-Condensable Gases." Bulletin of the American Physical Society (2022).
- Mohamad Jafari Gukeh, Tamal Roy, Uddalok Sen, Ranjan Ganguly, and Constantine Megaridis. "Lateral Spreading of Gas Bubbles on Submerged Horizontal Wettability-confined Tracks." In APS Division of Fluid Dynamics Meeting Abstracts, pp. F01-001. 2020.
- Mohamad Jafari Gukeh, Uddalok Sen, Ranjan Ganguly, and Constantine Megaridis. "Pumpless, directional transport of gas bubbles on wettability-patterned diverging tracks." Bulletin of the American Physical Society 63 (2018).